Novel Ligands Based on 2,6-Di(1*H*-pyrazol-5-yl)pyridine Derivatives and Applications in Spin Crossover and Transfer Hydrogenation Complexes

Thomas David Roberts

Submitted in accordance with the requirements for the degree of Doctor of Philosophy

The University of Leeds

School of Chemistry

April 2015

The candidate confirms that the work submitted is his/her own, except where work which has formed part of jointly authored publications has been included. The contribution of the candidate and the other authors to this work has been explicitly indicated below. The candidate confirms that appropriate credit has been given within the thesis where reference has been made to the work of others.

Three papers containing work from my PhD have been published at the time of writing, which contain results from Chapters 2, 3 and 4 of the thesis. Although I contributed to the preparation of these manuscripts, the final versions were completed by my supervisor Prof Halcrow, who is also the corresponding author on all the papers. The description of these results in Chapters 2, 3 and 4 is not directly reproduced from the papers, and has been written in my own words.

The references are:

"Iron(II) complexes of 2,6-di(1-alkylpyrazol-3-yl)pyridine derivatives – the influence of distal substituents on the spin state of the iron center", T. D. Roberts, M. A. Little, L. J. Kershaw Cook, S. A. Barrett, F. Tuna and
M. A. Halcrow, *Polyhedron*, **2013**, *64*, 4–12.

"Iron(II) complexes of 2,6-di(1*H*-pyrazol-3-yl)pyridine derivatives with hydrogen bonding and sterically bulky substituents", T. D. Roberts, M. A. Little, L. J. Kershaw Cook and M. A. Halcrow, *Dalton Transactions,* **2014**, *43,* 7577–7588.

"Spin state behaviour of iron(II)/dipyrazolylpyridine complexes: new insights from crystallographic and solution measurements", L. J. Kershaw Cook, R. Mohammed, G. Sherborne, T. D. Roberts, S. Alvarez and M. A. Halcrow, *Coordination Chemistry Reviews*, in the press, doi: 10.1016/j.ccr.2014.08.006.

Acknowledgements

Firstly I would like to thank my supervisor Prof. Malcolm Halcrow for giving me the fantastic opportunity to be a part of his research group and to work on this project. His chemical wisdom, support and guidance throughout the past four years has seen me come a long way from the blundering Masters student that began in his lab.

I would like to thank all the technical staff at the University of Leeds, Ms. Tanya Marinko-Covell, Mr. Ian Blakely, Mr. Simon Barrett, Mr. Martin Huscroft, Dr Algy Kazlauciunas and Dr. Tim Comyn for mass spectrometry, microanalysis, NMR, HPLC-MS, TGA and variable temperature x-ray diffraction. Special thanks goes to Dr Marc Little and Dr Chris Pask for patiently training me to use the x-ray diffractometer and for keeping the service running smoothly.

My thanks go out to all members, past and present, of the Halcrow, Hardie, McGowan and Willans groups for their advice, guidance and general ribaldry. In particular I would like to thank Laurence, Jonathan, Raf, Chris, Steph, Rianne, Carlo, Felix, Flora,Vikki, Mike, Ben, James and Jordan, all of whom I have shared hilarious nights, amazing conferences and brutal hangovers with. Special thanks go to Amedeo Santoro whose support over the past three years has been invaluable, and who helped to shape many of the ideas in this thesis. I will particularly miss lengthy debates about British Vs Italian cars and your legendary barbecues. Planet Rock also deserves a mention for keeping me sane in the lab.

In addition to the friends have made through university, I would also like to thank all my close friends I have kept since high school for their support. Their ability to always cheer me up when things aren’t quite going my way has undoubtedly kept me sane throughout the past few years. In particular I would like to thank my flatmates Ed and Ben for movie nights, epic mealtimes and some crazy holidays throughout the years. There will be many more to come.

Perhaps most importantly would like to thank my family for supporting me for my whole life and without whom I would be in no position to go to university. I thank my Granddad Roberts in particular, whose mentoring early in life has greatly contributed to my academic success. I would like to thank my Mum, Dad and Sally for all their moral and financial support and the Sunday dinners. It is to you that I dedicate this thesis. Finally I would like to thank my girlfriend Kerry for all her love, support, and the espresso machine which allowed me to write this thesis.

Table of Contents

List of Abbreviations

$^{13}C\{^1H\}$	Carbon NMR (proton decoupled)
1-bpp	2,6-Di(pyrazol-1-yl)pyridine
^1H	Proton NMR
$^{31}P\{^1H\}$	Phosphorous NMR (proton decoupled)
3-bpp	2,6-Di(1*H*-pyrazol-3-yl)pyridine
Å	Angstrom
All	Allyl
CLF	Cellular ligand field
CV	Cyclic voltammetry
DF	Density functional
DMSO	Dimethylsulphoxide
DN	Donor number
D_q	Ligand field splitting parameter
E_N	Solvent polarity
ES^+	Electro-spray ionisation (positive)
ESD	Estimated standard deviation
FT-IR	Fourier transform infra-red spectroscopy
G	Gibbs free energy
GC	Gas chromatography
H	Enthalpy
HPLC-MS	High pressure liquid chromatography coupled with mass spectrometry
HS	High spin
Hz	Hertz
^iPr	Isopropyl

ISC	Intersystem crossing
J	Coupling constant (NMR)
L	Ligand
LFSE	Ligand field stabilisation energy
LIESST	Light induced excited spin state trapping
LS	Low spin
m	Medium
Me	Methyl
Mes	Mesityl
MLCT	Metal-to-ligand charge-transfer
MRI	Magnetic resonance imaging
MS	Mass spectrometry
NMR	Nuclear magnetic resonance
PARACEST	Paramagnetic chemical exchange saturation transfer
Ph	Phenyl
PXRD	Powder x-ray diffraction
Py	Pyridyl
Pz	Pyrazolyl
S	Entropy
s	Strong
SB	Solvent basicity
SCO	Spin crossover
SQUID	Superconducting quantum interference device
T(LIESST)	Temperature threshold for the LIESST effect
$T_{1/2}$	Spin crossover transition temperature
^{t}Bu	*Tert*butyl
TFA	Trifluoroacetic acid

TGA	Thermogravimetric analysis
TH	Transfer hydrogenation
THF	Tetrahydrofuran
TOF	Turnover frequency
TON	Turnover number
UV/vis	Ultraviolet/visible spectroscopy
vs	Very strong
VTPXRD	Variable temperature powder x-ray diffraction
w	Weak
XRD	X-ray diffraction
ZFS	Zero field splitting
β	Hydrogen-bond acceptor basicity
δ	Chemical shift (ppm)
Δ_{oct}	Octahedral splitting energy
$\chi_M T$	Magnetic susceptibility ($cm^3mol^{-1}K$)

The University of Leeds

Novel 2,6-Di(1*H*-pyrazol-3-yl)pyridine Complexes for Applications
in Spin-Crossover and Transfer Hydrogenation
Submitted for the Degree of Ph.D.
April, 2015

Thomas David Roberts

Abstract

This thesis is an account of the synthesis of novel iron(II) and ruthenium(II) complexes using 2,6-di(1*H*-pyrazol-3-yl)pyridine based ligands and their efficacy as spin crossover complexes and transfer hydrogenation catalysts respectively.

Chapter 1 is an introduction to the spin crossover and transfer hydrogenation detailing significant literature examples, important influencing factors and applications.

Chapter 2 details the synthetic pathways towards all novel ligands used in this work, including numerous attempted pathways and problems which were overcome.

Chapter 3 describes the properties of a number of iron(II) complexes made using 2,6-di(alkylpyrazol-3-yl)pyridine ligands. It is shown here that subtle steric and electronic factors about the iron(II) coordination sphere hinder spin crossover.

Chapter 4 is a comparison of spin crossover properties of iron(II) complexes containing 2,6-di(1*H*-pyrazol-3-yl)pyridine ligands bearing a number of different substituents on different positions. The spin crossover behaviour of these complexes is rationalised based on crystal structures, powder x-ray diffraction and magnetic susceptibility measurements.

Chapter 5 is an explanation of the differing magnetic susceptibilities of a number of solid solutions of the complex $[Fe\mathbf{L}_2]X_2$ (**L** = 2,6-di(1*H*-5-methylpyrazol-3-yl)pyridine).

Chapter 6 shows the effectiveness of a number of ruthenium(II) pincer type complexes as catalysts for the transfer hydrogenation of acetophenone derivatives.

Chapter 7 is an account of all the synthetic procedures used in this work and includes the full analysis of all novel compounds synthesised.

Chapter 1

Introduction

1.1. The Spin Crossover Phenomenon

1.1.1. Background

The spin crossover (SCO) phenomenon has received much interest since its discovery in 1931, whereby Cambi and co-workers recorded an abrupt drop in the magnetic moment of *tris*(N,N-dialkyldithiocarbamato) iron(III) complexes at low temperatures.[1] The behaviour of these complexes was attributed to a chemical equilibrium between two magnetically isomeric forms. Around this time various ferrihemoglobin derivatives were also shown to possess either five or one unpaired electron and these differences were attributed to different combinations of ionic and covalent bonding to the iron centre.[2] These findings, however, were not properly understood until after the development of ligand field theory and it wasn't until over thirty years later that Cambi's results were revisited and explained as the thermally induced switching between two almost equi-energetic spin states.[3] This significant leap in the understanding of these systems resulted in an explosion of interest in the SCO phenomenon and to date examples of Co(II)/(III),[4-6] Ni(II),[7] Mn(II)/(III),[8, 9] and Fe(II)/(III)[10-12] complexes have been synthesised and shown to exhibit SCO behaviour.

In an octahedral coordination geometry interaction of the metal *d* orbitals with coordinating ligands breaks the degeneracy of the *d* orbitals (Figure 1.1). The d_{xy}, d_{xz} and d_{yz} orbitals are termed the t_{2g} orbitals and are non-bonding with respect to the metal–ligand bond. The d_{z2} and $d_{x2\text{-}y2}$ orbitals, termed the e_g orbitals, are anti-bonding with respect to the metal–ligand bond and raised to a higher energy than the t_{2g} orbitals and the barycentre.[13] The energy gap between the t_{2g} and e_g orbitals is termed the octahedral splitting energy, Δ_{oct}, or the ligand field splitting energy, 10Dq, and the magnitude is dependent on the field strength of the ligands, the specific metal centre and its oxidation state. The magnitude of this parameter can be determined by absorption spectra by observing the energy of the *d*-*d* transitions.

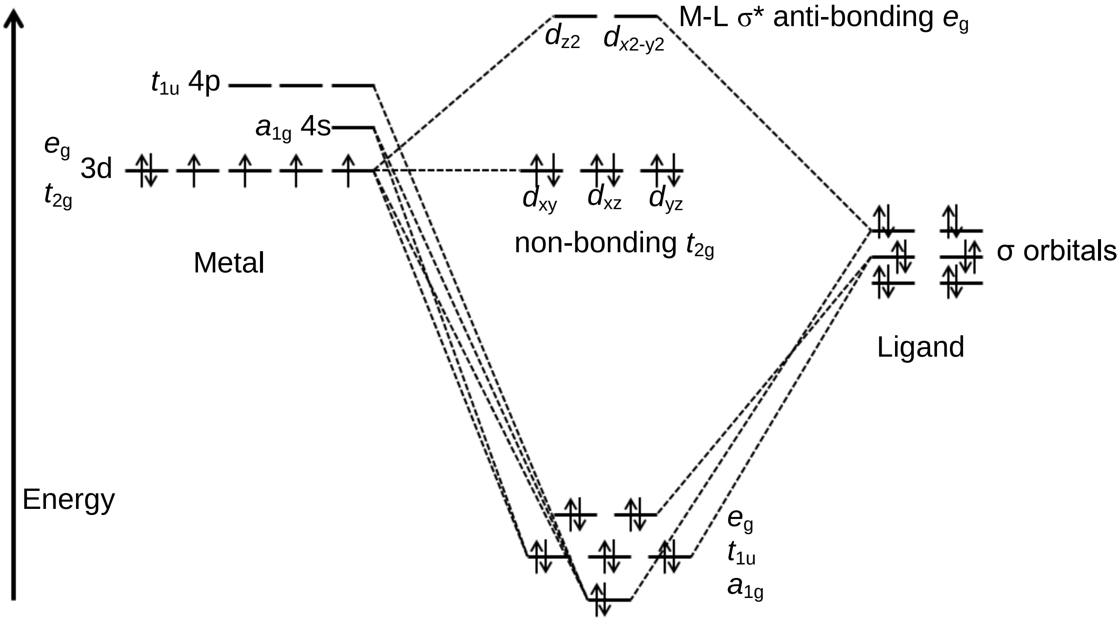

Figure 1.1
An MO diagram of a d^6 octahedral metal complex showing the origin of the ligand field splitting.

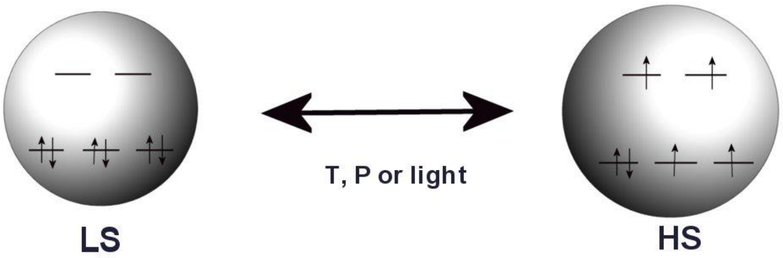

Figure 1.2
A simple representation of the SCO phenomenon.

Metal centres from d^4 to d^7 configurations can exist in either a high spin or low spin state, and whichever state is observed depends on the relative energies of the octahedral splitting energy, Δ_{oct}, and the Hund's rule exchange energy, P. The Hund's rule exchange energy, P, arises from the Pauli exclusion principle, which states that two electrons cannot occupy the same space. Therefore two electrons in the same orbital will repel one another, leading to an unfavourable gain in energy of the system. In the instance of a weak ligand field with a small Δ_{oct} electrons will occupy the t_{2g} and e_g orbitals in accordance to Hund's rule, thus avoiding the unfavourable energy gain from pairing electrons. In a d^6 metal centre such as iron(II) this will result in a high spin (HS) complex in the quintet $^5T_{2g}$ ($t_{2g}{}^4e_g{}^2$) state. However if Δ_{oct} is larger than the energy it costs to pair electrons, such as in a strong ligand field, then it will be energetically favourable to have as many electrons in the t_{2g} orbital as possible. In the case of a d^6 metal centre such as iron(II) this will result in a low spin (LS) singlet $^1A_{1g}$ (t_{2g}^6) state (Figure 1.2).

In the case where the difference in the minimum of the $^5T_{2g}$ and $^1A_{1g}$ potential energy wells, $E^0_{\mathrm{HS}} - E^0_{\mathrm{LS}}$, are approximately equal to the ambient thermal energy, k_BT, a spin transition can be triggered by variation of temperature (Figure 1.3). From Figure 1.1 and Figure 1.2 it is shown that in the HS state electrons occupy the e_g orbitals. As these orbitals are anti-bonding with respect to the M–L bonds this has the effect of weakening these bonds and expanding the coordination sphere. The value of Δ_{oct} is largely dependent on r(M–L) and will be smaller in magnitude in the HS complex due to the decreased proximity of the metal d and ligand orbitals. In contrast P is likely to change very little between states and may even be slightly larger in the HS state due to the nephelauxetic effect. The nephelauxetic effect is an expansion of the metal d orbitals and is caused by overlap of the metal d and ligand p orbitals.[14] In the HS complex the lower proximity of the metal and ligand orbitals results in smaller overlap, reducing the nephelauxetic effect and slightly increasing P. [15] this effect will be greatest in iron(II) complexes containing N-donor ligands, as the Fe–N bond length has been shown to be most affected by a spin transition.[16]

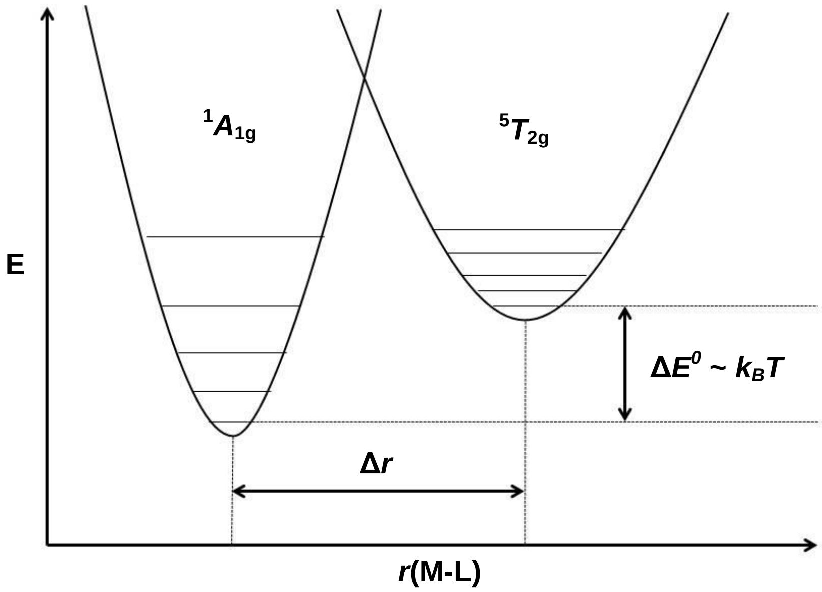

Figure 1.3
A diagram showing the potential energy wells of the LS $^1A_{1g}$ state and the HS $^5T_{2g}$ state.

In terms of enthalpy the LS state is most thermodynamically favoured due to its stronger M–L bonds. However it is the HS state that has the higher entropy, due to the increase in electronic entropy from placing electrons in a larger number of orbitals, and the increase in vibrational entropy.[17] The vibrational entropy contribution is due to the higher density of vibrational states in the HS state, which is shown arbitrarily in Figure 1.3. Around 25% of the entropy change comes from the electronic contribution, while the major contributors are the vibrational factors, of which vibrations and deformations of the M–L bonds are more important than lattice contributions (Equation 1.1).[18] At low temperatures the enthalpy effect dominates as the entropy term $T\Delta S$ is negligible, thus making the LS state the most thermodynamically stable state. Upon increasing the temperature however, the entropic term dominates, eventually resulting in a more thermodynamically stable HS state and so making a spin change favourable. The point where the change in Gibbs free energy, $\Delta G = 0$ J mol^{-1} there should be a 50:50 HS:LS ratio when kinetics are not taken into account, and this point of a spin transition is termed the transition temperature, $T_{1/2}$. The entropy change, ΔH, of a LS→HS transition is typically 10-20 kJmol^{-1}, where the enthalpy change, ΔS, is around 50-80 kJmol^{-1} therefore SCO is a process which is driven by the entropy of the system.[19]

Equation 1.1
Contributions to the total entropy change of a SCO system.

$$\Delta S = \Delta S_{\mathrm{el}} + \Delta S_{\mathrm{vib,mol}} + \Delta S_{\mathrm{vib,latt}}$$

A consequence of the occupation of the e_g orbitals in the HS state is a pronounced deviation from octahedral geometry around the metal centre. This is due to the weakening of the M–L bonds which creates a coordination sphere which is more easily distorted.[20] The distortions that arise can be quantified most commonly in terms of two parameters; the rhombic distortion parameter (Equation 1.2, Figure 1.4), Σ, which is a general measure of deviation from an octahedral geometry, and the trigonal distortion parameter (Equation 1.3, Figure 1.4), Θ, which is a measure of the tendency of the geometry towards trigonal prismatic. The trigonal distortion parameter was first used to compare HS iron(II) complexes and was found to be strongly related to the extent of intersystem crossing from the ${}^5T_{2g}$ to the ${}^1A_{1g}$ state.[21] The distortion parameters Σ and Θ can also be used in conjunction with M–L bond lengths to assess the spin state of metal centres in a structure.

Equation 1.2
Calculation of the rhombic distortion parameter, Σ.

$$\Sigma = \sum_{i=1}^{12} |90 - \alpha_i|$$

Equation 1.3
Calculation of the trigonal distortion parameter, Θ.

$$\Theta = \sum_{j=1}^{24} |60 - \theta_j|$$

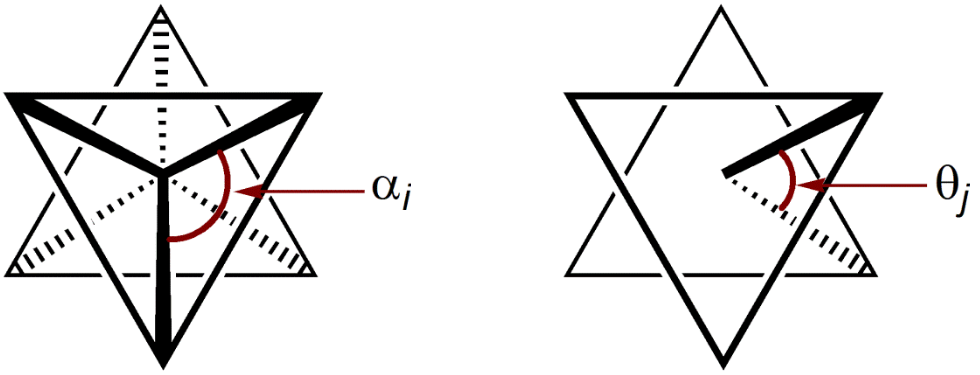

Figure 1.4
Origin of the angles α and θ used in Equation 1.2 and Equation 1.3 respectively.

In iron(II) complexes with two tridentate nitrogen donors such as 2,6-di(1*H*-pyrazol-3-yl)pyridine (3-bpp) two other distortions to the iron centre can be defined. These are the twist in the least squares planes of the ligands, θ, and the trans angle, ϕ, which in an ideal octahedral coordination should be 90º and 180º respectively (Figure 1.5). A deviation from these values indicates Jahn-Teller distortions in the geometry which reduces the symmetry from D_{2d} to C_2.[22] Distortions in the angles θ and ϕ can occur independently to one another and deviations in the angle ϕ are usually observed in a LS→HS transition. This is because the lattice can better accommodate a change in molecular size (the effect of a change in ϕ) than a change in molecular shape (the effect of a change in θ).[23]

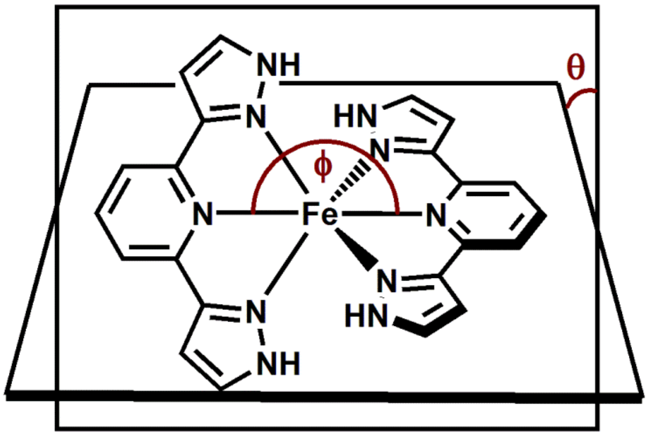

Figure 1.5
Description of the angles θ and ϕ in an $[Fe(3\text{-}bpp)_2]^{2+}$ complex.

The distortion parameters Σ, Θ and angles θ and ϕ are correlated. The rhombic distortion parameter, Σ, can be considered to show the overall magnitude of the Jahn-Teller distortions characterised by the angles θ and ϕ, where Θ gives a better indication of the type of distortion. Jahn-Teller distortions arise when a non-linear molecule with a spatially degenerate ground state undergoes a distortion to remove the degeneracy and lower the overall energy of the system. Often in octahedral complexes Jahn-Teller distortions are manifested as an elongation or compression of the *z* axis, however in this case the result is a distortion in the θ and ϕ angles. Ligands with relatively small bite angles such as 2,6-di(1*H*-pyrazol-3-yl)pyridine (Figure 1.5) and 2,6-di(pyrazol-1-yl)pyridine (~70-80º)[23] are often associated with larger Jahn-Teller distortions in the HS state. These distortions are important in SCO as a highly distorted HS state would have to undergo a large structural change to access the LS state. If this structural change is not accommodated by the lattice this can lead to a kinetically slow spin transition, or even trapping of the complex in the HS state at low temperatures.[24, 25] Therefore a complex which is expected to undergo a spin transition will have reasonable values for these distortion parameters (Figure 1.6).[23]

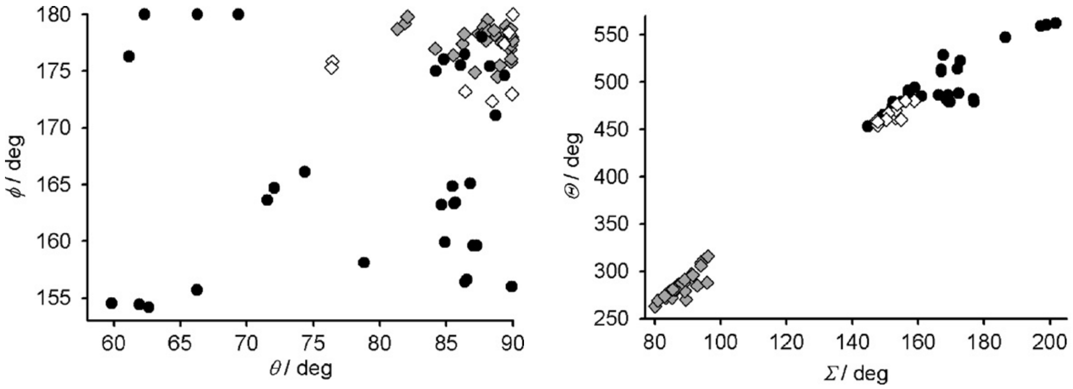

Figure 1.6
Plot of $[Fe(1\text{-}bpp)_2]^{2+}$ complexes correlated to the values of θ and ϕ (left) and Σ and Θ (right). Complexes which remain HS (●), HS complexes which undergo SCO (◇) and LS complexes (◆) are shown. Taken from Halcrow.[23] Copyright Elsevier.

There are two types of spin transition commonly observed in SCO compounds. A continuous spin transition occurs gradually over a large temperature range, where $T_{1/2}$ is defined as the point at which the HS:LS ratio is 50:50. This is generally the type of spin transition seen in solution, as adjacent complex molecules do not influence each other's spin state and a Boltzmann distribution is observed at a given temperature.[26] Discontinuous spin transitions on the other hand occur at a well defined $T_{1/2}$ and are seen as an abrupt change in the magnetic susceptibility over a narrow temperature range. This cooperative effect has been attributed to the change in crystal volume that accompanies a spin transition, and it has been shown that elastic interaction between complex molecules can result in long range effects.[27] The switching of small domains within a crystal creates an internal pressure which will stabilise the LS state resulting in a cascade effect. These spin state domains can even be seen to move through the crystal on a macroscopic scale.[28, 29] Thermal hysteresis is another phenomenon often associated with discontinuous spin transitions. This is where $T_{1/2}$ in the cooling mode is not the same as in the warming mode which can lead to bistability of the HS and LS states (Figure 1.7).

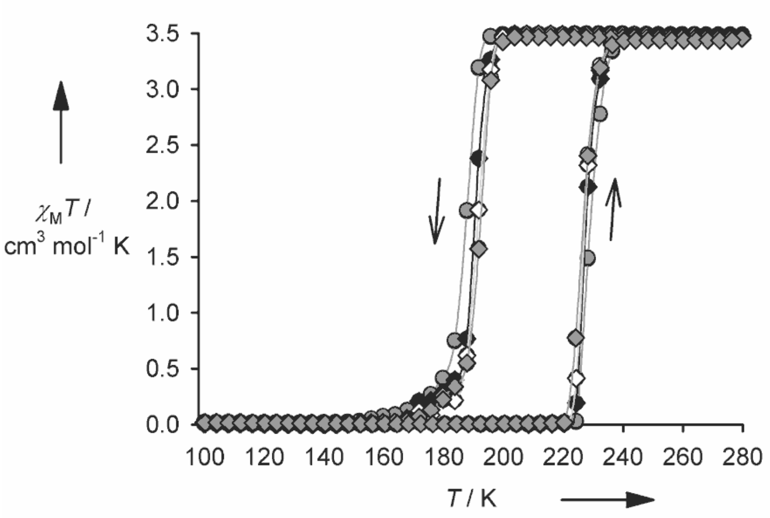

Figure 1.7
An example of an Fe(II) complex showing an abrupt transition with thermal hysteresis over multiple scans. Scan 1 (●); scan 2 (○); scan 3 (●); scan 4 (◆); scan 5 (◇); scan 6 (◆).[30] Reproduced by permission of The Royal Society of Chemistry.

There are a number of ways that cooperativity can be introduced into a crystal lattice. The number of intermolecular contacts within a crystal lattice have a strong correlation with the abruptness and hysteretic nature of a spin transition.[31] This supports the lattice pressure effects previously mentioned; a structure with a higher number of close intermolecular contacts between adjacent molecules will more easily transmit elastic interactions throughout the lattice. One particular structure which has shown to result in high cooperativity is the terpyridine embrace structure which is common in complexes containing terpyridine ligands and other rigid tridentate ligands of a similar shape.[32-34] This structural motif consists of layers of interlocking complex cations which are separated by layers of anions. These layers are able to convey cooperativity in two dimensions and result in compounds with abrupt transitions and wide thermal hysteresis.

Layering of this type is possible because of π-π interactions between the neighbouring molecules. π-π stacking interactions have also been observed in other types of structures which have exhibited abrupt hysteretic transitions.[35] Complexes which contain hydrogen bond donors and acceptors can often form hydrogen bonding networks which extend throughout a crystal lattice, and the number and strength of these interactions has been shown to be connected to cooperativity.[36] This is not ubiquitous however, as there are examples of complexes exhibiting hydrogen bonding networks which show continuous spin transitions.[36]

1.1.2. Detection of Spin Crossover

Due to the significant structural and electronic changes which occur during a spin transition there are a wide range of experimental techniques which can be used to confirm and quantify a spin transition. Due to the change in numbers of unpaired electrons accompanying a spin transition the most obvious measurement for a potential SCO complex to undergo is the magnetic susceptibility. Nowadays the most convenient method of measuring the magnetic susceptibility as a function of temperature is by a superconducting quantum interference device (SQUID). These devices are much more sensitive than Guoy and Faraday balances typically used to measure magnetic susceptibility and can collect data over a range of temperatures much more quickly. A typical DC SQUID consists of two superconductors separated by thin insulating layers to make two parallel Josephson junctions between which a sample is placed. A voltage across the junctions oscillates and the presence of magnetic flux changes these oscillations which are measured. These devices are very sensitive and are able to detect a signal as low as 10^{-6} emu. They also have the advantage of being able to operate at a sample temperature range of 3-380 K making them ideal for measuring the $\chi_M T$ *vs* T curves of SCO compounds.

Another invaluable technique in the field of SCO which allows a spin transition to be studied is Mössbauer spectroscopy. The Mössbauer effect involves the resonant absorption and emission of γ radiation and is a highly sensitive technique which can probe small changes to nuclei.[37] In a crystal lattice all the nuclei are bound together such that when a nucleus emits a γ ray the effective mass of the nucleus becomes that of the entire lattice, thus the fluorescence emission process can be considered to be recoilless. Significant energy loss through recoil of the nuclei, such as in the gas phase would result in failed resonant absorption. In Mössbauer spectroscopy the γ ray source must be of the same isotope as the nuclei being probed, and for iron complexes the source used is ^{57}Fe. As the absorption frequency will be slightly different due to the local environment of the sample the frequency is adjusted using the Doppler effect and Mössbauer spectra are plotted as intensity over detector speed. There are three main features of a Mössbauer spectrum; the isomer shift, quadrupole splitting and hyperfine splitting. The isotope shift is analogous to the chemical shift in NMR spectroscopy and is a shift of a peak which correlates to the amount of s electron density which penetrates the nucleus. Nuclei with angular momentum $l > 1/2$ show a splitting of the energy levels which is termed the quadrupole splitting and in the case of ^{57}Fe with $l = 3/2$ this results in a doublet. The hyperfine splitting is a result of an interaction with a magnetic field produced by the sample, and the spectrum will be a superposition of these effects. The extent of the quadrupole splitting can be used to determine the spin state of the iron centres and can show the HS:LS fraction present in the sample at a given temperature.

The magnetic susceptibility of SCO complexes can also be measured in solution and this is typically done via the Evans NMR method.[38] This method involves analysing the shift of solvent peaks in the NMR spectrum caused by the local magnetic fields created by the sample. The mass susceptibility of the dissolved sample is then given by Equation 1.4, where Δf is the peak shift, f is the NMR spectrometer frequency, c is the concentration of the sample, χ_0 is the mass susceptibility of the solvent and ρ_0 and ρ_s are the densities of the solvent and solution respectively. For highly paramagnetic samples omission of the last term still gives a reasonable error in the measurement.[38]

Equation 1.4
Calculation of the solution molar susceptibility via the Evans NMR method.

$$\chi_M = \frac{3\Delta f}{2\pi f c} + \chi_0 + \frac{\chi_0(\rho_0 - \rho_s)}{c}$$

One advantage of the Evans NMR method is that it can be done over a range of temperatures and involves widely available apparatus. This method is limited, however, to the solubility of the sample and the freezing point of the solvent, and any precipitation at low temperatures can have a significant effect on the values. The error in this method can also be relatively large, around 5-10% depending on the sample concentration.[39]

Due to the structural changes accompanying a transition which have been discussed in **1.1.1** the occurrence of SCO can be verified by x-ray crystallography. This technique is limited, however, to complexes for which high quality single crystals can be obtained. Also due to the long collection times associated with most data acquisitions x-ray crystallography is not always a viable technique to follow the entire spin transition in the same way as magnetic susceptibility. Nonetheless it is a very valuable tool to accompany magnetic data, as structures obtained at strategic points in the spin transition can give useful information about structural changes which occur. The high detail of crystal structures also means that features such as close contacts, hydrogen bonding or π–π stacking networks can be used to rationalise SCO behaviour in the solid state. This ability to attribute certain features of a spin transition, such as cooperativity, with those in the structure make x-ray crystallography an invaluable tool in elucidating structure/function relationships in SCO systems.

Where high quality single crystals cannot be obtained powder x-ray diffraction (PXRD) can still be a useful tool. Instead of giving structural information of the coordination sphere of the metal centre PXRD gives information about the unit cell and type of phase present. The powder patterns obtained can be compared qualitatively to one another or structural information obtained via Rietveld refinement.[40] Another advantage of PXRD to single crystal XRD is the shorter collection times, meaning this technique can be used to determine structural changes at a range of temperatures. In this way variable temperature powder x-ray diffraction (VTPXRD) can give information on phase changes which may accompany or cause abrupt hysteretic transitions.

Spectroscopic techniques such as Fourier transform infra-red (FT-IR) spectroscopy can be used to detect changes in the M–L bond lengths in a complex. As electrons are promoted to the anti-bonding e_g^* orbitals the M–L bonds are weakened, and this will result in a shift of their stretching frequency in the FT-IR spectrum. Occupation of the e_g^* orbitals also affects the symmetry of the molecule. As the complex becomes more distorted certain forbidden *d-d* transition will become more allowed and will show in the UV/vis spectrum. This is not always a useful technique as the relatively weak *d–d* transitions are often obscured by the much stronger metal–ligand charge transfer (MLCT) bands.

1.1.3. Applications of Spin Crossover

The bistability and measurable switching exhibited in SCO complexes has numerous potential applications when incorporated into a functional material.[41] At present however there are only very few examples of simple devices which have been made to demonstrate the potential of spin crossover compounds.[42] SCO compounds have a large potential for minimising data storage media compared to the silicon chips currently used which are close to reaching their full potential. The temperature dependence and tune-ability of SCO compounds also makes them useful in thermosensitive dyes and inks which can be used as temperature threshold indicators and reversible temperature controlled screens. Although in these cases the air and moisture sensitive compounds first need to be stabilised by pre-encapsulation.[43]

SCO compounds have been shown to have potential as temperature responsive paramagnetic chemical exchange saturation transfer (PARACEST) contrast agents in MRI imaging.[44] The paramagnetic high spin state will alter the T^2 relaxation times of water molecules in a similar way to the commonly used gadolinium MRI contrast agents. Therefore, if an SCO contrast agent can be made with an appropriate $T_{1/2}$ and hysteresis loop then it can be useful in medical applications such as monitoring of hyperthermic treatment of tumours via MRI (Figure 1.8).[45] In one example different treatment of a SCO contrast agent including doping to give the desired $T_{1/2}$ and preencapsulation to improve stability finds that the effect on the T^2 relaxation time is abrupt and reversible.[46]

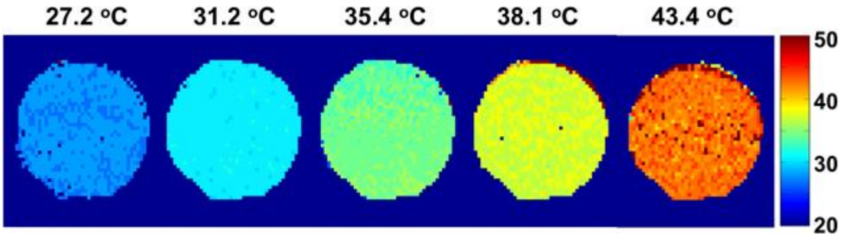

Figure 1.8
Temperature maps obtained from an imaging experiment using $[(Me_2NPY_5Me_2)Fe(H_2O)]^{2+}$ ($Me_2NPY_5Me_2$ = 4-dimethylamino-2,6-*bis*(1,1-*bis*(2-pyridyl)ethyl)pyridine) as a PARACEST contrast agent. Taken from Harris *et al.*[44] Reproduced by permission of The Royal Society of Chemistry.

One challenge for functionalising SCO compounds for data storage, optical and sensor applications is the deposition of thin films onto substrates whilst retaining the SCO properties of the bulk sample. Sequential assembly techniques provide an effective route to these thin films which involve the sequential chemisorption of building blocks onto a surface to give orientated multilayer thin films. This technique has been successful and it has been shown that guest molecules such as pyridine can influence the SCO properties of the film, highlighting the capability of these systems to be used as microsensors.[47] In one case host–guest interactions the HS state are stabilised by larger guests and an important feature is that they are synergistic; guest sorption can trigger a spin change but conversely a spin change can also cause guest desorption.[48] This effect has also been observed in solution, where host–guest interactions between anions and ligands affect the spin state of an iron(II) complex. This particular complex is LS when anions are bound to all three ligands and HS when they are unbound, and this can be detected either by a change in colour and magnetic susceptibility.[49]

As well as inorganic substrates such as silicon and quartz SCO complexes have been deposited on a biological membrane. ^{57}Fe Mössbauer spectroscopy has confirmed the occurrence of SCO but also the presence of an iron by-product resulting from interaction with the membrane.[50] This method has also been used to print nanodots of the SCO complex $[Fe(ptz)_6](BF_4)_2$ (ptz = 1-propyl-tetrazole) onto a silicon wafer and this technique provides a useful route to creating microsensor devices which could detect the presence of solvents or a change in temperature.[51]

There are also more subtle effects of a spin transition which can be exploited in future devices. One group has shown by doping an electroluminescence device with an SCO complex the system can become temperature dependant.[52] In this example the electroluminescent chlorophyll *a* layer is doped with $[Fe(1\text{-}bpp)_2](BF_4)_2$, a complex for which the SCO properties are well documented, and suggests that the LS state of the iron complex quenches the emission of the chlorophyll compared to that of a reference device. The authors attribute this to the change in energy levels of the complex when it undergoes spin crossover, and in the LS state energy transfer can occur from the chlorophyll *a* to the complex, thus quenching its emission.

In general for a SCO complex to be relevant to any applications it must exhibit an abrupt thermal hysteresis centred around room temperature with a wide hysteresis. Finding such a complex has been the focus of much of the research in this area, and with increased understanding of the factors affecting spin transitions a suitable complex can be rationally designed.

1.1.4. Ligand Design

In a metal complex Δ_{oct} depends on the metal, its oxidation state and the ligand field applied. Jørgensen's spectrochemical series places different ligand types in the order in which they affect the magnitude of Δ_{oct}.[53] Ligands which have occupied *p* orbitals, such as halides, are able to donate both σ and π electron density to the metal effectively increasing the M-L interaction and reducing the magnitude of Δ_{oct}. These types of ligand are termed weak field ligands and are usually more likely to give HS complexes. Conversely, ligands with empty π^* orbitals, in addition to donating σ electron density to the metal are also able to accept electron density from the appropriate d_π orbitals on the metal. This backbonding has the effect of increasing Δ_{oct} usually resulting in a LS complex and these types of ligand are termed strong field ligands. The spectrochemical series for a range of common donor ligands are shown below:

$I^- < Br^- < S^{2-} < SCN^- < Cl^- < F^- < OH^- < H_2O < NCS^- <$ MeCN $<$ pyridine $< NH_3 <$ 2,2-bipyridine $< PPh_3 < CN^- \approx CO$

In terms of SCO complexes an appropriate ligand and metal combination must be chosen in order to have a sufficiently small energy difference between LS and HS states in order to allow switching to occur. Iron(II) has a field strength such that it can be tuned into the SCO region by the careful selection of ligands and for this reason iron(II) SCO complexes are by far the most documented in the literature.

For an iron(II) complex to exhibit SCO an appropriate ligand must be reasonably strong field and have empty π^* orbitals which can accept electron density from the metal. Busch and co-workers used absorption spectra to investigate the D_q values of iron(II) with various ligands and suggested that a ligand with a field strength of $D_q = 1250 \pm 80$ cm^{-1} will allow population of both HS and LS states.[54] One large class of ligand which offers a field strength in this range are those based on multi-dentate imines. An additional advantage to this ligand class is that they can be derivatised with a wide range of substituents which can alter the σ donating and π accepting nature of the ligands, thus fine-tuning the ligand field. The diimine ligands 1,10-phenanthroline and 2,2'-bipyridine (Figure 1.9) make *tris*(diimine)iron(II) complexes which remain LS at room temperature, indicating that their field strength is too high for SCO to occur. Substituting electron donating groups such as methyl and methoxy groups adjacent to the imines has the effect of increasing the electron density in the π^* orbitals. This makes these π^* orbitals less able to accept electron density from the metal d_π orbitals, thus reducing the ligand field. In the *tris*(diimine)iron(II) complexes of 2-methyl-phenanthroline and 2-methoxy-phenanthroline this results in complexes which are HS and undergo a spin transition at low temperatures. The placement of these groups around the ring is also important, as substitution at positions further away from the donating nitrogens will have a smaller effect on the ligand field than those adjacent.[55]

Figure 1.9
The ligands 2,2'-bipyridine (left) and 1,10-phenanthroline (right) where R = H.

In addition to altering the field strength exerted by a particular ligand on the iron(II) centre the sterics of any substituents can play a large role in determining SCO properties. Because of the contraction of the coordination sphere accompanying a spin transition placing steric bulk adjacent to the imine groups may cause intramolecular contacts which inhibit a spin transition. These perturbations have been observed in complexes of 2,6-di(pyrazol-1-yl)pyridine, where the steric bulk of mesityl groups in the distal position gives a complex with Fe–N$_{\text{pyrazole}}$ bonds which are larger than for the equivalent methyl substituted complex in the LS state.[56] In the case of this example the effect of the bulk of the mesityl groups was not large enough to prevent access to the LS state, and this complex was LS at 290 K.

In triimine donors the bite angle, α, can also have an effect on the overall structure and likelihood of SCO. In ligands with a relatively small bite angle such as 2,6-di(pyrazol-1-

yl)pyridine derivatives (α ≈ 73º)[23] an unusual Jahn-Teller distortion can occur, which has already been discussed in **1.1.1** (Figure 1.5). Density functional (DF) calculations have shown that the ligand plane twist has a larger effect on the ligand field stabilisation energy and this distortion is favoured by narrower bite angles in the ligands.[22] The deviation of the $N_{pyridine}$–Fe–$N_{pyridine}$ bond angle from 180º tilts the pyrazole lone pairs away from one of the the d_{xz} and d_{yz} orbitals but tilts the pyridine lone pair towards the other. This results in an overall increase in the LFSE and cellular ligand field (CLF) calculations have shown that these combined distortions effectively stabilise the HS state. With this in mind, an ideal triimine ligand for SCO complexes should not have an excessively small bite angle.

Another factor which influences the extent of distortions around the metal centre can be the magnitude of intermolecular steric clashes. These clashes will arise more in complexes of ligands which have sterically bulky groups around their periphery. As previously mentioned, due to weaker M–L bonds the coordination sphere is more deformable in the HS state and bulky substituents are more likely to cause such distortion. This could lead to complexes being trapped in the HS state as a result of not being able to overcome lattice constraints. Where this isn't the case, however, these steric clashes could offer cooperativity within the lattice and result in abrupt transitions desirable for potential applications. This is due to the effect of increased internal pressure accompanying a spin transition which has already been discussed in **1.1.1**. The overall shape of the ligands influences the packing motif adopted by SCO complexes, and some of these motifs such as the terpyridine embrace have been shown to consistently give complexes with abrupt hysteretic transitions. [32-34]

As previously discussed in **1.1.1**, the introduction of hydrogen bonding networks into the lattice of a SCO complex can increase the cooperativity of the system. This is achieved by designing ligands which contain hydrogen bond donors and acceptors, and these groups can also form hydrogen bonds with solvent molecules and anions in the lattice. Weber has shown the importance of this hydrogen bonding effect in iron complexes by replacing hydrogen bond donors in coordinating imidazole ligands with deuterium, the effect being a 4 K reduction in the hysteresis width (Figure 1.10).[57] This was attributed to a slightly stronger N–D bond, resulting in weaker hydrogen bonds and therefore weaker intermolecular interactions.[58] These findings highlight the importance of hydrogen bonding networks in the solid state but the effect of hydrogen bonding can be difficult to predict and this still remains a challenge in ligand design.

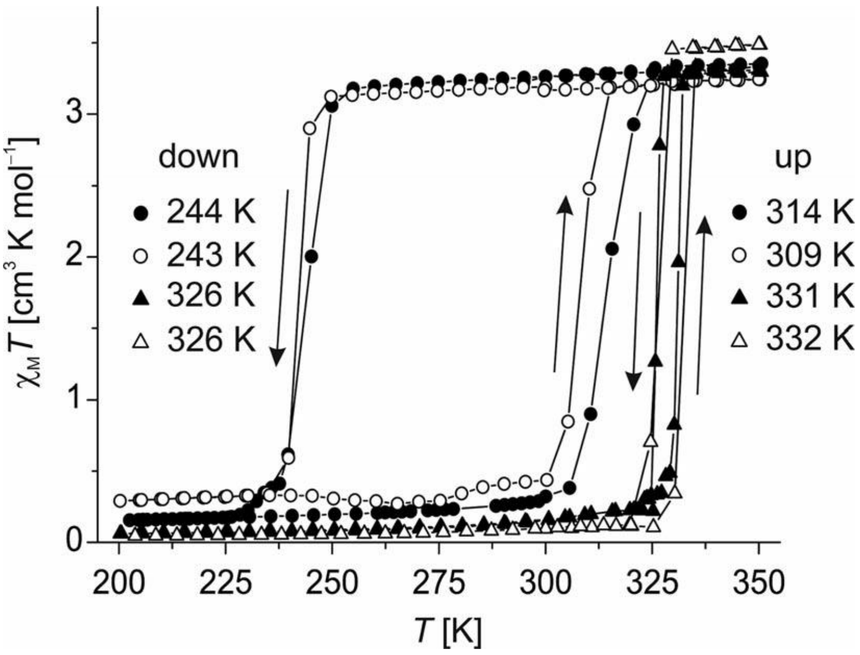

Figure 1.10
χ_MT *vs* T curves of two polymorphs of the complex [FeL(Im)$_2$], where L = (diethyl(*E*,*E*)-2,2_-[1,2-phenyl*bis*(iminomethylidyne)]*bis*[3-oxobutanoate](2–)-*N*,*N*',*O*^{3},*O*^{3}') and Im = imidazole comparing protonated (black) and deuterated (white) imidazole. Taken from Weber *et al.*[57] Reproduced by permission of Wiley.

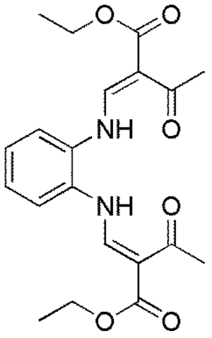

Figure 1.11
The ligand (diethyl(*E*,*E*)-2,2_-[1,2-phenyl*bis*(iminomethylidyne)]*bis*[3-oxobutanoate](2–)-*N*,*N*',*O*^{3},*O*^{3}') used by Weber *et al.*[57]

In addition to offering cooperativity in the solid state hydrogen bonding also has an effect on SCO in solution. In solution, however, the effect of hydrogen bonding is to shift $T_{1/2}$ by stabilising either the LS or HS state. In iron(II) complexes of the ligand 2,6-di(1*H*-pyrazol-3-yl)pyridine (3-bpp) the non-coordinating pyrazole NH groups are able to donate hydrogen bonds to solvent molecules. It has been shown via Evans NMR of [Fe(3-bpp)$_2$]$^{2+}$ complexes that solvents which are stronger hydrogen bond acceptors stabilise the LS state and increase $T_{1/2}$, with a considerable stabilisation in water compared to organic solvents (Figure 1.12).[59] This effect is a result of an increase in the electron density at the coordinating pyrazole nitrogens when the ligand is forming hydrogen bonds at the pyrazole NH groups. This increases the σ donating ability of the ligand, which in turn increases the ligand field and so stabilises the LS state.[60]

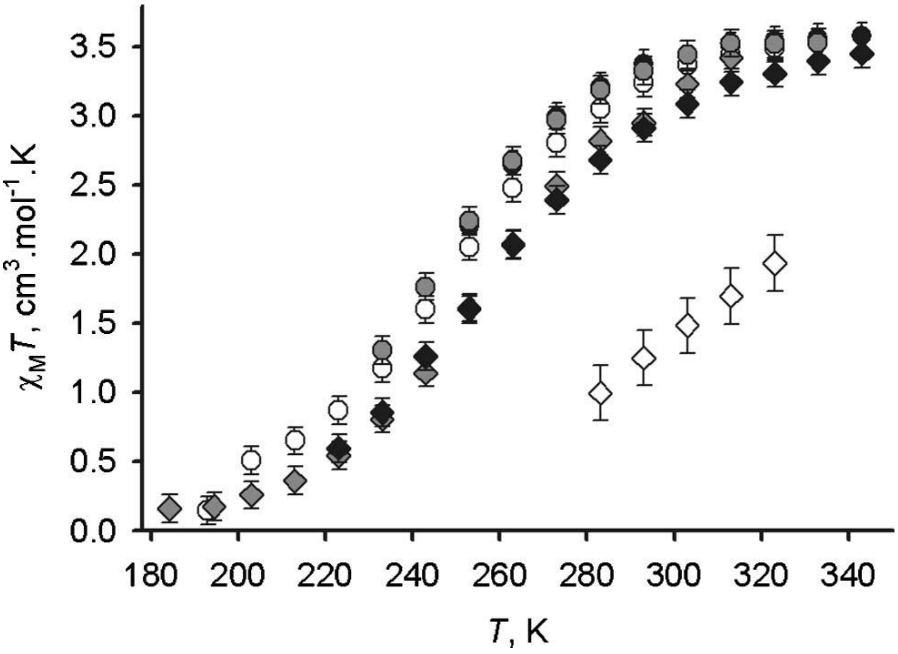

Figure 1.12
χ_MT *vs* T curves of [Fe(3-bpp)$_2$](BF$_4$)$_2$ in CD$_3$NO$_2$ (●), CD$_3$CN (●),(CD$_3$)$_2$CO (○), (CD$_3$)$_2$NCDO (◆), CD$_3$OD (◆) and D$_2$O (◇) determined via the Evans NMR method. Taken from Halcrow *et al.*[59] Reproduced by permission of The Royal Society of Chemistry.

1.1.5. Light Induced Excited Spin State Trapping (LIESST) Effect

The light-induced excited spin state trapping (LIESST) effect is the creation of a metastable HS state at low temperatures by irradiating the *d–d* and MLCT bands of the LS state with light of an appropriate wavelength and was first observed in the solid state by Decurtins in 1984.[61, 62] The LIESST process can also be reversed via application of a different wavelength of light, and this is known as the reverse LIESST effect. This effect is of particular interest for applications such as data storage, although the barrier to their development is the relatively short lifetime of the metastable HS state at working temperatures.

The LIESST process involves excitation of the $^1A_1$ state to either the $^1T_1$ state or the lower lying $^3T_1$ state. From these states the system undergoes intersystem crossing (ISC) to the HS $^5T_2$ state, and from the triplet state this ISC process is almost quantitative. The reverse LIESST effect involves the excitation of this metastable HS $^5T_2$ state to the ^5E state, followed by a subsequent ISC to relax back to the LS $^1A_1$ state (Figure 1.13).[63]

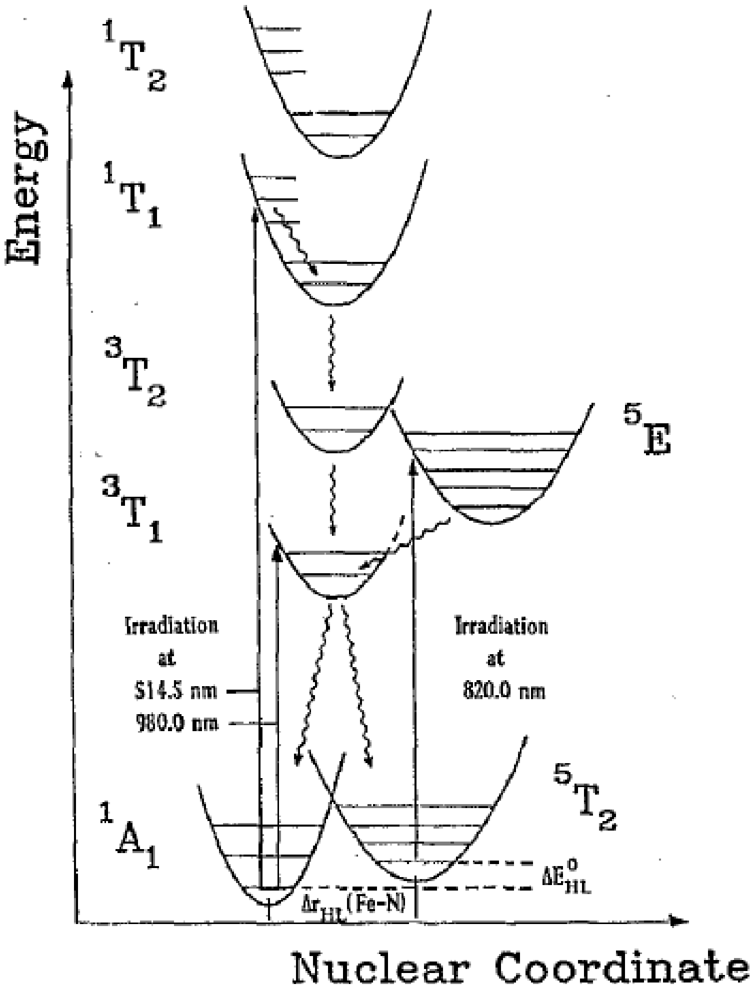

Figure 1.13
Diagram showing the potential energy wells of the ground states and excited states of a SCO system. Arrows show the pathways of LIESST and reverse LIESST. Reproduced from Hauser[63] with permission of AIP Publishing LLC.

The extent of the LIESST effect is measured by the T(LIESST) approach. This approach involves irradiating the sample at 10 K to generate the metastable HS state and then warming at a rate of 0.3 Kmin^{-1} until the metastable state decays back to the LS state. Laser diodes are typically used to excite the sample and the exact wavelength depends on the absorption transitions of the particular sample. The temperature threshold at which the metastable state is no longer long lived is termed T(LIESST) and this temperature is measured as the minimum of the $d\chi_M T/dT$ *versus* T curve (Figure 1.14).

It is relatively rare to observe the LIESST effect in iron(III) complexes, and by far the most examples to show the effect are in complexes of iron(II). This is due to the larger difference in M–L bond lengths between the HS and LS states in iron(II). The similarity in the HS and

LS potential wells in iron(III) results in more overlap between the vibrational wavefunctions and this allows the metastable state to relax via quantum mechanical tunnelling.[64]

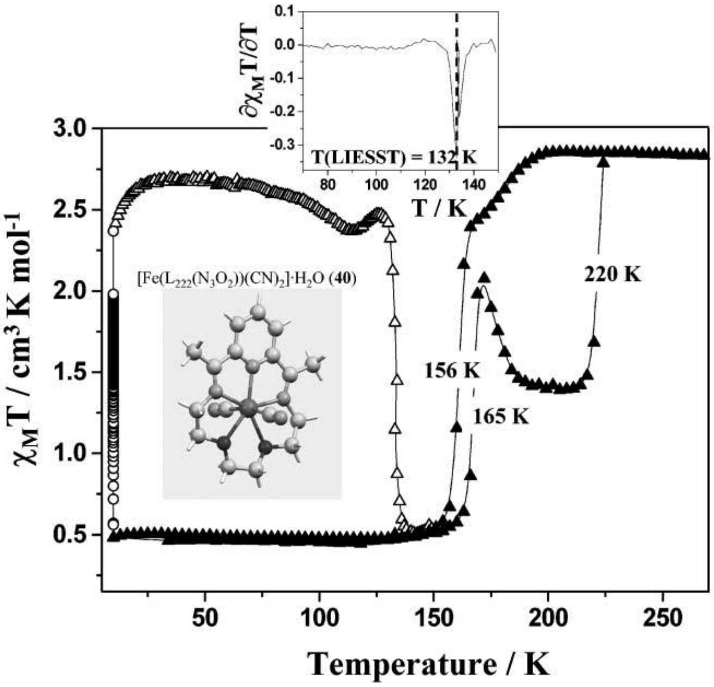

Figure 1.14
Example of a T(LIESST) experiment on an iron(II) complex. Cooling and warming without irradiation (▲), irradiation at 10 K (○) and the T(LIESST) measurement (Δ). The inset shows the first derivative used to accurately measure T(LIESST). Taken from Létard.[65] Reproduced by permission of The Royal Society of Chemistry.

There are two ways in which the lifetime of the metastable state can be increased. One is to create a particularly stable HS state which can be achieved by having a HS state in which the octahedral iron centre is particularly distorted. This slows the conversion back to the LS state in a similar way to the HS trapping observed in some complexes and T(LIESST) has been shown to be strongly correlated to the octahedral distortion.[65] Another proposed method for increasing the lifetime would be to excite the complex in the middle of a hysteresis loop. This would require a hysteresis loop of around 100 K at working temperatures, however, and obtaining such complexes is an ongoing struggle in the field of SCO.

1.1.6. Peturbations to Spin Crossover

In addition to temperature and light, a spin transition can also be triggered by application of external pressure. Because of the contraction of the coordination sphere the molecular volume decreases on a HS→LS transition, therefore the application of external pressure has the effect of stabilising the LS state. This in turn increases $T_{1/2}$ and also usually decreases the hysteresis width in a sample (Figure 1.15). It has been suggested that increasing pressure increases the zero point energy difference in the HS and LS potential wells, ΔE^0_{HL}, as well as reducing the activation energy of interconversion which leads to a higher population of the LS state.[66] These effects can also be accompanied by a change in shape of the $\chi_M T$ *vs* T curve but the exact nature of these perturbations are often dependant on the nature of the cooperativity in the system and can be difficult to predict. In some examples the opposite effect has been observed and has been attributed to a transformation to a new phase with a smaller unit cell volume.[67]

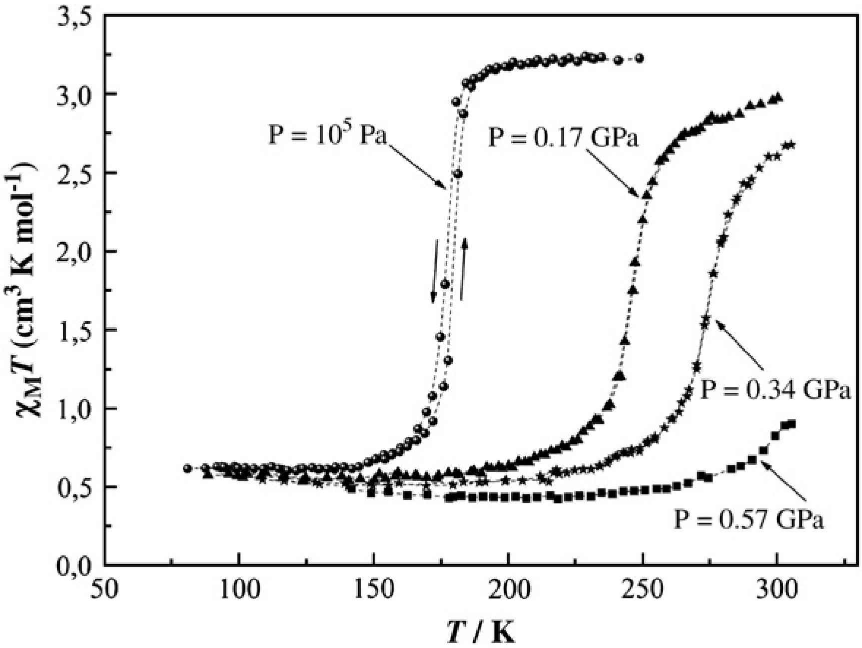

Figure 1.15
$\chi_M T$ *vs* T curves for the complex $[Fe(phen)_2(NCS)_2]$ at increasing pressures (phen = 1,10-phenanthroline). Taken from Gütlich *et al*.[66] Reproduced by permission of Elsevier.

Complexes of transition metals experience a stabilisation in an applied magnetic field. In the instance that two spin states are available the state with the most unpaired electrons will experience the most stabilisation. In the case of SCO systems this has the effect of stabilising the HS state and shifting $T_{1/2}$ to lower temperatures. This effect is relatively small; a shift of only -0.10 ± 0.04 K is observed when increasing the field strength from 1-5.5 T in the complex $[Fe(phen)_2(NCS)_2]$ (phen = 1,10-phenanthroline).[68] In larger fields of up to 30 T however an irreversible 10% increase in population of the HS state has been observed with a calculated temperature shift of -1.6 K in the mixed crystal complex $[Fe_{0.52}Ni_{0.48}(btr)_2(NCS)_2]\cdot H_2O$ (btr = 4,4'-*bis*(1,2,4-triazole).[69]

The effect of thermal scan rate has been investigated in complexes of iron(II) and Co(II) between 0.2-10 $Kmin^{-1}$. In both cases a slower thermal scan rate leads to a pronounced reduction in hysteresis width, the largest difference being that of the dinuclear $[Fe_2(PMPh^{tBu}T)_2](BF_4)_4\cdot 3.5H_2O$ ($PMPh^{tBu}T$ = Pyridin-2-ylmethyl-(5-{[(pyridin-2-ylmethyl)-amino]-methyl}-4H-[1,2,4]triazol-3-ylmethyl)-amine)complex with a reduction from 41-22 K.[70, 71] This observation is due to kinetic aspects of the spin transition. At slower scan rates a complex has more time to reach its equilibrium state at a given temperature, whereas a faster scan rate will have the effect of thermally trapping the spin states until the thermodynamics overcome the kinetics.

Many counter anions used in spin crossover complexes possess hydrogen bond acceptor groups, and this makes them capable of perturbing the H-bonding networks in the solid state. It has also been observed that not only the hydrogen bonding nature but also the size of the anion has an effect. This effect has been demonstrated by the magnetic susceptibility of a series of *tris*(2-aminomethylpyridine)iron(II) halides. It was found that the chloride gave an abrupt transition; the bromide gave a less abrupt transition with incomplete conversion to the LS state and the iodide showed very little SCO behaviour.[72]

The relationship between the anion size and the SCO temperature can be explained by inductive effects; smaller anions have a higher charge density, and can form stronger hydrogen bonding interactions with the ligands. This draws electron density away from coordinating nitrogens, making them less basic and weakening the M–L bond, causing it to lengthen. This lengthening of the M–L bonds stabilises the HS state, and leads to a decrease in the SCO transition temperature, $T_{1/2}$. This effect has been confirmed by experiment and density functional theory calculations for complexes with imidazole type ligands however due to the sensitivity of SCO on many different variables this trend does not apply to all classes of compounds.[73] The effect of the anion size has also been investigated for less simple anions such as ZrF_6^{2-}, but using the volume rather than the ionic radius in order to determine linear relationships between anion size and the spin transition temperature, and the authors were able to construct a database which could aid in predicting $T_{1/2}$ in potential SCO complexes.[74]

The presence of solvent within a crystal lattice can also have implications on the cooperativity of a SCO system as those with hydrogen bond donors and acceptors can contribute to the hydrogen bonding networks (Figure 1.16). These are not exclusive and networks can exist between complex cations, anions and solvent molecules. The effect of the solvent has been shown by the complex *tris*(2-aminomethylpyridine)iron(II) chloride discussed above which can be crystallised from a number of solvents. In this case it has been observed that the methanol solvate gives a more gradual transition than the ethanol solvate, and the monohydrate gives a hysteretic spin transition with a higher $T_{1/2}$.[75] The dihydrate however gives a fully LS complex, so the effect of solvation with a hydrogen bonding solvent on cooperativity can be difficult to predict and is due to subtle structural factors.

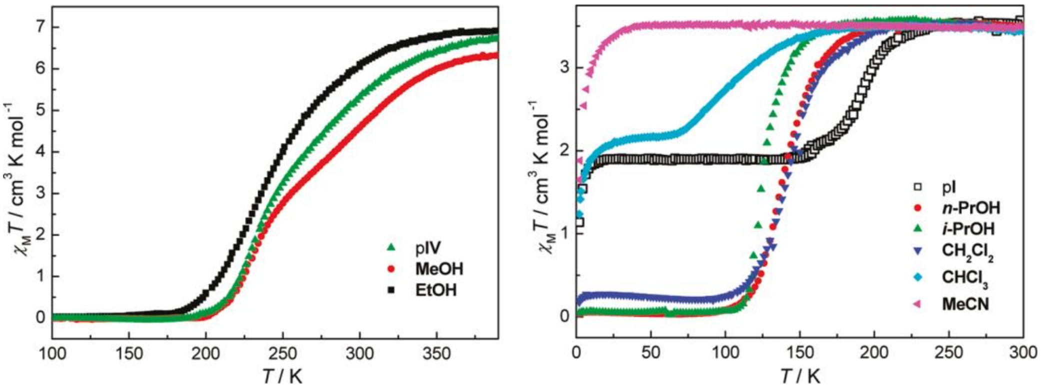

Figure 1.16
$\chi_M T$ *vs* T curves for different sovates of the complex [Fe(tpa)(NCS)$_2$] (tpa = tri(2-pyridylmethyl)amine). pI and pIV refer to the polymorph of the complex. Reprinted (adapted) with permission from Wei et al.[76] Copyright 2011 American Chemical Society.

As with solvent effects in solution, implications of the presence of solvent in the solid state have also been investigated using deuterium labelling techniques. In one particular example a complex was prepared in protonated and deuterated methanol to make the dimethanol solvate and their properties were compared. It was found that protonated methanol gave a hysteresis width of 82 K, whereas deuterated methanol gave a smaller width of 79 K.[57] It is difficult, however, to correlate this difference to the number and strength of hydrogen bonds. In this same example it is also shown that the complete removal of methanol from the structure causes the transition to become gradual and lose hysteresis, indicating that the solvent molecules play an important role in inferring cooperativity in the structure.

This sensitivity of SCO compounds to solvation may provide potential applications. Some SCO materials have been made which show reversible and irreversible exchange of solvent molecules in the lattice.[76] This process is accompanied by a change in SCO properties and if they exhibit thermochromism, complexes of this kind could have implications in sensor applications. In this case the differences in properties were attributed to the differences in intermolecular forces which alter the field strength of the ligands, which in turn affect the ligand field splitting.

When in solution hydrogen bonding interactions with the solvent involving hydrogen bond donors close to coordinating nitrogen atoms has the effect of stabilising the LS state and reducing $T_{1/2}$. In this work the characteristics of the solvent will be described using four parameters. E_N is a normalised scale of solvent polarity based on the molar electronic transition energies of a probe dye.[77] DN is the donor number, and is a measure of lewis basicity of the solvent or how readily it donates its’ lone pair.[78] SB is the solvent basicity[79] and the β parameter is a scale of the hydrogen-bond acceptor basicity, or how readily it donates its electron pair to form a hydrogen bond.[80]

1.2. Transfer Hydrogenation Catalysis

Transfer hydrogenation (TH) is the process of reducing a substrate such as a ketone or imine to their respective alcohols and amines using hydrogen from a donor molecule such as an alcohol. This is a desirable method in industry as it avoids using high pressures of hydrogen gas which can be dangerous and impractical. Ruthenium(II) complexes containing the BINAP ligand (BINAP = 2,2'-*bis*(diphenylphosphino)-1,1'-binapthyl) (Figure 1.17) have proved very successful in the asymmetric transfer hydrogenation of ketones into their corresponding optically active secondary alcohols.[81, 82] This process is useful in the production of many pharmaceuticals and the enantioselectivity of the reaction negates the chiral resolution process and allows maximum yields to exceed 50%.

Figure 1.17
Structures of the chiral ligands (*R*)-BINAP and (*S*)-BINAP.

Towards this application η^6-arene-ruthenium complexes and their isoelectronic rhenium and iridium complexes have been shown to be highly effective TH catalysts.[83] The general catalytic cycle for TH in ruthenium catalysts first involves the generation of the active catalyst which is a ruthenium hydride species. This is typically formed via β-elimination of a donor alcohol such as *iso*propanol to produce acetone as a by-product. This 18 electron ruthenium hydride species is then able to bind the carbonyl or imine substrate and then reductively eliminate to give the desired alcohol or amine product. This then regenerates the 16 electron ruthenium species which will bind another *iso*propoxide ion and reform the catalytic hydride species via β-elimination to continue the catalytic cycle (Figure 1.18).[84]

For this cycle to occur the carbonyl must bind to the metal in such an orientation to favour the reductive elimination step which forms the product. An electrophilic metal is more likely to form an "end-on" σ bonded species at the carbonyl oxygen. This conformation makes it difficult for a hydride to reach the carbonyl π^* orbital in order to react and so these systems are not expected to make efficient catalysts. In cases where the substrate carbonyl is π bonded in a "side-on" fashion the hydrido ligand has much better access to the π^* orbital on the carbon and this is expected to result in effective TH catalysts. Because the occurrence of this conformation relies on the electrophilicity of the metal used and an appropriate

LUMO on the substrate this limits these TH reactions to just a few transition metals and substrates.

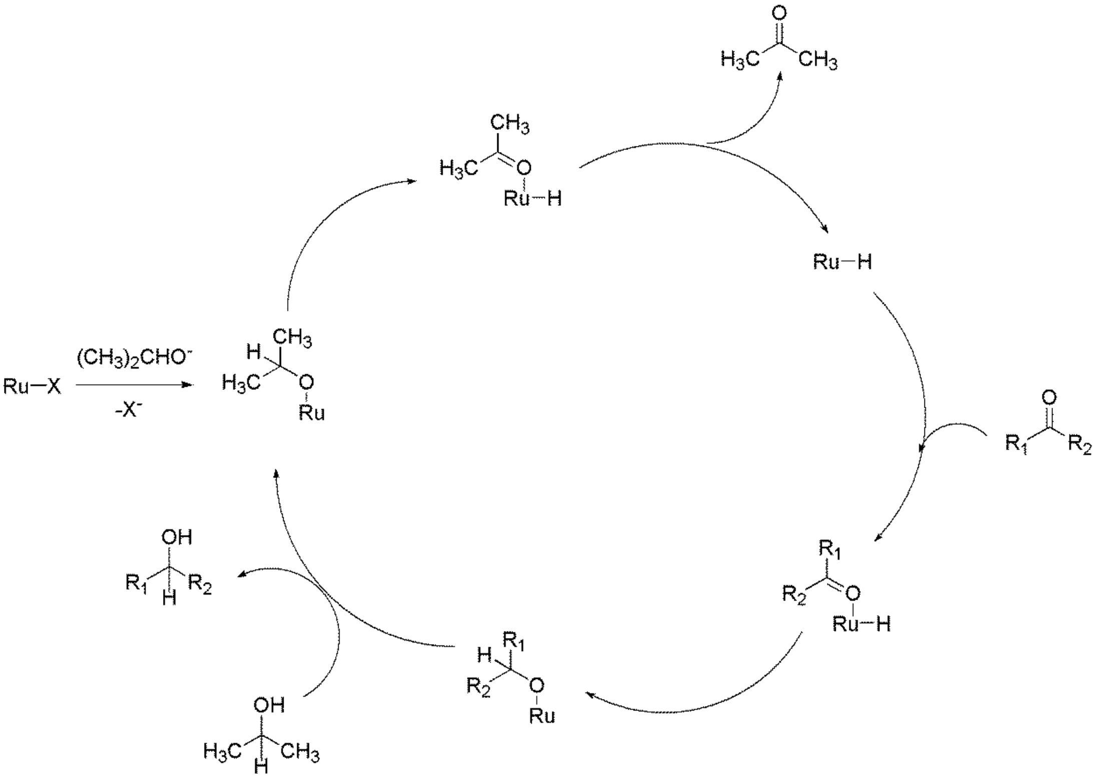

Figure 1.18
A typical catalytic cycle of a ruthenium TH catalyst.

Another advantage of using TH catalysts as a route towards alcohols is its' ability to afford them in potentially high enantiomeric purity. This enantioselectivity is achieved by the incorporation of chiral ligands onto the metal centre which transfer their chirality to the substrate by influencing their binding to the metal. The TH reaction is reversible, however, and enantioselectivity is influenced by both kinetic and thermodynamic factors. Over time this can lead to a decrease in enantioselectivity. Also because of the reversibility of the reaction TH can be very sensitive to substrate and hydrogen donor concentrations. Ruthenium complexes bearing C_2 symmetric ligands such as substituted ferrocenes and 2-(sulphonamide)cyclohexanes have been shown to hydrogenate acetophenone and 1-acetylnapthalene under mild conditions with good conversion (> 95%) and reasonable enantioselectivity (*ee* > 80%).[85] In this case the synthetic routes to the ligands allowed high enantioselectivity without the need for any chiral resolution, making these systems viable asymmetric TH catalysts.

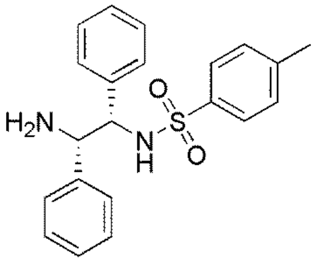

Figure 1.19
(1S, 2S)- N-(*p*-toluenesulfonyl)- 1,2-diphenylethylenediamine [(S,S)-Ts-DPEN].

Some of the first asymmetric ruthenium(II) TH catalysts were prepared by Noyori *et al*. and used chiral (1S, 2S)- N-(*p*-toluenesulfonyl)- 1,2-diphenylethylenediamine [(S,S)-Ts-DPEN] and BINAP ligands (Figure 1.17, Figure 1.19). These complexes were able to convert acetophenone to (S)-1-phenylethanol at room temperature with 97% *ee* and 95% conversion.[86] In this example the % conversion and enantioselectivity were also affected by the substitution on the phenyl ring and the adjacent alkyl group (Figure 1.20). The reaction was slowed by *ortho* substitution on the phenyl ring and where R_1 is a sterically bulky substituent such as an *iso*butyl group the reaction didn't proceed at all. Conversely substitution of an electron withdrawing group (EWG) at the *meta* position on the phenyl ring gave the best results with 98% conversion and 98% *ee*.

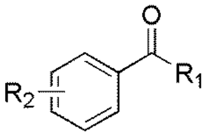

Figure 1.20
Structure of acetophenone derivatives.

It was also observed that the electronic properties of the chiral ligand also had an effect on the reactivity of Noyori-type catalysts. When the (S,S)- DPEN ligand was substituted with electron withdrawing groups such as trifluoromethanesulphonate this led to a decrease in the catalytic activity, and found that the tosylate group gave the best balance of activity and enantioselectivity.[86]

Tridentate imine ligands are very attractive in terms of ruthenium(II) TH catalysts. In addition to forming stable complexes with ruthenium(II) they also possess potential to be sterically and electronically tuned in order to create a catalyst system with the desired properties. Complexes of the type $[RuCl(NNN)(PPh_3)_2]Cl$ (where NNN is a triimine donor ligand) have proven to be efficient catalysts for the TH of acetophenone derivatives and some have achieved up to 100% conversion with a final turnover frequency (TOF) of 180000 h^{-1} after only 20 seconds.[87] The authors ascribed this high catalytic activity to the asymmetric environment around the ruthenium(II) centre which is generated by the asymmetrically substituted 2,6-di(1*H*-benzimidizol-2-yl)pyridine ligand. Interestingly the presumed catalytically active RuH species obtained from basic *iso*propanol solution was isolated and structurally resolved. In this report a ruthenium(II) complex bearing a similar asymmetric ligand was also investigated for enantioselectivity in the TH reaction of acetophenone derivatives. It was found that this complex gave yields of >95%, but the enantiomeric purity ranged from 56-79% *ee* which is less than the previously mentioned catalysts made by Noyori *et al*. Ruthenium(II) complexes bearing NNN type ligands, however, have been shown numerous times to be more active than their similar *p*-cymene half sandwich complexes.[88, 89]

These tridentate imine ligands have also been used in conjunction with bidentate NN and NO^- type ligands. In the latter, the bidentate ligands used were pyridine carboxlates and the hard donor O^- has the effect of stabilising the Ru(III) oxidation state. In the case of NN type ligands however the catalytic rate seemed less dependent on the bidentate ligand used and instead depended more on the acetophenone substrate used.[88] Bulkier phenyl substituents on the acetophenone substrate such as a 2,4,6-triphenyl group substantially lowered the overall yield to between 8-38% for the catalysts studied.

A neutral ruthenium(II) complex of the type $[RuCl_2L(PPh_3)]$ has been reported where L is the asymmetric ligand 2-(3,5-dimethyl-pyrazol-1-yl)-6-(1*H*-pyrazol-3-yl)-pyridine (Figure 1.21). This complex showed extremely high catalytic activity in the TH of acetophenone derivatives achieving a final TOF of 720000 h^{-1} for 2-bromoacetophenone.[90] The authors attribute this high catalytic activity to the asymmetry, hemilability and the presence of an NH functionality on the ligand. The asymmetry of the ligand infers an asymmetric coordination sphere to the ruthenium(II) which has been shown to increase catalytic activity.[87] The NH function on this ligand is presumed to be a major contributing factor to the accelerated activity by acting as a proton donor which facilitates the acceleration of the catalytic mechanism. While this NH function is deprotonated under basic conditions the catalytic intermediate was not isolated in this case, however the authors expect the mechanism to follow a similar mechanism to the catalytic cycle shown in Figure 1.18.

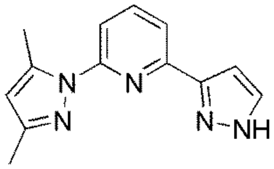

Figure 1.21
The asymmetric ligand 2-(3,5-dimethyl-pyrazol-1-yl)-6-(1*H*-pyrazol-3-yl)-pyridine.

1.3. Project Aims

The aim of this project is primarily to synthesise novel ligands for use in the areas of SCO and TH. Their iron(II) and ruthenium(II) complexes will then be made with the objective of (i) making novel complexes with behaviours desirable for potential applications such as data storage and (ii) improving the understanding of the factors that affect the functionality of these complexes. Both SCO and TH complexes have utilised derivatives of the 2,6-di(pyrazol-1-yl)pyridine (1-bpp). This ligand is able to be substituted on nearly every position by literature procedures and so the ligands sterics and electronics are easily tuneable. This property makes them ideal triimine ligands towards these applications and a wealth of interesting iron(II) SCO compounds and a few ruthenium(II) TH complexes. Specific examples of these will be discussed in the subsequent chapters.

The focus of this project, however, is on the structural isomer of 1-bpp, 2,6-di(1*H*-pyrazol-3-yl)pyridine (3-bpp) (Figure 1.22). This ligand has very similar steric and electronic properties to its 1-bpp isomer, but the most interesting feature of this ligand is the availability of the pyrazole NH function. In terms of SCO complexes these groups can act as hydrogen bond donors which may lead to the formation of hydrogen bond networks which increase the cooperativity of the system in the solid state. Complexes of this type could also be more susceptible to the hydrogen bonding nature of a solvent when in solution, which is expected to affect their $T_{1/2}$.

Figure 1.22
The two isomers 2,6-di(pyrazol-1-yl)pyridine (1-bpp) and 2,6-di(1*H*-pyrazol-3-yl)pyridine (3-bpp).

However, there are fewer examples of 3-bpp SCO complexes in the literature. This is due to the relative synthetic difficulty of making substituted 3-bpp compared to those of substituted 1-bpp. Therefore a primary aim of this project is to devise synthetic routes to novel 3-bpp derivatives. Some of these were comparable to their 1-bpp analogues, in which case the properties of their resulting complexes were compared and any differences accounted for in an attempt to further understanding of structure/function relationships in SCO compounds of iron(II). Other ligands were made with the aim of maximising intermolecular interactions within subsequent iron(II) SCO complexes, such as by adding steric bulk, hydrogen bond donors/acceptors or a combination of both to certain positions in the hope of increasing cooperativity. In addition a novel synthesis was utilised to synthesise the first examples of asymmetrically substituted 3-bpp ligands. These complexes were then characterised primarily by x-ray diffraction and magnetic susceptibility measurements in an attempt to identify any factors which affect the function.

The availability of the pyrazole NH groups also has implications in ruthenium(II) TH catalysts. These ligands are expected to form pincer type complexes, and this sets up the pyrazole NH function in a favourable position to be delivered to a substrate. This NH availability has been suggested to greatly increase the reaction rate and final TOF. Therefore ruthenium(II) complexes of the type $[RuCl(3\text{-bpp})(PPh_3)_2]Cl$ were made and characterised. Preliminary results were then obtained in order to ascertain their effectiveness as catalysts and to identify any trends which may occur as a result of the structure of the ligands.

1.4. References

[1] L. Cambi, L. Szegö and A. Cagnasso, *Atti Accad. Naz. Lincei, Cl. Sci. Fis., Mat. Nat., Rend.* **1932**, *15*, 329-335.

[2] C. D. Coryell, F. Stitt and L. Pauling, *J. Am. Chem. Soc.* **1937**, *59*, 633-642.

[3] A. H. Ewald, R. L. Martin, I. G. Ross and A. H. White, *Proc. R. Soc. London, Ser. A* **1964**, *280*, 235-257.

[4] S. Hayami, K. Kato, Y. Komatsu, A. Fuyuhiro and M. Ohba, *Dalton Trans.* **2011**, *40*, 2167-2169.

[5] G. Navon and W. Klaeui, *Inorg. Chem.* **1984**, *23*, 2722-2725.

[6] W. Klaeui, W. Eberspach and P. Gütlich, *Inorg. Chem.* **1987**, *26*, 3977-3982.

[7] K. Ono, M. Yoshizawa, M. Akita, T. Kato, Y. Tsunobuchi, S. I. Ohkoshi and M. Fujita, *J. Am. Chem. Soc.* **2009**, *131*, 2782-2783.

[8] G. G. Morgan, K. D. Murnaghan, H. Müller-Bunz, V. McKee and C. J. Harding, *Angew. Chem., Int. Ed.* **2006**, *45*, 7192-7195.

[9] M. D. Walter, C. D. Sofield, C. H. Booth and R. A. Andersen, *Organometallics* **2009**, *28*, 2005-2019.

[10] M. Sorai, Y. Maeda and H. Oshio, *J. Phys. Chem. Solids* **1990**, *51*, 941-951.

[11] Y. Maeda, H. Oshio, K. Toriumi and Y. Takashima, *J. Chem. Soc., Dalton Trans.* **1991**, 1227-1235.

[12] S. Schenker and A. Hauser, *J. Am. Chem. Soc.* **1994**, *116*, 5497-5498.

[13] A. Hauser, *Top. Curr. Chem.* **2004**, *233*, 49-58.

[14] A. L. Tchougréeff and R. Dronskowski, *Int. J. Quant. Chem.* **2009**, *109*, 2606-2621.

[15] C. E. Schaffer and C. K. Jørgensen, *J. Inorg. Nucl. Chem.* **1958**, *8*, 143-148.

[16] E. König, *Prog. Inorg. Chem.* **1987**, *35*, 527-622.

[17] E. König, G. Ritter and S. K. Kulshreshtha, *Chem. Rev.* **1985**, *85*, 219-234.

[18] M. Sorai and S. Seki, *J. Phys. Chem. Solids* **1974**, *35*, 555-570.

[19] E. König, *Struct. Bonding* **1991**, *76*, 51-152.

[20] M. A. Halcrow, *Chem. Soc. Rev.* **2011**, *40*, 4119-4142.

[21] J. K. McCusker, A. L. Rheingold and D. N. Hendrickson, *Inorg. Chem.* **1996**, *35*, 2100-2112.

[22] J. M. Holland, J. A. McAllister, C. A. Kilner, M. Thornton-Pett, A. J. Bridgeman and M. A. Halcrow, *J. Chem. Soc., Dalton Trans.* **2002**, 548-554.

[23] M. A. Halcrow, *Coord. Chem. Rev.* **2009**, *253*, 2493-2514.

[24] V. A. Money, C. Carbonera, J. Elhaïk, M. A. Halcrow, J. A. K. Howard and J. F. Létard, *Chem. Eur. J.* **2007**, *13*, 5503-5514.

[25] T. D. Roberts, M. A. Little, L. J. Kershaw Cook and M. A. Halcrow, *Dalton Trans.* **2014**, *43*, 7577-7588.

[26] N. Ortega-Villar, A. L. Thompson, M. C. Munoz, V. M. Ugalde-Saldivar, A. E. Goeta, R. Moreno-Esparza and J. A. Real, *Chem. Eur. J.* **2005**, *11*, 5721-5734.

[27] H. Spiering, T. Kohlhaas, H. Romstedt, A. Hauser, C. Bruns-Yilmaz, J. Kusz and P. Gütlich, *Coord. Chem. Rev.* **1999**, *190-192*, 629-647.

[28] A. Hauser, J. Jeftic, H. Romstedt, R. Hinek and H. Spiering, *Coord. Chem. Rev.* **1999**, *190-192*, 471-491.

[29] M. Sy, F. Varret, K. Boukheddaden, G. Bouchez, J. Marrot, S. Kawata and S. Kaizaki, *Angew. Chem., Int. Ed.* **2014**, *53*, 7539-7542.

[30] T. D. Roberts, F. Tuna, T. L. Malkin, C. A. Kilner and M. A. Halcrow, *Chem. Sci.* **2012**, *3*, 349-354.

[31] T. M. Pfaffeneder, S. Thallmair, W. Bauer and B. Weber, *New J. Chem.* **2011**, *35*, 691-700.

[32] J. McMurtrie and I. Dance, *CrystEngComm* **2005**, *7*, 230-236.

[33] J. McMurtrie and I. Dance, *CrystEngComm* **2010**, *12*, 2700-2710.

[34] M. L. Scudder, H. A. Goodwin and I. G. Dance, *New J. Chem.* **1999**, *23*, 695-705.

[35] S. Hayami, K. Hiki, T. Kawahara, Y. Maeda, D. Urakami, K. Inoue, M. Ohama, S. Kawata and O. Sato, *Chem. Eur. J.* **2009**, *15*, 3497-3508.

[36] I. Nemec, R. Herchel and Z. Travnicek, *Dalton Trans.* **2015**, Ahead of Print.

[37] R. L. Mössbauer and D. H. Sharp, *Rev. Mod. Phys.* **1964**, *36*, 410-417.

[38] D. F. Evans, *J. Chem. Soc.* **1959**, 2003-2005.

[39] L. A. Yatsunyk and F. A. Walker, *Inorg. Chem.* **2004**, *43*, 757-777.

[40] H. M. Rietveld, *J. Appl. Crystallogr.* **1969**, *2*, 65-71.

[41] A. Bousseksou, G. Molnar, L. Salmon and W. Nicolazzi, *Chem. Soc. Rev.* **2011**, *40*, 3313-3335.

[42] J. F. Létard, P. Guionneau and L. Goux-Capes, *Top. Curr. Chem.* **2004**, *235*, 221-249.

[43] O. Kahn, C. Jay, E. Codjovi and L. Sommier in *Spin-transition compounds and display devices comprising a screen with an active medium including at least one of these compounds*, Philips Electronics N. V., Neth. . **1998**, p. 31 pp.

[44] I. R. Jeon, J. G. Park, C. R. Haney and T. D. Harris, *Chem.Sci.* **2014**, *5*, 2461-2465.

[45] S. L. Fossheim, K. A. Il'yasov, J. Hennig and A. Bjornerud, *Acad. Radiol.* **2000**, *7*, 1107-1115.

[46] R. N. Müller, E. L. Vander and S. Laurent, *J. Am. Chem. Soc.* **2003**, *125*, 8405-8407.

[47] C. Bartual-Murgui, A. Akou, L. Salmon, G. Molnar, C. Thibault, J. A. Real and A. Bousseksou, *Small*, **2011**, *7*, 3385-3391.

[48] P. D. Southon, L. Liu, E. A. Fellows, D. J. Price, G. J. Halder, K. W. Chapman, B. Moubaraki, K. S. Murray, J. F. Létard and C. J. Kepert, *J. Am. Chem. Soc.* **2009**, *131*, 10998-11009.

[49] Z. Ni and M. P. Shores, *J. Am. Chem. Soc.* **2009**, *131*, 32-33.

[50] A. D. Naik and Y. Garcia, *Hyperfine Interact.* **2012**, *206*, 7-11.

[51] A. D. Naik, L. Stappers, J. Snauwaert, J. Fransaer and Y. Garcia, *Small* **2010**, *6*, 2842-2846.

[52] M. Matsuda, H. Isozaki and H. Tajima, *Chem. Lett.* **2008**, *37*, 374-375.

[53] C. K. Jørgensen, *Absorption Spectra and Chemical Bonding in Transition Metal Complexes*, Pergamon, Oxford, UK, **1962**, p.

[54] M. A. Robinson, J. D. Curry and D. H. Busch, *Inorg. Chem.* **1963**, *2*, 1178-1181.

[55] H. A. Goodwin, *Top. Curr. Chem.* **2004**, *233*, 59-90.

[56] J. M. Holland, S. A. Barrett, C. A. Kilner and M. A. Halcrow, *Inorg. Chem. Commun.* **2002**, *5*, 328-332.

[57] B. Weber, W. Bauer, T. Pfaffeneder, M. M. Dîrtu, A. D. Naik, A. Rotaru and Y. Garcia, *Eur. J. Inorg. Chem.* **2011**, *2011*, 3193-3206.

[58] Y. Kikuta, T. Ishimoto and U. Nagashima, *Chem. Phys.* **2008**, *354*, 218-224.

[59] S. A. Barrett, C. A. Kilner and M. A. Halcrow, *Dalton Trans.* **2011**, *40*, 12021-12024.

[60] K. H. Sugiyarto, D. C. Craig, A. D. Rae and H. A. Goodwin, *Aust. J. Chem.* **1994**, *47*, 869-890.

[61] G. C. De Graaf and C. Sousa, *Chem. Eur. J.* **2010**, *16*, 4550-4556.

[62] S. Decurtins, P. Gütlich, C. P. Köhler, H. Spiering and A. Hauser, *Chem. Phys. Lett.* **1984**, *105*, 1-4.

[63] A. Hauser, *J. Chem. Phys.* **1991**, *94*, 2741-2748.

[64] S. Hayami, K. Hiki, T. Kawahara, Y. Maeda, D. Urakami, K. Inoue, M. Ohama, S. Kawata and O. Sato, *Chem. Eur. J.* **2009**, *15*, 3497-3508.

[65] J. F. Létard, *J. Mater. Chem.* **2006**, *16*, 2550-2559.

[66] P. Gütlich, A. B. Gaspar, Y. Garcia and V. Ksenofontov, *C. R. Chim.* **2007**, *10*, 21-36.

[67] V. Ksenofontov, G. Levchenko, H. Spiering, P. Gütlich, J. F. Létard, Y. Bouhedja and O. Kahn, *Chem. Phys. Lett.* **1998**, *294*, 545-553.

[68] Y. Qi, E. W. Müller, H. Spiering and P. Gütlich, *Chem. Phys. Lett.* **1983**, *101*, 503-505.

[69] N. Negre, M. Goiran, A. Bousseksou, J. Haasnoot, K. Boukheddaden, S. Askenazy and F. Varret, *Synth. Met.* **2000**, *115*, 289-292.

[70] R. Kulmaczewski, J. Olguin, J. A. Kitchen, H. L. C. Feltham, G. N. L. Jameson, J. L. Tallon and S. Brooker, *J. Am. Chem. Soc.* **2014**, *136*, 878-881.

[71] R. G. Miller, S. Narayanaswamy, J. L. Tallon and S. Brooker, *New J. Chem.* **2014**, *38*, 1932-1941.

[72] G. A. Renovitch and W. A. Baker, Jr., *J. Am. Chem. Soc.* **1967**, *89*, 6377-6378.

[73] G. Lemercier, N. Brefuel, S. Shova, J. A. Wolny, F. Dahan, M. Verelst, H. Paulsen, A. X. Trautwein and J. P. Tuchagues, *Chem. Eur. J.* **2006**, *12*, 7421-7432.

[74] M. M. Dîrtu, A. Rotaru, D. Gillard, J. Linares, E. Codjovi, B. Tinant and Y. Garcia, *Inorg. Chem.* **2009**, *48*, 7838-7852.

[75] M. Sorai, J. Ensling, K. M. Hasselbach and P. Gütlich, *Chem. Phys.* **1977**, *20*, 197-208.

[76] R. J. Wei, J. Tao, R. B. Huang and L. S. Zheng, *Inorg. Chem.* **2011**, *50*, 8553-8564.

[77] C. Reichardt, *Chem. Rev.* **1994**, *94*, 2319-2358.

[78] Y. Marcus, *Chem. Soc. Rev.* **1993**, *22*, 409-416.

[79] J. Catalan, C. Diaz, V. Lopez, P. Perez, P. J. L. G. De Paz and J. G. Rodriguez, *Liebigs Ann.* **1996**, 1785-1794.

[80] M. J. Kamlet, J. L. M. Abboud, M. H. Abraham and R. W. Taft, *J. Org. Chem.* **1983**, *48*, 2877-2887.

[81] R. Noyori, T. Ikeda, T. Ohkuma, M. Widhalm, M. Kitamura, H. Takaya, S. Akutagawa, N. Sayo and T. Saito, *J. Am. Chem. Soc.* **1989**, *111*, 9134-9135.

[82] M. Kitamura, T. Ohkuma, S. Inoue, N. Sayo, H. Kumobayashi, S. Akutagawa, T. Ohta, H. Takaya and R. Noyori, *J. Am. Chem. Soc.* **1988**, *110*, 629-631.

[83] T. Ikariya, K. Murata and R. Noyori, *Org. Biomol. Chem.* **2006**, *4*, 393-406.

[84] R. Noyori, M. Yamakawa and S. Hashiguchi, *J. Org. Chem.* **2001**, *66*, 7931-7944.

[85] K. Puentener, L. Schwink and P. Knochel, *Tetrahedron Lett.* **1996**, *37*, 8165-8168.

[86] S. Hashiguchi, A. Fujii, J. Takehara, T. Ikariya and R. Noyori, *J. Am. Chem. Soc.* **1995**, *117*, 7562-7563.

[87] W. Ye, M. Zhao, W. Du, Q. Jiang, K. Wu, P. Wu and Z. Yu, *Chem. Eur. J.* **2011**, *17*, 4737-4741.

[88] O. Dayan, N. Ozdemir, Z. Serbetci, M. Dincer, B. Cetinkaya and O. Buyukgungor, *Inorg. Chim. Acta* **2012**, *392*, 246-253.

[89] S. Gunnaz, N. Ozdemir, S. Dayan, O. Dayan and B. Cetinkaya, *Organometallics* **2011**, *30*, 4165-4173.

[90] W. Jin, L. Wang and Z. Yu, *Organometallics* **2012**, *31*, 5664-5667.

Chapter 2

Ligand Synthesis

2.1. Introduction

This chapter is concerned with the synthesis of all novel ligands used in this research. The aims of this part of the project were to create, by modifying existing literature procedures, a series of ligands based on the 2,6-di(1*H*-pyrazol-3-yl)pyridine skeleton. These would then be used to make iron complexes in the hope that by tuning their sterics and electronics spin crossover could be achieved. While there are examples of SCO complexes containing imine ligands based on 2,2-bipyridine,[1] terpyridine,[2] Schiff base,[3] and porphyrin ligands[4] one of the most conducive areas of research have focused on 2,6-di(pyrazol-1-yl)pyridine (1-bpp) derivatives.[5] These tridentate ligands, as with other aromatic imines, are strong σ-donors to the metal but also contain low lying π^* orbitals which allow backbonding from the metal d^{π} orbitals thus strengthening the M–L interaction.[6] These ligands in particular provide a good N^6 coordination sphere to promote SCO behaviour in iron(II). The factors which determine whether a complex will undergo a spin transition were discussed in detail in Chapter 1.

In the literature there are plentiful examples of 1-bpp ligands which have been substituted on almost all positions on both the pyridine and pyrazole rings.[7-10] This is largely due to the versatility of the synthetic procedure which involves heating the 2,6-dibromopyridine with the desired pyrazolate ion (Scheme 2.1). This procedure can be applied to various pyridine and pyrazole derivatives, although the yield is reduced when bulkier pyrazole derivatives are used.[8]

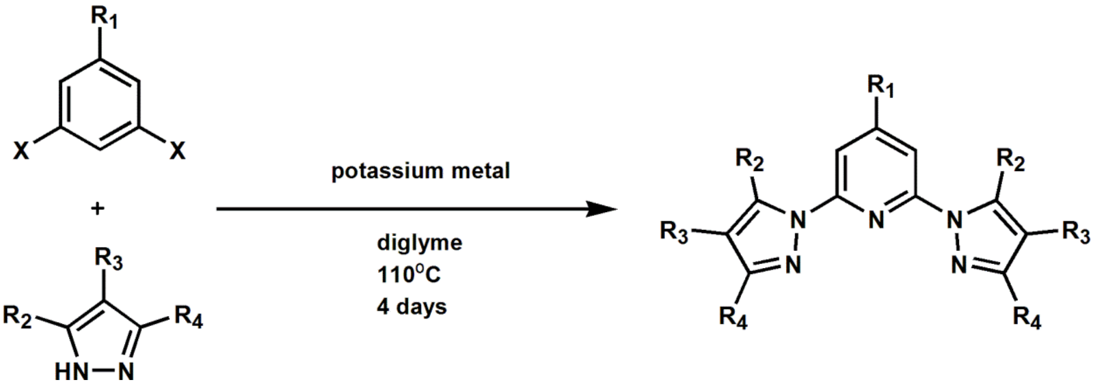

Scheme 2.1
Scheme showing the synthesis of 1-bpp derivatives, where X = Cl, Br.

While some simple substituted pyrazoles are commercially available, synthetic routes to more complicated derivatives are can also be utilised.[11] By using 2,6-dichloro-isonicotinic acid methyl ester as the pyridine moiety in the reaction scheme shown in Scheme 2.1, the resulting 2,6-di-pyrazol-1-yl-isonicotinic acid methyl ester can, through a succession of steps, be converted to 4-iodo-2,6-di-pyrazol-1-ylpyridine, whose iodo functionality can allow a wide range of substituents to be added to the pyridyl *C*4 position via a Suzuki cross coupling reaction.[12, 13]

In addition to the considerable success achieved in the field of SCO using these ligands there has also been interest in its structural isomer 2,6-di(1*H*-pyrazol-3-yl)pyridine (3-bpp).[14] There are far fewer examples of substituted 3-bpp ligands in the literature, however. The general procedure for making unsubstituted 3-bpp starts with 2,6-diacetyl pyridine. Heating this with N,N-dimethylformamide dimethylacetal gives two oxopropene groups which are predisposed to cycloaddition with hydrazine, thus forming the pyrazole rings *in situ* (Scheme 2.2).[15, 16]

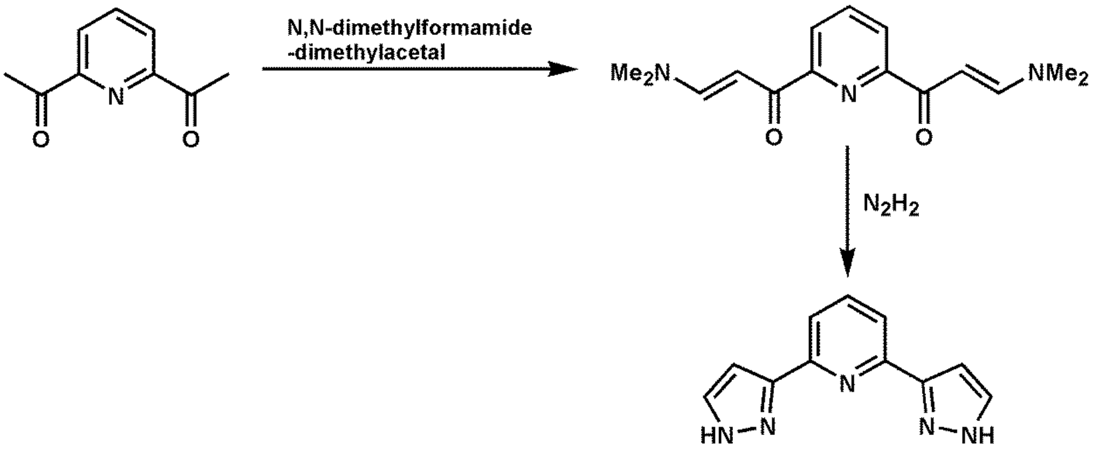

Scheme 2.2
Scheme showing the synthesis of unsubstituted 3-bpp.

Although this method provides a convenient route to unsubstituted 3-bpp, it lacks the versatility of the 1-bpp synthesis which would allow the introduction of peripheral substituents. By changing the reagent in the first step substituents can be added to the pyrazolyl *C*5 position, however the derivatives of N,N-dimethylformamide dimethylacetal which are commercially available are very limited.[17]

More recently there have been examples photoluminescent and catalytically active transition metal complexes using 3-bpp ligands substituted at the pyrazolyl *C*5 position, and these ligands have also been used for actinide(III)/lanthanide(III) separation.[18-20] The synthetic route utilised by Chen *et al* involves a Claisen condensation using a base to form an enolate which can then displace the methoxy groups in dimethyl 2,6-pyridinedicarboxylate. [21, 22] This produces a *bis*diketone which can subsequently react with hydrazine to form the pyrazole rings incorporating the R group present in the initial ketone (Scheme 2.3).

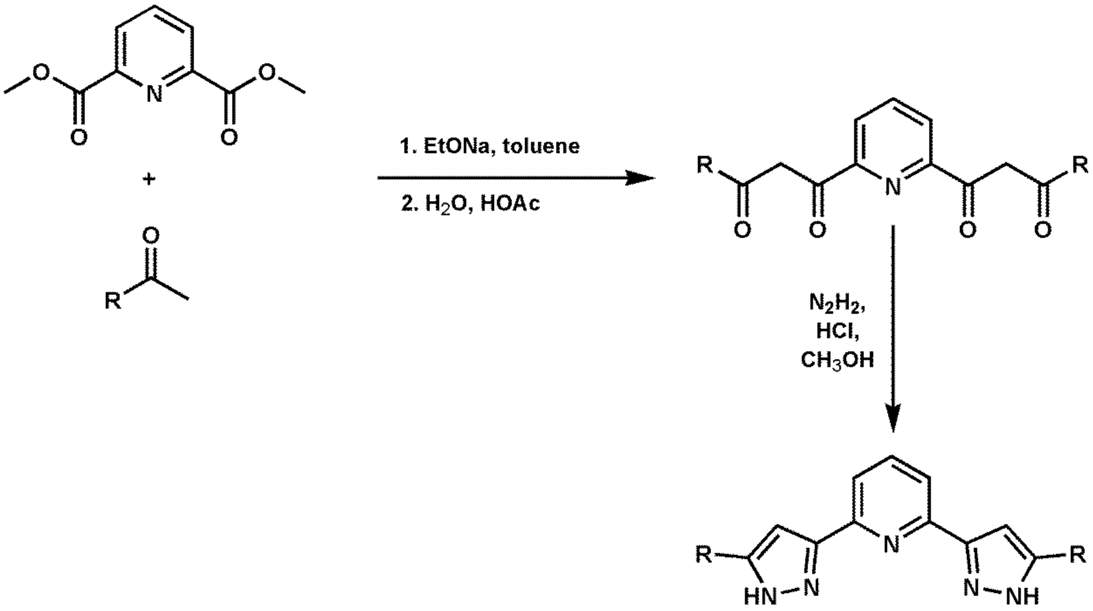

Scheme 2.3
Scheme showing a synthetic route towards 3-bpp derivatives bearing alkyl substituents on the pyrazolyl *C*5 position.[21]

Despite the occurrence of these ligands they have rarely been used in iron SCO complexes as a method of sterically or electronically tuning the environment around the iron centre. With these available synthetic methods we hoped to introduce a number of substituents to the 3-bpp skeleton, specifically electron donating and withdrawing groups, sterically bulky groups and hydrogen bond donators and acceptors, so that their effects on SCO can be compared in order to establish any structure/function relationships that might exist.

2.2. *N*1 Substituted 2,6-Di(1*H*-pyrazol-3-yl)pyridine Derivatives

Substitution at the pyrazole NH group takes place via a nucleophilic substitution of an appropriate alkyl halide by a pyrazolate ion formed *in situ*. This procedure can be performed using 3-bpp, after it has been synthesised by the standard procedure described above.[23] In this work four ligands were synthesised using this method each with a different alkyl group on the pyrazolyl NH position (Figure 2.1).

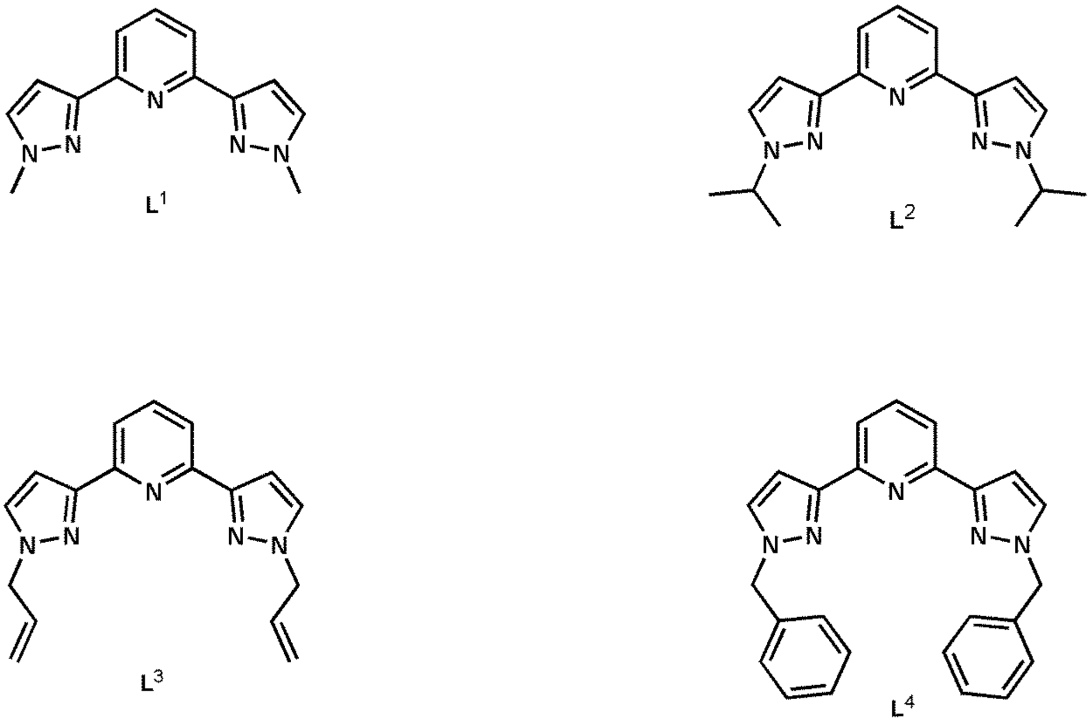

Figure 2.1
The pyrazole NH substituted ligands discussed in this work and their abbreviations.

The methyl substituent was chosen because it is isostructural to a 1-bpp analogue which has previously produced interesting SCO complexes.[24] The isopropyl group was added in order to study the effects of increasing steric bulk at this position, however during the synthetic workup this proved troublesome as the white solid product was unexpectedly soluble in water, and could not be extracted into any organic solvent. Microanalysis also showed that its C, H and N values were significantly lower than expected, which was initially thought to be due to the presence of sodium iodide which is usually removed by washing with water. However, the reason for this behaviour is now thought to be that the ligand is able to form a stable six-coordinate complex with a sodium ion, increasing its water solubility and so making it difficult to isolate.[25] The solution to this problem was to change the base used from sodium methoxide to lithium hydride. As Li^+ is smaller than Na^+ it does not form complexes with such high stability and so does not become a problem during the workup.

Allyl substituents were next chosen and they add additional functionality to the ligand; the allyl groups could potentially coordinate to another metal such as silver to create coordination polymers or, should their iron complexes prove interesting, they could be used as precursors towards additional functional groups. In this case allyl bromide was used instead of the iodide because it was more available and the reaction proceeded favourably. Benzyl bromide was also used to attach the benzyl appendages for the same reason and both of these reactions used lithium hydride as a base to avoid the problem of forming sodium complexes.

Evidence for the formation of the desired products came from the proton NMR spectrum, which clearly shows the absence of the broad pyrazolyl NH peaks which usually come between 9 – 12 ppm, and are replaced by expected shifts for the distal substituents in both the ^1H and ^{13}C {^1H} NMR spectra (Figure 2.2). Formation of the ligands was also confirmed by high resolution mass spectrometry, microanalysis and their expected structures were observed in the crystal structures of their subsequent iron complexes which are discussed in detail in Chapter 3.

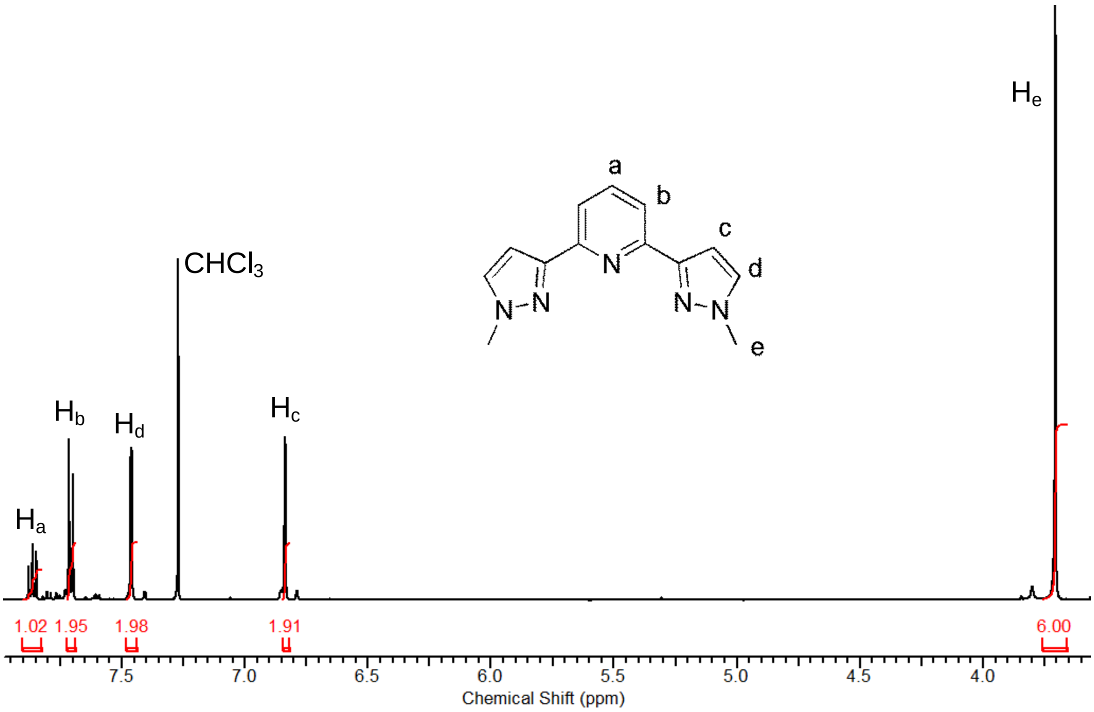

Figure 2.2
^1H NMR spectrum of 2,6-di(1-methylpyrazol-3-yl)pyridine (**L**^{1}) recorded at 500 MHz in $CDCl_3$.

It would have been desirable to attach a phenyl group directly to the pyrazolyl NH functionality. This would prove difficult by the method described above as the sp^2 hybridised carbon in benzene is not reactive enough to undergo nucleophilic substitution unless there are electron withdrawing groups present on the ring. An attempt was made to obtain this ligand by replacing hydrazine in the pyrazole ring forming step with phenylhydrazine, although a mixture of products were obtained. HPLC-MS shows three separate peaks all of m/z = 364.2 corresponding to $[MH]^+$ of the desired product (Figure 2.3). It is suspected that these three peaks correspond to three possible structural isomers of 2,6-di-(1-phenylpyrazol-3-yl)-pyridine which arise from the possibility of the phenylhydrazine to attack either ketone. This would give rise to two symmetric and one unsymmetric ligands and these are yet to be successfully isolated (Scheme 2.4).

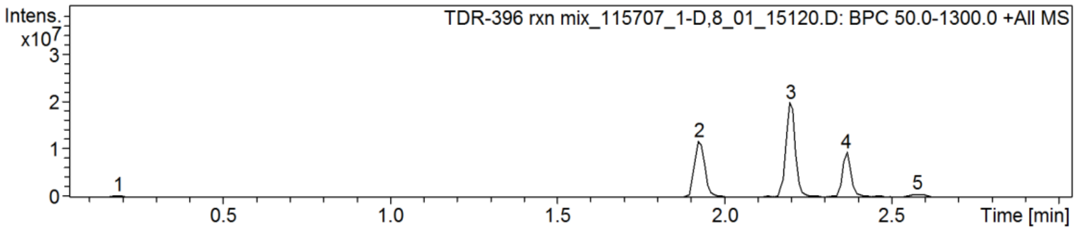

Figure 2.3
HPLC-MS chromatogram of 2,6-di-(phenylpyrazol-3-yl)-pyridine attempt. Peaks 2, 3 and 4 correspond to m/z 364.2 $[MH]^+$.

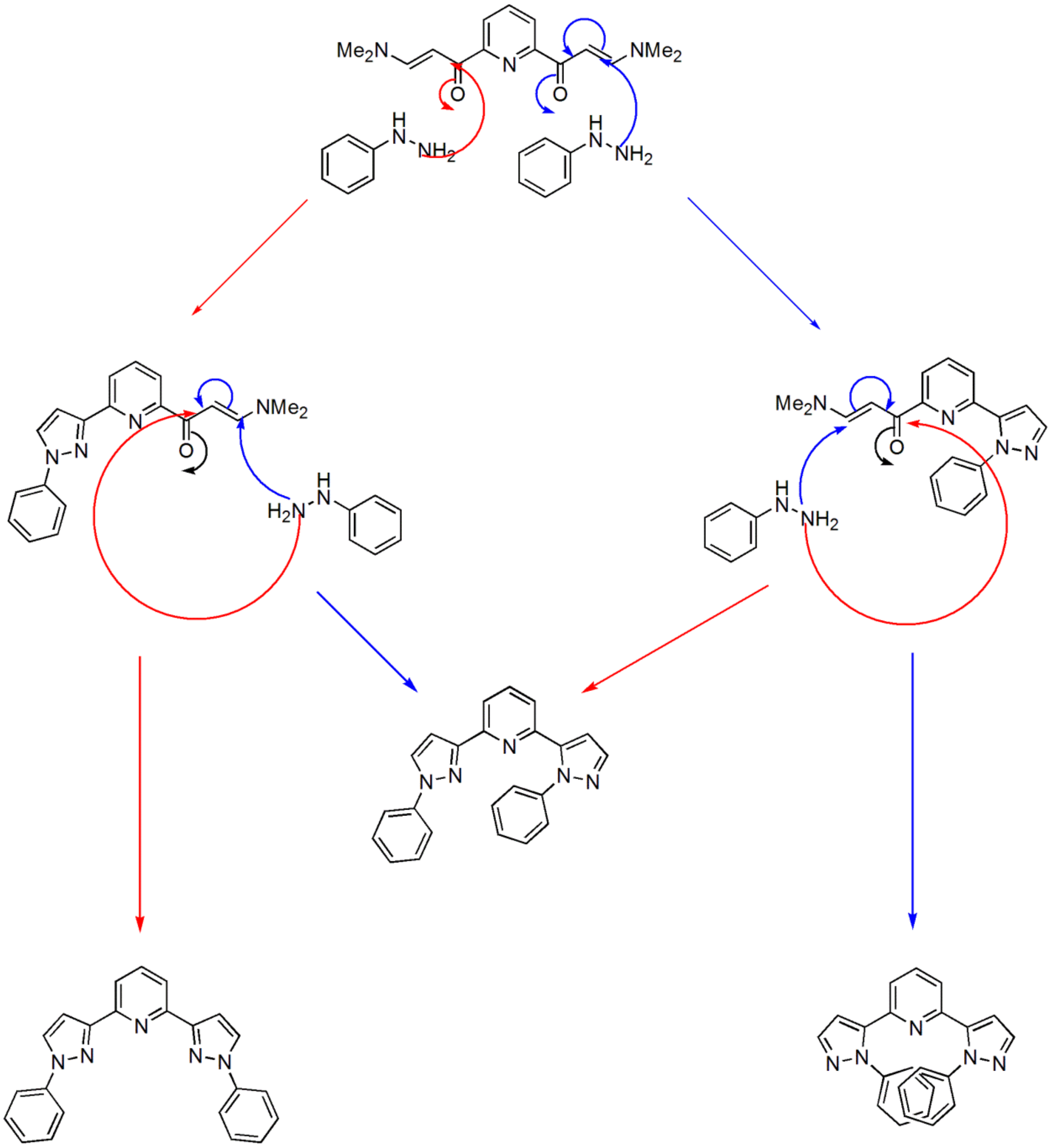

Scheme 2.4
Proposed mechanism of the initial step in the formation of 3 isomers of 2,6-di-(phenylpyrazol-3-yl)-pyridine from the ring closing of 2,6-di[(N,N-dimethylamino)-1-oxoprop-2-en-1-yl]pyridine with phenylhydrazine.

Scheme 2.4 shows that the initial step in the proposed mechanism is important in determining the different regiochemistry of these isomers. Note that the mechanism follows through a number of subsequent steps (not shown). These involve the formation of an imine and an enamine and all of these steps are reversible, meaning that each isomer must have a very similar thermodynamic stability.

Another halide which was used for this reaction was 4-chloropyridine in an attempt to attach a 4-pyridyl group onto the pyrazolyl NH in a similar manner. Pyridines are much more reactive towards nucleophilic substitution than benzene rings, but even so after 5 days reflux in tetrahydrofuran the mixture still contained a considerable amount of starting material.

2.3. 2,6-Di(5-amino-1*H*-pyrazol-3-yl)pyridine Derivatives

As a first step towards creating 3-bpp derivatives with modifications which may have implications in a SCO complex we were interested in adding additional hydrogen donor/acceptor groups which would inherently be electron withdrawing, tuning the electronics of the ligand while possibly increasing cooperativity. One synthetically available ligand which meets all these requirements is 2,6-di(5-amino-1*H*-pyrazol-3-yl)pyridine (**L^5**), since a procedure for its synthesis has quite recently been outlined in the literature.[26] This method involves a Knoevenagel condensation using sodium hydride to deprotonate acetonitrile.[27] The nucleophilic acetonitrile anion can then attack the carbonyl carbons on 2,6-pyridine dicarboxylic methyl ester to produce 2,6-di-(3-oxo-3-propanenitrile)pyridine. This 3-oxo-3-propanenitrile functionality can then react with hydrazine to form the pyrazolyl rings which incorporate amino groups on the *C*5 position. It was difficult to obtain an accurate microanalysis for this product as the sample seemed to retain significant amounts of atmospheric water which caused fluctuations in the weight of the sample before combustion. This water was also seen to be removed during the melting point determination and is probably due to the increased hydrogen bonding nature of the compound. Evidence of the formation of the ligand came from the ^{1}H NMR spectrum which is similar to that quoted in the literature. The ES$^+$ mass spectrum also shows the expected peak at *m/z* 242.1 Corresponding to $[MH]^+$.

2.3.1. Synthesis of Amides

One obvious transformation of the **L^5** ligand is to react with an acid chloride to produce amides (Figure 2.4). The commercial availability of a wide range of acid chlorides makes this a synthetically simple route towards substituting larger groups at the pyrazolyl *C*5 position. Initially attempts were made using acetyl chloride, trimethylacetyl chloride and benzoyl chloride. In the case of acetyl chloride the high reactivity of this acid chloride resulted in a mixture of products, one of which appeared to be a result of tetrasubstitution of the amino groups and the pyrazolyl NH groups, which was observed as a peak at *m/z* 410 in the HPLC-MS. The reactions with the less reactive trimethylacetyl chloride and benzoyl chloride however proceeded much more cleanly and **L^6** and **L^7** were obtained as their hydrochloride salts. The hydrochloride salts were then deprotonated using a biphasic saturated sodium carbonate solution/chloroform mixture to produce the desired ligands.[28]

The successful synthesis of the *tert*butyl amide ligand **L^6** was confirmed by the large singlet at 1.27 ppm in the ^{1}H NMR which integrated at 18H, corresponding to the *tert*butyl groups and a peak at 175 ppm in the ^{13}C {^{1}H} NMR spectrum corresponding to the amide carbonyl group (Figure 2.5). The ES^{+} mass spectrum also showed the expected mass of *m/z* 432.2 corresponding to the [MNa]$^{+}$ ion. The formation of **L^{7}** was confirmed by the presence of an additional two triplets and one doublet between 7.5 – 8.1 ppm which integrated to 10H in total. The ^{13}C {^{1}H} NMR also showed a peak at 164.6 ppm which confirms the presence of the amide carbonyl function. The IR spectrum showed a very distinctive C=O stretching frequency at 1672 cm^{-1} and ν(N–H) has been shifted to a higher frequency of ~3400 cm^{-1}, compared with a frequency of 3302 cm^{-1} for **L^{5}**. In both these cases the hydrochloride salts and the ligands could only be distinguished from one another by CHN analysis which showed the absence of any chlorine and an increase in the C, H and N values confirming that the deprotonation was successful and had proceeded to completion.

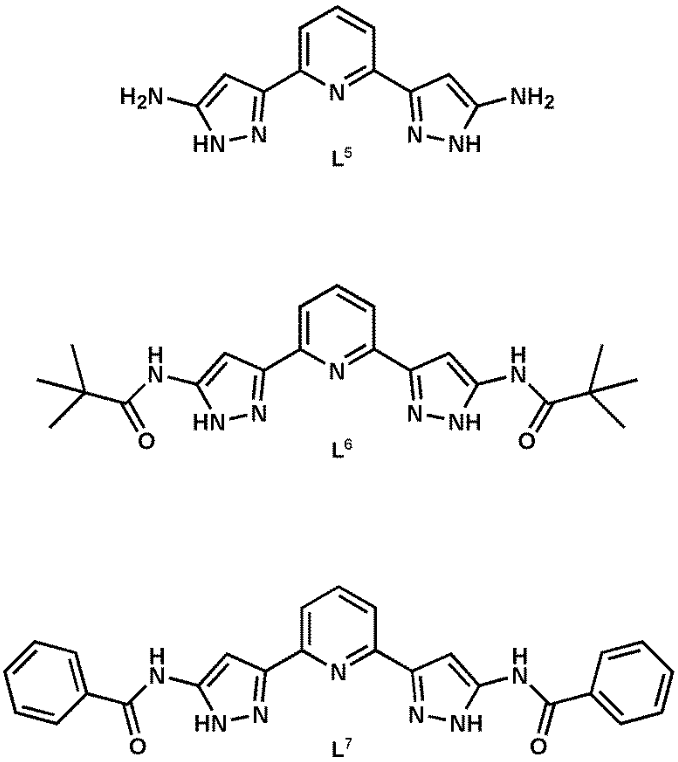

Figure 2.4
Successfully synthesised 3-bpp ligands bearing amino and amide groups on the pyrazolyl *C*5 position, and their abbreviations.

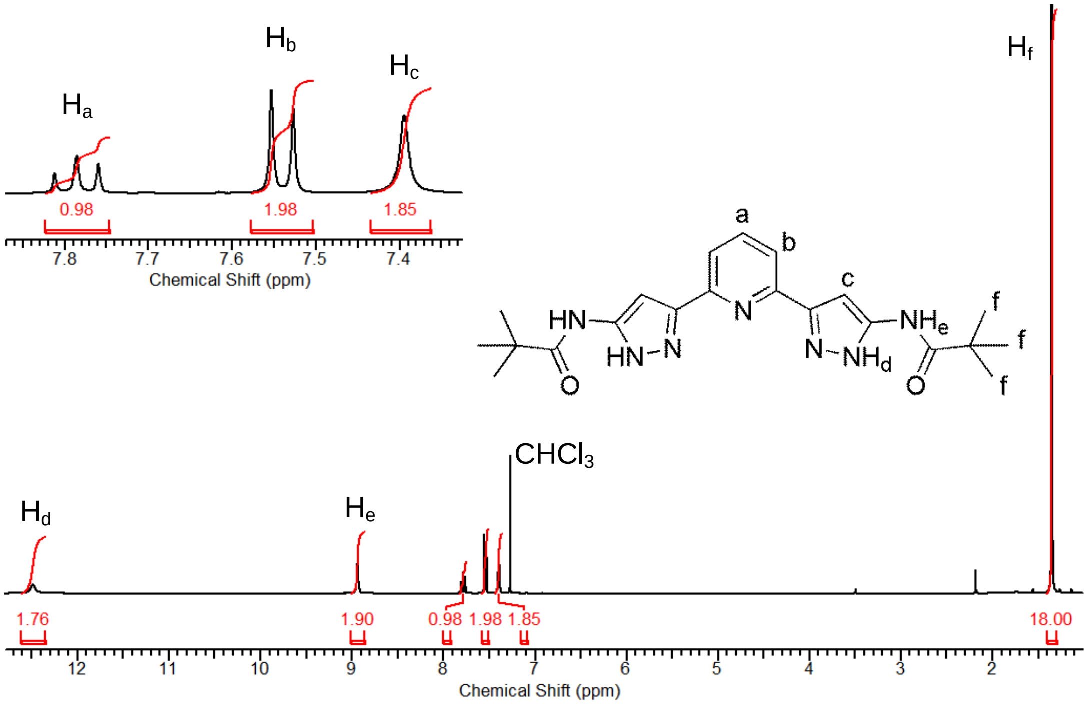

Figure 2.5
^{1}H NMR spectrum of 2,6-di(5-{*tert*butylamide}-1*H*-pyrazol-3-yl)pyridine (**L**^{6}) recorded at 300 MHz in $CDCl_3$.

2.3.2. Synthesis of Thioureas

Thioureas are another class of compounds which were thought to be obtainable from the amino ligand **L**^{5} by reaction with isothiocyanates (Scheme 2.5). Like the acid chlorides there are a wide range of commercially available isothiocyanates which could be used to introduce different substituents to the pyarazolyl *C*5 position. However it is the hydrogen bonding capabilities of thioureas that were interesting from a SCO perspective. 3-bpp derivatised with two thiourea groups at the pyrazolyl *C*5 positions will possess four additional hydrogen bond donors. While sulphur is considered a weaker hydrogen bond acceptor than N and O due to its lower electronegativity, it has been shown that sulphur is capable of forming multiple hydrogen bonds which may influence the morphology of any subsequent complexes.[29]

As a starting point two equivalents of methyl isothiocyanate were heated at reflux in acetonitrile for 18 hours. After this time HPLC-MS of the crude mixture showed that some starting material was still present and so an excess of methyl isothiocyanate was added to complete the reaction, giving a white amorphous powder in 50 % yield. This was confirmed as the desired product, 2,6-di(5-{methylthiourea}-1*H*-pyrazol-3-yl)pyridine (**L**^{8}), by CHN and S microanalysis, ES$^+$ mass spectrum and NMR. The ES$^+$ mass spectrum shows a peak at *m/z* 410.1 which correlates to the $[MNa]^+$ adduct. ^{1}H NMR shows a peak at 3.11 ppm which integrates for 6 H confirming the addition of the methyl groups, and ^{13}C {^{1}H} NMR shows a peak at 206.6 ppm confirming the presence of the C=S groups.

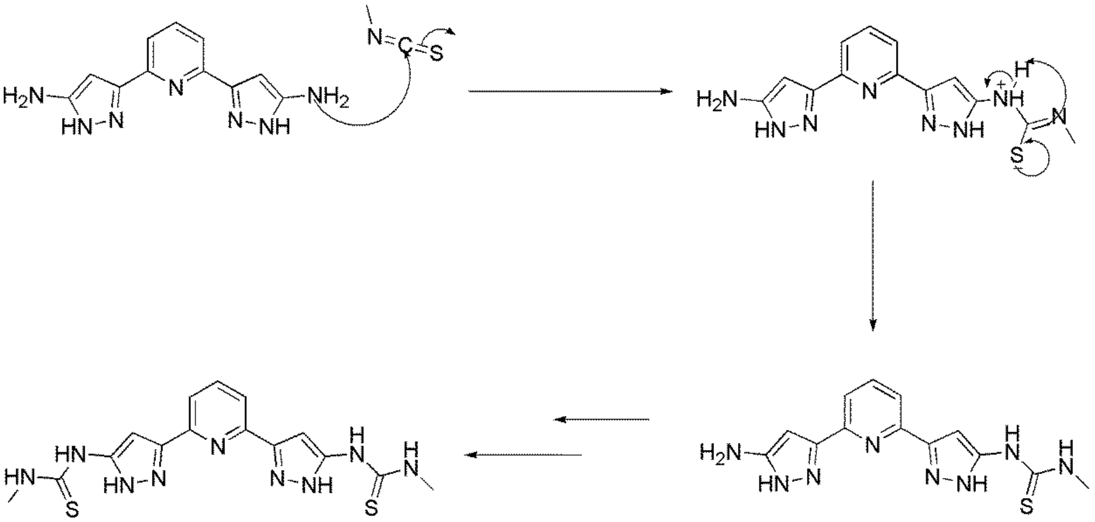

Scheme 2.5
Proposed mechanism for the formation of 2,6-di(5-{methylthiourea}-1*H*-pyrazol-3-yl)pyridine (**L^8**).

It was hoped that this synthetic procedure could be applied to a number of alkyl isothiocyanates to produce a number of novel 3-bpp derivatives. As the **L^8** proved to be sparingly soluble in most common solvents *tert*butyl isothiocyanate was used in an attempt to make a more soluble thiourea. However numerous attempts at this reaction returned only starting material and could be due to the steric bulk or inductive effects of the *tert*butyl group. The reaction was also attempted using cyclohexyl isothiocyanate and phenyl isothiocyanate though no products could be isolated in these cases. In a reaction using cyclohexyl isothiocyanate, after heating at reflux for 36 hours in acetonitrile HPLC-MS showed the presence of approximately 10 % of desired product with roughly equal amounts of starting material and monosubstituted product accounting for the remainder of the material.

During an attempted complexation with iron tetrafluoroborate hexahydrate crystals of the ligand **L^8** were obtained after three months which were suitable for x-ray diffraction. However the structure obtained did not correspond to the expected structure. Instead of thiourea groups on the pyrazolyl *C*5 position the structure contained two methylthioamides on these positions, and the pyrazolyl NH groups had been methylated (Figure 2.6). The reaction mechanism for the formation of this product is not clear, but looks to have proceeded through some kind of rearrangement. This structure does not fit the ^{1}H NMR obtained for **L^8** which clearly shows only one methyl environment integrating as 6 H, and one would expect an additional peak at around 3.8 ppm corresponding to the methyl group on the pyrazolyl NH functionality. The ^{1}H NMR spectrum also shows the presence of the pyrazolyl NH environments as a peak at 12.15 ppm. This suggests that the change that resulted in this structure is likely to have occurred during or in the months after the complexation reaction.

The structure of $\mathbf{L^8}\cdot C_4H_9NO\cdot(C_2H_5)_2O$ was collected in the orthorhombic space group *Pnma* (a = 13.9215(8); b = 29.2705(14); c = 8.1439(4) Å, $\alpha = \beta = \gamma$ = 90º, V = 3318.5(3) Å^3) and the ligand lies on a C_2 crystallographic axis which intersects the pyridine through N(4) and C(1). The angle between C(7)-C(11)-S(12) = 123.5(3)° and is a result of the steric contact between S(12) and the C(10) methyl group.

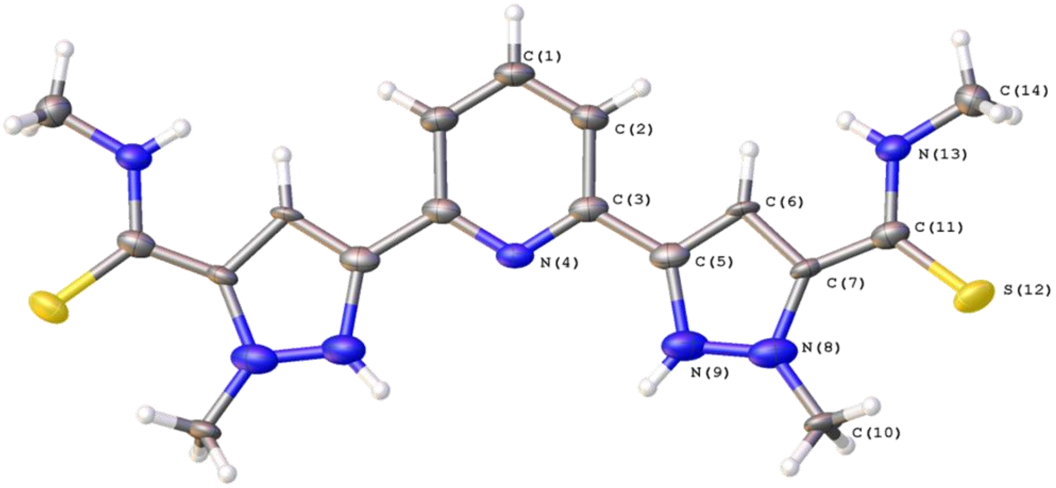

Figure 2.6
Obtained crystal structure of $\mathbf{L^8}\cdot C_4H_9NO\cdot(C_2H_5)_2O$. Thermal displacement ellipsoids are set at 50% probability and disordered solvent molecules have been omitted for clarity.

2.4. Substitution at the Pyrazolyl *C*5 Position

Interest in substituting alkyl groups on the pyrazolyl *C*5 position stems from previous work which involved complexes containing the ligand 2,6-di-(5-methyl-1*H*-pyrazol-3-yl)-pyridine ($\mathbf{L}^9$) giving systems exhibiting complex phase behaviour accompanied by an abrupt thermal hysteresis.[30] These will be discussed in some detail in Chapter 5. The synthesis of $\mathbf{L}^9$ follows a similar method to that for unsubstituted 3-bpp, the only difference being that N,N-dimethylacetamide dimethylacetal was used instead of N,N-dimethylformamide dimethylacetal. This gave an intermediate which is predisposed to ring closure using hydrazine, except with methyl groups which are incorporated into the pyrazole rings (Scheme 2.6).

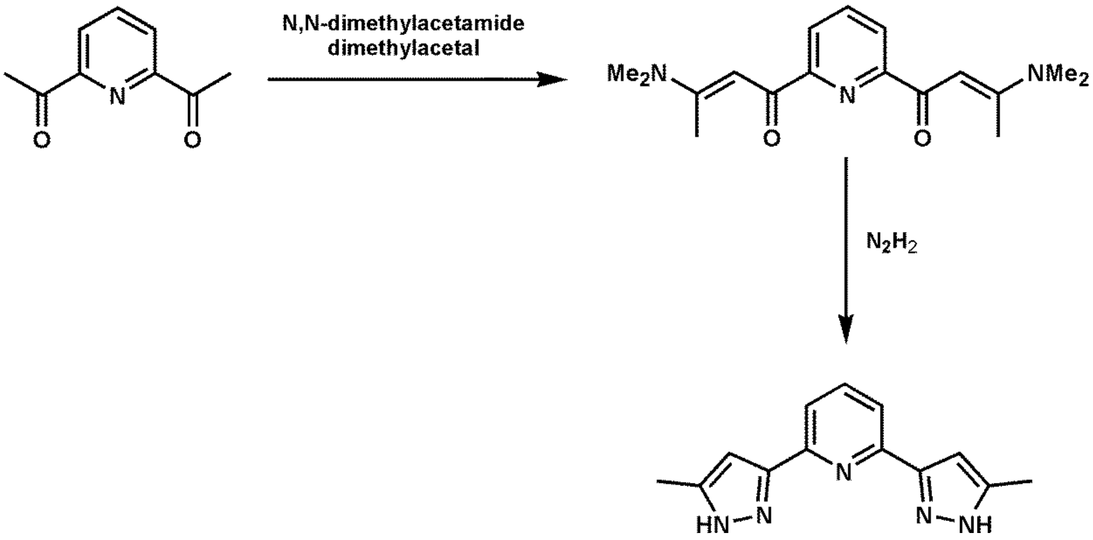

Scheme 2.6
Scheme showing the synthetic route towards 2,6-di-(5-methyl-1*H*-pyrazol-3-yl)-pyridine ($\mathbf{L}^9$).

This procedure works very well with an overall yield of 53 %, with the first step being the lower yielding of the two. Despite this the procedure is very limited in terms of the range of the substituents that can be placed on the pyrazolyl *C*5 position, since other substituted N,N-dimethylformamide dimethylacetal reagents are not available. One way around this is to react dimethyl 2,6-pyridinedicarboxylate with a ketone in the presence of a base in the manner previously shown in Scheme 2.3. As there are a vast array of ketones available this method can be applied to place a large number of substituents on the pyrazolyl *C*5 position. The base used for these reactions was usually sodium methoxide, and this was used in excess along with a small excess of the ketone.

2.4.1. Substitution with Alkyl Groups

Initially ligands were synthesised which attempted to build on the success of **L**^{9} and investigate the effects of modifying the steric bulk and inductive effects on the resulting iron complexes. 2,6-Di(5-ethyl-1*H*-pyrazol-3-yl)pyridine (**L**^{10}), 2,6-di(5-isopropyl-1*H*-pyrazol-3-yl)pyridine (**L**^{11}) and 2,6-di(5-*tert*butyl-1*H*-pyrazol-3-yl)pyridine (**L**^{12}) were all successfully synthesised via the method shown in Scheme 2.3 with yields ranging from 12 – 64 % (Figure 2.7). In these cases using sodium methoxide as a base in the diketone formation gave good results, with only minimal byproducts resulting from reaction on only one side of the dimethyl 2,6-pyridinedicarboxylate starting material.

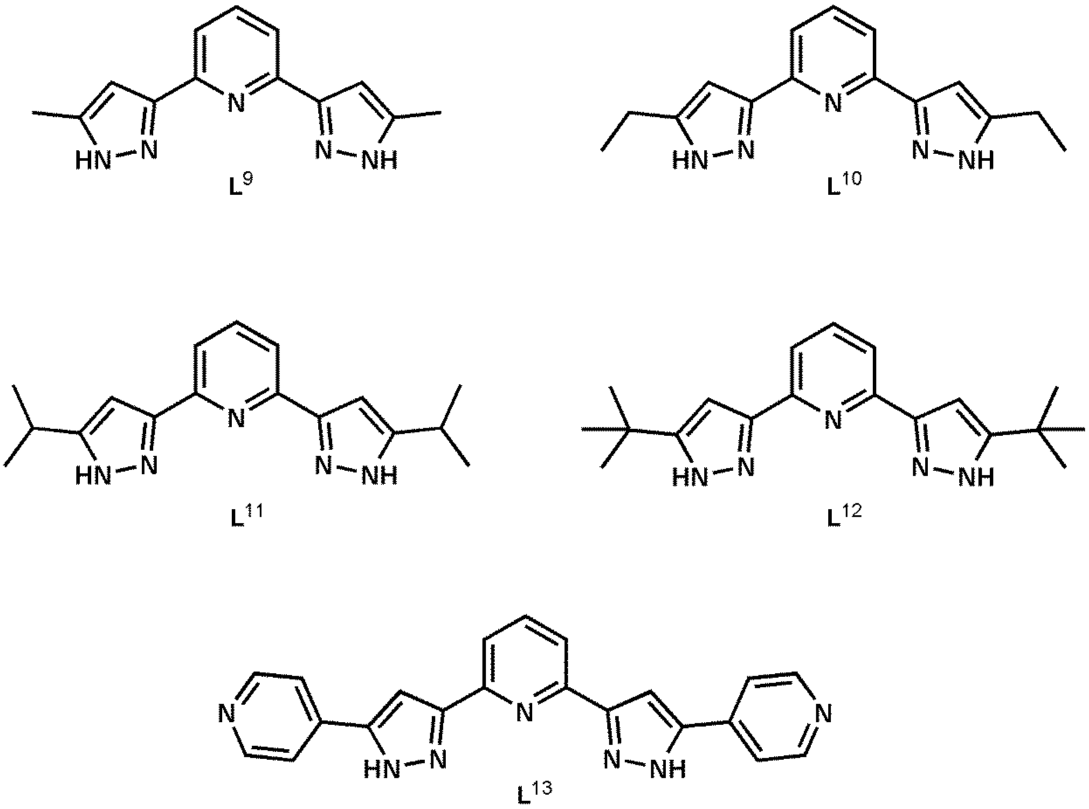

Figure 2.7
Structures of some successfully synthesised 3-bpp derivatives bearing substituents on the pyrazolyl *C*5 position.

Evidence for the formation of these ligands should come from a broad signal at around 12 ppm, however in the case of **L**^{10} and **L**^{12} this signal was lost due to exchange with the deuterium in the NMR solvent and is quite common for these ligands. More characteristic were the signals for the alkyl appendages which integrated correctly and had very distinct splitting patterns. The spectrum of **L**^{10} has one quartet and one triplet at 2.50 and 1.06 ppm respectively, corresponding to the ethyl groups. The spectrum of **L**^{11} shows two separate singlets at 1.28 and 1.30 ppm each equating to 6 H and which correspond to the isopropyl CH_3 groups. In addition to this was the very distinctive septuplet arising from the isopropyl CH which was coupling to the two methyl groups and integrated to 2 H. **L**$^{\mathbf{12}}$ simply showed a large singlet integrating to 18 H and corresponded to two *tert*butyl groups. Another indication to the success of these reactions was the singlet peak for the pyrazolyl CH group between 6 – 7 ppm which is indicative of substitution at the pyrazolyl *C*5 position.

ES^+ mass spectra of these ligands also showed the expected mass; **L**$^{\mathbf{10}}$ was observed as the sodium adduct $[MNa]^+$ at *m/z* 290.1, **L**$^{\mathbf{11}}$ as the protonated cation at *m/z* 296.2 and **L**$^{\mathbf{12}}$ as the protonated cation $[M]^+$ at *m/z* 324.2. Good CHN values determined via microanalysis were obtained for **L**$^{\mathbf{11}}$ and **L**$^{\mathbf{12}}$ but a good value for **L**$^{\mathbf{10}}$ could not be obtained. This could be a result of the fact that this ligand did not crystallise out when the solvent was evaporated to leave a dry white solid, but instead formed a viscous liquid which needed to be dried thoroughly under high vacuum. When this occurs with these ligands it has been noted that it can be more difficult to obtain high purity samples, however it may still be suitable for forming iron complexes.

In all these cases the intermediate diketone was isolated and analysis obtained. In general it was found to be easier to purify these ligands after the formation of the pyrazolyl rings so purication of the diketones at this stage was not considered to be essential. The key features of the ^1H NMR spectra of these intermediates were very similar to those mentioned above with the main difference being the absence of the pyrazolyl NH (dependant on deuterium exchange) and the integration of the CH_2 group of the diketone. This region often appeared quite messy in the spectra, however instead of impurities this is likely to be caused by the existence of resonance structures (Scheme 2.7).

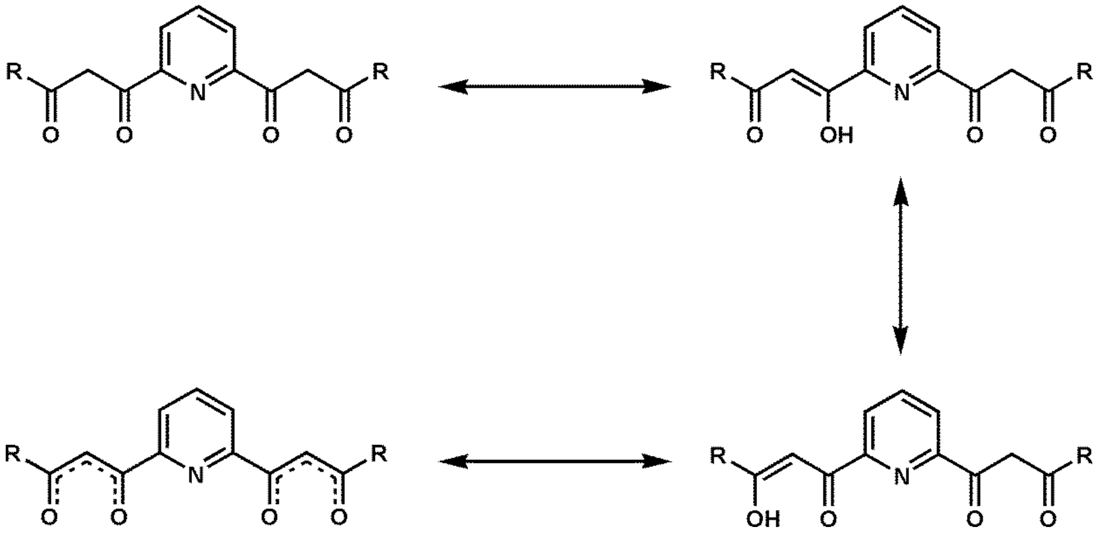

Scheme 2.7
Possible resonance structures responsible for the complications in the ^{1}H NMR spectra of the diketone intermediates.

2.4.2. Substitution with Pyridine

This method was utilised in an attempt to synthesise a 3-bpp ligand with 4-pyridyl groups on the pyrazolyl *C*5 position, which was eventually successful. The resulting ligand was of particular interest because in addition to potential π-stacking interactions and additional hydrogen bond acceptors it is also conceivable that iron complexes of this ligand could form multi-dimensional coordination polymers.

The synthetic procedure for this ligand is identical to the method described for the alkyl substitution proceeding via the diketone intermediate. In this case the ketone reagent used was 4-acetylpyridine and sodium hydride was used as a base. It was found that using sodium methoxide gave mainly starting material and a product which had only reacted on one side. For this ligand the ring closing step had to be refined; it was found that the reaction didn't proceed to completion when using just ethanol as a solvent. The reason for this was thought to be the pyridine rings making the solution slightly basic, which isn't favourable for the acid catalysed ring closure with hydrazine. The solution to this was to use a 7:3 mixture of ethanol/acetic acid as a solvent for the reaction, which resulted in the clean, quantitative formation of the product at room temperature and worked so efficiently that it was adopted as the standard procedure for the pyrazole ring formation. This produced 2,6-di(5-{4-pyridyl}-1*H*-pyrazol-3-yl)pyridine (**L**^{13}) as light orange microcrystals.

The ES^{+} mass spectrum for **L**^{13} showed a peak with *m/z* of 366.2 for the protonated cation, compared with the protonated cation [M]$^{+}$ of the ketone intermediate which had an *m/z* of

374.1, confirming pyrazole ring formation. The distinguishing features in the ^{1}H NMR for **L^{13}** are the two doublets at 7.85 and 8.55 ppm each integrating to 4 H and correspond to the two environments on the pyridyl appendages (Figure 2.8). The central pyridine consists of two hydrogen environments; a doublet at 7.74 ppm integrating to 2 H and a triplet at 7.90 ppm which integrates to 1 H. The ^{13}C NMR shows seven peaks which were assigned with the aid of a HMQC spectrum. The two missing peaks could not be found in the spectrum; the NMR sample was either too weak due to the low solubility of the ligand or the peaks are hidden amongst stronger signals.

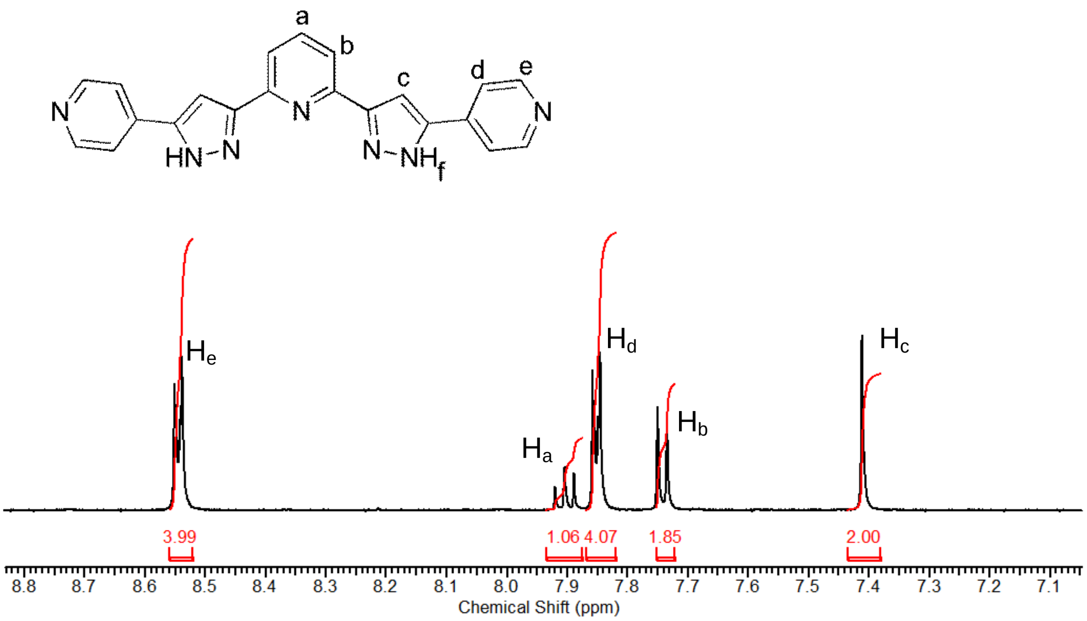

Figure 2.8
^{1}H NMR spectrum of **L^{13}** recorded at 500 MHz in CD_3OD.

2.4.3. Asymmetric Substitution

In the synthesis of the diketone it was noted that unless an excess of ketone and base was used the resulting mixture contained significant amounts of a by-product where only one side of the dimethyl 2,6-pyridinedicarboxylate had reacted. If the ratio of dicarboxylate/ketone/base were reduced to 1:1:1 and the mixture heated at 60°C in toluene for 8 hours then this by-product became the major product. This crude product could then be reacted again by the same method, but if a different ketone was used the resulting ligand would possess different groups on each pyrazolyl group.

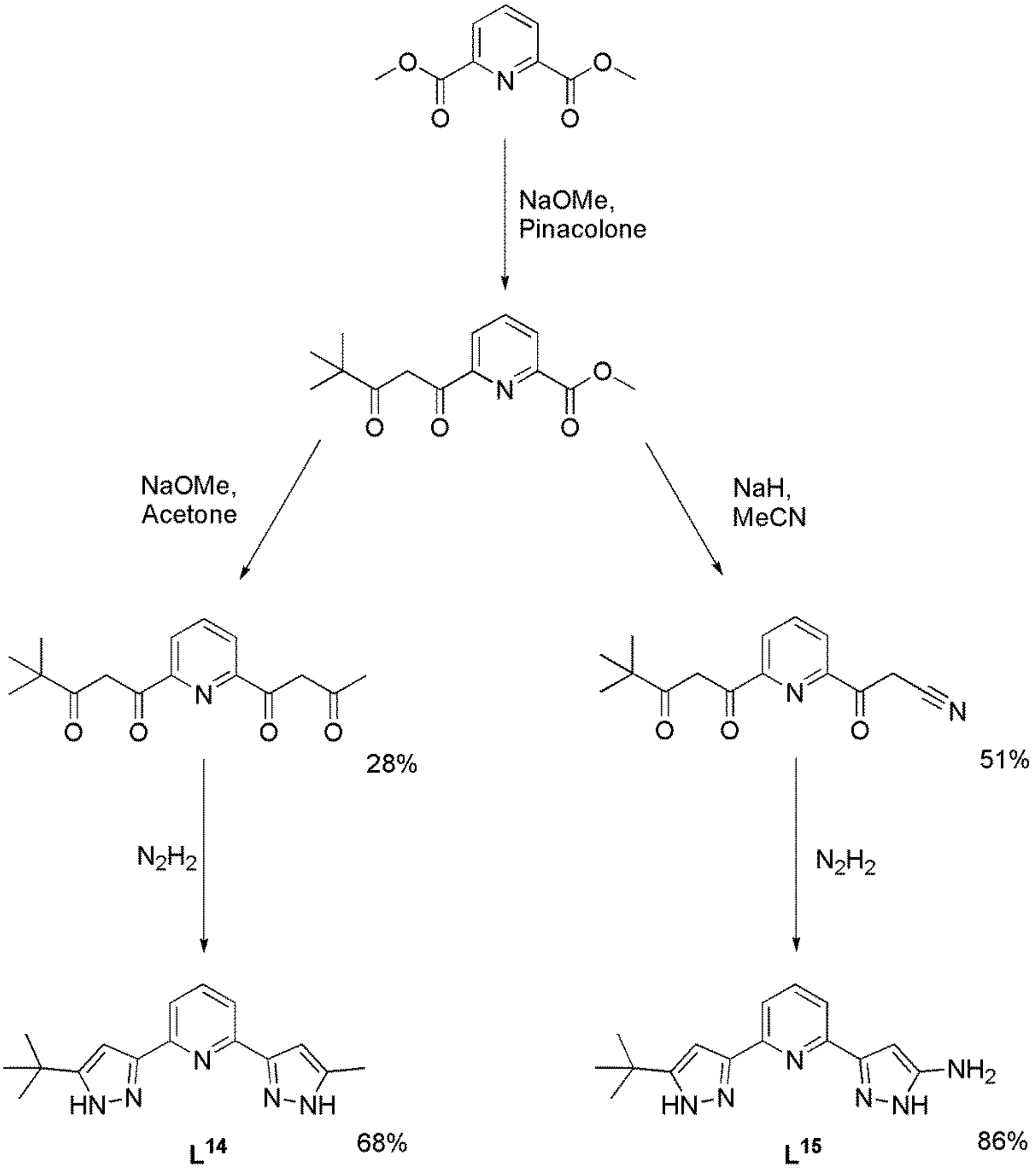

Scheme 2.8
Synthetic routes towards 2-(5-*tert*butyl-1*H*-pyrazol-3-yl)-6-(5-methyl-1*H*-pyrazol-3-yl)-pyridine (**L**^{14}) and 5-[6-(5-*tert*butyl-1*H*-pyrazol-3-yl)-pyridin-2-yl]-2*H*-pyrazol-3-ylamine (**L**^{15}).

A number of different combinations of substituents were used but only 2-(5-*tert*butyl-1*H*-pyrazol-3-yl)-6-(5-methyl-1H-pyrazol-3-yl)-pyridine (**L**^{14}) and 5-[6-(5-*tert*butyl-1*H*-pyrazol-3-yl)-pyridin-2-yl]-2*H*-pyrazol-3-ylamine (**L**^{15}) were obtained in sufficient purity and yield (Scheme 2.8). Once the reaction was found to work the two steps to make the asymmetric diketone were done in a one pot reaction; the mixture was heated with pinacolone and sodium methoxide and after 10 hours the next reagent and more base was added. The crude diketones were reacted with hydrazine without further purification and the high solubility of **L**^{12}, in this case the by-product, allowed the crude product to be purified simply by washing with diethyl ether.

Confirmation for the successful synthesis of these ligands came from the ^{1}H and ^{13}C NMR spectra, ES$^+$ mass spectrometry and microanalysis. The ^{1}H NMR spectra show that the hydrogen environments on the two pyrazolyl *C*4 positions and the pyridyl *C*4, *C*5 positions are no longer equivalent, due to each having a different group on the pyrazolyl *C*5 position (Figure 2.9). In both **L^{14}** and **L^{15}** the integrals match up perfectly with those expected for the desired products, and in **L^{15}** the amino NH is only just seen as a low and very broad peak at around 5 ppm.

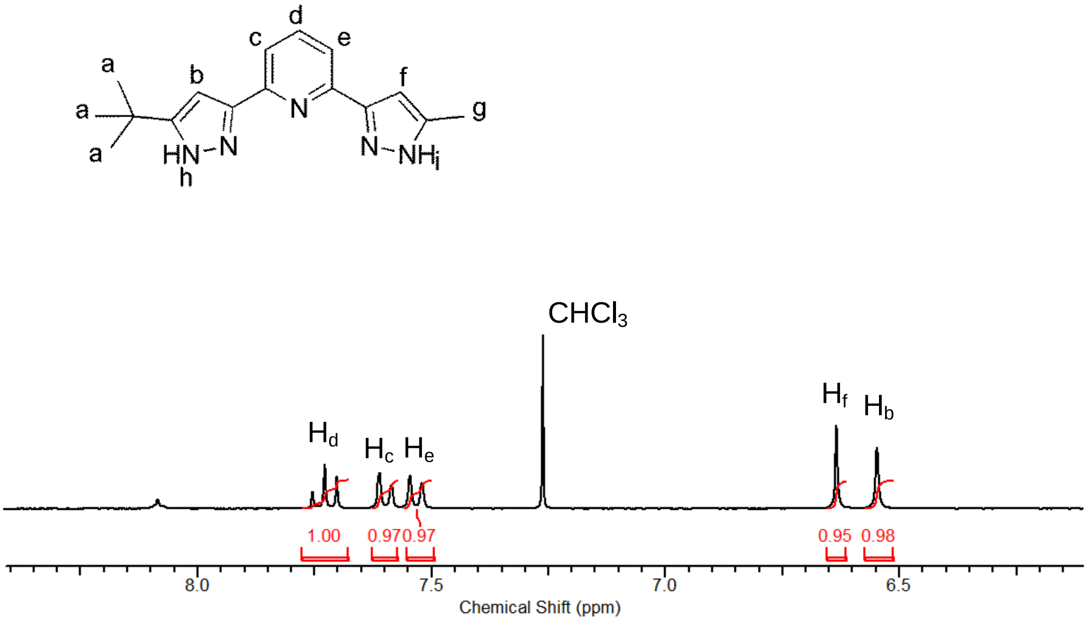

Figure 2.9

^{1}H NMR spectrum of **L^{14}** recorded at 300 MHz in CDCl$_3$.

Numerous attempts were made to make a ligand bearing a tertbutyl group on one pyrazolyl *C*5 and a 4-pyridyl group on the other using this method. However in all these cases a turbid red oil was obtained which HPLC-MS indicated was a mixture of products, including what could be the desired product and significant amounts of the symmetric *tert*butyl substituted ligand. The successful isolation of the desired product was not achieved.

2.5. Substitution at the Pyridyl *C*4 Position

As previously mentioned the range of substituted 1-bpp ligands is far greater than that of substituted 3-bpp and one position of interest is the pyridyl *C*4 position. In addition to providing further means of tuning the sterics and electronics of the ligand, substitution at the pyridyl *C*4 also provides potential to link ligands together and attach them to surfaces, a property which could be useful for any potential applications.[31-33] While there are a limited number of examples of substitution at the pyridyl *C*4 position of 3-bpp these are mainly in ruthenium dye sensitisers and actinide extractor systems and there are no examples of SCO complexes made with these ligands.[34-36] Therefore it was in our interest to devise the most effective synthesis for 3-bpp ligands substituted in this position and attempt to rationalise the effects certain modifications to this position have on the properties of a SCO complex.

One particular group which was desirable at the pyridyl *C*4 position was a halide as there are a large number of reactions which could be used to interconvert this group, including cross coupling reactions to introduce more complex groups. From a halide it is also quite simple to convert to a thiol which would offer means for attachment to gold surfaces.[37, 38] The first route attempted involved a similar process to that shown in Scheme 2.3 which involved making the diketone. Firstly 4-chloro-pyridine-2,6-dicarboxylic acid diethyl ester was made by reacting chelidamic acid with phosphorous pentachloride and quenching the mixture with ethanol.[39] This method was later replaced by one which uses thionyl chloride in place of phosphorous pentachloride.[40] This produced an ester which was then reacted with acetone in the presence of sodium methoxide to give the diketone, which was then reacted with hydrazine. However the white solid obtained after the hydrazine addition proved to be very insoluble forming a gel in dimethylsulphoxide. It is suspected that the chloro group has reacted under the reaction conditions to make a polymer but due to its insolubility analysis has been very limited. Because the chloro group is so reactive it was thought this route may be more successful if the chlorination of the hydroxyl group on chelidamic acid were performed after the pyrazole ring formation step. The reaction of chelidamic acid with acetone in the presence of base did not produce the desired diketone, however. An attempted conversion of the ester groups to acetyl groups to facilitate a reaction with N,N-dimethylformamide dimethylacetal also affected the chloro group.[41]

Next the carboxylic acid groups on chelidamic acid were esterified to make them better leaving groups and the resulting ester was reacted with acetone in the presence of base, but this reaction was again unsuccessful. The exact reason for this is unknown but it was thought that the hydroxyl group on the pyridyl *C*4 position must have some involvement. With this in mind the next step was to protect the hydroxyl group using a benzyl ether which is stable in the basic conditions needed for the reaction with acetone but can later be removed by heating in strongly acidic conditions.[42] Unfortunately this route also led to a mixture and HPLC-MS did not show the expected mass for the desired product. These routes are summarised below in Scheme 2.9.

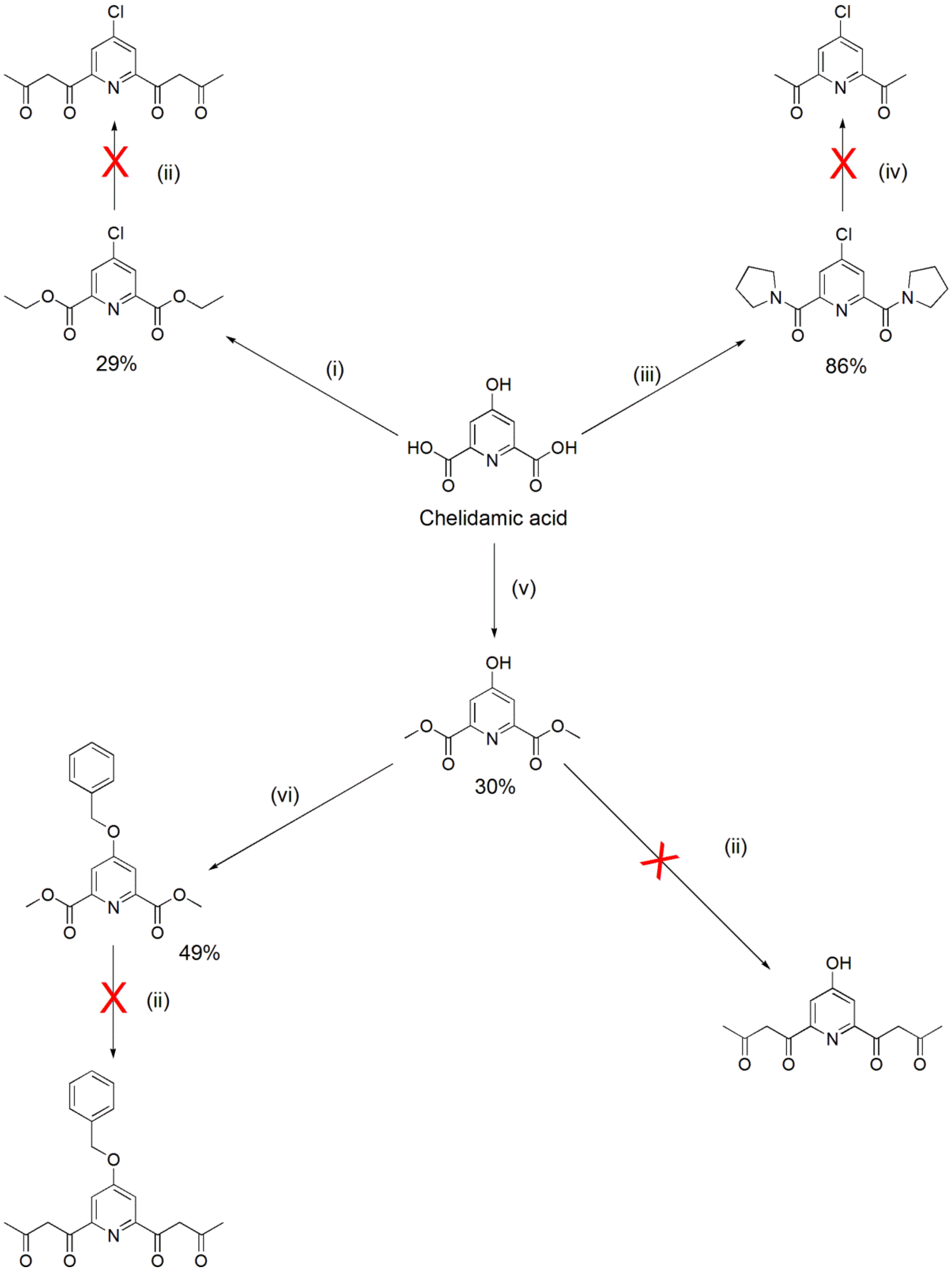

Scheme 2.9
Routes attempted from chelidamic acid. Reagents: (i) $SOCl_2$, EtOH; (ii) $(CH_3)_2CO$, NaOMe; (iii) $SOCl_2$, pyrrolidine; (iv) 2 equiv. MeMgBr; (vi) BzBr, K_2CO_3.

After numerous attempts at the reactions shown in Scheme 2.9 the routes using chelidamic acid as a starting material were abandoned in favour of directly attaching a pyrazole moiety to 2,6-dichloro-4-aminopyridine. This was done by first protecting the pyrazolyl NH group with dimethylsulphamoyl chloride and then lithiating at the pyrazolyl *C*5 position. This lithiated pyrazole was initially reacted directly with 2,6-difluoro-4-methoxypyridine, and once this was found not to work the lithiated pyrazole was converted to a boronate and attached to 2,6-dichloro-4-aminopyridine via a double Suzuki coupling. It was discovered that the lithiation of the pyrazole was not regioselective and a mixture of products was observed on a TLC of the subsequent boronate. This problem was overcome by changing the protecting group to tetrahydropyranyl, which directs the lithium to the adjacent carbon (Scheme 2.10), and the success of this method was confirmed in the ^{1}H NMR spectrum.[43] Mass spectrometry also showed that the pyrazole had only been lithiated once.

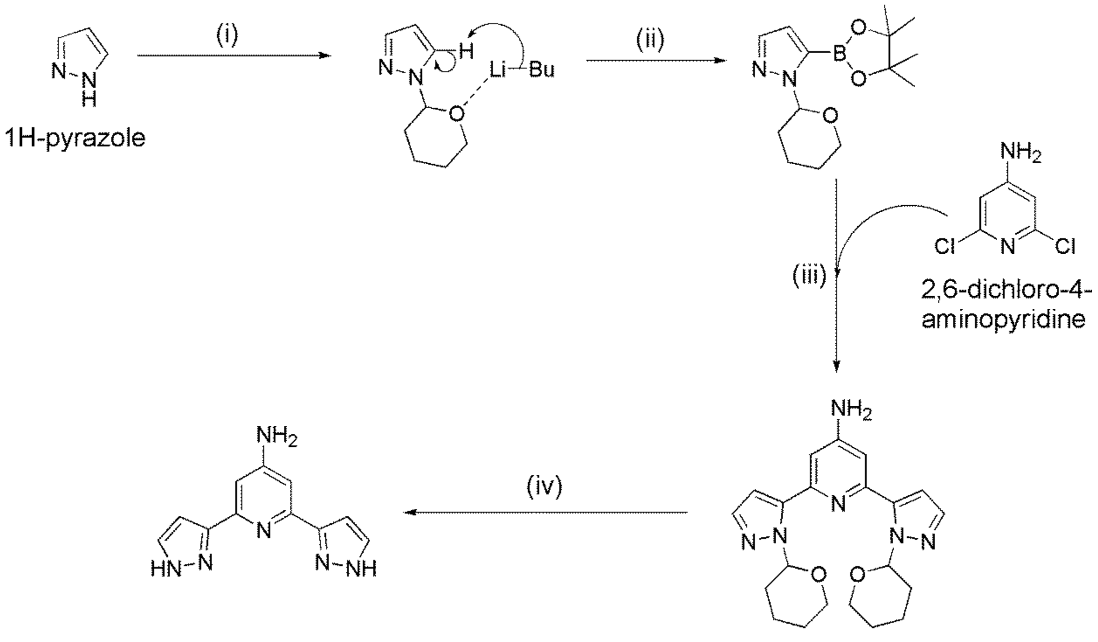

Scheme 2.10
The synthetic route towards 2,6-di-(1*H*-pyrazol-3-yl)-pyridin-4-ylamine (**L^{16}**). Reagents: (i) THP, TFA; (ii) Li^{n}Bu, B(O^{i}Pr)$_3$, pinacol; (iii) K_3PO_4, Pd(dba)$_2$, PCy$_3$·HBF$_4$; (iv) H$^+$.

HPLC-MS of the crude mixture after the Suzuki coupling showed ~70% of the desired product had formed. Problems occurred when attempting to isolate this product as its' interaction with silica was unexpectedly strong and the material could only be removed from the column by a mixture of water/dichloromethane/methanol (2:2:6) which also eluted any impurities. There were also problems in the deprotecting step as HPLC-MS showed that only one of the tetrahydropyran groups was removed, even on increasing the temperature. It was thought that this might be the result of some kind of equilibrium, so the reaction was set up again in methanol using either trifluoroacetic acid or hydrochloric acid and a layer of pentane was placed on top. The intention was that when the pyrazole was deprotected some of the free tetrahydropyran would move into the layer of pentane, removing it from the reaction and shifting the equilibrium favourably in the direction of deprotection. This improved the reaction and allowed 2,6-di(1*H*-pyrazol-3-yl)-pyridin-4-ylamine (**L^{16}**) to be isolated as a pale yellow solid, though in poor yield. Its formation was confirmed by ES$^+$ mass spectrum and NMR spectra. Nonetheless this allowed for the formation of an iron complex and an attempt at modifying the amine at the pyridyl *C*4 position.

With a small sample of **L^{16}** an attempt was made to brominate at the pyridyl *C*4 position using a method previously described by Kershaw Cook to brominate 1-bpp derivatives at the pyridyl *C*4 site.[44] This method involved diazotisation at the amine followed by substitution with bromide (Scheme 2.11). No clean product could be isolated from the reaction mixture and HPLC-MS showed that the residue was a mixture of materials with the major peak belonging to the starting material. It is believed that this procedure could be modified to produce the desired product, and also that of the chloride, however because **L^{16}** was produced in such poor yields this synthetic pathway could not be investigated further. Therefore further efforts would have to be made to find a high yielding synthetic route towards **L^{16}** which would allow additional examination into this modification.

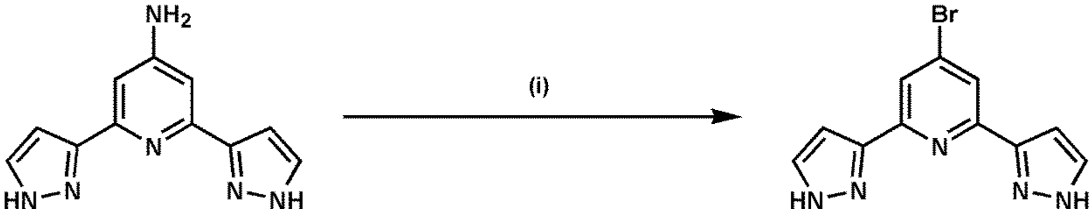

Scheme 2.11
Attempt to brominate the pyridyl *C*4 position of **L^{16}**. Reagents: (i) $NaNO_2$, KBr, HBr.

During the attempts at purifying the products of the Suzuki coupling via column chromatography it was noticed that sometimes another product could be isolated where the coupling reaction had occurred on only one side. This was confirmed by ES$^+$ mass spectrometry, microanalysis and the integrals on the ^{1}H NMR, which clearly corresponded to the number of hydrogens in each environment for the monosubstituted product. The ^{1}H NMR spectra below 3 ppm is complicated by the equatorial and axial hydrogen environments in tetrahydropyran, and the $^{13}C\{^1H\}$ NMR was assigned with the aid of a HMQC spectrum (Figure 2.10). The ES$^+$ mass spectrum shows peaks at m/z 279.1, 280.1 and 281.1 corresponding to $[MH]^+$ and show the isotopic pattern expected of a compound containing one equivalent of chlorine (Figure 2.11).

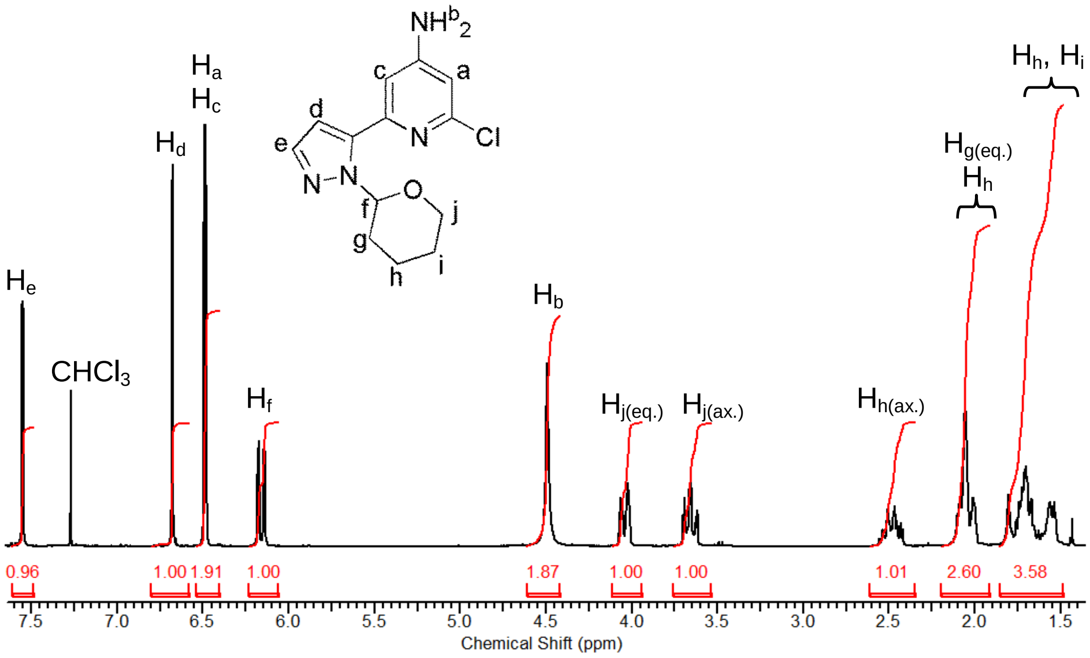

Figure 2.10
^1H NMR spectrum of 2-Chloro-6-[2-(tetrahydro-pyran-2-yl)-2*H*-pyrazol-3-yl]-pyridin-4-ylamine recorded at 300 MHz in $CDCl_3$.

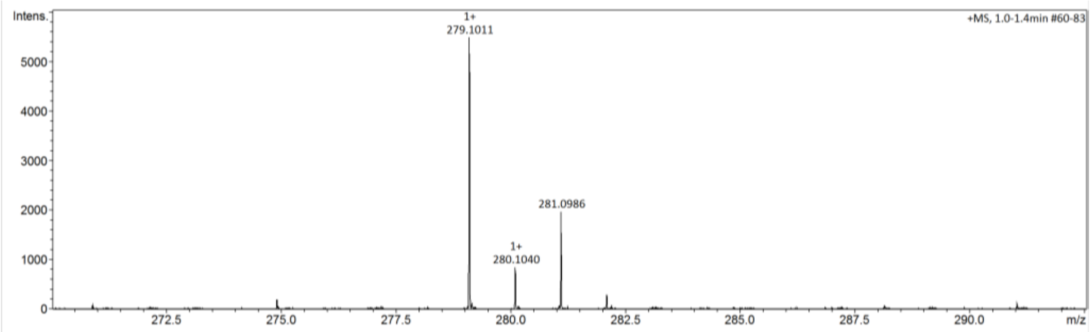

Figure 2.11
ES^+ mass spectrum of 2-Chloro-6-[2-(tetrahydro-pyran-2-yl)-2*H*-pyrazol-3-yl]-pyridin-4-ylamine showing the isotope pattern.

This product was of particular interest because it made available pathways to an asymmetric ligand. An attempt was made at substituting the remaining chloride with 1*H*-pyrazole in order to obtain a ligand which has both 1-pyrazolyl and 5-pyrazolyl rings (Scheme 2.12). This was attempted by deprotonating 1*H*-pyrazole with sodium hydride and heating at 110ºC for 5 days in a similar manner to the synthesis of 1-bpp shown in Scheme 2.1. This however was unsuccessful and insufficient material was collected to allow additional attempts.

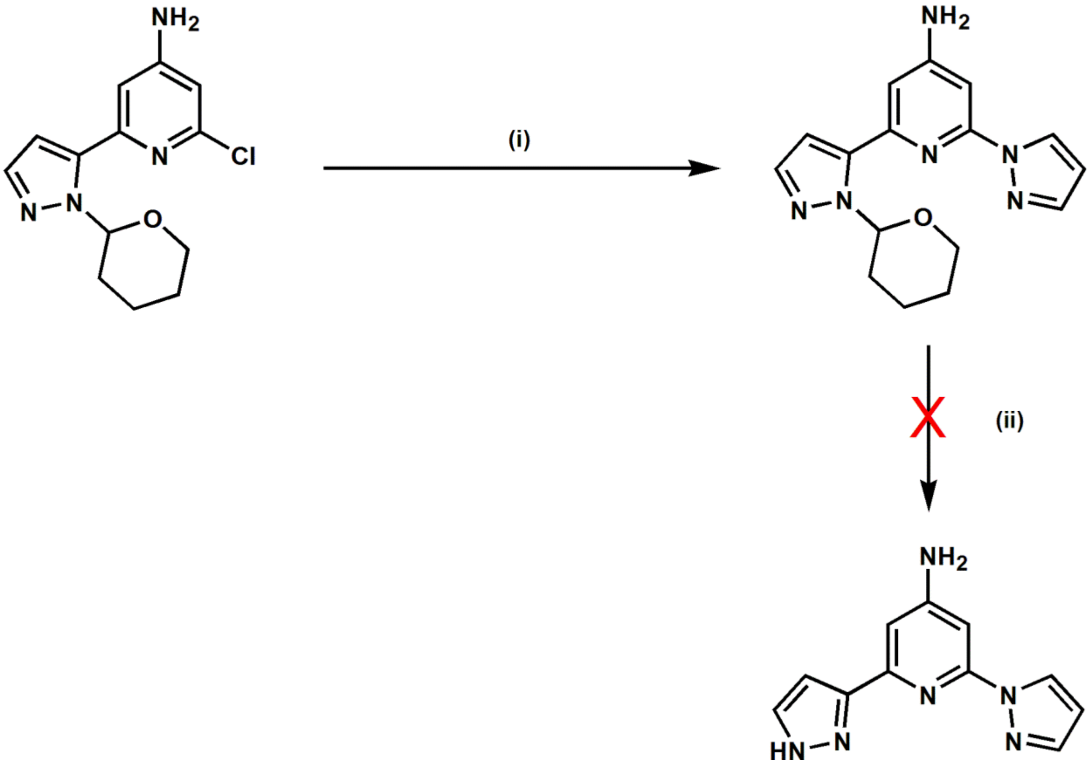

Scheme 2.12
Proposed synthetic procedure for 2-pyrazol-1-yl-6-(1*H*-pyrazol-3-yl)-pyridin-4-ylamine. Reagents: (i) NaH, 1*H*-pyrazole; (ii) H^+.

2.6. Halogenation of the Pyrazolyl *C*4 Position

Previously in the group methods were investigated which allowed 1-bpp to be substituted on the pyrazolyl *C*4 positions to give 2,6-di(4-halopyrazolyl)pyridines.[45] As these methods were post synthetic modifications to the 1-bpp structure we were interested in investigating whether these methods could be applied to the 3-bpp isomer to tune the electronics and sterics or introduce additional functionality.

2,6-Di-(4-chloro-1*H*-pyrazol-3-yl)-pyridine (**L**^{17}) was synthesised by the literature method used for the 1-bpp chlorination, without any modification.[45] This involved reaction with sodium hypochlorite in acetic acid solution at room temperature and afforded a pale yellow solid. This was confirmed as the desired product by CHN analysis which showed the presence of 2 equivalents of chlorine and by ^{1}H NMR. The key changes in the ^{1}H NMR spectrum was the absence of the two doublets corresponding to the two pyrazolyl hydrogen environments and instead shows only one singlet corresponding to the pyrazolyl *C*5 position (Figure 2.12). ES$^+$ mass spectrometry did not pick up the expected **M**$^+$ peak but this technique does not always work for some 3-bpp derivatives and even unsubstituted 3-bpp requires EI$^+$ mass spectrometry in order to observe **M**$^+$. The ligand structure was also seen in the crystal structures of subsequent complexes.

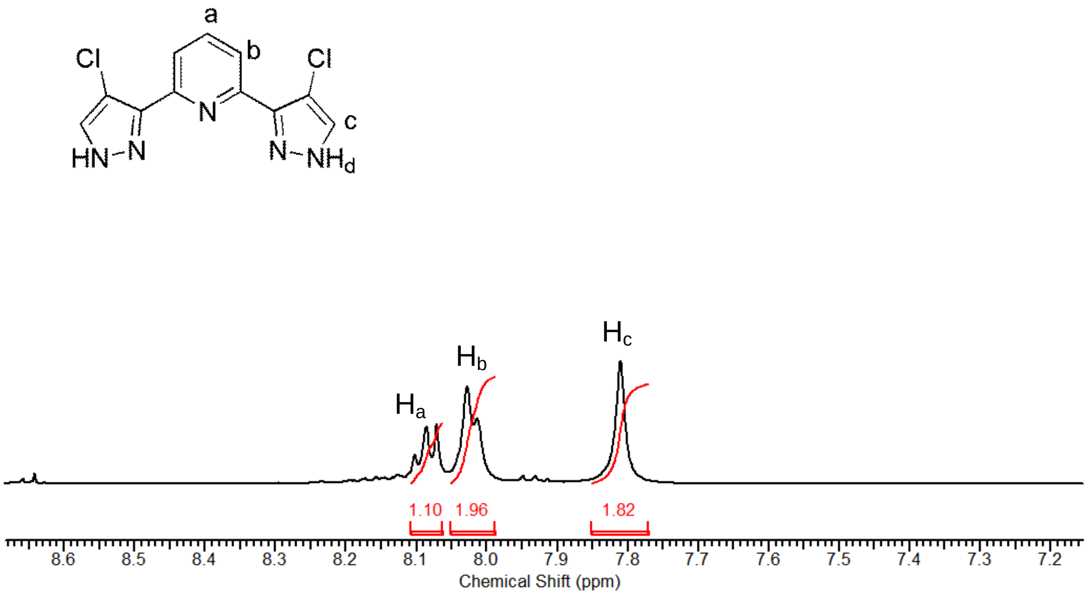

Figure 2.12

^{1}H NMR spectrum of 2,6-di-(4-chloro-1*H*-pyrazol-3-yl)-pyridine (**L**^{17}) taken at 500 MHz in $(CD_3)_2SO$.

2,6-Di-(4-bromo-1*H*-pyrazol-3-yl)-pyridine (**L^{18}**) was also synthesised by heating 3-bpp with N-bromosuccinimide. This formed a white precipitate which was insoluble in most common solvents. Due to this insolubility the NMR obtained were weak but the ^{1}H NMR showed broadened peaks in a similar pattern to those shown for **L^{17}** in Figure 2.12, as well as an additional broad peak just below 14 ppm corresponding to the pyrazolyl NH groups, showing that they remained intact. These were not seen in the spectrum of **L^{17}**, probably due to deuterium exchange with the solvent. **L^{18}** was also observed in the ES$^+$ mass spectrum as a peak at *m/z* 369.9 which corresponds to [M]$^+$, and also shows the isotope pattern expected for a species containing two bromine atoms. This ligand was also observed in the crystal structures of subsequent iron complexes.

A further reaction was attempted on **L^{18}** which involved a Suzuki coupling with 4-biphenyl boronic acid using the same conditions as those used when synthesising **L^{16}** (Scheme 2.13). However HPLC-MS of the crude mixture indicated that no coupling had occurred and returned only the starting material **L^{18}**. This could be due to this position on the pyrazole being in close contact with the pyridine and thus making it difficult for a large biphenyl group to substitute the bromine. Results of this steric effect can be seen in the conformation of the ligand in the crystal structure of its iron complex, which will be discussed in more detail in a Chapter 4.

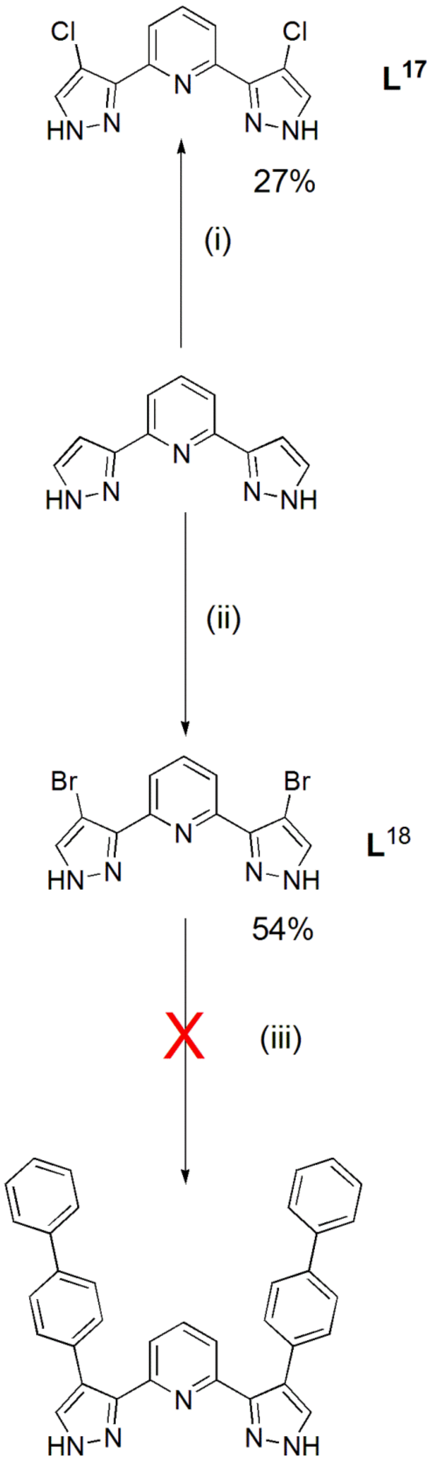

Scheme 2.13
Routes towards substitution at the pyrazolyl *C*4 position. Reagents: (i) NaClO, AcOH; (ii) NBS; (iii) K_3PO_4, Pd(dba)$_2$, PCy$_3$·HBF$_4$.

2.7. Conclusions

In total sixteen novel 3-bpp ligands have been successfully synthesised in sufficient yield and purity to allow iron and ruthenium complexes to be made. These are summarised in Figure 2.13 and Table 2.1. The facile reaction of 3-bpp with alkyl halides forms *N*1 substituted ligands in 24-51% yields and good purity however did not work using halides at sp^2 centres such as bromobenzenes and bromopyridines.

Reaction of $\mathbf{L^5}$ with acid chlorides and isothiocyanates worked reasonably well and in moderate to high yields, although the overall yield was stunted by the low yielding synthesis of $\mathbf{L^5}$ (of which the first step is the lower yielding).

Synthesis of derivatives via the route involving formation of a diketone ($\mathbf{L^{10\text{-}15}}$) produced comparatively high yields due to the procedure being only a two step process. Care did have to be taken however to ensure that the reaction was driven to completion in the formation of the diketones but this aspect of the reaction worked as an advantage in the synthesis of the asymmetric ligands.

A considerable amount of time was spent on devising a high yielding pathway to a 3-bpp ligand substituted with a halogen on the pyridyl *C*4 position. This would have opened up potential to further derivatise using a number of reactions including Suzuki couplings. The reaction pathways which began with chelidamic acid were becoming long and cumbersome and so the preferred route was a double Suzuki coupling of protected pyrazole triisopropylborates with 2,6-dichloro-4-aminopyridine which would have been only a three step process towards 4-halo 3-bpp (not including synthesis of the pyrazole triisopropylborate). However there were problems with the removal of the tetrahydropyranyl protecting group which led to poor yields making a number of further reactions impractical.

Finally two further ligands were synthesised by halogenating the pyrazolyl *C*4 positions. Formation of the bromo ligands occurred in 54% yield, whereas the chloro ligand formation only occurred in 27% yield. There is potential to further modify these groups, however an attempted Suzuki coupling using $\mathbf{L^{18}}$ proved unsuccessful.

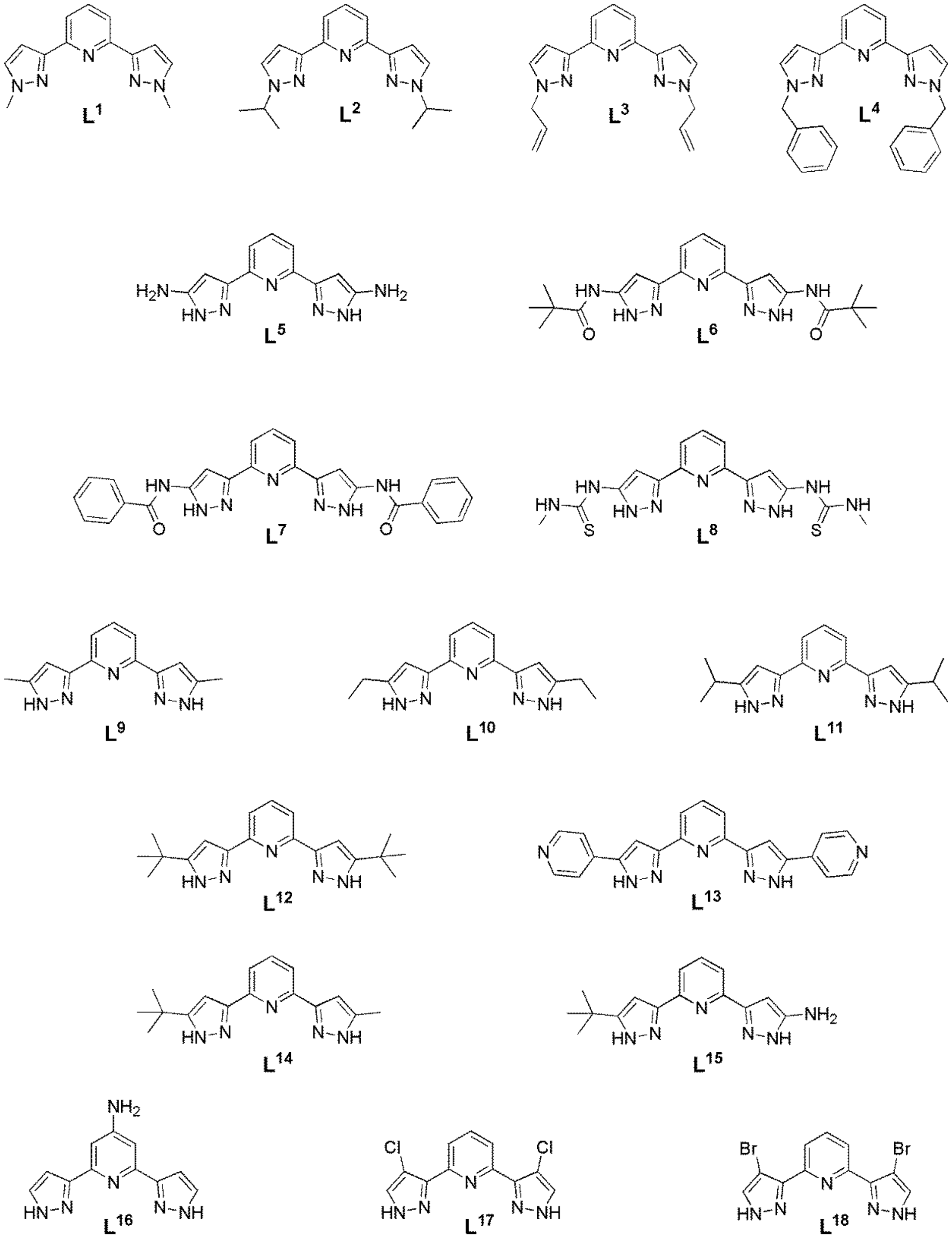

Figure 2.13
The ligands used in this work. All are novel at the time of writing with the exception of **L**^{5} [26] and **L**^{9} [30].

Table 2.1
Comparison of overall yields of synthesised 3-bpp ligands with reference to Figure 2.14.

Compound	R^1	R^2	R^3	R^4	R^5	% Yield
L^1	Me	H	H	H	H	26.4
L^2	^{i}Pr	H	H	H	H	51.6
L^3	All	H	H	H	H	29.0
L^4	Bz	H	H	H	H	24.3
L^5	H	NH_2	NH_2	H	H	19.7
L^6	H	NHCO^{t}Bu	NHCO^{t}Bu	H	H	10.4
L^7	H	NHCOBz	NHCOBz	H	H	16.0
L^8	H	NHCSNHMe	NHCSNHMe	H	H	9.8
L^9	H	Me	Me	H	H	53.3
L^{10}	H	Et	Et	H	H	42.2
L^{11}	H	^{i}Pr	^{i}Pr	H	H	41.6
L^{12}	H	^{t}Bu	^{t}Bu	H	H	48.7
L^{13}	H	Py	Py	H	H	15.6
L^{14}	H	^{t}Bu	Me	H	H	19.2
L^{15}	H	^{t}Bu	NH_2	H	H	43.9
L^{16}	H	H	H	NH_2	H	6.9
L^{17}	H	H	H	H	Cl	14.7
L^{18}	H	H	H	H	Br	29.1

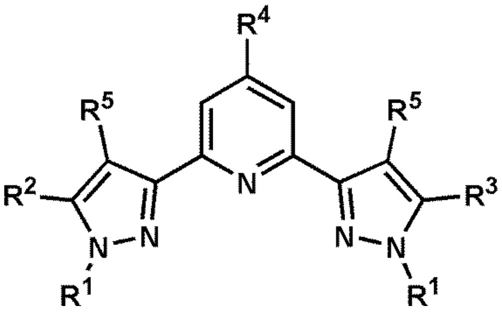

Figure 2.14
Substitution positions of 3-bpp.

2.8. References

[1] M. Konno and M. Mikami-Kido, *Bull. Chem. Soc. Jpn.* **1991**, *64*, 339-345.

[2] E. C. Constable, G. Baum, E. Bill, R. Dyson, R. Van Eldik, D. Fenske, S. Kaderli, D. Morris, A. Neubrand, M. Neuburger, D. R. Smith, K. Wieghardt, M. Zehnder and A. D. Zuberbühler, *Chem. Eur. J.* **1999**, *5*, 498-508.

[3] B. R. Müller, G. Leibeling and E. G. Jäger, *Chem. Phys. Lett.* **2000**, *319*, 368-374.

[4] T. Ikeuc, Y. Ohgo, T. Yamaguchi, M. Takahashi, M. Takeda and M. Nakamura, *Angew. Chem., Int. Ed.* **2001**, *40*, 2617-2620.

[5] M. A. Halcrow, *Coord. Chem. Rev.* **2009**, *253*, 2493-2514.

[6] H. A. Goodwin, *Top. Curr. Chem.* **2004**, *233*, 59-90.

[7] J. Elhaïk, D. J. Evans, C. A. Kilner and M. A. Halcrow, *Dalton Trans.* **2005**, 1693-1700.

[8] D. L. Jameson and K. A. Goldsby, *J. Org. Chem.* **1990**, *55*, 4992-4994.

[9] R. Pritchard, C. A. Kilner and M. A. Halcrow, *Tetrahedron Lett.* **2009**, *50*, 2484-2486.

[10] J. Elhaïk, C. M. Pask, C. A. Kilner and M. A. Halcrow, *Tetrahedron* **2006**, *63*, 291-298.

[11] A. Haouas, N. Ben Hamadi, A. Nsira and M. Msadek, *J. Chem. Res.* **2013**, *37*, 435-437.

[12] C. Rajadurai, F. Schramm, S. Brink, O. Fuhr, M. Ghafari, R. Kruk and M. Ruben, *Inorg. Chem.* **2006**, *45*, 10019-10021.

[13] N. Miyaura, K. Yamada and A. Suzuki, *Tetrahedron Lett.* **1979**, 3437-3440.

[14] H. A. Goodwin and K. H. Sugiyarto, *Chem. Phys. Lett.* **1987**, *139*, 470-474.

[15] E. Bejan, H. A. Haddou, J. C. Daran and G. G. A. Balavoine, *Synthesis* **1996**, 1012-1018.

[16] S. A. J. L. Y. I. Lin, *J. Heterocycl. Chem.* **1977**, *14*, 345-347.

[17] A. Z. A. El Baset Hassanien, *J. Chem. Res.* **2004**, *8*, 536-540.

[18] J. L. Liao, Y. Chi, Y. D. Su, H. X. Huang, C. H. Chang, S. H. Liu, G. H. Lee and P. T. Chou, *J. Mater. Chem.* **2014**, *2*, 6269-6282.

[19] C. Chen, Q. Sun, D. X. Ren, R. Zhang, F. Y. Bai, Y. H. Xing and Z. Shi, *Cryst. Eng. Comm.* **2013**, *15*, 5561-5573.

[20] A. Bremer, C. M. Ruff, D. Girnt, U. Müllich, J. Rothe, P. W. Roesky, P. J. Panak, A. Karpov, T. J. J. Müller, M. A. Denecke and A. Geist, *Inorg. Chem.* **2012**, *51*, 5199-5207.

[21] Y. Zhou, W. Chen and D. Wang, *Dalton Trans.* **2008**, 1444-1453.

[22] L. C. Claisen, A., *Berichte der Deutschen Chemischen Gesellschaft* **1881**, *14*, 2460–2468.

[23] C. M. Che, C. F. Chow, M. Y. Yuen, V. A. L. Roy, W. Lu, Y. Chen, S. S. Y. Chui and N. Zhu, *Chem. Sci.* **2011**, *2*, 216-220.

[24] V. A. Money, C. Carbonera, J. Elhaïk, M. A. Halcrow, J. A. K. Howard and J. F. Létard, *Chem. Eur. J.* **2007**, *13*, 5503-5514, S5503/5501-S5503/5505.

[25] G. L. Taghizadeh, S. Farsadpour, Y. Sun and W. R. Thiel, *Eur. J. Inorg. Chem.* **2011**, *2011*, 3431-3437.

[26] K. A. Ali, *Arkivoc* **2010**, *11*, 55-63.

[27] E. Knoevenagel, *Berichte der Deutschen Chemischen Gesellschaft* **1898**, *31*, 2596-2619.

[28] C. M. Pask, C. A. Kilner, and M. A. Halcrow, *Tet. Let.* **2006**, *47*, 2531-2534.

[29] B. M. Francuski, S. B. Novakovic and G. A. Bogdanovic, *Cryst. Eng. Comm.* **2011**, *13*, 3580-3591.

[30] T. D. Roberts, F. Tuna, T. L. Malkin, C. A. Kilner and M. A. Halcrow, *Chem. Sci.* **2012**, *3*, 349-354.

[31] J. F. Létard, P. Guionneau and L. Goux-Capes, *Top. Curr. Chem.* **2004**, *235*, 221-249.

[32] A. Abhervé, M. Clemente-León, E. Coronado, C. J. Gómez-García and M. López-Jordà, *Dalton Trans.* **2014**, *43*, 9406-9409.

[33] S. Basak, P. Hui, S. Boodida and R. Chandrasekar, *J. Org. Chem.* **2012**, *77*, 3620-3626.

[34] T. Satou in *Organic electroluminescent element*, Fujifilm Corporation, Japan . **2008**, p. 26.

[35] C. C. Chou, K. L. Wu, Y. Chi, W. P. Hu, S. J. Yu, G. H. Lee, C. L. Lin and P. T. Chou, *Angew. Chem., Int. Ed.* **2011**, *50*, 2054-2058.

[36] A. Geist, U. Müllich, T. Zevaco, A. Karpov and T. Müller in *Preparation of alkylated bis(pyrazolyl)pyridines for the selective extraction of actinides*, Karlsruher Institut fuer Technologie, Germany . **2010**, p. 19.

[37] L. Testaferri, M. Tiecco, M. Tingoli, D. Chianelli and M. Montanucci, *Synthesis* **1983**, 751-755.

[38] C. Silien, M. Buck, G. Goretzki, D. Lahaye, N. R. Champness, T. Weidner and M. Zharnikov, *Langmuir* **2009**, *25*, 959-967.

[39] D. G. Markees and G. W. Kidder, *J. Am. Chem. Soc.* **1956**, *78*, 4130-4135.

[40] R. N. De Rycke, F. Couty and O. R. P. David, *Tetrahedron Lett.* **2012**, *53*, 462-466.

[41] B. Su, J. Zhao, Y. Cui, Y. Liang and W. Sun, *Synth. Commun.* **2005**, *35*, 2317-2324.

[42] P. G. M. Wuts and T. W. Greene in *Protection for the Hydroxyl Group, Including 1,2- and 1,3-Diols*, John Wiley & Sons, Inc., **2006**, p. 16-366.

[43] M. McLaughlin, K. Marcantonio, C. Y. Chen and I. W. Davies, *J. Org. Chem.* **2008**, *73*, 4309-4312.

[44] L. J. Kershaw Cook in *Crystal Engineering and Bifunctionality in Spin-Crossover Materials*, *PhD* University of Leeds, **2013**.

[45] R. Pritchard, H. Lazar, S. A. Barrett, C. A. Kilner, S. Asthana, C. Carbonera, J. F. Létard and M. A. Halcrow, *Dalton Trans.* **2009**, 6656-6666.

Chapter 3

Iron(II) Complexes of 2,6-Di(1-alkylpyrazol-3-yl)pyridine Derivatives

3.1. Introduction

This chapter is concerned with novel iron(II) complexes of 2,6-di(1-alkylpyrazol-3-yl)pyridine derivatives, whose synthesis has previously been described. Modification of the corresponding distal substituents on 1-bpp (at the pyrazolyl *C*3 position) has been shown to have a steric influence on the coordination geometries of Cu complexes.[1-3] The inductive effects of the distal substituents have also been shown to greatly influence the donor strength of the ligand, with the 2,4,6-trimethylphenyl (Mes) group increasing donor strength and isopropyl (^{i}Pr) groups decreasing the donor strength.[4] The iron(II) complexes of the same substituted 1-bpp ligands have also been investigated with regards to SCO activity both in the solid state and in solution, showing that ^{i}Pr and phenyl (Ph) groups afford complexes which are HS between 180-300 K in solution, and Mes substituents give complexes which remain LS in solution.[5] The absence of lattice constraints in solution means that these effects are probably due to the inductive effects of these substituents (Figure 3.1).

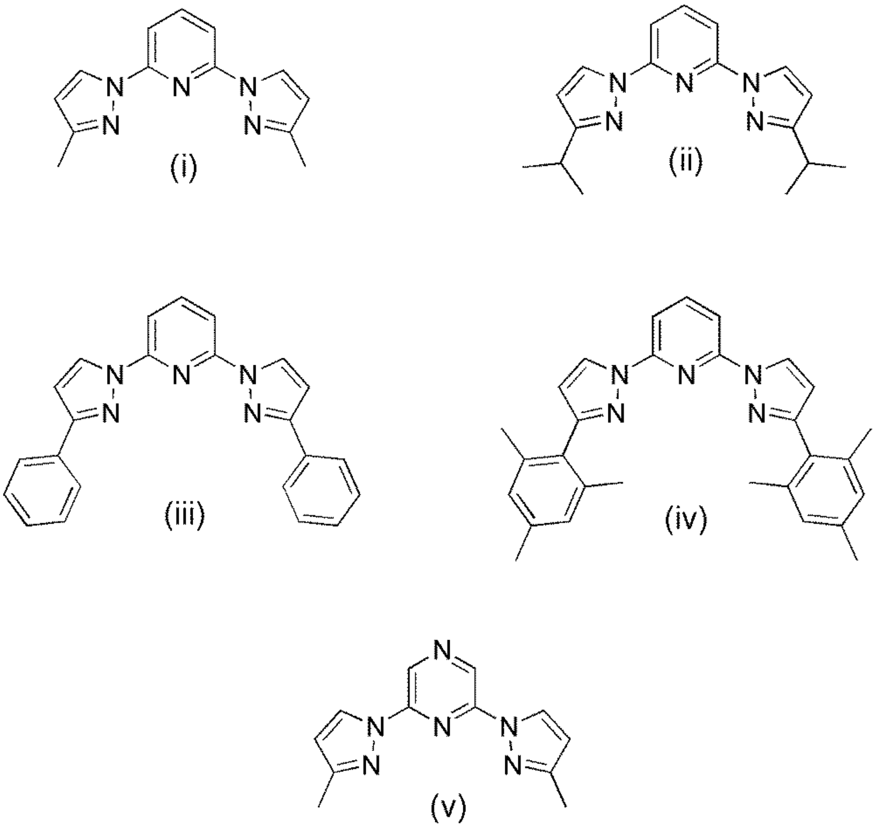

Figure 3.1
Examples of 1-bpp ligands bearing distal substituents. (i) 2,6-di(1-methylpyrazol-3-yl)pyridine, (ii) 2,6-di(1-isopropylpyrazol-3-yl)pyridine, (iii) 2,6-di(1-phenylpyrazol-3-yl)pyridine, (iv) 2,6-di-{3-[2,4,6-trimethylphenyl]pyrazol-1-yl}pyridine and (v) 2,6-di(3-methylpyrazol-1-yl)pyrazine.

Iron(II) complexes of these substituted 1-bpp derivatives can also exhibit interesting SCO properties. One example uses the ligand 2,6-di-(3-methyl-pyrazol-1-yl)pyridine (Figure 3.1 (i)) whose iron(II) complex exhibits spin state behaviour that is anion dependent and sensitive to solvation. The hydrated tetrafluoroborate salt of this ligand undergoes two hysteretic transitions, the first centred around 147 K and the second an incomplete transition centred around 105 K. This second transition was shown to be kinetically slow below 130 K and the fully LS state was achieved by rapid cooling to and annealing at 100 K for two hours.[6] In contrast the perchlorate salt of this complex shows a very gradual ST centred at around 267 K which was attributed to the lack of cooperativity in the lattice due to the structural similarity of the HS and LS phases.[7] Interestingly the hexafluorophosphate and hexafluoroantimonate salts of the same complex remain fully HS between 5-300 K reflecting conformational strain arising from an intermolecular steric contact between adjacent molecules.[8, 9] This creates a distortion in the coordination sphere that favours the HS state and creates a high kinetic energy barrier for conversion to the LS state.

An unusual ST is also observed for complex salts of the isosteric ligand 2,6-di(3-methylpyrazol-1-yl)pyrazine (Figure 3.1 (v)) which show a two stage transition, the first of which is quite abrupt while the second is gradual (Figure 3.2).[10] ST's of this type can be caused by the existence of inequivalent iron centres responsible for each transition, crystallographic phase changes or local ordering of spin states caused by intra and intermolecular forces. In this case the two step transition was attributed to an ordering of the anions at the temperature that the gradient of the ST changes.[11] While 2,6-di(3-methylpyrazol-1-yl)pyrazine is sterically very similar to 2,6-di(1-methylpyrazol-3-yl)pyridine, it differs in both donor strength and its ability to form hydrogen bonds through the non-coordinating pyrazine *N*4 position, which could have implications for SCO complexes both in the solid state and in solution.

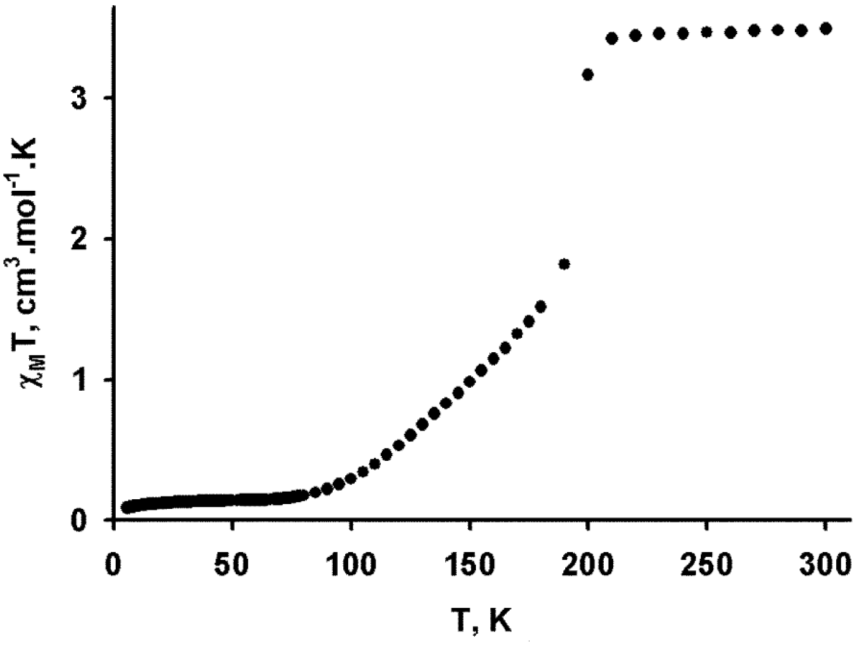

Figure 3.2
χ_MT *vs* T curve of $[FeL_2](ClO_4)_2$ where L = 2,6-di(3-methylpyrazol-1-yl)pyrazine. Taken from Elhaik *et al.*[10] Copyright the Royal Society of Chemistry.

In contrast to $[Fe(1\text{-bpp})_2](BF_4)_2$, the corresponding complex $[Fe(3\text{-bpp})_2](BF_4)_2$ has a significantly lower transition temperature in the solid state, centred around 178 K but a wider hysteresis of 10 K. This was also the first compound to exhibit the LIESST effect generating a metastable high spin state at temperatures as high as 80 K.[12] The complex also exhibits a spin-state trapping effect when rapidly cooled, due to the same slow rate of conversion from the quintet high spin state to the singlet low spin state.[13] As a result of this, much research has gone into investigating the LIESST properties of these complexes.[12, 14-18] One major difference between the two isomers 1-bpp and 3-bpp are the pyrazolyl NH groups in 3-bpp, which are capable of forming hydrogen bonds to solvent molecules in the crystal lattice and in solution. Both of these factors have been shown to affect SCO.[19, 20] However on addition of distal substituents to the 3-bpp ligand these hydrogen bond donors are removed, as these substituted ligands are structurally and electronically very similar to their 1-bpp counterparts one would expect their resulting iron complexes to behave in a similar manner.

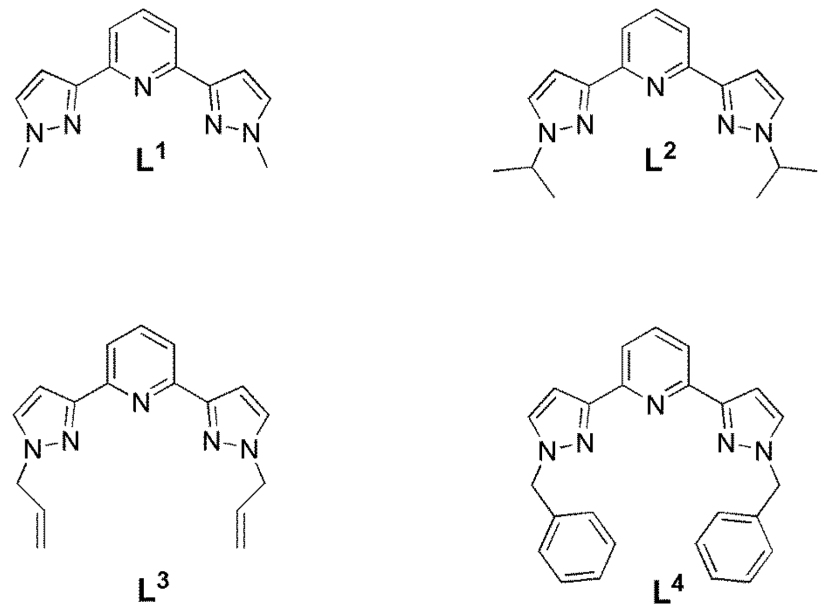

Figure 3.3
Ligands discussed in this chapter. 2,6-di(1-methylpyrazol-3-yl)pyridine (**L**^{1}), 2,6-di(1-isopropylpyrazol-3-yl)pyridine (**L**^{2}), 2,6-di(1-allylpyrazol-3-yl)pyridine (**L**^{3}) and 2,6-di(1-benzylpyrazol-3-yl)pyridine (**L**^{4}).

Table 3.1
The complexes discussed in this chapter and their abbreviations. The nature of the anion, X, and any solvation are specified throughout.

Complex	**Abbreviation**
[Fe(**L**^{1})$_2$](X)$_2$	**1**(X)$_2$
[Fe(**L**^{2})$_2$](X)$_2$	**2**(X)$_2$
[Fe(**L**^{3})$_2$](X)$_2$	**3**(X)$_2$
[Fe(**L**^{4})$_2$](X)$_2$	**4**(X)$_2$

To investigate this a series of novel iron(II) complexes were synthesised using the ligands 2,6-di(1-methylpyrazol-3-yl)pyridine (**L**^{1}), 2,6-di(1-isopropylpyrazol-3-yl)pyridine (**L**^{2}), 2,6-di(1-allylpyrazol-3-yl)pyridine (**L**^{3}) and 2,6-di(1-benzylpyrazol-3-yl)pyridine (**L**^{4}) (Figure 3.3), whose synthesis has been described previously in Chapter 2. The resulting complexes were then subjected to crystallographic study and magnetic measurements in order to illustrate any similarities or differences to their comparable 1-bpp analogues with any differences being rationalised with regards to structure/function relationships.

3.2. Iron(II) Complexes of $\mathbf{L^1}$ ($\mathbf{1(X)_2}$)

The ligand $\mathbf{L^1}$ was synthesised as previously described and was then used to make the tetrafluoroborate, perchlorate and hexafluorophosphate salts of $[Fe(\mathbf{L^1})_2]^{2+}$, which were all recrystallised from methanol/diethyl ether to give bright yellow microcrystalline solids. Crystals suitable for single crystal x-ray diffraction were obtained of all three salts via slow vapour diffusion of diethyl ether into their methanol solutions. It was important that single crystals were obtained from the same solvents as the bulk powder samples, as different solvate structures can greatly affect SCO properties.[21] In this way it was hoped that any measurements taken on the bulk microcrystalline phase would be representative of the structures elucidated via x-ray crystallography.

3.2.1. $\mathbf{1(BF_4)_2{\cdot}H_2O}$

Yellow crystals of $\mathbf{1}(BF_4)_2{\cdot}H_2O$ were obtained via slow vapour diffusion of diethyl ether into a methanol solution $\mathbf{1}(BF_4)_2$. An x-ray crystal structure of $\mathbf{1}(BF_4)_2H_2O$ was obtained at 150 K in the monoclinic space group $C2/c$ (a = 17.1632(16); b = 20.9906(19); c = 19.1771(17) Å, α = 90º, β = 96.605(5)º, γ = 90º, V = 6863.0(11) Å^3). The unit cell consists of two inequivalent half complex molecules, two anions and disordered water giving the formula $\mathbf{1}(BF_4)_2{\cdot}xH_2O$ (Figure 3.4). The asymmetric unit contains two crystallographically distinct BF_4^- anions which are disordered over two positions with occupancy ratios of 0.6 : 0.4, and additional electron density which was assigned as a water molecule is disordered over three positions with their total occupancy being equal to 1 (Figure 3.4). Both cation molecules span the C_2 rotoinversion axis 0, y, 1/4 which intersects the iron centre. With Fe1B, this rotation axis runs along the PyN–Fe–Npy bonds, whereas with Fe(1A) the axis intersects along the equatorial xy plane of the molecule directly in-between the Fe–N bonds. The cation molecules are related via a two-fold screw axis at 1/4, y, 1/4 which runs down the length of the b crystallographic axis (Figure 3.5). Adjacent $[\mathbf{1}]^{2+}$ cations do not appear to be in close contact with one another, but are separated by a layer of BF_4^- anions (Figure 3.6).

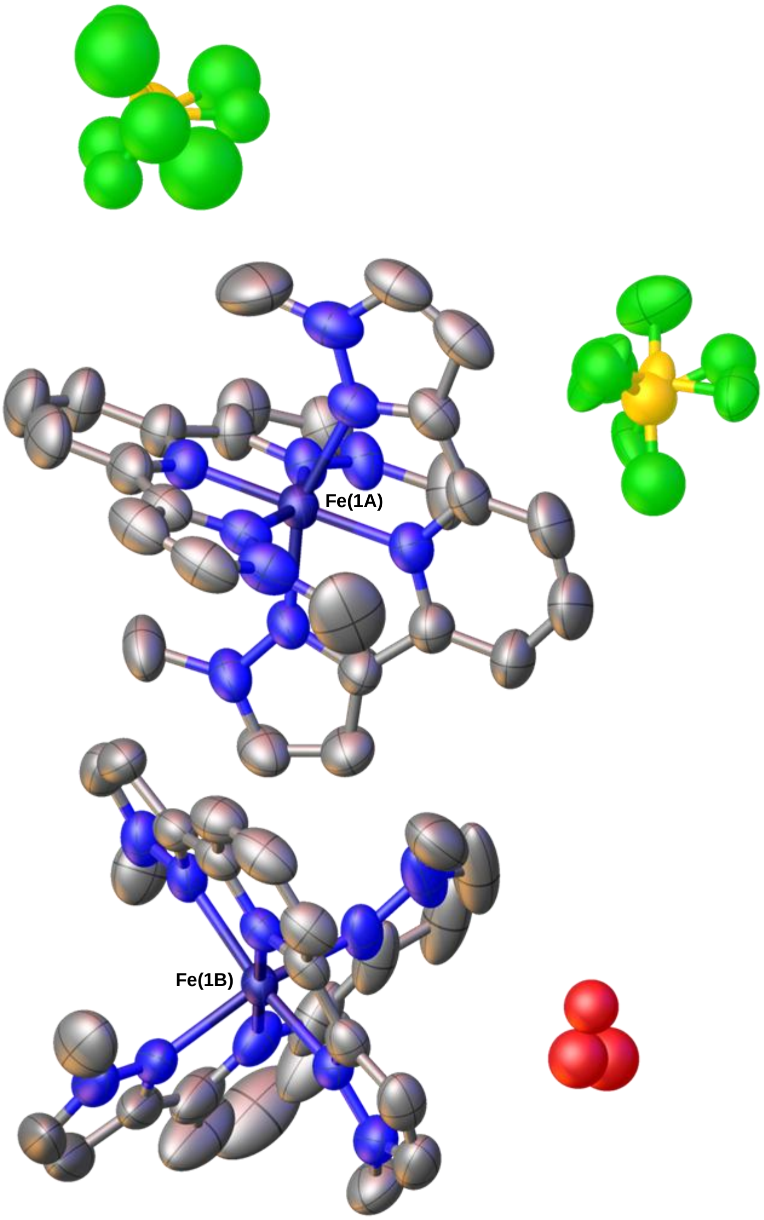

Figure 3.4
Crystal structure of **1**$(BF_4)_2 \cdot H_2O$ at 150 K. Thermal ellipsoids are set at 50 % probability and hydrogen atoms have been omitted for clarity.

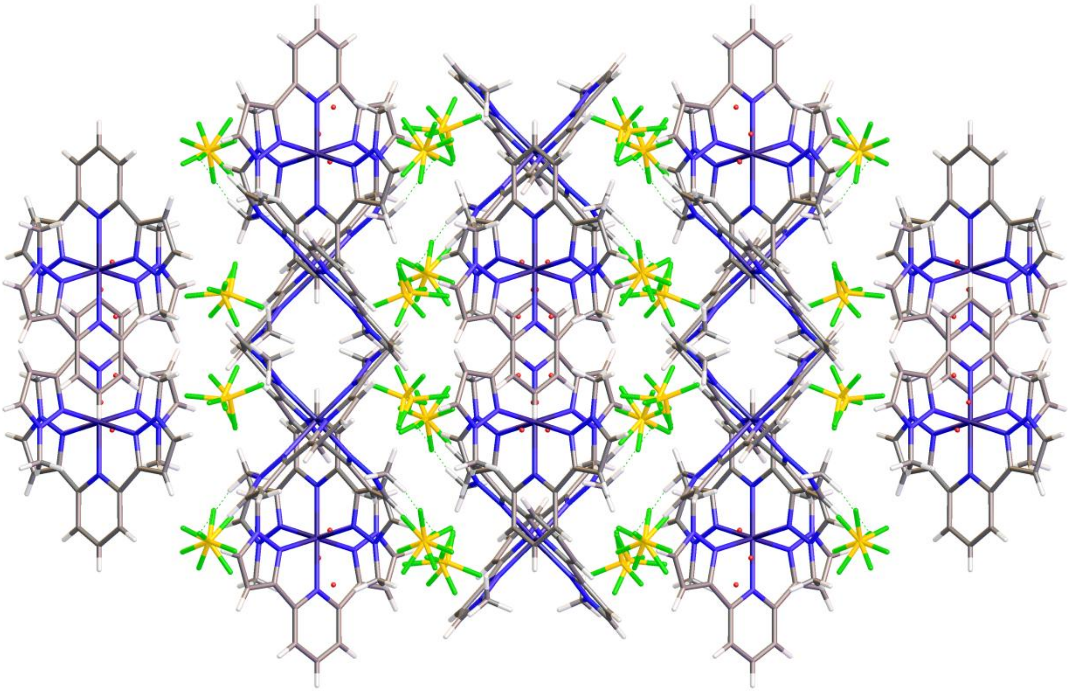

Figure 3.5
View down the *c* axis of **1**$(BF_4)_2 \cdot H_2O$.

This complex does not have the capability to form hydrogen bonds, however there are close interactions where the distances between adjacent atoms is smaller than the sum of their Van der Waals radii (Figure 3.6) These kinds of steric conflicts usually give highly ordered structures which have been suggested to hinder a spin transition in the solid state.[22]

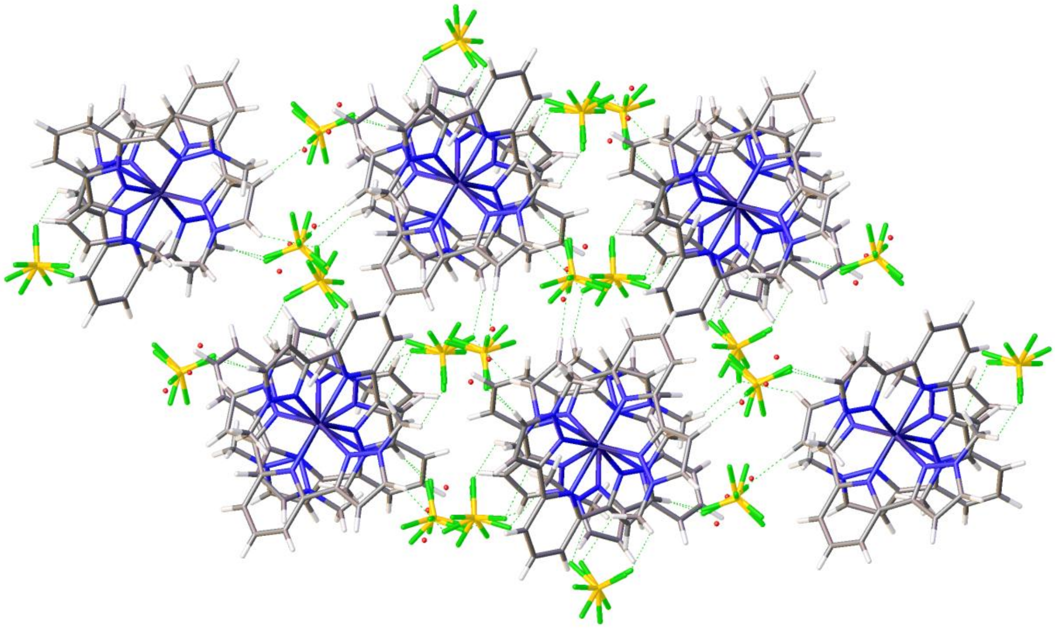

Figure 3.6
View down the a axis of **1**$(BF_4)_2 \cdot H_2O$ showing close contacts between complex molecules and anions (green dotted lines).

Table 3.2
Selected bond lengths and geometric parameters for the two distinct iron centres in **1**$(BF_4)_2 \cdot H_2O$. [a] Atom coordinates lie on a crystallographic axis so no associated ESD.

	Fe(1A)	**Fe(1B)**
Fe-PyN (Å)	1.961(4)	2.0445(6)
Fe-PzN (Å)	2.021(4)	2.0905(4)
α(°)	157.59(19)	154.4(3)
θ(°)	86.836(6)	86.27(7)
φ(°)	180[a]	178.6(3)
Σ(°)	98.24	113.66
Θ(°)	351.30	348.78

On closer inspection of the iron coordination spheres it appears that the two inequivalent iron centres are in different spin states. The main indication for this is the difference in their Fe–N bond lengths and deviations from an ideal octahedral geometry (Table 3.2). The nature of these distortions are discussed in detail in Chapter 1. As a comparison typical values for the pyrazole Fe–N bond lengths in a high spin and low spin complex are 2.16 Å[23] and 1.97 Å[24] respectively.

The θ and ϕ angles are both close to 90° and 180° respectively which shows that both iron centres have geometry not too distorted from the ideal D_{2h} octahedral symmetry. However the Σ and Θ parameters are similar for both iron centres and in between those of high and low spin $[Fe(1\text{-}bpp)_2](BF_4)_2$.[25]

The Fe–N bond lengths in this structure suggest that the two Fe centres have different spin state populations, therefore this is a good candidate for SCO in the solid state. The χ_MT *vs* T was recorded by a DC SQUID magnetometer in a field of 5 kG and it shows that contrary to the crystal data that the complex remains fully high spin over the entire temperature range (Figure 3.7). The exponential drop-off in χ_MT below 50 K is due to the zero field splitting (ZFS). This is a Zeeman effect which occurs in systems where $S \geq 1$ and is a result of the interaction of spins through spin-orbit coupling. The Zeeman effect causes a splitting of S into m_s of different energies depending on their relative orientations to the magnetic field. This has a pronounced effect at very low temperatures where $k_B T < \Delta E m_s$, the difference in energy of the m_s states, at which point the population of states becomes unequal. Therefore at low temperatures the lowest energy state of m_s will become solely occupied, leading to a dramatic reduction in the value for χ_MT.[26] The value of χ_MT from 75-300 K is around 3.8 cm^3 mol^{-1} K, which is quite typical of a high spin iron(II) complex.[24]

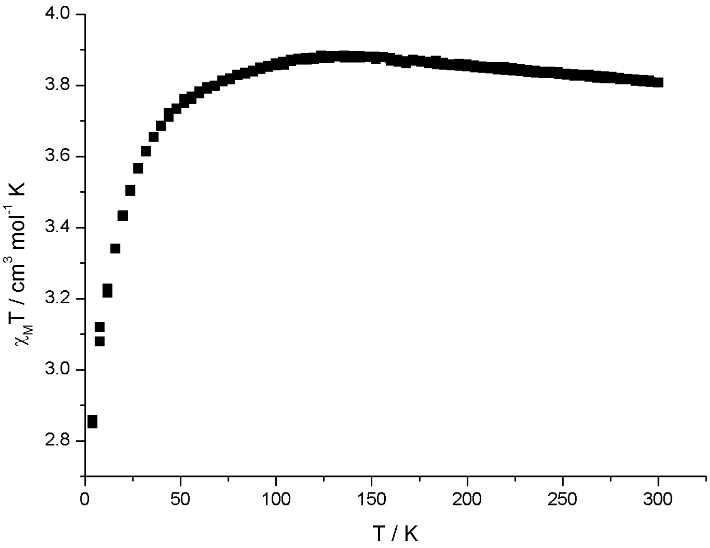

Figure 3.7
χ_MT *vs* T curve of **1**$(BF_4)_2\cdot H_2O$. Recorded at a scan rate of 2 K min^{-1} in settle mode.

This discrepancy between the crystal structure and the bulk sample could be due to them being different solvates. The thermogravimetric analysis shows that no solvent is lost from the bulk powder up to around 250 ºC, at which point the sample begins to lose mass as it thermally decomposes (Figure 3.8). Hence, the water of crystallisation that is apparent in the crystalline sample is not present in the bulk material. The residue left is 12.43 % of the starting mass of the sample corresponding to the thermal degradation products. This shows that even though the two samples were obtained from the same solvents (methanol/diethyl ether) they have a different solvent content, and so are possibly different polymorphs which show different properties. In order to confirm this an x-ray powder pattern was recorded from the SQUID sample and compared to a powder pattern simulated from the single crystal data. By comparison of the PXRD data collected from the same bulk sample used for the SQUID measurements with the pattern calculated from the crystal structure it can be seen that the two samples are significantly different. The collected powder pattern belongs to the trigonal space group $R3_2$ and is isostructural to the anhydrous perchlorate salt discussed in **3.2.2** (Figure 3.9 and Figure 3.10). This is evidence that the bulk powder and the single crystal are different polymorphs, and explains the discrepancy between the crystal structure and the magnetic behaviour.

The problem of obtaining different solvate phases from single crystals and bulk samples of the same complex has been experienced by the group before, and it has even been observed that an un-solvated complex obtained by heating was different to the un-solvated complex obtained via slow diffusion.[27, 28] There is also a possibility that the solvent was lost from the bulk sample over time. Efforts to collect variable temperature magnetic susceptibility data on a bulk sample of the monohydrate have been unsuccessful.

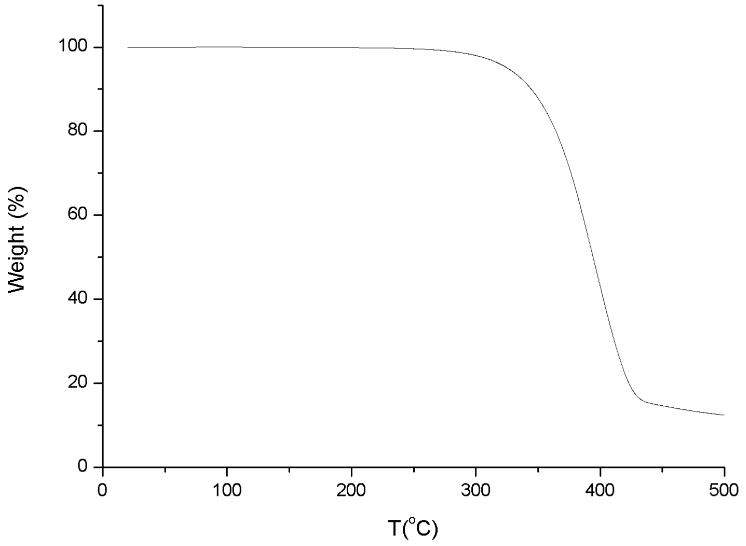

Figure 3.8
Thermogravimetric analysis of **1**$(BF_4)_2 \cdot H_2O$.

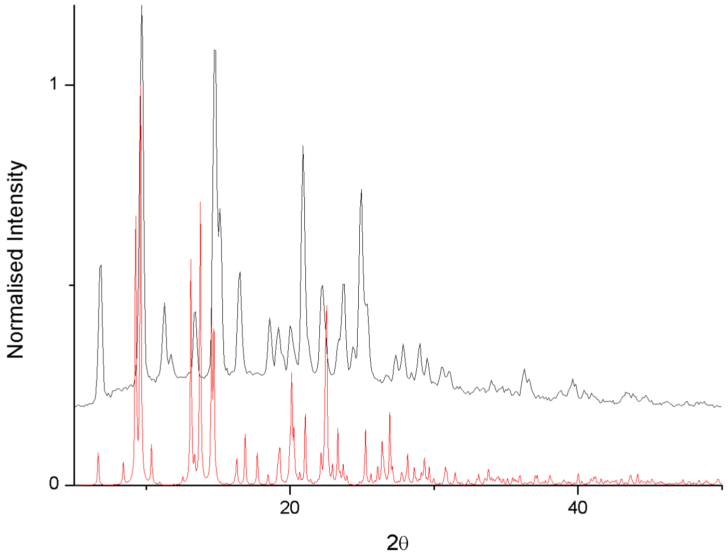

Figure 3.9
Collected (black) and simulated (red) powder pattern of **1**$[BF_4] \cdot H_2O$.

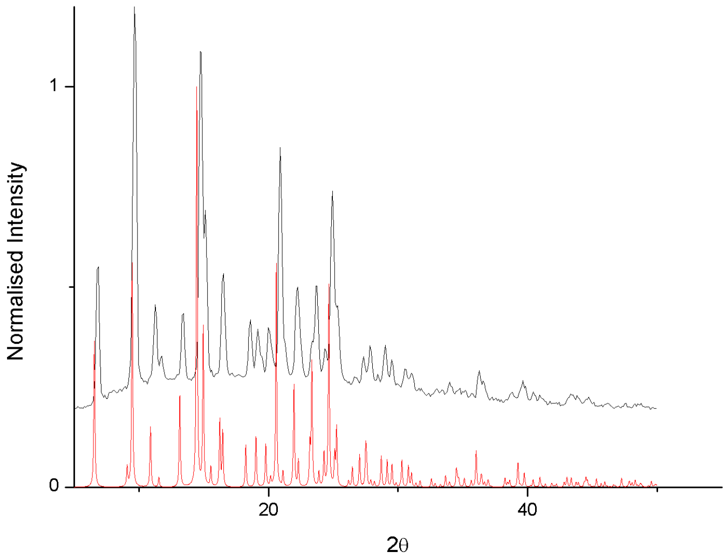

Figure 3.10
Collected PXRD data for **1**$(BF_4)_2 \cdot H_2O$ compared with the simulated powder pattern for **1**$(ClO_4)_2$ (red).

As a comparison with the SQUID data the variable temperature magnetic susceptibility of this complex was measured in deuterated acetone solution using the Evans NMR method.[29] These results are very similar to the SQUID data and show that the complex has a $\chi_M T$ of around 3.5 cm^3 mol^{-1} K over the temperature range of 193-312 K with a small drop off at higher temperatures (Figure 3.11). These results show that the high spin state of the complex, at least between 193-312 K, is not due to packing effects alone and that there must be some electronic effects which govern the spin state. The system may undergo a gradual spin transition in solution at lower temperatures, however the measurement below 190 K is limited by the freezing point of the solvent. Acetone was chosen as a solvent for this experiment because it has the lowest freezing point of the most common deuterated solvents that dissolve metal complexes, at 178 K. One disadvantage of using the Evans NMR method is that there is a relatively large error in $\chi_M T$ of between 5-10%, depending on sample concentration.[30] This could have been the reason for the drop off in $\chi_M T$ observed at higher temperatures.

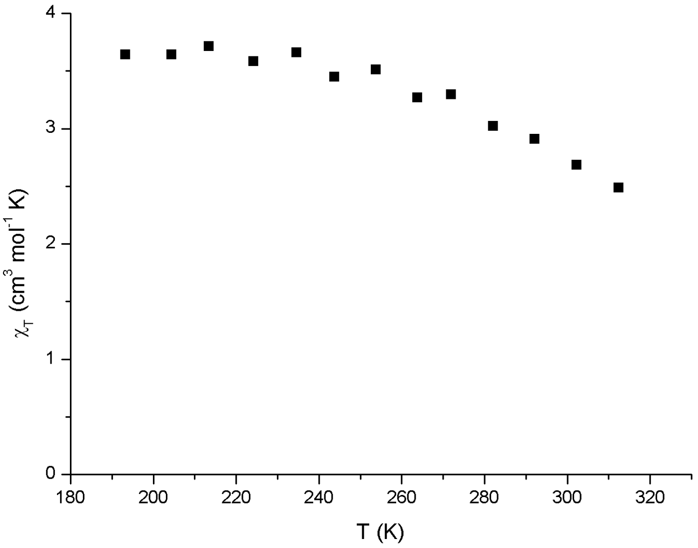

Figure 3.11
χ_MT *vs* T data collected using the Evans NMR method in $(CD_3)CO$ at 500 MHz for **1**$(BF_4)_2{\cdot}H_2O$. Calculations were made using the shift in the acetone peak.

3.2.2. 1(ClO_4)$_2$

Yellow crystals of **1**(ClO_4)$_2$ were obtained via slow vapour diffusion of diethyl ether into a methanol solution of **1**(ClO_4)$_2$, and a structure was determined at 150 K. This salt crystallised in the trigonal space group $R3_2$ (a = 18.6378(12); b = 18.6378(12); c = 24.3461(14) Å, α = 90º, β = 90º, γ = 120º, V = 7324.0(8) Å^3) , and the asymmetric unit contains half a complex molecule and three partially occupied anion sites (Figure 3.12). One third of an anion lies on a C_3 axis, half an anion on a C_2 axis and one sixth of a disordered anion lies on a C_3 axis and three C_2 axes. The iron centre itself lies on a C_2 crystallographic axis which intersects between the Fe–N bonds in the equatorial plane of the molecule. One of the pyrazole rings in the asymmetric unit is disordered equally over two positions, and this could be due to close contacts in the lattice between these adjacent pyrazolyl groups (Figure 3.13). Attempts to extend this disorder to the entire complex cation didn't produce a reasonable refinement, however. Complex molecules in close contact form chains along the length of the c axis which are separated by channels of perchlorate anions (Figure 3.14).

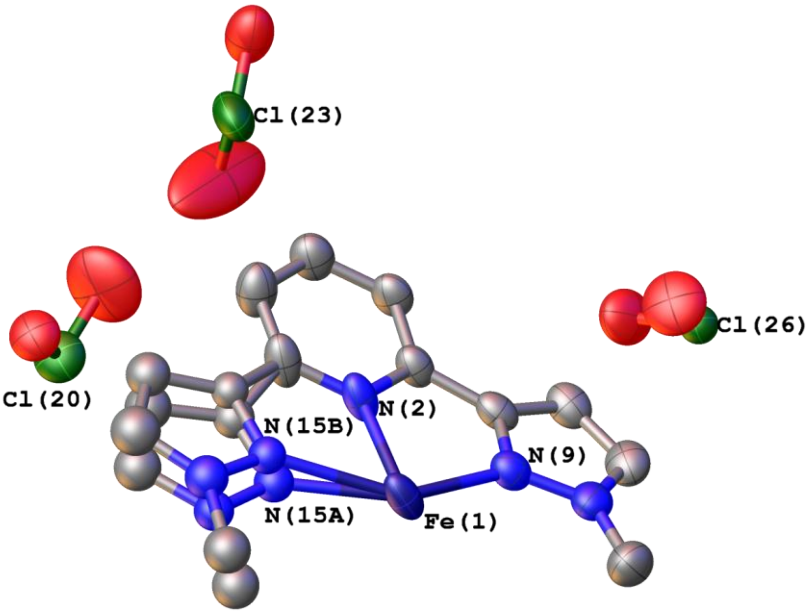

Figure 3.12
The asymmetric unit of **1**(ClO_4)$_2$ collected at 150 K. Thermal ellipsoids are set at 50 % probability and hydrogen atoms have been omitted for clarity.

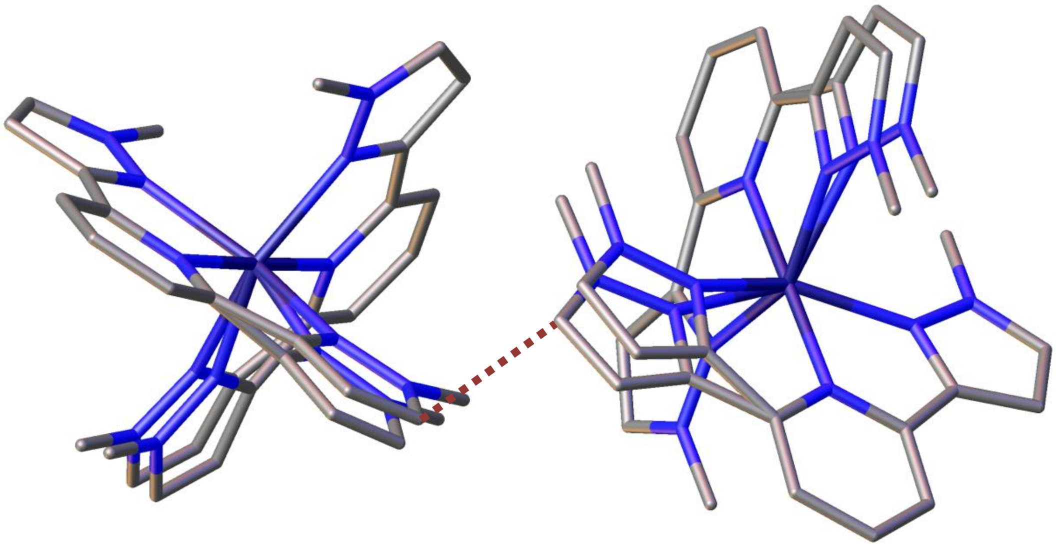

Figure 3.13
Symmetry generated structure of **1**$(ClO_4)_2$ showing close contact between the disordered pyrazole rings.

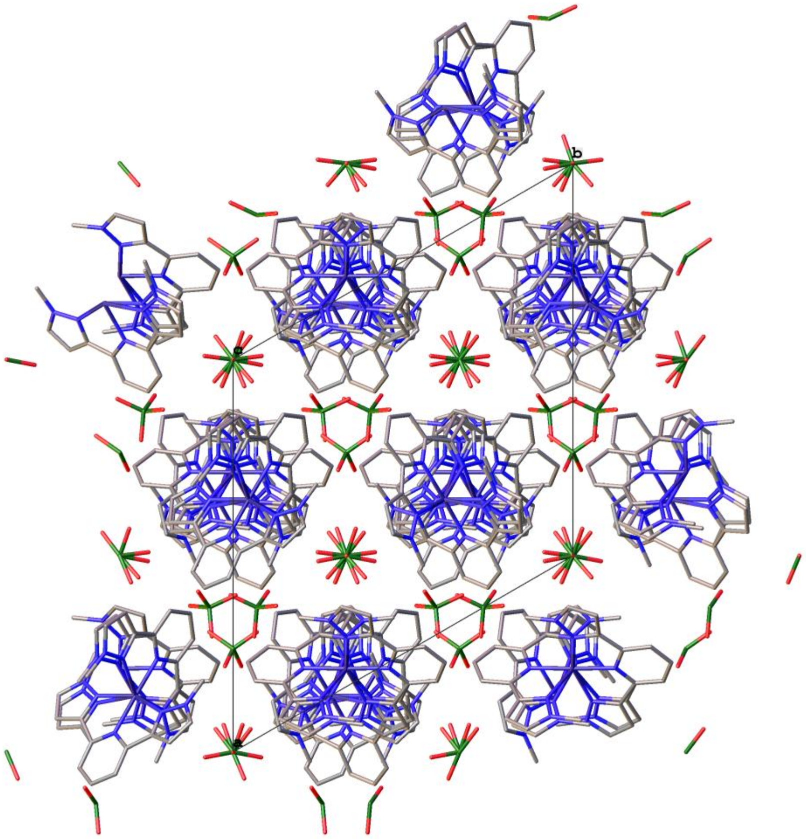

Figure 3.14
View down the c axis of the structure of **1**$(ClO_4)_2$.

The geometric parameters were calculated for each position of the disordered pyrazole ring separately (Table 3.3). The Fe–N bond lengths are also those typical of high spin iron(II) complexes suggesting that this complex is almost fully high spin at 150 K, and the plane twist angle (θ) and the *trans* angle (ϕ) are both close to 90º and 180º respectively. A noticeable difference between this structure and the structure of **1**$(BF_4)_2 \cdot H_2O$ is that the rhombic distortion parameter is significantly larger, indicating a shift from ideal octahedral towards a more rhombohedral geometry.

Table 3.3
Tabulated values of the bond lengths and geometric parameters around the iron centre in **1**$(ClO_4)_2$. (A) and (B) refer to the suffix of the atom names in the structure used for each position of the disordered pyrazole.

	1$(ClO_4)_2$ (A)	**1$(ClO_4)_2$ (B)**
Fe-PyN (Å)	2.140(3)	2.140(3)
Fe-PzN (Å)	2.079(6)	2.329(6)
α(°)	149.2(2)	147.0(2)
θ(°)	89.13(6)	96.70(6)
ϕ(°)	178.79(13)	178.79(13)
Σ(°)	150.82	153.91
Θ(°)	344.29	342.23

As was expected the variable temperature magnetic susceptibility measured using a SQUID magnetometer in a field of 5 kG showed that $\chi_M T$ held a value of approximately 3.7 $cm^3 mol^{-1} K$ between 300-75 K before dropping at lower temperatures due to the effect of zero field splitting (Figure 3.15). This value for $\chi_M T$ is typical for a HS iron(II) complex and shows that, like the tetrafluoroborate salt, the bulk sample remains trapped in the HS state.

PXRD measurements recorded using the same sample which was used for the SQUID measurements correlate well with those calculated from the crystal structure of **1**$(ClO_4)_2$ (Figure 3.16). Therefore the structure obtained via x-ray crystallography is representative of the bulk phase and the fully HS nature of this compound could have been predicted from the structure.

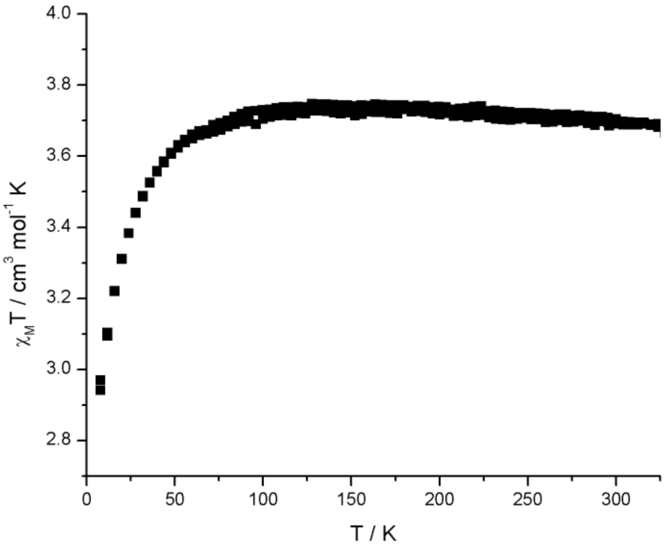

Figure 3.15
χ_MT *vs* T curve of **1**(ClO_4)$_2$. Recorded at a scan rate of 2 K min^{-1} in settle mode.

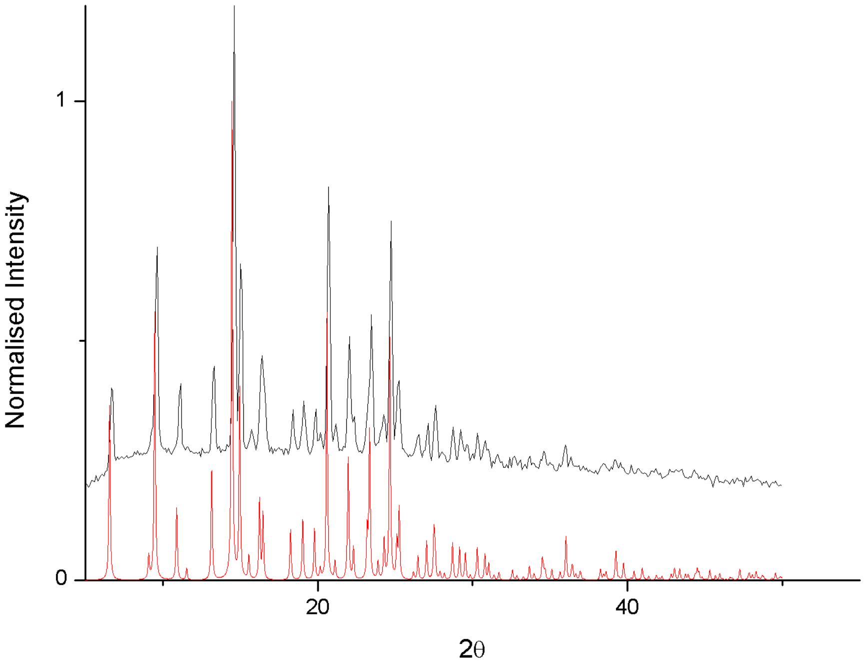

Figure 3.16
PXRD data obtained from the bulk sample of **1**(ClO_4)$_2$ (black) compared with the powder pattern calculated from the crystal structure (red).

3.2.3. **1**$(PF_6)_2$

Yellow crystals of **1**$(PF_6)_2$ were obtained via slow vapour diffusion of diethyl ether into a methanol solution of **1**$(PF_6)_2$ and a structure determined at 150 K. **1**$(PF_6)_2$ crystallised in the monoclinic space group *C*2/*c* (a = 34.124(3); b = 12.3128(11); c = 17.6817(17) Å, α = 90º, β = 114.441(6)º, γ = 90º, V = 6763.4(11) Å^3). The asymmetric unit contains one complete formula unit and was solved without any disorder or restraints applied (Figure 3.17).

The complex molecules are arranged in pairs which interlock such that the planes of the ligands on separate complex molecules come into close contact to one another (Figure 3.18). The distance between the two adjacent mean squares ligand planes, however, is 6.2288(5) Å which is too far to suggest that any π-π interactions are occurring between the adjacent complex molecules. These kind of interactions are seen in structures exhibiting the terpyridine embrace, although in these cases the interaction is four-fold and results in 2-dimensional sheets of complex cations.[25, 31-33]

The molecules are symmetry related by C_2 rotation axes and C_2 screw axes which run in the direction of the *b* axis, but no atoms lie directly on any of these axes (Figure 3.19). As with the tetrafluoroborate and perchlorate salts there are close interactions between complex and anion molecules, but there are also close interactions between adjacent complex molecules.

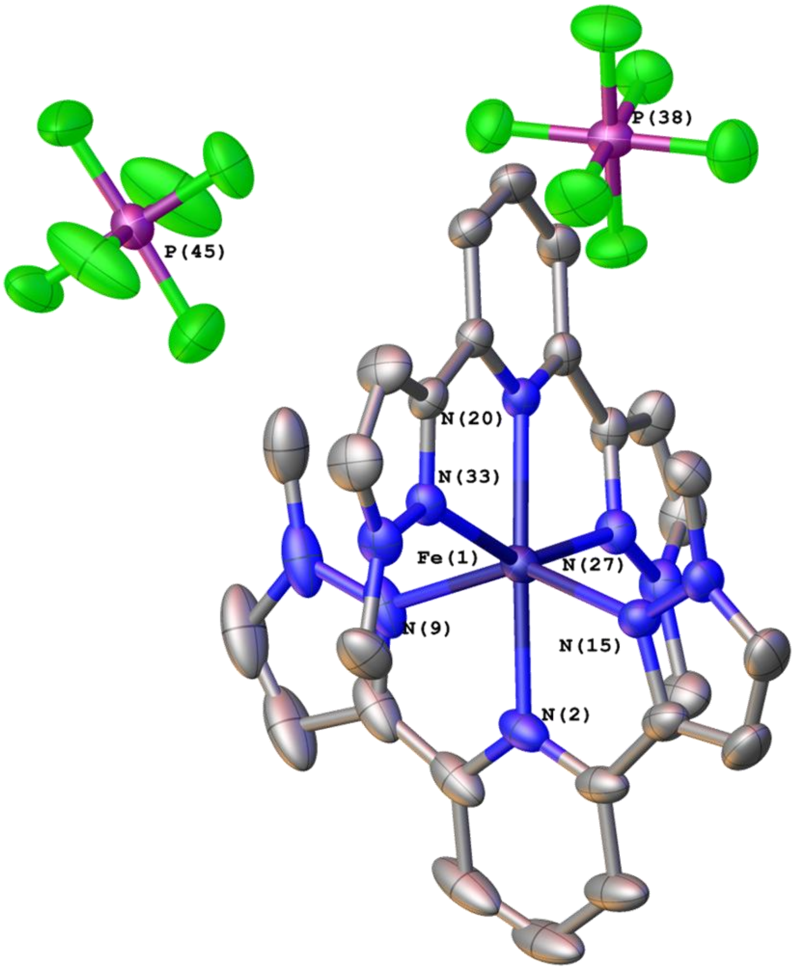

Figure 3.17
Asymmetric unit of **1**(PF_6)$_2$. Thermal ellipsoids are set at 50% probability and hydrogen atoms have been omitted for clarity.

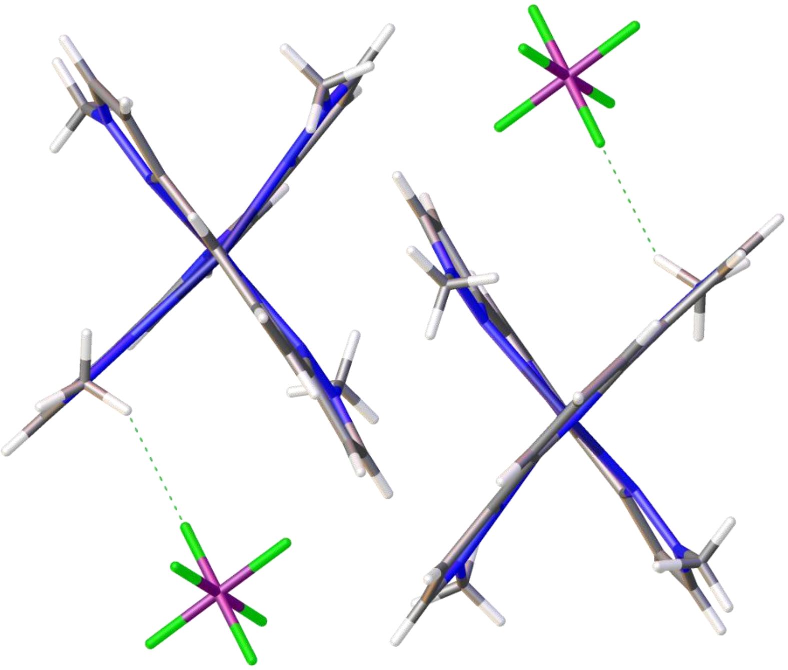

Figure 3.18
Symmetry generated view of **1**(PF_6)$_2$ showing the interactions between adjacent molecules.

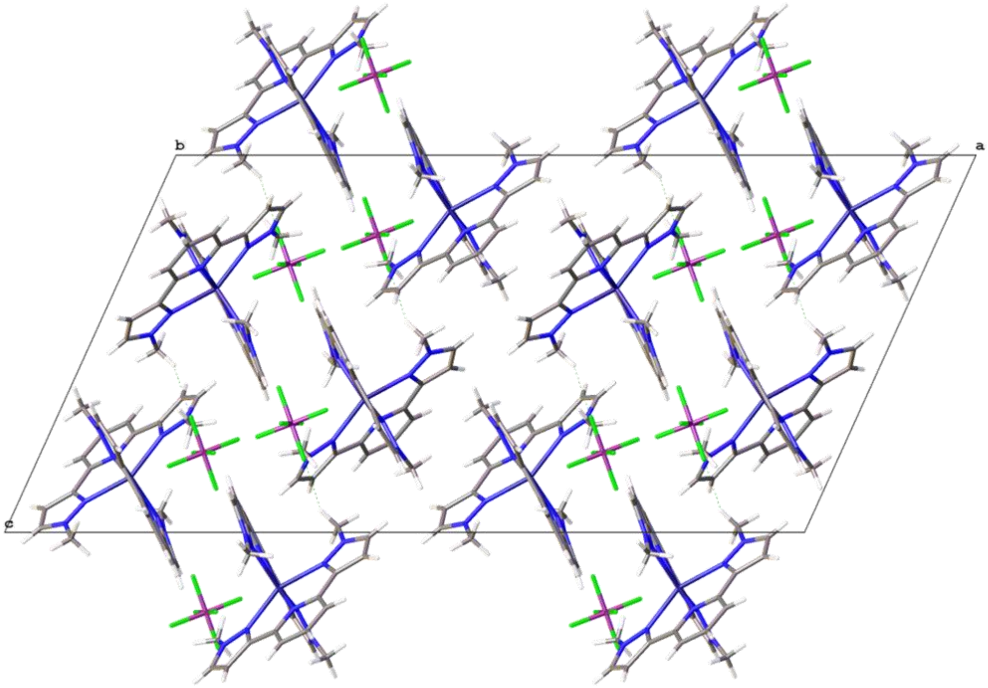

Figure 3.19
View down the *b* axis of **1**(PF_6)$_2$.

The coordination sphere around the iron centre is noticeably more distorted than for the tetrafluoroborate and perchlorate salts, but the rhombic and trigonal distortion parameters are fairly close to those of the perchlorate salt. One major geometric difference which distinguishes this from the other two salts is the trans angle, ϕ, which is significantly less than 180º (Table 3.4). Both ϕ and θ reduce the symmetry from the D_{2h} of a perfect octahedron to C_2 and the lattice may not accommodate a conversion back to D_{2h} symmetry which would accompany a spin transition.[34] As a comparison the smallest angle for ϕ in the literature for an iron(II)/bpp type complex is 154.52º which belongs to unsolvated $[Fe(L)_2](SbF_6)_2$, where L = 2,6-di(pyrazol-1-yl)pyrazine.[35]

Table 3.4
Tabulated values of the bond lengths and geometric parameters around the iron centre in **1**$(PF_6)_2$.

	1$(PF_6)_2$
Fe-PyN (Å)	2.1521(19)
Fe-PzN (Å)	2.2430(18)
α(°)	146.86(7)
θ(°)	79.29(2)
ϕ(°)	168.92(7)
Σ(°)	147.77
Θ(°)	341.72

The Fe–N bond lengths correspond with the distortion parameters and suggest that this complex is fully high spin at 150 K. Variable temperature magnetic susceptibility data confirms that this complex remains high spin over the entire temperature range. This is very similar to that of **1**$(BF_4)_2$ and **1**$(ClO_4)_2$ which show no evidence of a spin transition. The complex remains almost completely high spin with a constant $\chi_M T$ of around 3.8 cm^3 mol^{-1} K, which is quite typical for a high spin iron complex (Figure 3.20). PXRD data show that there are only minor differences between the bulk phase and the single crystal so the two structures are likely to be similar (Figure 3.21).

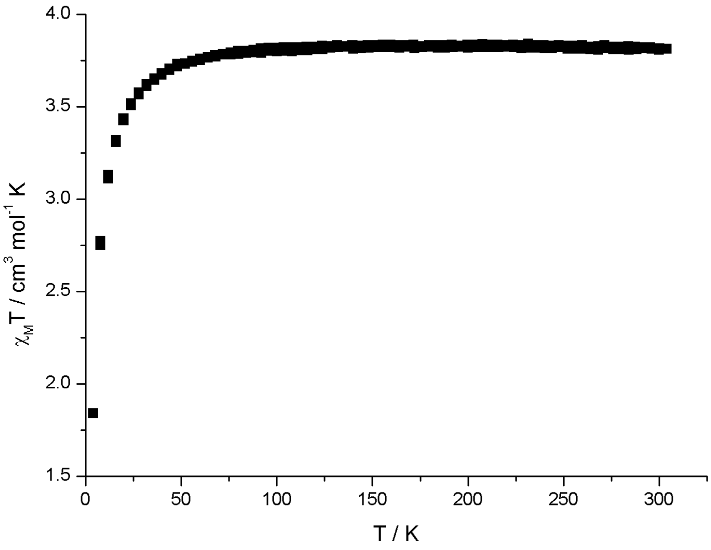

Figure 3.20
χ_MT *vs* T curve of **1**(PF_6)$_2$. Recorded at a scan rate of 2 K min^{-1} in settle mode.

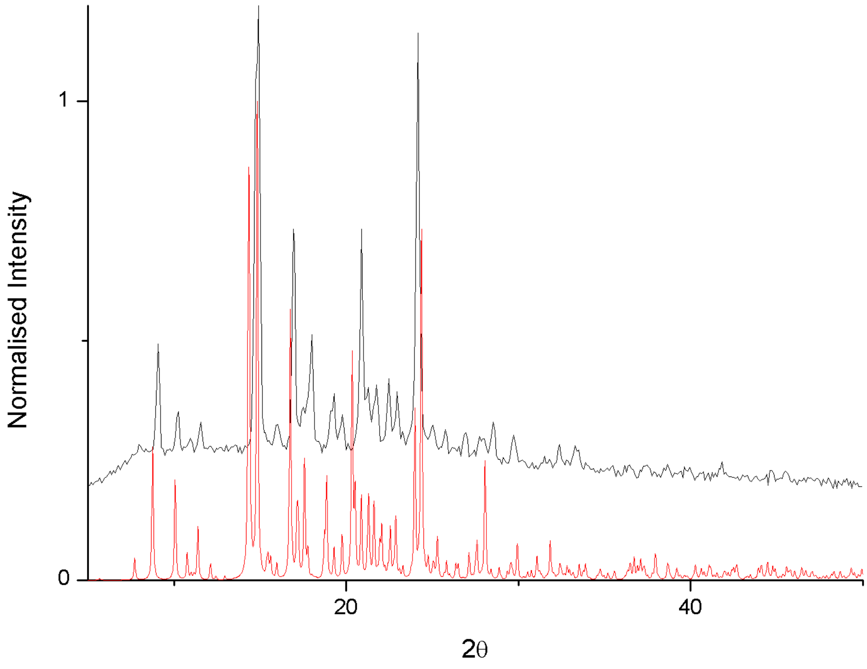

Figure 3.21
PXRD data obtained from the bulk sample of **1**(PF_6)$_2$ (black) compared with the powder pattern calculated from the crystal structure (red).

3.3. Iron(II) Complexes of L^2 ($2(X)_2$)

Iron (II) tetrafluoroborate and perchlorate salts were obtained by mixing two equivalents of the ligand $\mathbf{L^2}$ with iron(II) tetrafluoroborate or perchlorate in methanol. The hexafluorophosphate salt was obtained by first making the iron(II) chloride and then performing a salt exchange with ammonium hexafluorophosphate.

Single crystals were obtained for the $\mathbf{2}(BF_4)_2$, $\mathbf{2}(ClO_4)_2$ and $\mathbf{2}(PF_6)_2$ salts via slow diffusion of diisopropyl ether into acetonitrile, however it was crystals of $\mathbf{2}(PF_6)_2{\cdot}2CH_3CN$ which were the strongest diffractors. This complex salt crystallised in the monoclinic space group $P2_1/n$ (a = 20.494(2); b = 23.257(3); c = 20.609(2) Å, α = 90º, β = 101.271(6)º, γ = 90º, V = 9633.4(18) Å^3) and turned out to be the di-acetonitrile solvate $\mathbf{2}(PF_6)_2{\cdot}2CH_3CN$, with the asymmetric unit containing two formula units (Figure 3.22). There is also a significant amount of disorder in this complex; one of the isopropyl groups is disordered over two positions in a ratio of roughly 0.8:0.2, one of the acetonitrile molecules is disordered approximately 0.5:0.5 over two positions. The two hexafluorophosphate anions also show significant disorder, one being disordered roughly 0.5:0.5 over two positions and the other is disordered 0.4:0.4:0.2 over three positions. This disorder could be the cause of the poor quality crystals when compared to salts of $\mathbf{1}^{2+}$ and this is the reason a crystal structure of only the $\mathbf{2}(PF_6)_2{\cdot}2CH_3CN$ could be acquired. The asymmetric unit repeats via two-fold screw axes, which do not intersect any of the molecules and run along the b direction (Figure 3.23). There is a close contact between the disordered isopropyl group and the disordered acetonitrile, and it is probably this interaction which leads to the disorder in these two molecules (Figure 3.24). There are only close interactions between dication molecules and ions, and no close interactions between adjacent complex molecules in this structure.

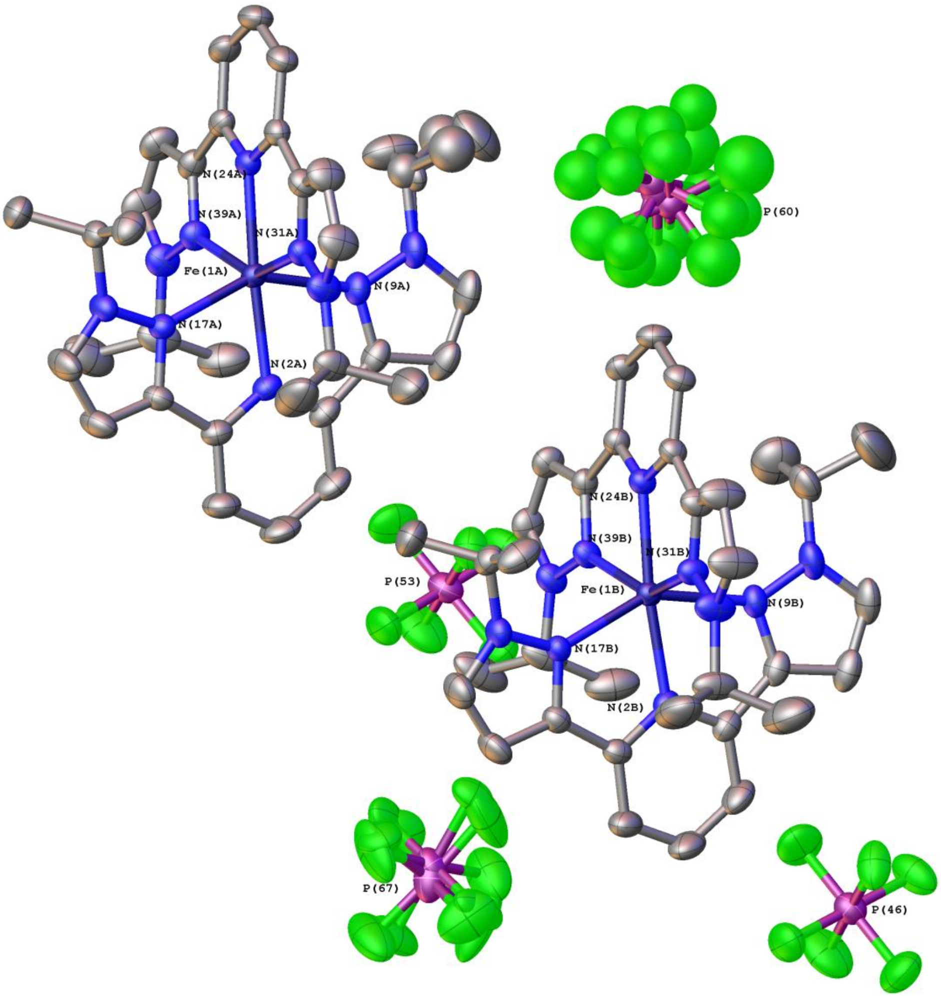

Figure 3.22
Asymmetric unit of **2**$(PF_6)_2 \cdot 2CH_3CN$. Thermal ellipsoids have been set at 50% probability and hydrogen atoms and solvent molecules have been omitted for clarity.

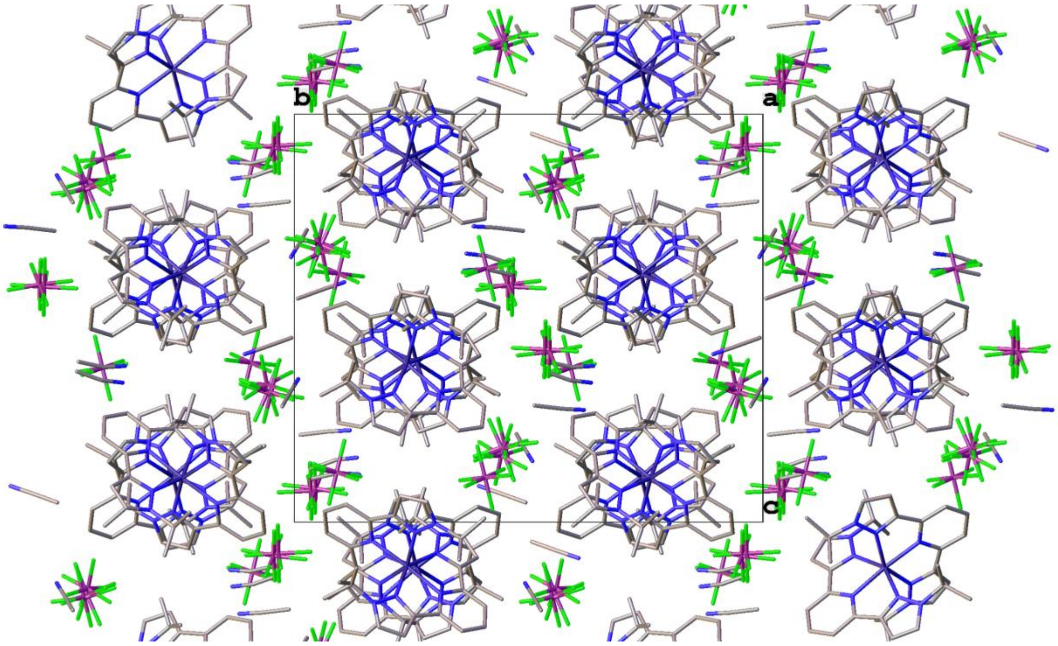

Figure 3.23
View of the structure of **2**$(PF_6)_2 \cdot 2CH_3CN$ down the *a* axis.

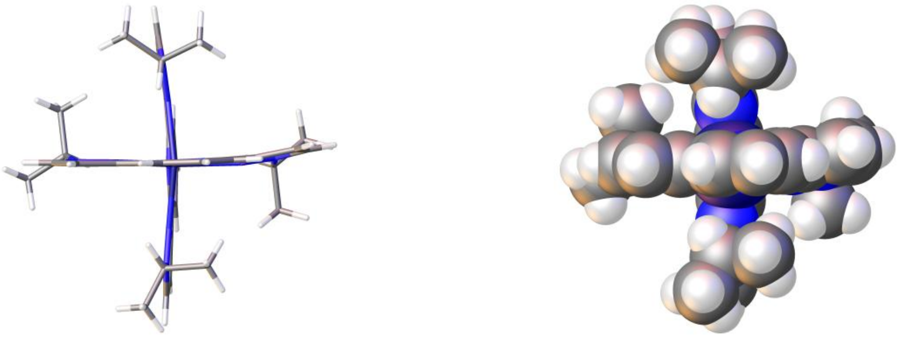

Figure 3.24
Stick (left) and spacefill (right) representations of the **2**$^{2+}$ cation showing the proximity of the *i*Pr groups to the ligand backbone.

Table 3.5
Tabulated values for the geometric parameters around the iron centres in **2**$(PF_6)_2 \cdot 2CH_3CN$.

	Fe(1A)	**Fe(1B)**
Fe-PyN (Å)	2.151(3)	2.144(2)
Fe-PzN (Å)	2.226(2)	2.227(2)
α(°)	147.79(9)	147.31(8)
θ(°)	88.45(3)	88.64(3)
ϕ(°)	175.94(8)	173.50(8)
Σ(°)	145.62	146.53
Θ(°)	341.71	342.05

The geometries of the coordination spheres around the iron centres are almost identical and are very similar to **1**$(BF_4)_2 \cdot H_2O$ and **1**$(ClO_4)_2$, but do not show as much distortion in the θ and ϕ angles as **1**$(PF_6)_2$ (Table 3.5). This is very clearly a high spin complex at 150 K by examination of the Fe–N bond lengths and distortion parameters. This was confirmed by $\chi_M T$ *vs* T measurements of **2**$(BF_4)_2 \cdot H_2O$ both in the solid state and in $(CD_3)_2CO$ solution (Figure 3.25 and Figure 3.26). **2**$(BF_4)_2 \cdot H_2O$ was used in this instance because of its higher solubility in acetone than **2**$(PF_6)_2$. The two sets of data are very similar and give a typical $\chi_M T$ value of around 3.5 $cm^3\ mol^{-1}$ K, and this shows that the high spin nature of this complex is not entirely due to packing effects in the lattice.

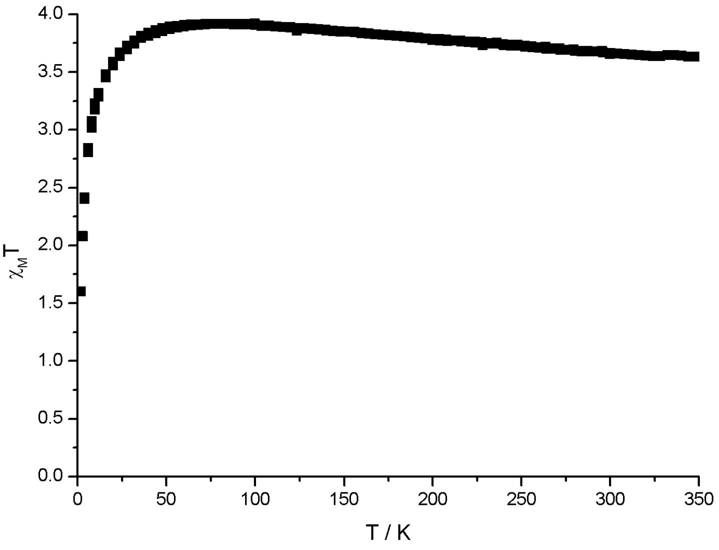

Figure 3.25
$\chi_M T$ *vs* T curve of **2**$(BF_4)_2\cdot H_2O$. Recorded at a scan rate of 2 K min^{-1} in settle mode.

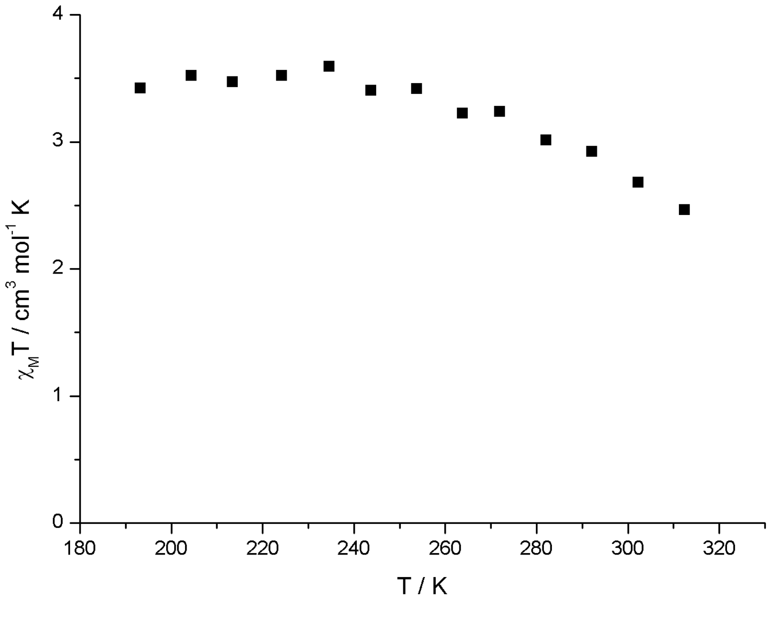

Figure 3.26
$\chi_M T$ *vs* T for **2**$(BF_4)_2\cdot H_2O$ in $(CD_3)_2CO$ solution.

The magnetic susceptibility via the Evans NMR method shows a value of $\chi_M T$ of around 3.5 cm^{3}mol^{-1}K which is also quite typical of HS iron(II). The drop off at higher temperatures is likely to be the density of the acetone solution which is used to calculate $\chi_M T$, as density data is only available on neat acetone the presence of a solute may affect this. It was also noted that after the measurement some of the complex had precipitated out of solution, which will affect both the concentration and the density used in the calculation. However these measurements clearly show that the complex remains fully HS from 190-310 K in acetone solution.

This is an unexpected result as the isopropyl groups are electron donating substituents, and so should serve to raise the transition temperature in this complex by increasing the basicity of the donating nitrogens and thus stabilising the LS state.[36] However the corresponding 1-bpp complex, which is geometrically and sterically similar is also high spin over the entire temperature range and so this result could be due to the steric effects of the substituents.[5, 37] In particular the close intramolecular contacts between the ^{i}Pr groups and the 3-bpp structure as seen in the space filling diagram in Figure 3.24 could serve to prevent the contraction of the coordination sphere upon a HS→LS transition and so inhibit SCO in this complex.[5]

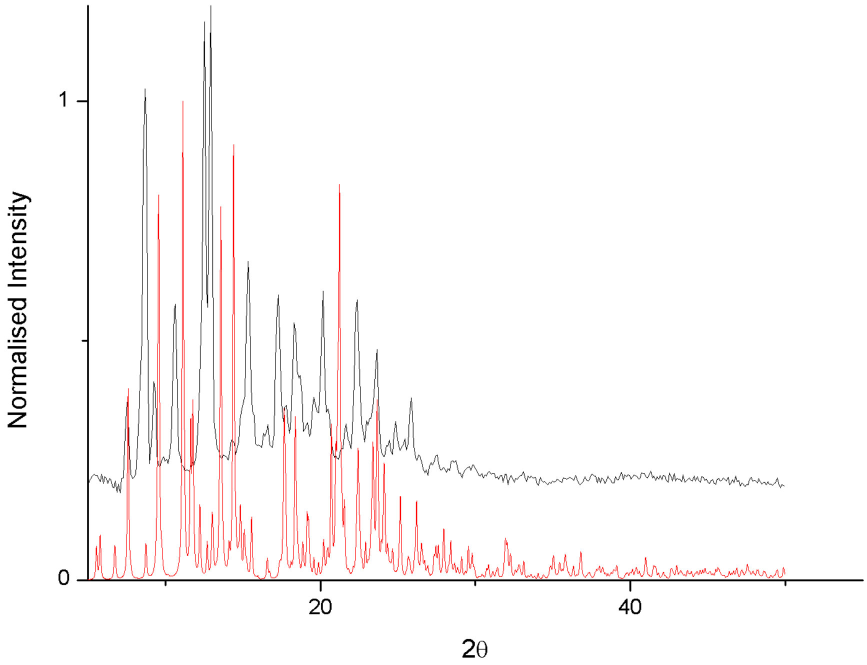

Figure 3.27
PXRD data obtained from the bulk sample of **2**$(PF_6)_2$ (black) compared with the powder pattern calculated from the crystal structure (red).

By comparison of the PXRD data obtained from the bulk sample and the powder pattern calculated from the crystal structure it can be seen that they are very different (Figure 3.27).

This could be due to loss of acetonitrile from the crystal which may trigger a structural change. This has not been confirmed, however.

3.4. Iron(II) Complexes of L^3 ($3(X)^2$)

Mixing two equivalents of the ligand $\mathbf{L^3}$ with iron(II) tetrafluoroborate hexahydrate afforded the complex $\mathbf{3}(BF_4)_2$ as a microcrystalline yellow solid. Crystals suitable for x-ray diffraction were obtained via slow vapour diffusion of diisopropyl ether into an acetonitrile solution of $\mathbf{3}(BF_4)_2$ and a structure was determined at 150 K. This complex crystallised in the cubic space group $I\text{-}4_2d$ ($a = b = c = 22.8650(18)$ Å, $\alpha = \beta = \gamma = 90$º, $V = 11954.0(16)$ Å^3) with the asymmetric unit containing a quarter of a complex molecule, and half a tetrafluoroborate anion (Figure 3.28). The allyl substituent is disordered over three positions in the ratios 0.6:0.25:0.15. Fe(1) and N(2) lie on a 4-fold rotoinversion axis and the half anion lies on a C_3 rotation axis. When the disordered allyl groups are in their major orientation they tuck in neatly into the plane of the ligands (Figure 3.29). Despite the fairly large allyl groups the coordination around the iron centre has very little distortion, which is probably a reflection of the flexibility of these groups. The bond lengths however suggest that the iron is in its HS state at 150 K (Table 3.6).

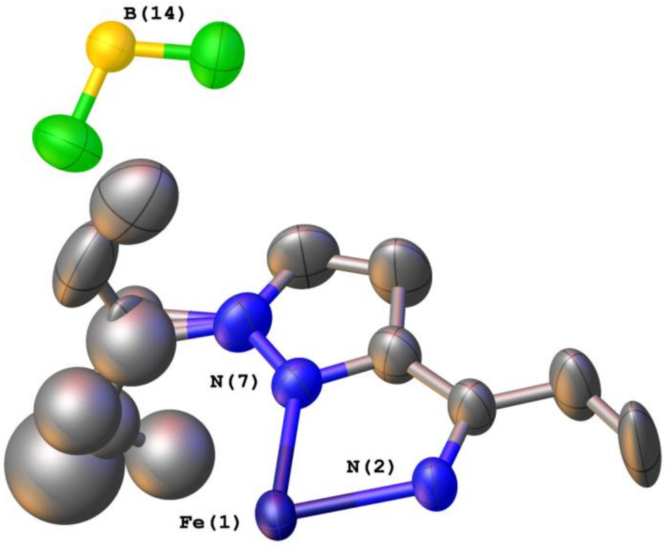

Figure 3.28
Asymmetric unit of $\mathbf{3}(BF_4)_2$. Thermal ellipsoids are set at 50% probability and hydrogens have been omitted for clarity.

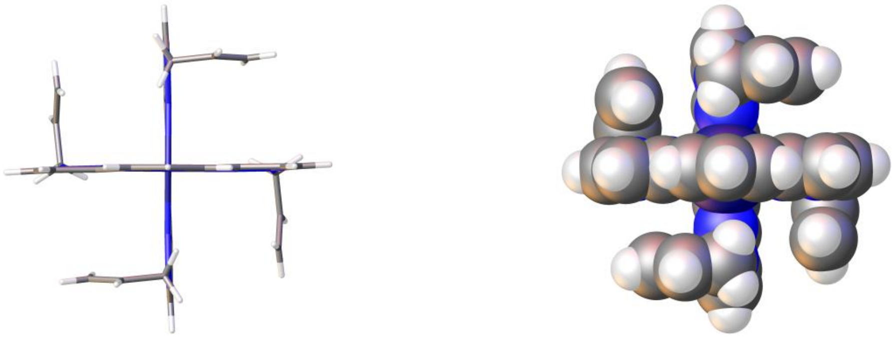

Figure 3.29
Stick (left) and spacefill (right) representations of the 3^{2+} cation showing the proximity of the allyl groups to the ligand backbone when in their major orientation.

Table 3.6
Selected bond lengths and geometric parameters for the iron centre in $\mathbf{3}(BF_4)_2$. [a] Atom coordinates lie on a crystallographic axis so no associated ESD.

	$\mathbf{3(BF_4)_2}$
Fe-PyN (Å)	2.129(3)
Fe-PzN (Å)	2.217(3)
α(°)	149.07(13)
θ(°)	90.0000(16)
ϕ(°)	180[a]
Σ(°)	140.08
Θ(°)	343.64

The rhombic and trigonal distortion parameters are very similar to previous complexes however there is no distortion whatsoever in the *trans* angle which is exactly 180º. Looking down the axis of the pyridine N–Fe bonds the steric clashes between the allyl groups do not seem to be as great as those seen in $\mathbf{4}^{2+}$ (discussed in **3.5**).

Evidence for the high spin state is further supported by the solid state magnetic susceptibility measurements, which show that this complex is fully high spin over the entire temperature range (Figure 3.30). This shows that it is not necessarily the distortion in the *trans* angle which traps the complex in the high spin state, so this must be a combination of other steric and electronic factors. In addition measurements of the magnetic susceptibility in acetone solution show that this complex is fully HS between 190-310 K (Figure 3.31). When conducting the Evans NMR experiment for this complex a lower concentration was used, which avoided the problem of precipitate forming at lower temperatures and reducing the drop-off in $\chi_M T$ seen at higher temperatures.

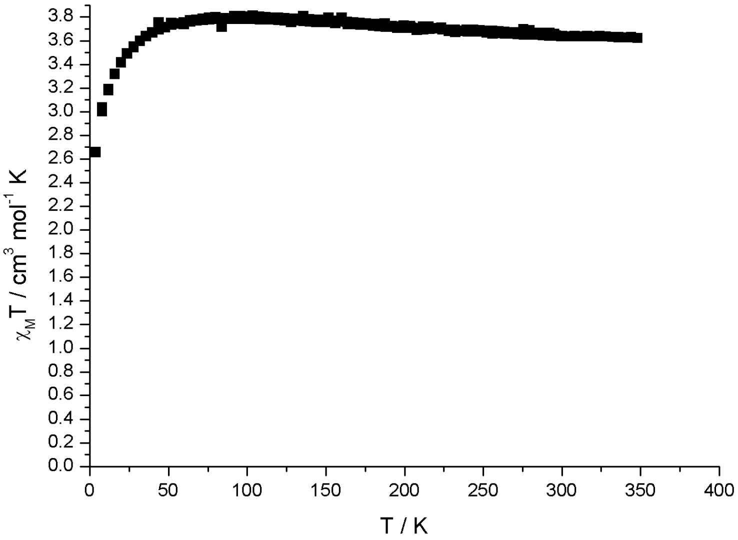

Figure 3.30
$\chi_M T$ *vs* T for **3**$(BF_4)_2$. Recorded at a scan rate of 2 K min^{-1} in settle mode.

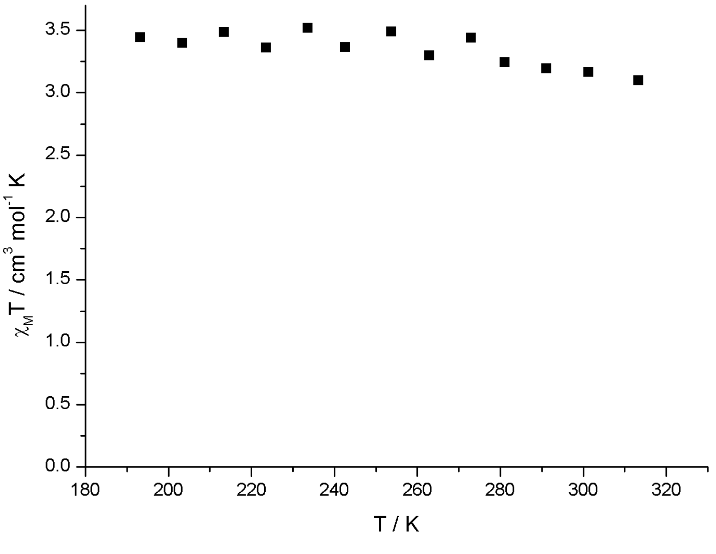

Figure 3.31
$\chi_M T$ *vs* T for **3**$(BF_4)_2$ in $(CD_3)_2CO$ solution.

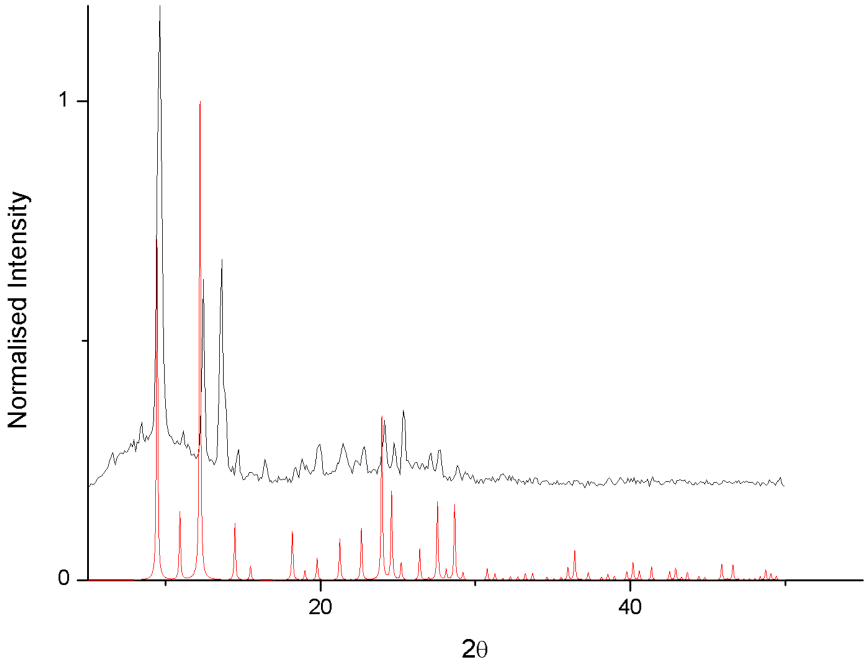

Figure 3.32
PXRD data obtained from the bulk sample of **3**$(BF_4)_2$ (black) compared with the powder pattern calculated from the crystal structure (red).

By comparing the PXRD data obtained from the bulk sample and that calculated from the crystal structure it can be seen that the two are very similar, although there are a few additional peaks and a hump indicating some amorphous material present (Figure 3.32). This suggests that the bulk sample could be a mixture of phases including the one observed in the crystal structure. However the value of $\chi_M T$ suggests that it is likely any additional phases are also HS from 5-300 K.

3.5. Iron(II) Complexes of L^4 ($4(X)_2$)

Two equivalents of the ligand $\mathbf{L^4}$ were mixed with iron(II) salts producing **4**$(BF_4)_2$, **4**$(ClO_4)_2$ and **4**$(PF_6)_2$ as microcrystalline yellow solids. Crystals suitable for x-ray structure determination were obtained from the tetrafluoroborate salt via slow vapour diffusion diisopropyl ether into an acetonitrile solution of **4**$(BF_4)_2$ and the structure was determined at 150 K. **4**$(BF_4)_2$ crystallised in the orthorhombic space group *Pbca* (a = 15.4334(17); b = 14.0656(17); c = 43.884(5) Å, $\alpha = \beta = \gamma = 90^\circ$, V = 9526.3(19) Å). The asymmetric unit contains one complete formula unit with no lattice solvent being present (Figure 3.33).There is no apparent disorder in the benzyl groups; three of the groups are tucked in parallel to the plane of the other ligand in what could be a π-π stacking interaction and this sort of packing motif has been seen before in transition metal complexes of similar ligands.[38] The other benzyl group is pointing away from the complex, and this could be due to some close interactions which exist between pairs of adjacent molecules (Figure 3.34). The molecules are symmetry related by 2-fold screw axes in the *a*, *b* and *c* direction.

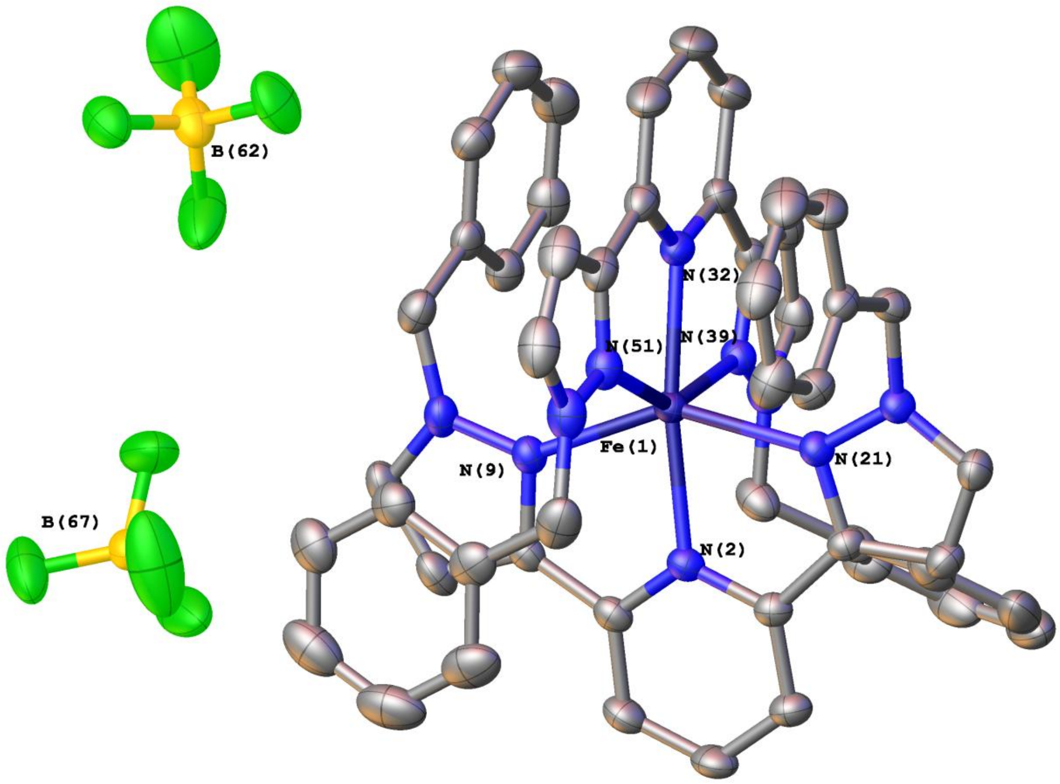

Figure 3.33
Asymmetric unit of **4**$(BF_4)_2$. Thermal ellipsoids are set at 50% probability and hydrogens have been omitted for clarity.

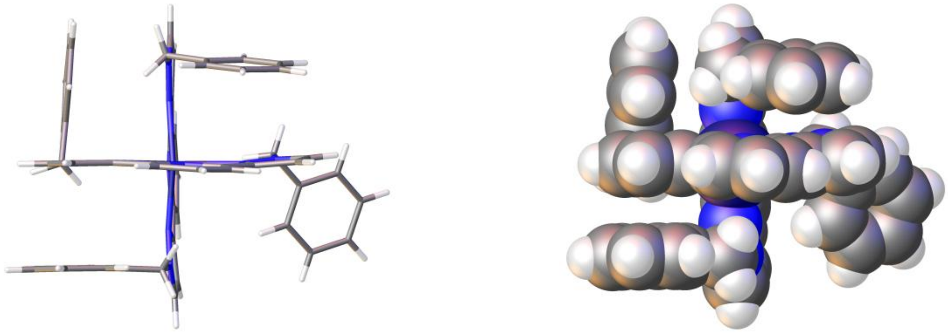

Figure 3.34
Stick (left) and spacefill (right) representations of the **4**$^{2+}$ cation showing the proximity of the benzyl groups to the ligand backbone.

Table 3.7
Selected bond lengths and geometric parameters for the iron centre in **4**(BF$_4$)$_2$.

	4(BF$_4$)$_2$
Fe-PyN (Å)	2.1396(14)
Fe-PzN (Å)	2.2260(15)
α(°)	148.60(6)
θ(°)	89.607(15)
ϕ(°)	171.00(6)
Σ(°)	141.79
Θ(°)	342.75

The distortions around the iron centre are again characteristic of a high spin iron(II) complex and very similar to the complexes mentioned previously in this chapter (Table 3.7). Also there is a noticeable deviation of the ϕ angle away from 180º, which could lead to trapping of the high spin state over the entire temperature range.

The magnetic susceptibility of this complex was recorded both in the solid state and in acetone solution. The solid state SQUID data support the geometric parameters derived from the crystal data, showing the absence of a spin transition and a similar magnetic profile to those seen for the previous complexes (Figure 3.35). The solution magnetic susceptibility recorded using the Evans NMR method also shows a high spin complex between 193 K and 312 K (Figure 3.36). This helps to explain that the HS nature of the complex is likely to be caused by the inductive effect of the benzyl substituents as opposed to packing effects alone.

It can also be seen from the comparison of the experimental and calculated PXRD data that the bulk phase of **4**(BF_4)$_2$ is identical to the phase observed in the crystal structure (Figure 3.37). This reflects the absence of lattice solvent in the structure making the bulk sample less likely to change over time.

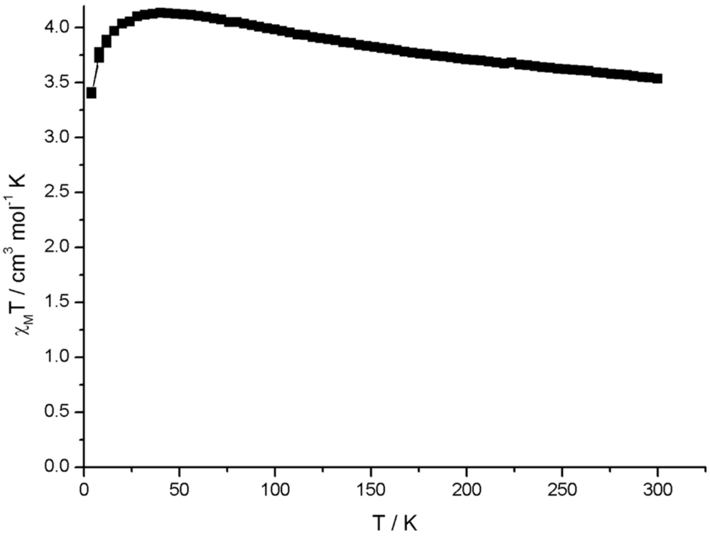

Figure 3.35
χ_MT *vs* T for **4**(BF_4)$_2$. Recorded at a scan rate of 2 K min^{-1} in settle mode.

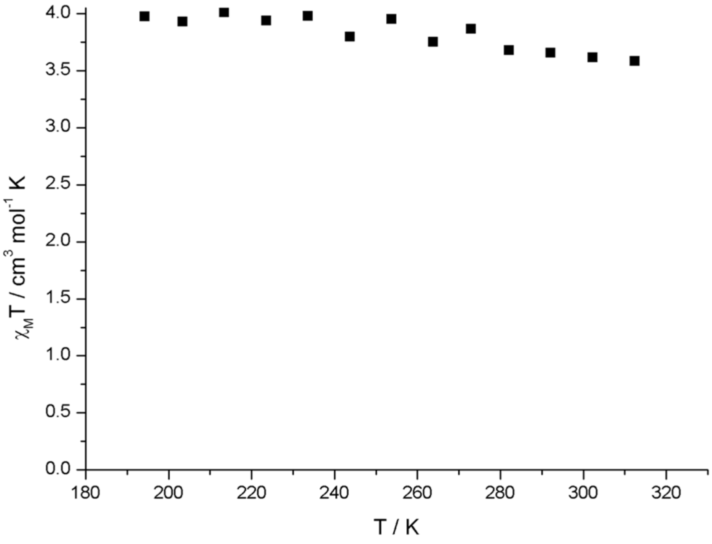

Figure 3.36
χ_MT *vs* T for **4**(BF_4)$_2$ in $(CD_3)_2CO$ solution.

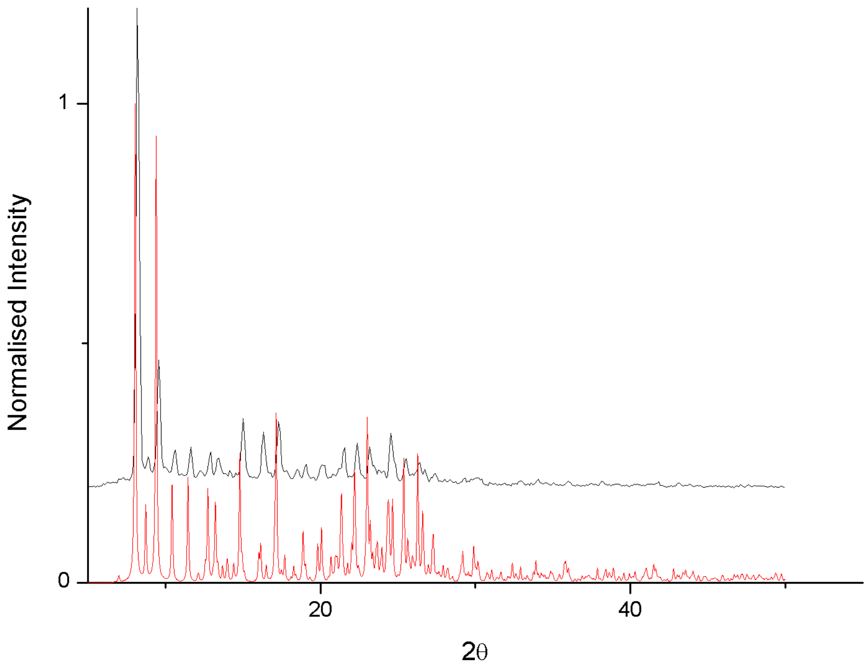

Figure 3.37
PXRD data obtained from the bulk sample of **4**$(BF_4)_2$ (black) compared with the powder pattern calculated from the crystal structure (red).

3.6. Conclusion

From the crystal structures and magnetic susceptibility data presented here it is clear to see that none of the complex salts undergo SCO. Only the crystalline hydrate **1**$(BF_4)_2\cdot H_2O$, which contains two distinct iron centres of apparently different spin states, has the potential to undergo a spin transition. A bulk sample of the hydrate for magnetic susceptibility measurements has not yet been obtained, however. It has been determined by PXRD that the bulk phase of this complex is not the same phase as the single crystal and that it is in fact isostructural to **1**$(ClO_4)_2$. Although the crystal structures have different unit cells, packing motifs and disorder the variable temperature magnetic susceptibility of all six complexes discussed here show they are all high spin over the entire temperature range (Figure 3.38).

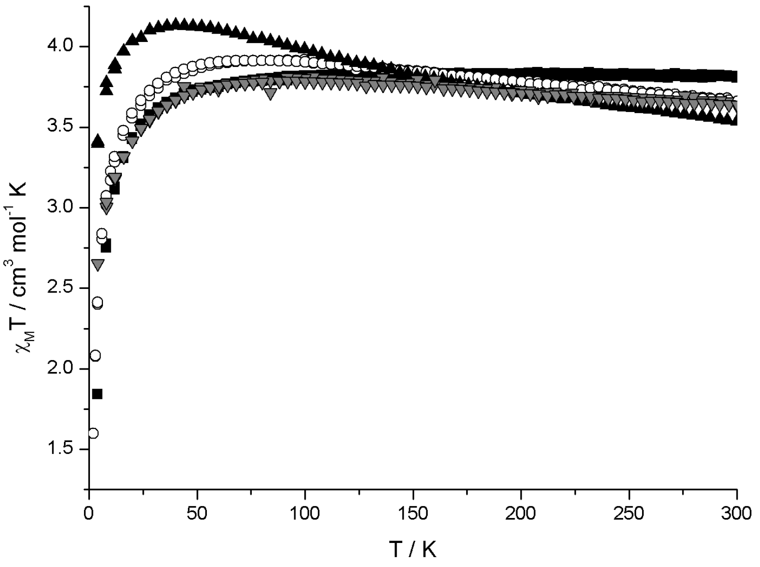

Figure 3.38
Comparison of the χ_MT *vs* T data for **1**(PF_6) (■), **2**$(BF_4)_2$ (○), **3**$(BF_4)_2$ (▼) and **4**$(BF_4)_2$ (▲).

The complexes of **L**^{2} correlate well with their 1-bpp counterparts which have a very similar magnetic profile to this complex. It is possible that the steric bulk of this isopropyl group is hindering the contraction of the coordination sphere and so making a HS→LS transition unfeasible. For the complexes of **L**^{3} and **L**^{4} there are no known isostructural 1-bpp complexes to compare to but the crystal structures obtained show that the substituents wrap around the complex and show some close interactions with the opposing ligand. While this may serve to hinder SCO in the same way as complexes of **L**^{2}, the flexibility of the allyl and benzyl substituents may also serve to reduce this effect.

Interestingly the complex salts of **L**^{1} are fully high spin over the entire temperature range while some of their counterparts from the 1-bpp series are SCO active. This discrepancy must arise from a combination and balance of subtle steric and electronic factors which influence the spin states of these complexes.

3.7. References

[1] A. J. Bridgeman, M. A. Halcrow, M. Jones, E. Krausz and N. K. Solanki, *Chem. Phys. Lett.* **1999**, *314*, 176-181.

[2] N. K. Solanki, M. A. Leech, E. J. L. McInnes, J. P. Zhao, F. E. Mabbs, N. Feeder, J. A. K. Howard, J. E. Davies, J. M. Rawson and M. A. Halcrow, *J. Chem. Soc. Dalton Trans.* **2001**, 2083-2088.

[3] N. K. Solanki, E. J. L. McInnes, F. E. Mabbs, S. Radojevic, M. McPartlin, N. Feeder, J. E. Davies and M. A. Halcrow, *Angew. Chem. Int. Ed.* **1998**, *37*, 2221-2223.

[4] J. M. Holland, C. A. Kilner, M. Thornton-Pett and M. A. Halcrow, *Polyhedron* **2001**, *20*, 2829-2840.

[5] J. M. Holland, S. A. Barrett, C. A. Kilner and M. A. Halcrow, *Inorg. Chem. Commun.* **2002**, *5*, 328-332.

[6] V. A. Money, C. Carbonera, J. Elhaïk, M. A. Halcrow, J. A. K. Howard and J. F. Létard, *Chem. Eur. J.* **2007**, *13*, 5503-5514.

[7] J. Elhaïk, C. A. Kilner and M. A. Halcrow, *Eur. J. Inorg. Chem.* **2014**, *2014*, 4250-4253.

[8] J. Elhaïk, C. A. Kilner and M. A. Halcrow, *Dalton Trans* **2006**, 823-830.

[9] M. A. Halcrow and R. Kulmaczewski, unpublished data, **2014**.

[10] J. Elhaïk, V. A. Money, S. A. Barrett, C. A. Kilner, I. R. Evans and M. A. Halcrow, *Dalton Trans.* **2003**, 2053-2060.

[11] V. A. Money, J. Elhaïk, E. I. Radosavljevic, M. A. Halcrow and J. A. K. Howard, *Dalton Trans* **2004**, 65-69.

[12] T. Buchen, P. Gütlich and H. A. Goodwin, *Inorg. Chem.* **1994**, *33*, 4573-4576.

[13] H. A. Goodwin and K. H. Sugiyarto, *Chem. Phys. Lett.* **1987**, *139*, 470-474.

[14] S. Marcén, L. Lecren, L. Capes, H. A. Goodwin and J. F. Létard, *Chem. Phys. Lett.* **2002**, *358*, 87-95.

[15] C. Baldé, C. Desplanches, P. Gütlich, E. Freysz and J. F. Létard, *Inorg. Chim. Acta* **2008**, *361*, 3529-3533.

[16] J. F. Létard, J. S. Costa, S. Marcén, C. Carbonera, C. Desplanches, A. Kobayashi, N. Daro, P. Guionneau and J. P. Ader, *J. Phys.: Conf. Ser.* **2005**, *21*, 23-29.

[17] A. Bhattacharjee, J. Kusz, V. Ksenofontov, K. H. Sugiyarto, H. A. Goodwin and P. Gütlich, *Chem. Phys. Lett.* **2006**, *431*, 72-77.

[18] J. F. Létard, C. Carbonera, E. Courcot and J. S. Costa, *Bull. Mater. Sci.* **2006**, *29*, 567-571.

[19] K. H. Sugiyarto, K. Weitzner, D. C. Craig and H. A. Goodwin, *Aust. J. Chem.* **1997**, *50*, 869-873.

[20] S. A. Barrett, C. A. Kilner and M. A. Halcrow, *Dalton Trans.* **2011**, *40*, 12021-12024.

[21] Y. Hasegawa, R. Sakamoto, K. Takahashi and H. Nishihara, *Inorg. Chem.* **2013**, *52*, 1658-1665.

[22] D. L. Reger, J. R. Gardinier, M. D. Smith, A. M. Shahin, G. J. Long, L. Rebbouh and F. Grandjean, *Inorg. Chem.* **2005**, *44*, 1852-1866.

[23] K. H. Sugiyarto, M. L. Scudder, D. C. Craig and H. A. Goodwin, *Aust. J. Chem.* **2000**, *53*, 755-765.

[24] K. H. Sugiyarto, D. C. Craig, A. D. Rae and H. A. Goodwin, *Aust. J. Chem.* **1994**, *47*, 869-890.

[25] C. Carbonera, C. A. Kilner, J. F. Létard and M. A. Halcrow, *Dalton Trans.* **2007**, 1284-1292.

[26] R. Boca, *Coord. Chem. Rev.* **2004**, *248*, 757-815.

[27] T. D. Roberts, M. A. Little, F. Tuna, C. A. Kilner and M. A. Halcrow, *Chem. Commun.* **2013**, *49*, 6280-6282.

[28] T. D. Roberts, F. Tuna, T. L. Malkin, C. A. Kilner and M. A. Halcrow, *Chem. Sci.* **2012**, *3*, 349-354.

[29] D. F. Evans, *J. Chem. Soc.* **1959**, 2003-2005.

[30] L. A. Yatsunyk and F. A. Walker, *Inorg. Chem.* **2004**, *43*, 757-777.

[31] M. L. Scudder, H. A. Goodwin and I. G. Dance, *New J. Chem.* **1999**, *23*, 695-705.

[32] R. Pritchard, C. A. Kilner and M. A. Halcrow, *Chem. Commun.* **2007**, 577-579.

[33] C. A. Tovee, C. A. Kilner, J. A. Thomas and M. A. Halcrow, *Cryst. Eng. Comm.* **2009**, *11*, 2069-2077.

[34] M. A. Halcrow, *Coord. Chem. Rev.* **2009**, *253,* 2493-2514.

[35] C. A. Kilner and M. A. Halcrow, *Polyhedron* **2006**, *25*, 235-240.

[36] T. D. Roberts, M. A. Little, L. J. Kershaw Cook, S. A. Barrett, F. Tuna and M. A. Halcrow, *Polyhedron* **2013**, *64,* 4-12.

[37] J. Elhaïk, D. J. Evans, C. A. Kilner and M. A. Halcrow, *Dalton Trans.* **2005**, 1693-1700.

[38] Q. H. Wei, S. P. Argent, H. Adams and M. D. Ward, *New J. Chem.* **2008**, *32,* 73-82.

Chapter 4

Substitution of 2,6-Di(1*H*-pyrazol-3-yl)pyridine at the Pyrazolyl *C*4, *C*5 Positions and the Pyridyl *C*4 Position and Implications on Spin Crossover

4.1. Introduction

It was shown in Chapter 3 that modification of the 2,6-di(1*H*-pyrazol-3-yl)pyridine structure at the pyrazole 1H position by simple hydrocarbon groups does not lead to SCO behaviour in their iron(II) complexes, unlike some of their 2,6-di(pyrazol-1-yl)pyridine analogues.[1] Synthetic routes towards substituted 3-bpp derivatives are somewhat limited in the literature. However there are routes towards substitution at the pyrazolyl *C*5 position to make 2,6-di(5-amino-1*H*-pyrazol-3-yl)pyridine, and some 2,6-di(5-alkyl-1*H*-pyrazol-3-yl)pyridine derivatives [2-4] Substitution of the ligand at this position has the advantage of leaving the pyrazolyl NH group with the ability to form hydrogen bonds, which are often associated with high cooperativity within their crystalline complexes. This cooperativity is thought to lead to abrupt spin transitions, although these interactions are not the only influencing factor.[5] In addition to retaining the NH bonding capabilities, substitution at the pyrazole *C*5 position can lead to additional hydrogen bonding interactions, steric clashes and inductive effects being introduced into the system.

This is not the first time substitution at the pyrazolyl *C*5 position of 3-bpp has been investigated by the group, and one ligand which proved to be particularly fruitful was 2,6-di(5-methyl-1*H*-pyrazol-3-yl)pyridine ($\mathbf{L^9}$). Firstly, the tetrafluoroborate salt $[Fe(\mathbf{L^9})_2](BF_4)_2$ readily takes up atmospheric moisture to give the $[Fe(\mathbf{L^9})_2](BF_4)_2{\cdot}2H_2O$ solvate which adopts a 1:1 HS:LS ratio. However this can be thermally dehydrated to give the anhydrous HS complex which undergoes an abrupt spin transition on cooling with a wide thermal hysteresis. This hysteresis is initially 65 K wide but with repeated thermal cycling narrows to 37 K. This complex also has very complex phase behaviour associated with the transition, with an additional non-isostructural anhydrous phase available from recrystallisation.[6] This example will be discussed in more detail in Chapter 5.

There are many manipulations which could be performed on the pyrazolyl *C*5 position which could affect spin crossover. The ligand field can be altered by addition of electron withdrawing and donating groups and it can be seen in the literature that for complexes of substituted 1-bpp the $T_{1/2}$ appears to be higher for electron donating and lower for electron withdrawing substituents on the pyrazolyl rings.[7-9] Therefore substituting electron withdrawing groups at the pyrazolyl *C*4 position stabilises the high spin state. However this trend does not seem to apply to all ligand types.[10]

In addition to these effects certain groups, such as those capable of forming intermolecular interactions, will also increase the cooperativity by communicating spin state changes between adjacent molecules and give a more abrupt spin transition possibly accompanied by hysteresis.[11, 12] It would therefore be of interest to use various synthetic routes to obtain a series of 3-bpp ligands which are substituted at the pyrazolyl *C*5 position, and vary these substituents so as to influence the inductive effects, steric bulk and intermolecular interactions (Figure 4.1). As previously stated in Chapter 2, there are not as many synthetic routes available to 3-bpp derivatives as there are for the 1-bpp isomer, and the methods employed to make the ligands discussed in this chapter were described in that chapter.

Table 4.1
The complexes discussed in this chapter and their abbreviations. The nature of the anion, X, and any solvation are specified throughout.

Complex	Abbreviation
$[Fe(\mathbf{L}^{5})_2](X)_2$	$\mathbf{5}(X)_2$
$[Fe(\mathbf{L}^{6})_2](X)_2$	$\mathbf{6}(X)_2$
$[Fe(\mathbf{L}^{7})_2](X)_2$	$\mathbf{7}(X)_2$
$[Fe(\mathbf{L}^{10})_2](X)_2$	$\mathbf{10}(X)_2$
$[Fe(\mathbf{L}^{11})_2](X)_2$	$\mathbf{11}(X)_2$
$[Fe(\mathbf{L}^{12})_2](X)_2$	$\mathbf{12}(X)_2$
$[Fe(\mathbf{L}^{14})_2](X)_2$	$\mathbf{14}(X)_2$
$[Fe(\mathbf{L}^{15})_2](X)_2$	$\mathbf{15}(X)_2$
$[Fe_2(\mathbf{L}^{15})_2](X)_4$	–
$[Fe(\mathbf{L}^{16})_2](X)_2$	$\mathbf{16}(X)_2$
$[Fe(\mathbf{L}^{17})_2](X)_2$	$\mathbf{17}(X)_2$
$[Fe(\mathbf{L}^{18})_2](X)_2$	$\mathbf{18}(X)_2$

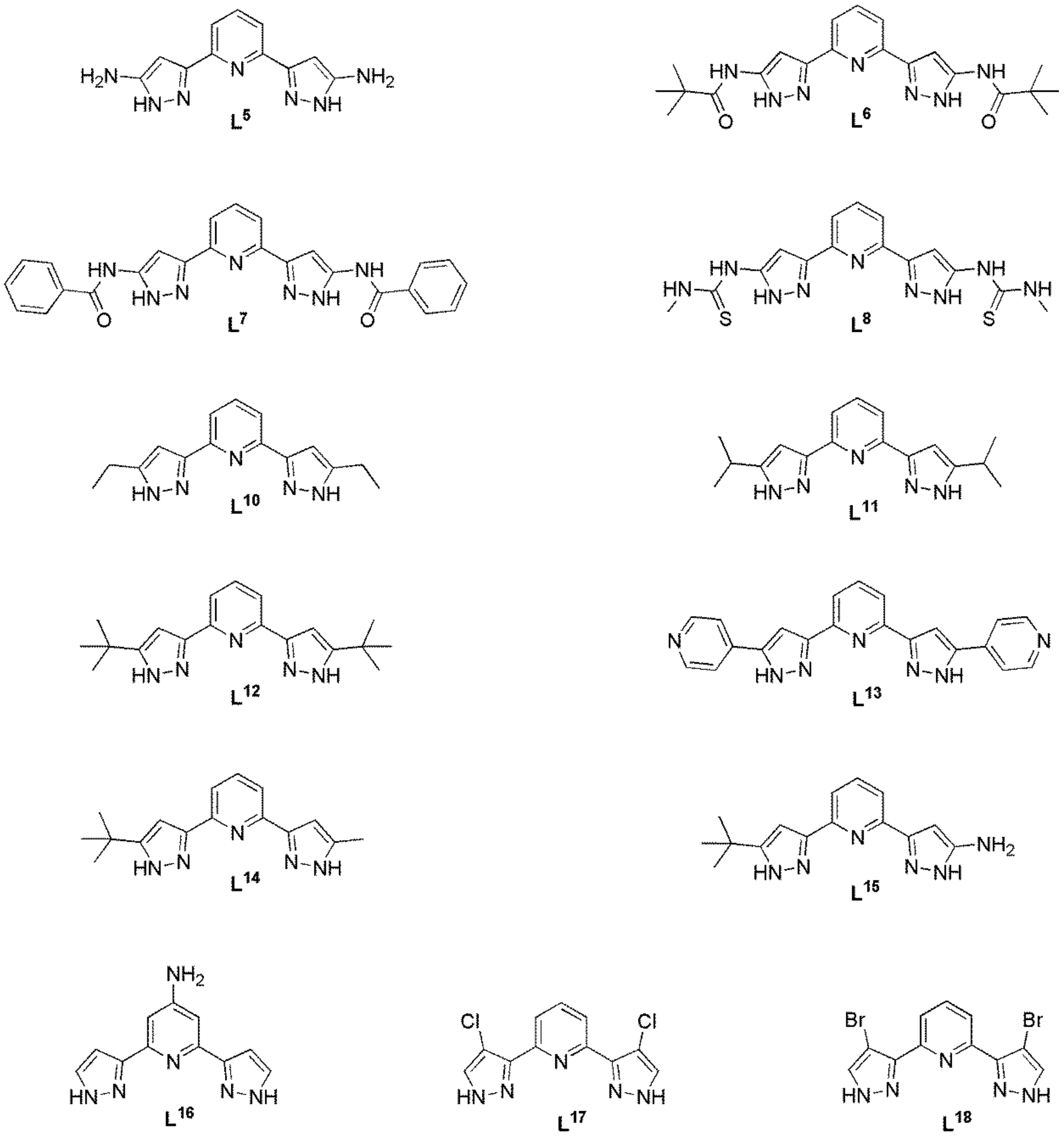

Figure 4.1
The ligands referred to in this chapter and their abbreviations.

4.2. Complexes of 2,6-Di(5-amino-1*H*-pyrazol-3-yl)pyridine ($\mathbf{L^5}$)

2,6-Di(5-amino-1*H*-pyrazol-3-yl)pyridine ($\mathbf{L^5}$) is of interest because the amino groups are strong hydrogen bond donors and acceptors and which increases the chance of a H-bonding network in the lattice of any iron(II) complexes formed. Although there are no SCO complexes of the isostructural 1-bpp isomer of this ligand in the literature, the electronegativity of nitrogen is somewhere in between chlorine and bromine, both of which have been substituted onto the *C*4 position of 1-bpp and their iron(II) complexes characterised.[9, 13] Therefore if only electronic effects were taken into consideration then it is expected that an isostructural iron(II) complex of $\mathbf{L^5}$ would switch somewhere between 202 K and 253 K.

The tetrafluoroborate and perchlorate salts of $[\mathrm{Fe}(\mathbf{L^5})_2]^{2+}$ ($\mathbf{5}^{2+}$) both turned from an orange/brown colour to a dark green over a few days in solution and the solid state, indicating oxidation of the iron(II) complex to iron(III).[14] PXRD of this green species suggest that it is amorphous making it difficult to obtain crystals for x-ray diffraction, however it is reasonable to assume that the ligand has been deprotonated to give an iron(III) species, which isn’t uncommon in metal complexes.[15, 16] Iron(II) complexes of bpp type ligands are usually air stable and it was initially thought that the electron withdrawing nature of the amino groups could be responsible for this behaviour. Cyclic voltammetry was employed to test this theory and the oxidation potentials, $E_{1/2}$, for $\mathbf{5}(\mathrm{ClO_4})_2$, $[\mathrm{Fe}(\mathbf{L^9})2](\mathrm{ClO_4})_2$ ($\mathbf{9}(\mathrm{ClO_4})_2$) and $[\mathrm{Fe(3\text{-}bpp)_2}](\mathrm{ClO_4})_2$ are 0.10 V, 0.36 V and 0.54 V respectively *vs* the ferrocene/ferrocenium couple (Figure 4.2). This shows that the amino groups substantially decrease $E_{1/2}$ of the iron complex, therefore are actually electron donating in this instance, even more so than a methyl group. This is probably due to the lone pair on the nitrogen being delocalised into the pyrazole rings, making them more electron rich and able to donate more electron density to the iron, which in turn makes it more easily oxidised.

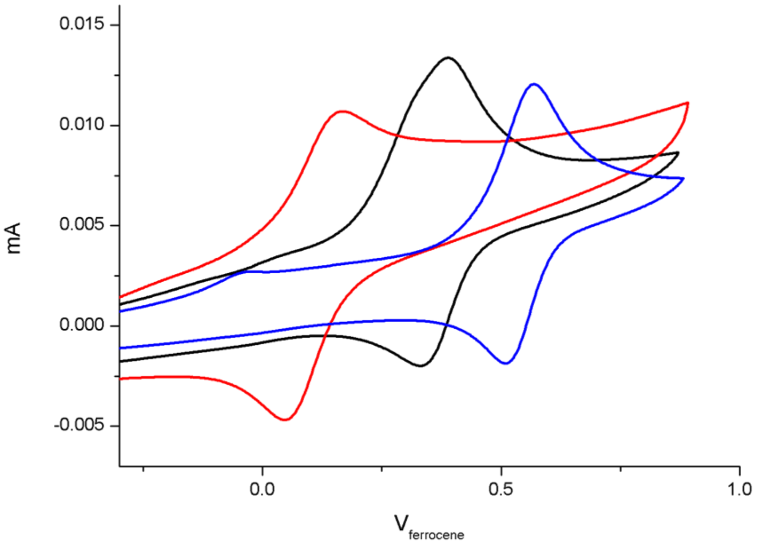

Figure 4.2
Cyclic voltammagrams of $\mathbf{5}(ClO_4)_2$ (red), $\mathbf{9}(ClO_4)_2$ (black) and $[Fe(3\text{-bpp})_2](ClO_4)_2$ (blue) recorded at a scan rate of 100 mVs^{-1} using ferrocene as a reference.

Because of this instability a good microanalysis could only be obtained of the hydrate, $\mathbf{5}(ClO_4)_2{\cdot}H_2O$, however because of its relative stability in air for many of the bulk measurements the nitromethane/diethylether solvate $\mathbf{5}(ClO_4)_2{\cdot}2(C_2H_5)_2O{\cdot}CH_3NO_2$ was used and will be discussed here. The structure of $\mathbf{5}(ClO_4)_2{\cdot}2(C_2H_5)_2O{\cdot}CH_3NO_2$ was found to crystallise in the orthorhombic space group *Pbcn* (a = 14.5138(7); b = 23.2609(11); c = 12.8419(6) Å, $\alpha = \beta = \gamma = 90°$, V = 4335.5(4) Å^3). The asymmetric unit contains half a cation molecule intersected by a crystallographic C_2 axis at the Fe centre, one anion, one diethyl ether and a disordered nitromethane molecule lying on a C_2 axis (Figure 4.3). On one pyrazolyl group the NH, H(10), forms a hydrogen bonding interaction with the diethyl ether oxygen O(27) while one of the amino hydrogens forms an interaction with the perchlorate oxygen O(23). On the other pyrazolyl ring the NH, H(16), forms an interaction with the perchlorate oxygen O(22) while one of the amino hydrogens H(19A) forms interactions with the oxygen O(24), creating a ring of type $R_2^2(8)$.[17] In addition the other amino hydrogen, H(19B) forms a bifurcated hydrogen bond to the O(21) and O(23) oxygen atoms form a symmetry generated perchlorate (Figure 4.4). These extensive hydrogen bonding interactions combine to create creating a network analogous to a fluorite topology, with the complex dications acting as 8 coordinate centres and the perchlorate anions acting as 4 coordinate centres (Figure 4.5).[18]

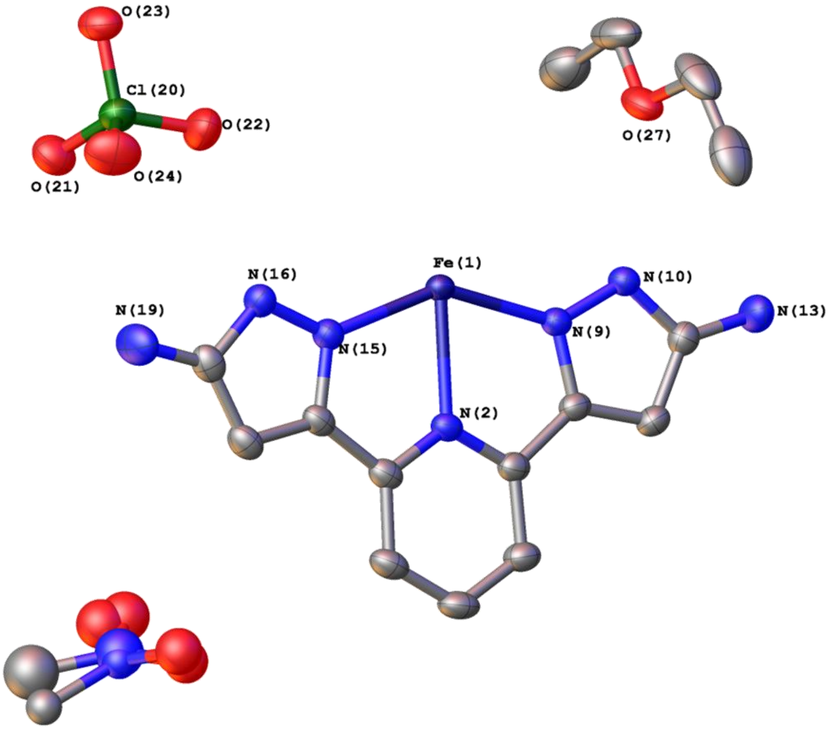

Figure 4.3
The asymmetric unit of **5**$(ClO_4)_2\cdot 2(C_2H_5)_2O\cdot CH_3NO_2$. Thermal ellipsoids have been set at 50% probability and hydrogens have been omitted for clarity.

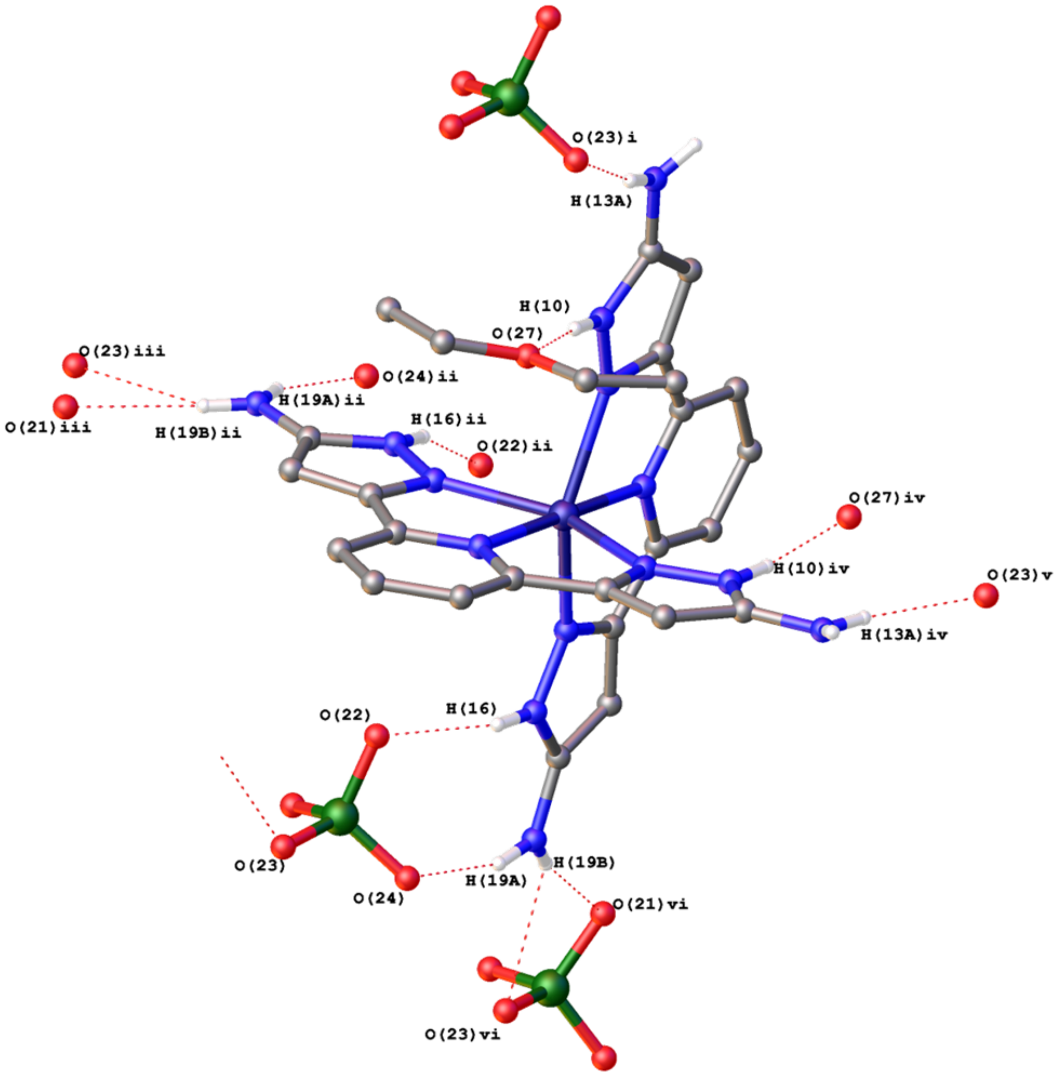

Figure 4.4
Grown structure showing the extent of hydrogen bonding in $\mathbf{5}(ClO_4)_2\cdot 2(C_2H_5)_2O\cdot CH_3NO_2$. The disordered nitromethane and any hydrogens which do not take part in any interactions have been omitted for clarity. Symmetry codes: (i) 1/2+*x*, 3/2-*y*, -*z*; (ii) 1-*x*, +*y*, 1/2-*z*; (iii) 1-*x*, 1-*y*, -*z*; (iv) 1-*x*, +*y*, 1/2-*z*); (v) 1/2-*x*, 3/2-*y*, 1/2+*z*; (vi) +*x*, 1-*y*, 1/2+*z*.

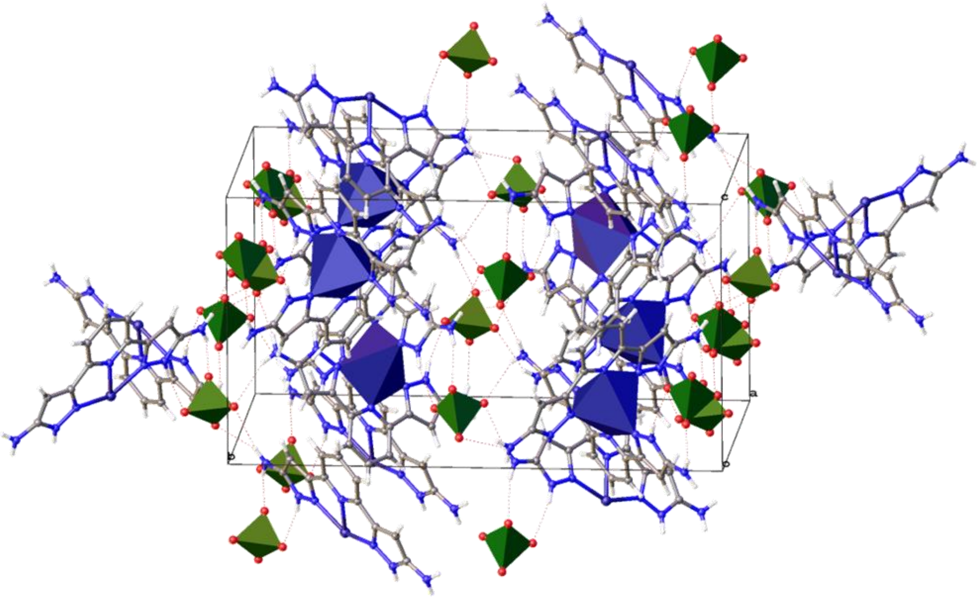

Figure 4.5
View of the topology of **5**$(ClO_4)_2 \cdot 2(C_2H_5)_2O \cdot CH_3NO_2$.

Table 4.2
Values for the hydrogen bonding distances in the structure of **5**$(ClO_4)_2 \cdot 2(C_2H_5)_2O \cdot CH_3NO_2$.

Interaction	Distance (Å)
N(10) – H(10) · · · O(27)	1.932(16)
N(13) – H(13A) · · · O(23)	2.175(17)
N(13) – H(13B) · · · O(21)	2.507(19)
N(16) – H(16) · · · O(22)	2.116(16)
N(19) – H(19A) · · · O(24)	2.190(18)
N(19) – H(19B) · · · O(21)	2.299(18)
N(19) – H(19B) · · · O(23)	2.59(2)

Table 4.3
Selected geometric parameters for **5**$(ClO_4)_2{\cdot}2(C_2H_5)_2O{\cdot}CH_3NO_2$.

	5$(ClO_4)_2{\cdot}2(C_2H_5)_2O{\cdot}CH_3NO_2$
Fe-PyN	2.1567(12)
Fe-PzN	2.1936(12)
α(°)	146.87(5)
θ(°)	87.940(3)
ϕ(°)	177.33(6)
Σ(°)	151.16
Θ(°)	341.38

The hydrogen bond distances in the crystal structure of **5**$(ClO_4)_2{\cdot}2(C_2H_5)_2O{\cdot}CH_3NO_2$ are considerably smaller than the combined Van Der Waals radii of 2.72 Å, indicating that significant hydrogen bonding interactions are occurring (Table 4.2).[19] These hydrogen bonding networks would be expected to infer some cooperativity between molecules in the lattice and thus lead to an abrupt spin transition.

Furthermore, by examination of the Fe–N bond lengths it can be deduced that this complex is in the HS state at 150 K, as shorter bond lengths would be expected for a LS complex. This is also supported by the rhombic and trigonal distortion parameters which show the kind of deviation from octahedral geometry that would be expected of a HS complex (Table 4.3).[20, 21] The origin of these distortion parameters are discussed in Chapter 1. The *trans* angle, ϕ, is only slightly lower than the octahedral ideal of 180° and the plane angle, θ, between the two ligand planes is also fairly close to the octahedral ideal of 90°. Therefore it is unlikely that this complex will be trapped in the HS state due to these Jahn-Teller distortions. It is however unlikely that a sample of **5**$(ClO_4)_2{\cdot}2(C_2H_5)_2O{\cdot}CH_3NO_2$ as this particular polymorph will undergo a spin transition above this temperature.

A bulk sample on which to perform magnetic measurements was made by grinding orange crystals obtained by the same vapour diffusion method and this was used to obtain magnetic susceptibility measurements in the solid state using a SQUID magnetometer (Figure 4.6) as well as in solution using the Evans NMR method (Figure 4.7). With the tendency of this complex to form the green iron(III) complex over a few hours, these measurements were taken as quickly as possible on a freshly prepared sample. The SQUID data show a small transition centred around 170 K with a 10 K wide hysteresis which looks to be two magnetic profiles superimposed on top of one another, one of which is a very gradual ST and the other is abrupt and hysteretic. The value of χ_MT reaches a maximum value of 3.1 cm^{3}mol^{-1}K which is slightly lower than that expected for a fully HS iron(II) complex and so the gradually transitioning phase is probably not fully HS at 300 K. This is also supported by the powder pattern of a freshly prepared sample; while most of the peaks are obscured by a large background caused by amorphous material some of the more intense peaks can be seen and match up well with that calculated from the crystal structure (Figure 4.8). Importantly the sample used for the PXRD was obtained via the same crystallisation method as was used to obtain the single crystals so as to give comparable results.

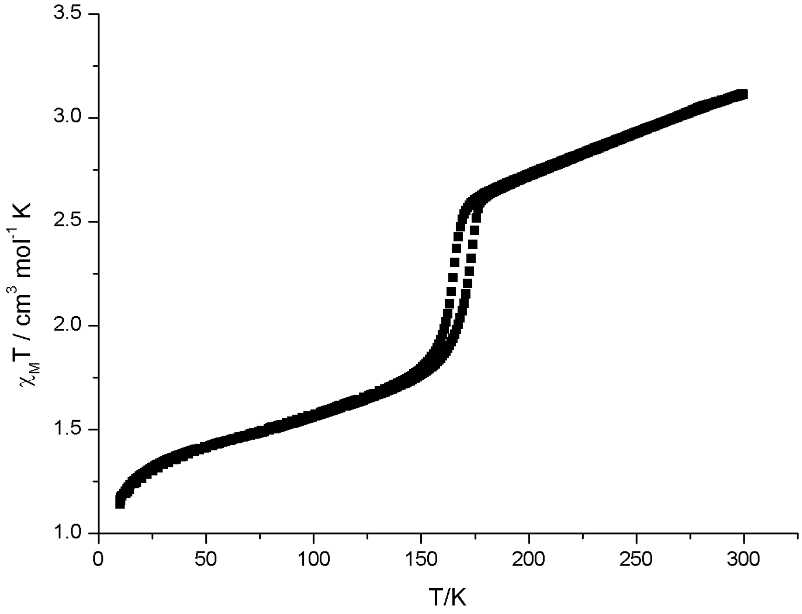

Figure 4.6
χ_MT *vs* T data of $(ClO_4)_2 \cdot 2(C_2H_5)_2O \cdot CH_3NO_2$ collected at a scan rate of 2 K min^{-1} in sweep mode.

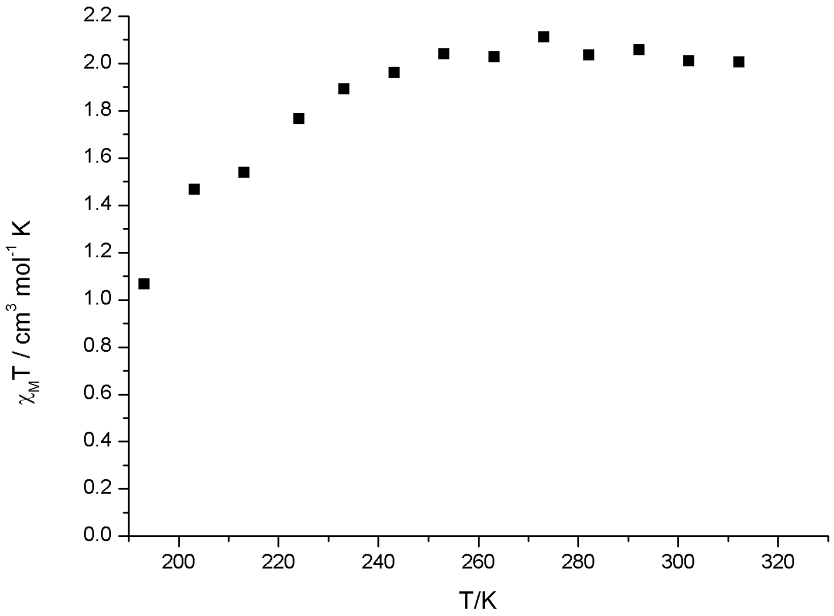

Figure 4.7
χ_MT *vs* T data for **5**$(ClO_4)_2$ in $(CD_3)_2CO$ solution.

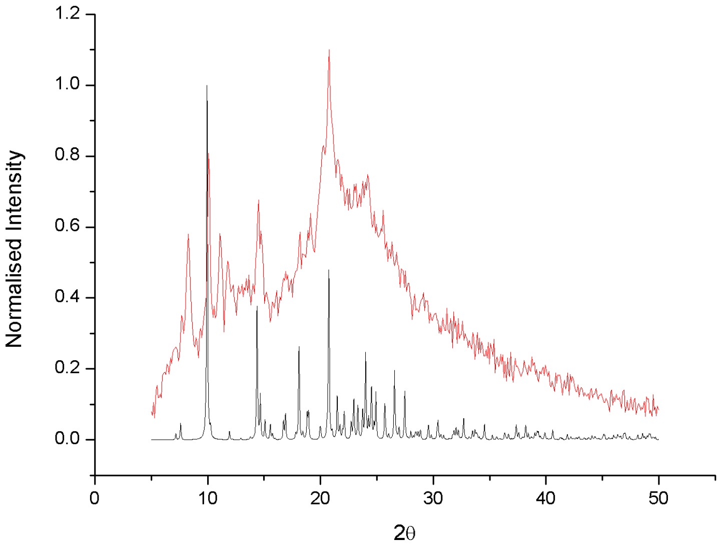

Figure 4.8
PXRD data for a freshly prepared sample of $(ClO_4)_2 \cdot 2(C_2H_5)_2O \cdot CH_3NO_2$ (red)compared with that calculated from the crystal structure (black).

The Evans data show that the magnetic susceptibility of this complex in acetone solution begins to drop below around 250 K, higher than in the powdered sample. Because the data are incomplete due to the freezing point of the solvent it is difficult to determine an exact value for the transition temperature, $T_{1/2}$, however a rough estimate would be at approximately 190 K. Although there aren't the close contacts and lattice effects that are present in the solid state, hydrogen bonding interactions with the solvent in solution can still affect the spin transition.[22] This particular complex may be even more susceptible to these kinds of interactions because of the four amines acting as additional hydrogen bond donors and acceptors. The degree of hydrogen bonding at these groups will affect the electron density at the coordinating nitrogens and so alter the ligand field. It was therefore expected that repeating the same experiment in D_2O would give a lower $T_{1/2}$ as it would stabilise the LS state. This was not possible however because of the instability of the complex in water which didn't allow enough time to collect the data. In addition the insolubility of the complex in other common NMR solvents meant that the predicted effect of the hydrogen bonding capabilities of the solvent on $T_{1/2}$ could not be confirmed.

4.3. Complexes of 5-Amidopyrazole Ligands 2,6-Di(5-*tert*butylamido-1*H*-pyrazol-3-yl)pyridine ($\mathbf{L}^{6}$) and 2,6-Di(5-benzylamido-1*H*-pyrazol-3-yl)pyridine ($\mathbf{L}^{7}$)

From $\mathbf{L}^{5}$ the two ligands 2,6-di(5-*tert*butylamido-1*H*-pyrazol-3-yl)pyridine ($\mathbf{L}^{6}$) and 2,6-di(5-benzylamido-1*H*-pyrazol-3-yl)pyridine ($\mathbf{L}^{7}$) were synthesised and a number of different salts of their iron(II) complexes were made. In addition attempts were made at making iron(II) complexes using 2,6-di(5-{methylthiourea}-1*H*-pyrazol-3-yl)pyridine ($\mathbf{L}^{8}$), however these proved to be insoluble in most common solvents which limited their characterisation.

After numerous crystallisation attempts the only complexes for which suitable crystals for x-ray diffraction were obtained were for $[Fe(\mathbf{L}^{6})_2](BF_4)_2$ (**6**$(BF_4)_2$) and $[Fe(\mathbf{L}^{6})_2](ClO_4)_2$ (**6**$(ClO_4)_2$), which were isostructural acetonitrile solvates formed via slow vapour diffusion of diisopropyl ether into an acetonitrile solution. These two structures were both solved in the triclinic space group P-1 (a = 12.8890(4); b = 13.3521(4); c = 19.1548(6) Å, α = 104.759(2)°, β = 100.581(2)°, γ = 108.536(2)°, V = 2893.71(17) $Å^3$ for **6**$(BF_4)_2{\cdot}3CH_3CN$). The only major difference between the two was the higher degree of disorder in the *tert*butyl groups in the structure of **6**$(ClO_4)_2{\cdot}3CH_3CN$. The asymmetric unit contains one complete formula unit and three acetonitrile molecules, two of which form hydrogen bonding interactions with a pyrazolyl 1 H(6) and H(9) (Figure 4.9). Three of the amido groups are in an *anti* conformation with respect to the corresponding pyrazole NH which can then form an intramolecular hydrogen bonding interaction of the type $S_1^1(6)$. In two of these groups the pyrazolyl NH forms an interaction with an acetonitrile molecule, while the amido NH forms an interaction with an anion. The remaining amido group is *syn* to its corresponding pyrazolyl NH with both the pyrazolyl NH, H(13), and the amido NH, H(14), forming interactions with two separate fluorine atoms on the same BF_4^- anion (Figure 4.10, Table 4.4). This hydrogen bonding network extends in one dimension along the crystallographic *a* axis in a ladder type topology (Figure 4.11). These hydrogen bonding motifs are also seen in the structure of the perchlorate salt (Table 4.5)

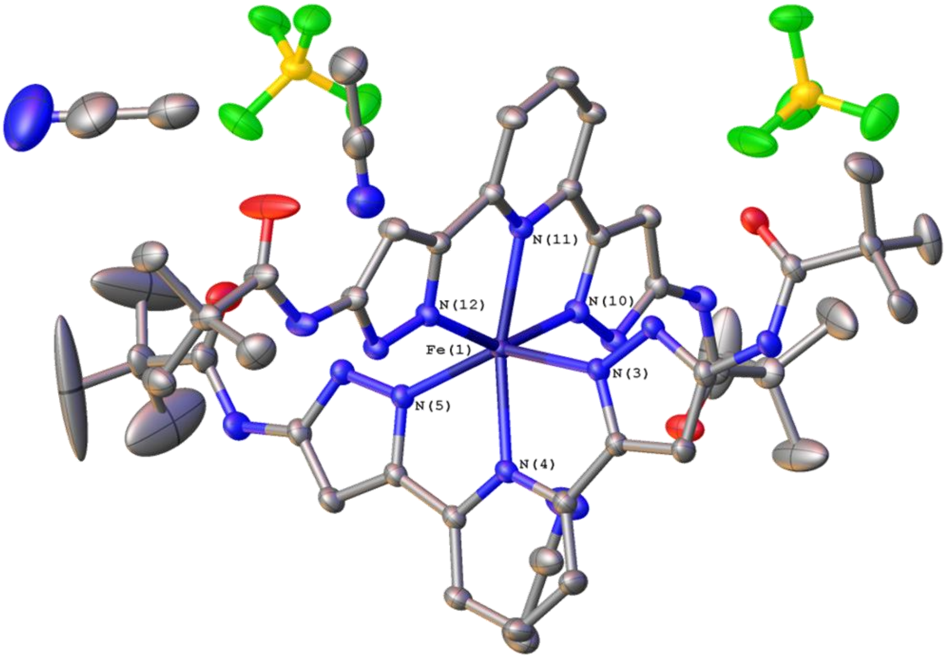

Figure 4.9
Asymmetric unit of **6**$(BF_4)_2 \cdot 3CH_3CN$. Thermal ellipsoids are set at 50% probability and hydrogens have been omitted for clarity.

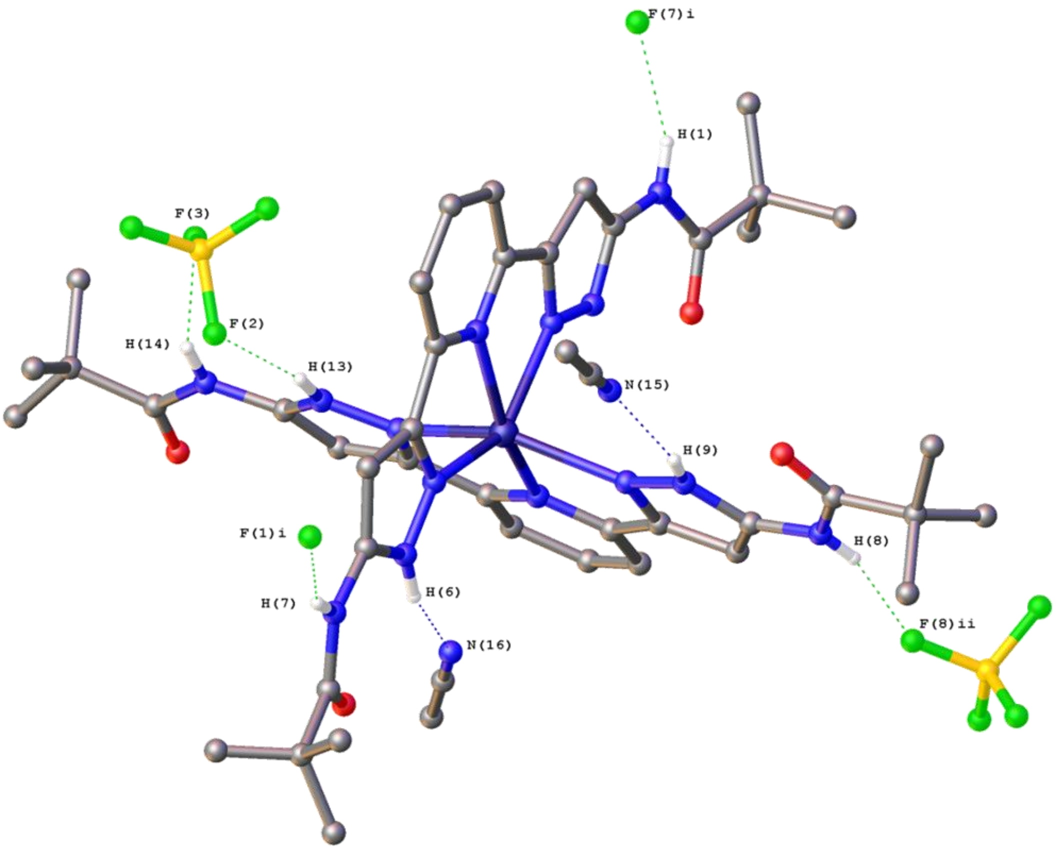

Figure 4.10
View of the hydrogen bonding interactions in the asymmetric unit of **6**$(BF_4)_2 \cdot 3CH_3CN$. Any fragments and hydrogens not participating in interactions have been omitted. Symmetry codes: (i) –*x*, 1-*y*, 1-*z*; (ii) 1-*x*, 1-*y*, 1-*z*.

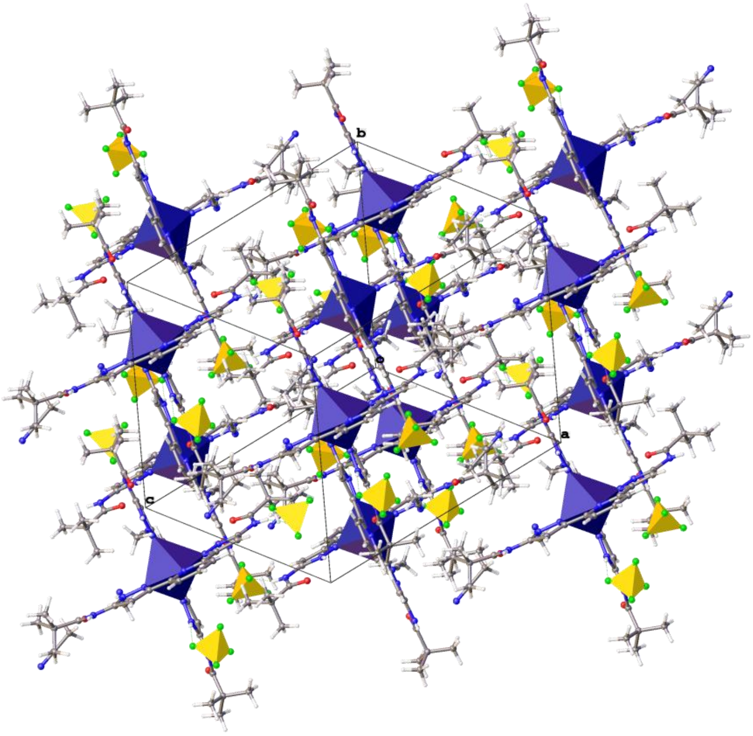

Figure 4.11
Packing diagram of **6**$(BF_4)_2{\cdot}3CH_3CN$ showing Fe octahedral and BF_4^- tetrahedra.

Table 4.4
Distances for hydrogen bonding interactions in **6**$(BF_4)_2{\cdot}3CH_3CN$.

Interaction	**Distance (Å)**
N(6)-H(6)···O(1)	2.6893(19)
N(6)-H(6)···N(16)	2.994(3)
N(7)-H(7)···F(1)	2.927(2)
N(1)-H(1)···F(7)	2.9196(19)
N(14)-H(14)···F(3)	2.9027(19)
N(13)-H(13)···F(2)	2.8094(19)
N(9)-H(9)···N(15)	2.926(2)

Table 4.5
Distances for hydrogen bonding interactions in **6**$(ClO_4)_2$·$3CH_3CN$.

Interaction	**Distance (Å)**
N(6)-H(6)···O(1)	2.712(3)
N(6)-H(6)···N(16)	3.002(4)
N(8)-H(8)···O(5)	2.998(3)
N(9)-H(9)···O(6)	2.882(3)
N(13)-H(13)···N(15)	2.939(4)
N(14)-H(14)···O(10)	2.958(4)

Table 4.6
Selected geometric parameters for **6**$(BF_4)_2$·$3CH_3CN$ and **6**$(ClO_4)_2$·$3CH_3CN$.

	6$(BF_4)_2$·$3CH_3CN$	**6**$(ClO_4)_2$·$3CH_3CN$
Fe-PyN (Å)	2.1447(13)	2.134(2)
Fe-PzN (Å)	2.1970(13)	2.1952(15)
α(°)	147.32(5)	148.23(8)
θ(°)	89.607(13)	90.87(2)
ϕ(°)	158.29(5)	158.91(7)
Σ(°)	152.72	151.35
Θ(°)	355.02	354.24

From these data, particularly the Fe–N bond distances and distortion parameters of the iron centre, it can be inferred that both salts of this complex are fully HS at 173 K (Table 4.6). This conclusion is supported by the variable temperature magnetic susceptibility measurements which show values of $\chi_M T$ of around 3.5-4.0 $cm^3 mol^{-1} K$ between 10-300 K (Figure 4.12). The reason for this is believed to be due to the large distortion in the *trans* angle, ϕ, which would require a large reorganisation of the lattice in order to revert to the more perfectly octahedral LS state (Figure 4.13, Table 4.6).[23] In this case it seems that the energy barrier to reorganisation of the lattice is too high and so the complex remains kinetically trapped in its HS state at low temperatures.

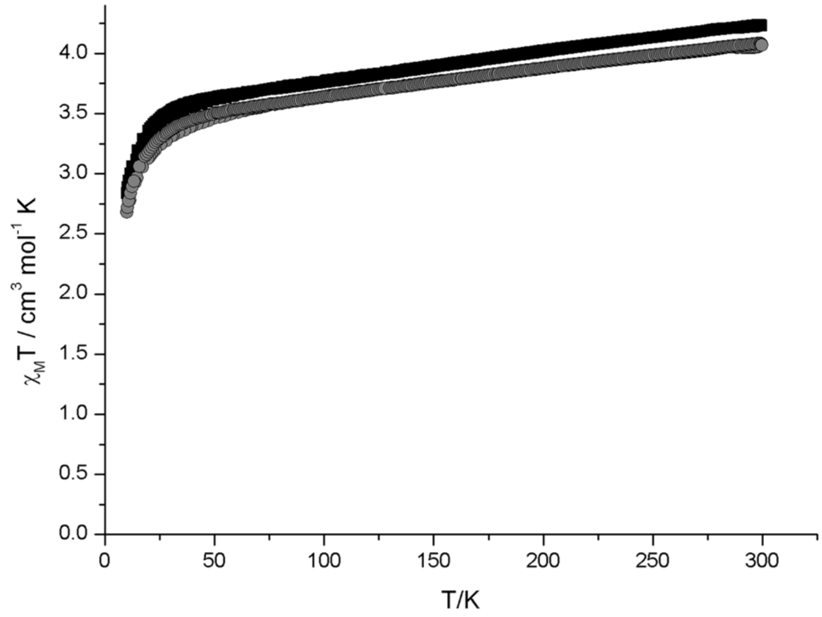

Figure 4.12
$\chi_M T$ *vs* T data for **6**$(BF_4)_2 \cdot 3CH_3CN$ (■) and **6**$(ClO_4)_2 \cdot 3CH_3CN$ (●). Collected at a scan rate of 2 K min^{-1} in sweep mode.

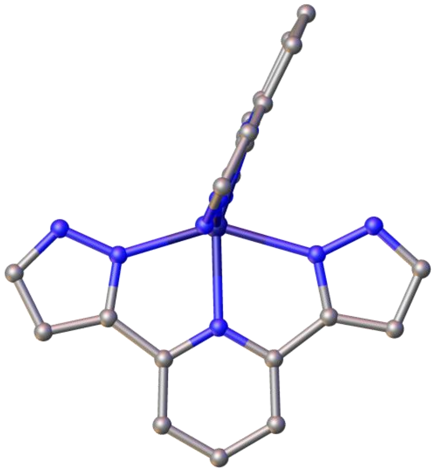

Figure 4.13
The coordination sphere of the iron centre in **6**$(BF_4)_2 \cdot 3CH_3CN$ showing the large distortion in the *trans* angle, ϕ.

The PXRD data for both **6**$(BF_4)_2$ and **6**$(ClO_4)_2$ show substantial differences from the powder patterns calculated from the crystal structures, which could be due to a loss of acetonitrile from the lattice facilitated by the elevated operating temperature of the diffractometer, which can be around 50º C (Figure 4.14, Figure 4.15). Microanalysis approximates both of these complexes as the hydrates, which also suggests that over time acetonitrile could be lost and replaced by atmospheric water. Although the powder patterns are different from their calculated patterns the unsolvated phases of the tetrafluoroborate and perchlorate salts still seem to remain isostructural to one another.

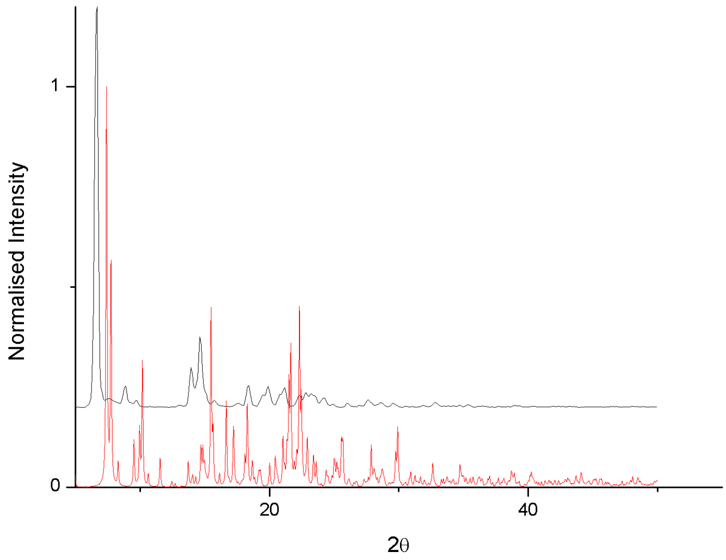

Figure 4.14
PXRD data for a sample of **6**$(BF_4)_2 \cdot H_2O$ (black) compared with the powder pattern calculated from the crystal structure (red).

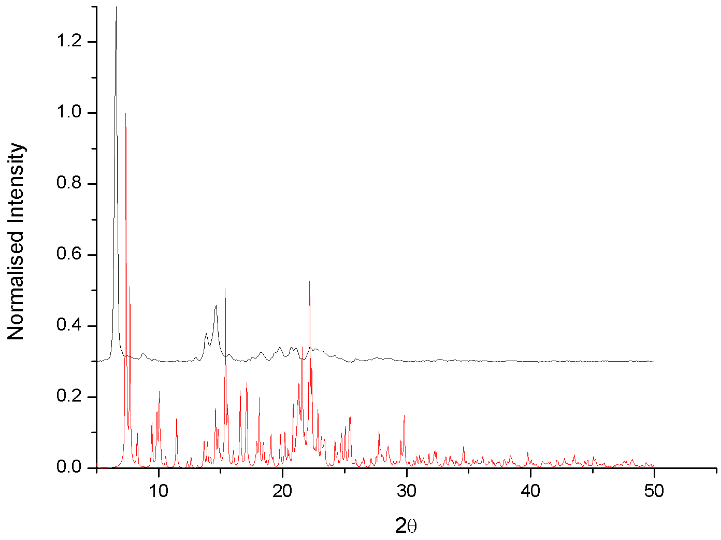

Figure 4.15
PXRD data for **6**(ClO$_4$)$_2$·2H$_2$O (black) compared with the powder patter calculated from the crystal structure (red).

As with complexes of **L**^{5} it was of interest to study the spin states of **6**(BF$_4$)$_2$ in solution via NMR, as there are a number of hydrogen bond donors and acceptors which could interact with the solvent. In the case of **6**(BF$_4$)$_2$ the *tert*butyl groups increase the solubility of the complex in organic solvents. This allows the complex to be studied in a wider range of NMR solvents in order to determine the effects of solvent polarity (E$_N$), donor number (DN), solvent basicity (SB) and hydrogen bond acceptor basicity (β).[24-27] The parameters E$_N$, DN, SB and β are described in Chapter 1. A shift of the NMR signal of a proton capable of forming hydrogen bonds could indicate the extent of these interactions in a given solvent and also indicate a change in the ligand field exerted on the metal.

Table 4.7
Correlation of the hydrogen environments of **6**(ClO$_4$)$_2$ in different NMR solvents. All NMR spectra were recorded at 500 MHz and all shifts quoted in units of ppm.

Solvent	**E$_N$**	**DN**	**SB**	**β**	**δ H$_a$**	**δ H$_b$**	**δ H$_c$**	**δ NH$_d$**	**δ NH$_e$**
Methanol *d* 4	0.7620	19.1	0.545	0.62	21.93	54.71	57.75	-	-
Ethanol *d* 6	0.6540	32.0	0.658	0.77	22.23	54.84	57.8	-	-
Nitromethane *d* 3	0.4810	2.7	0.236	0.06	24.62	55.17	61.03	29.72	15.11
N,N-Dimethylformamide *d* 7	0.3860	26.6	0.613	0.69	23.61	54.55	59.19	34.5	15.23
Acetonitrile *d* 3	0.4600	14.1	0.286	0.31	22.64	54.57	58.88	34.48	15.66
Acetone *d* 6	0.3550	17.0	0.475	0.48	24.23	54.96	60.29	31.5	15.23

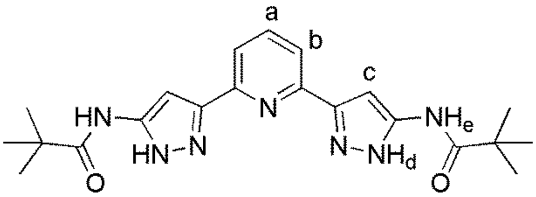

Figure 4.16
Assignment of the hydrogen environments referred to in Table 4.7.

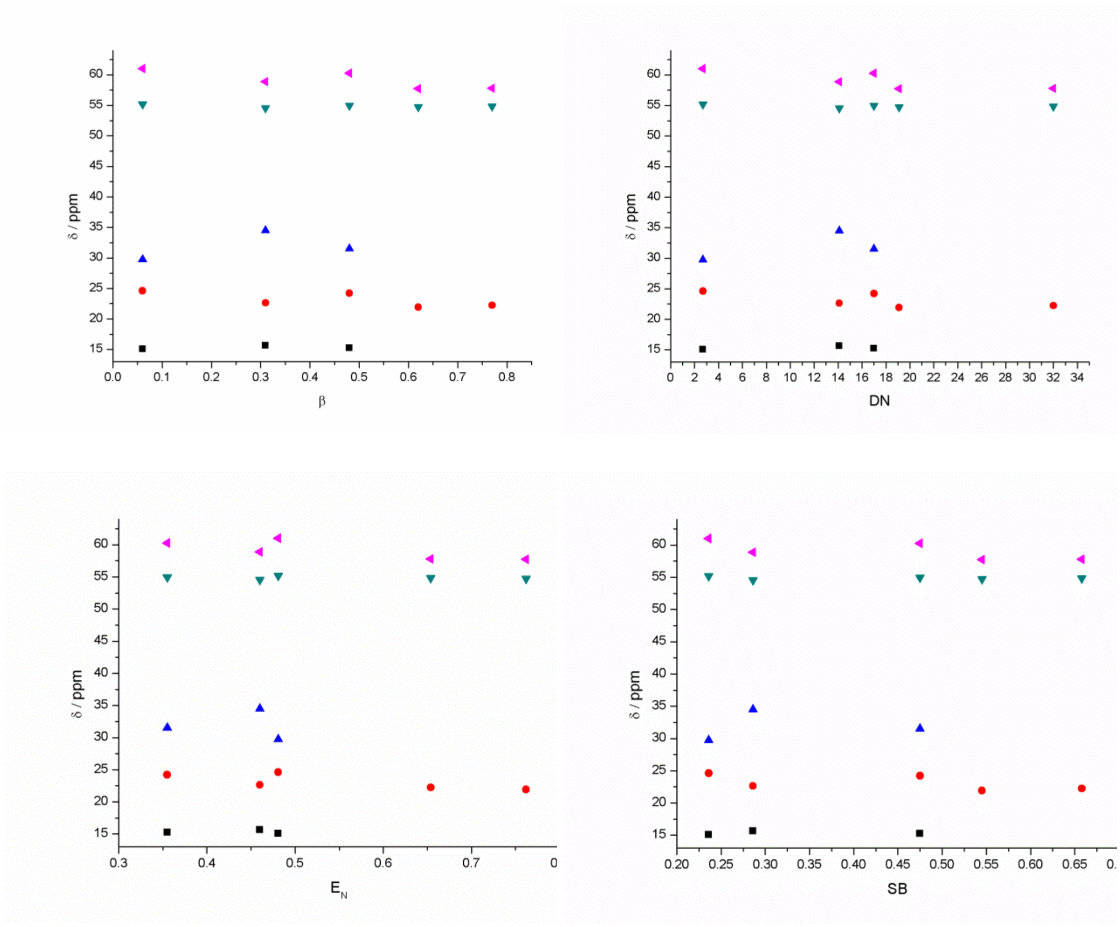

Figure 4.17
^{1}H NMR shifts plotted against the different solvent parameters showing H_a (●), H_b (▲), H_c (▲), NH_d (▲) and NH_e (■).

Although there is little variation in the organic solvents, it could be argued that H_a and H_c decrease most linearly with the β and DN parameter, both of which are measures of hydrogen bonding capabilities, and H_b shows little variation at all. However since the variation of this data is slight and a limited number of solvents were used these patterns could be speculative. The NH groups were not observed in the more protic solvents due to deuterium exchange and although there is significant variation it is difficult to attribute this to a solvent property with this data (Figure 4.17, Table 4.7).

It would have been interesting to compare these results to those obtained from D_2O, as this is one of the most strongly hydrogen bonding solvents. However this complex is not soluble in neat D_2O and so D_2O/CD_3CN mixtures were used and the peak shifts recorded for increasing D_2O fractions (Figure 4.18).

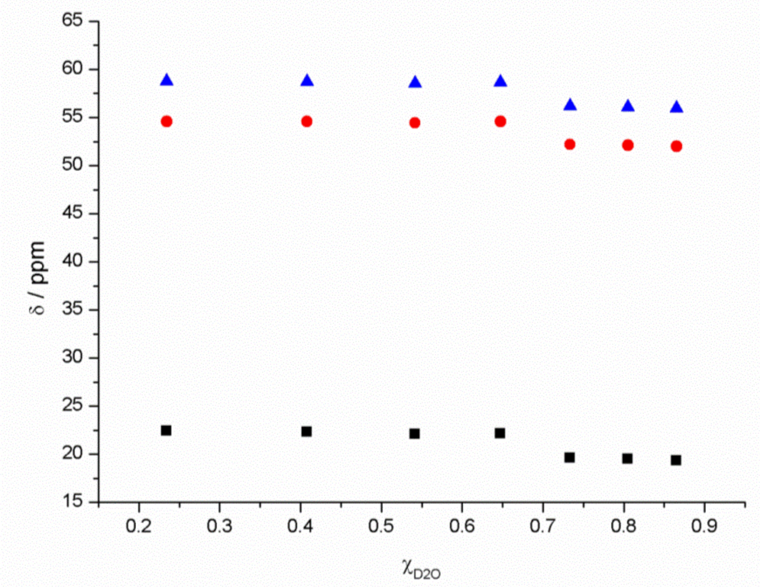

Figure 4.18
Graph showing how the H_a (■), H_b (●) and H_c (▲) chemical shifts change with increasing mole fraction of D_2O.

The system shows a clear shifting upfield at higher mole fractions of D_2O, however it is not clear which, if not both NH groups are responsible for this as their signals are lost due to deuterium exchange. This shifting is due to additional electron density being introduced from the lone pairs on water during a hydrogen bonding interaction. This shields the protons from the applied magnetic field, causing them to shift upfield in the spectrum. This measureable change in electron density at the ligand will affect the ligand field around the iron centre and in turn Δ_{oct}, which ultimately affects spin crossover. It is interesting how the system shows little variation up to about $\chi_{D2O} = 0.65$, after which there is an abrupt drop of around 1.3 ppm in all peaks.

The Evans NMR method was employed to determine whether or not SCO occurred in $(CD_3)_2CO$ solution of this complex, however the results showed abnormally low values for the $\chi_M T$. This could potentially be due to the complex dissociating in solution, reducing the effective concentration as this has happened with similar complexes previously made by the group. Another factor which will have affected the results is precipitation at lower temperatures which will also lower the effective concentration of the sample. A remedy for this would be to use lower concentrations of the sample, however this would also reduce the visibility of the peaks in the spectrum.

4.4. Complexes of 5-Alkylpyrazole Ligands

Using methods previously described the ligands 2,6-di(5-ethyl-1*H*-pyrazol-3-yl)pyridine (**L**^{10}), 2,6-di(5-isoprop-1*H*-pyrazol-3-yl)pyridine (**L**^{11}), 2,6-di(5-*tert*but-1*H*-pyrazol-3-yl)pyridine (**L**^{12}) and 2,6-di(5-[4-pyridyl]-1*H*-pyrazol-3-yl)pyridine (**L**^{13}) were synthesised and their subsequent iron(II)complexes were made. Numerous crystallisation attempts on different salts of these complexes yielded crystals of [Fe(**L**^{10})$_2$](ClO$_4$)$_2$ (**10**(ClO$_4$)$_2$), [Fe(**L**^{11})$_2$](BF$_4$)$_2$ (**11**(BF$_4$)$_2$) and [Fe(**L**^{12})$_2$](BF$_4$)$_2$ (**12**(BF$_4$)$_2$). However, the only case where sufficient data to elucidate a full structure were obtained was that of **12**(BF$_4$)$_2$. It was not possible to grow any sort of crystals for x-ray diffraction of the complex **11**(BF$_4$)$_2$ and so structural characterisation of this complex is limited to bulk techniques.

4.4.1. [Fe(L^{10})$_2$](ClO$_4$)$_2$·2H$_2$O (10(ClO$_4$)$_2$·2H$_2$O)

10(ClO$_4$)$_2$ was determined as the dihydrate via microanalysis and yielded large red block like crystals from diffusion of diisopropyl ether into nitromethane solutions. These crystals produced good diffraction at low angles which diminished at higher angles, and so data were collected at 100 K using the more intense diamond light source with the hope of collecting sufficient data to obtain a structure. However it proved difficult to find the unit cell using the data, which suggests that these crystals could be twinned and thus difficult to solve. The best solution came from the cubic space group *Fm*-3*c* ($a = b = c$ = 46.6618(5) Å, $\alpha = \beta = \gamma$ = 90°, V = 101598.1(18) Å^3). While a solution for the ligand complex cation structure can be resolved it is not chemically plausible and there are a number of large q-peaks which cannot be reasonably assigned. A powder pattern obtained also showed that the bulk sample of this complex was completely amorphous and no peaks could be unambiguously resolved.

Despite this lack of structural data variable temperature magnetic susceptibility measurements of this sample from 4-350 K were recorded (Figure 4.19). These data show that the $\chi_M T$ gradually increases from around 2.7-3.0 cm^{3}mol^{-1}K which indicated that not all of the iron centres are in the HS state, however if the temperature were increased further it is possible this could be achieved. As the temperature is decreased $\chi_M T$ again decreases gradually but remains slightly higher than the initial warming cycle. This anomaly could be due to a loss of solvent at elevated temperatures which could accompany a phase change as is quite common in complexes of this type.[6] The $\chi_M T$ of the sample then continues to decrease gradually until the gradient changes at around 140 K, where it almost seems to plateau before the zero point splitting effect causes an abrupt drop at around 20 K. Just above 20 K, $\chi_M T$ has a value of approximately 1.5 cm^{3}mol^{-1}K indicating that around 40% of the iron centres remain HS, which could be due to a HS phase impurity being present. The warming profile back to 300 K is identical to the cooling so there is no evidence of highly cooperative effects causing hysteresis in this complex. The linear shape of this $\chi_M T$ *vs* T curve is also quite unusual in SCO complexes, which often show a more sigmoidal curve.

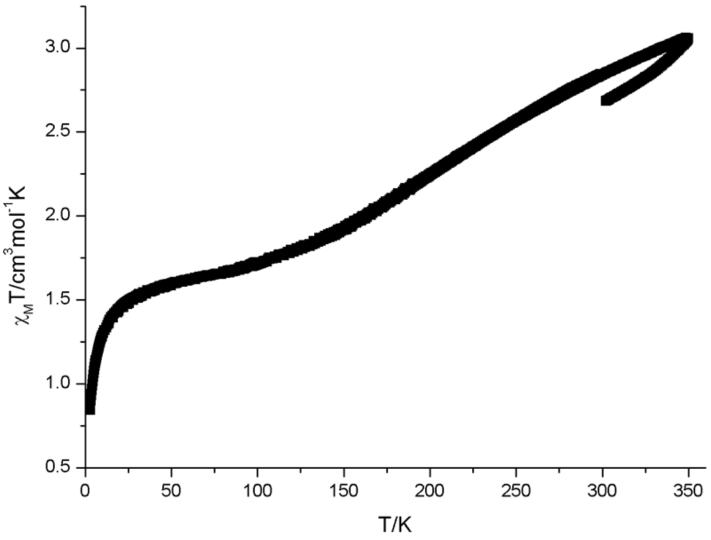

Figure 4.19
$\chi_M T$ *vs* T data for **10**$(ClO_4)_2 \cdot 2H_2O$. Collected at a scan rate of 2 K min^{-1} in sweep mode.

4.4.2. $[Fe(L^{12})_2](BF_4)_2 \cdot 1.5CF_3CH_2OH \cdot 0.7(C_2H_5)_2O$ $(\mathbf{12}(BF_4)_2 \cdot 1.5CF_3CH_2OH \cdot 0.7(C_2H_5)_2O)$

12$(BF_4)_2$ yielded small yellow crystals via slow vapour diffusion of diethyl ether into a trifluoroethanol solution and was found to crystallise in the orthorhombic space group $P2_12_12_1$ (a = 17.588(2); b = 19.509(2); c = 32.399(5) Å, $\alpha = \beta = \gamma$ = 90º, V = 11117(2) Å^3). The asymmetric unit contains two formula units in addition to three positions containing partially occupied trifluoroethanol and one partially occupied and disordered diethyl ether position giving the formula of roughly **12**$(BF_4)_2 \cdot 1.5CF_3CH_2OH \cdot 0.7(C_2H_5)_2O$ (Figure 4.20).

The microanalysis approximates as approximately the mono-trifluoroethanol solvate, indicating that the volatile diethyl ether has been lost. The two dication molecules are quite similar and both show large distortion in the angle between the two ligand planes, θ, and some of the ligand planes themselves deviate significantly from planarity (Figure 4.21). This distortion is more pronounced in molecule A and could be a result of some close intermolecular interactions within the crystal lattice. Each pyrazolyl NH group donates a hydrogen bond to the fluorine of a BF_4^- anion which in turn accepts a hydrogen bond from one other pyrazolyl NH group on another cation (Figure 4.20, Table 4.8). On each dication two of these linkages are to crystallographically inequivalent dications (i.e. A···B) and these connections form four-fold helices in the direction of the crystallographic *c* axis, while the other two linkages are to equivalent dications (i.e. A···A, B···B) which link the helices together in an interpenetrating manner.

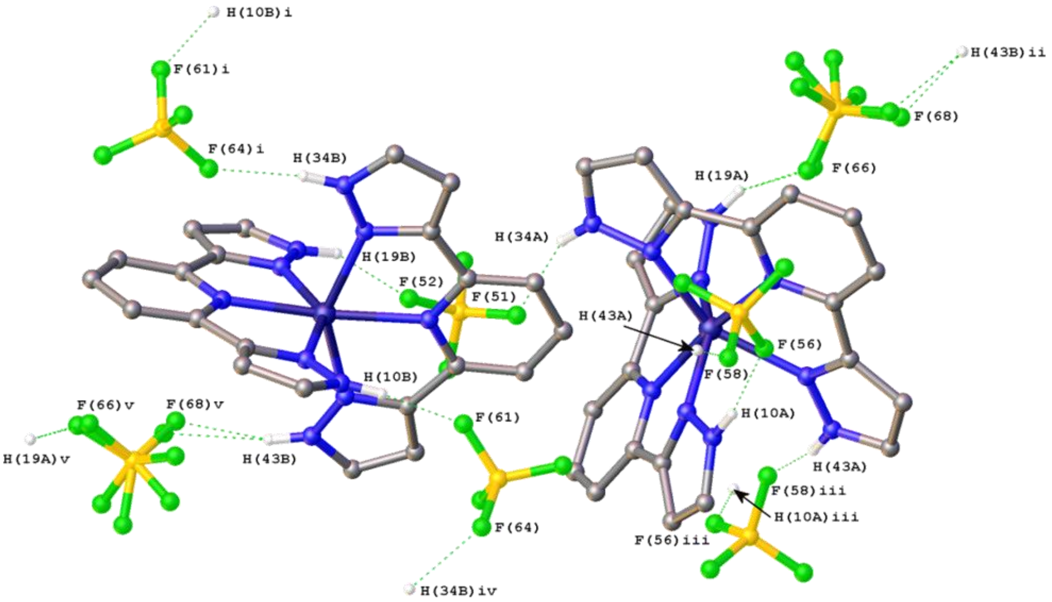

Figure 4.20
Crystal structure of **12**$(BF_4)_2 \cdot 1.5CF_3CH_2OH \cdot 0.7(C_2H_5)_2O$ showing the hydrogen bond connections between adjacent molecules. Hydrogens not participating in interactions, solvent molecules and the *tert*butyl groups have all been omitted for clarity. Symmetry codes: (i) -1/2+*x*, 1/2+*y*, -*z*; (ii) 1/2-*x*, 1-*y*, 1/2+*z*; (iii) 1-*x*, 1/2+*y*, 1/2-*z*; (iv) 1/2+*x*, 1/2-*y*, -*z*; (v) 1/2-*x*, 1-*y*, -1/2+*z*.

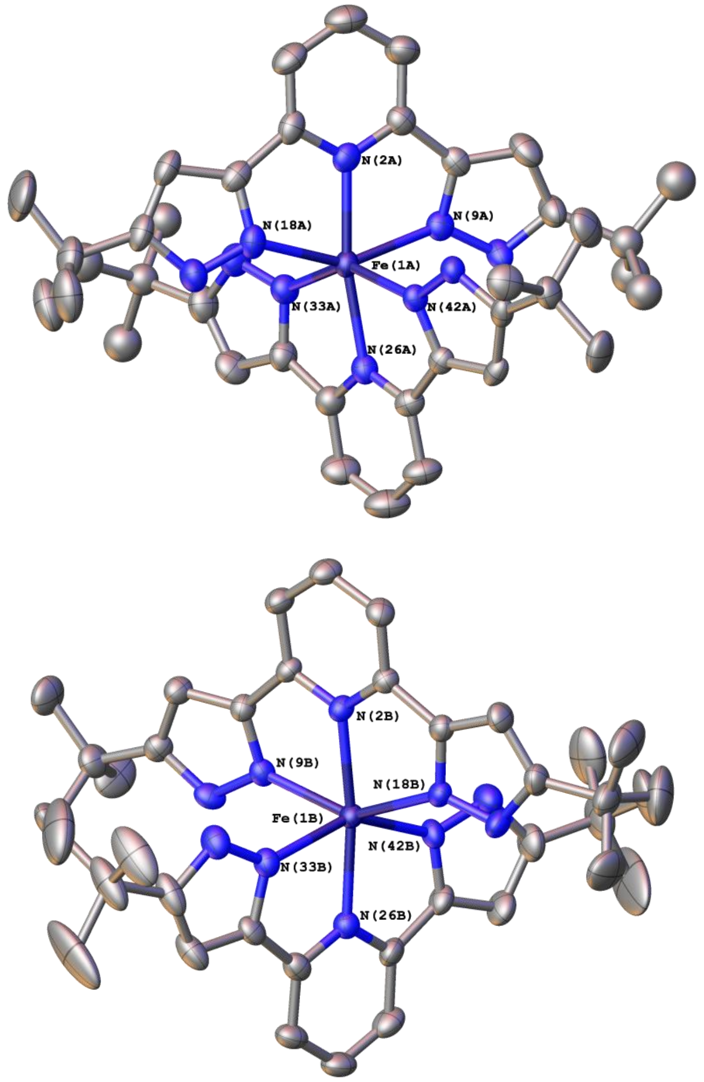

Figure 4.21
View of each unique cation A (top)and B (bottom) of **12**$(BF_4)_2$·1.5CF_3CH_2OH·0.7$(C_2H_5)_2O$. Thermal ellipsoids are set at 50% probability, disordered *tert*butyl groups are shown only in one position and hydrogens have been omitted for clarity.

Table 4.8
Distances for hydrogen bonding interactions in **12**$(BF_4)_2 \cdot 1.5CF_3CH_2OH \cdot 0.7(C_2H_5)_2O$.

Interaction	Distance (Å)
N(10A)-H(10A)···F(56)	2.886(5)
N(19A)-H(19A)···F(66)	2.728(16)
N(34A)-H(34A)···F(51)	2.846(6)
N(43A)-H(43A)···F(58)	2.787(5)
N(10B)-H(10B)···F(61)	2.799(5)
N(19B)-H(19B)···F(52)	2.769(6)
N(34B)-H(34B)···F(64)	2.827(5)
N(43B)-H(43B)···F(68)	2.829(8)

Table 4.9
Selected geometric parameters for the iron centres in **12**$(BF_4)_2 \cdot 1.5CF_3CH_2OH \cdot 0.7(C_2H_5)_2O$.

	Fe(1A)	Fe(1B)
Fe-PyN (Å)	2.138(4)	2.168(3)
Fe-PzN (Å)	2.205(4)	2.246(3)
α(°)	148.40(14)	146.98(14)
θ(°)	68.01(4)	71.70(3)
ϕ(°)	170.30(13)	171.82(13)
Σ(°)	158.53	172.29
Θ(°)	342.80	340.9

It can be seen from the geometric parameters that both these iron centres are fully HS at 150 K, and this probably reflects the large distortion and steric constraints of the crystal lattice preventing access to the LS state in a similar manner to that seen in **6**$(BF_4)_2$ and **6**$(ClO_4)_2$ (Table 4.9). Contrasting to this a powdered sample was seen to undergo a very gradual transition from 5-100 K, however the values of $\chi_M T$ were abnormally high and PXRD showed that the powdered phase was not the same phase as the single crystal (Figure 4.22, Figure 4.23). The difference in phase is probably due to loss of solvent in the powdered sample as the diethyl ether will be readily lost from the sample due to its high vapour pressure, especially at the elevated operating temperature of the diffractometer. This curve also has a very linear shape similar to that observed for **11**$(BF_4)_2$ which again is unusual for a SCO complex.

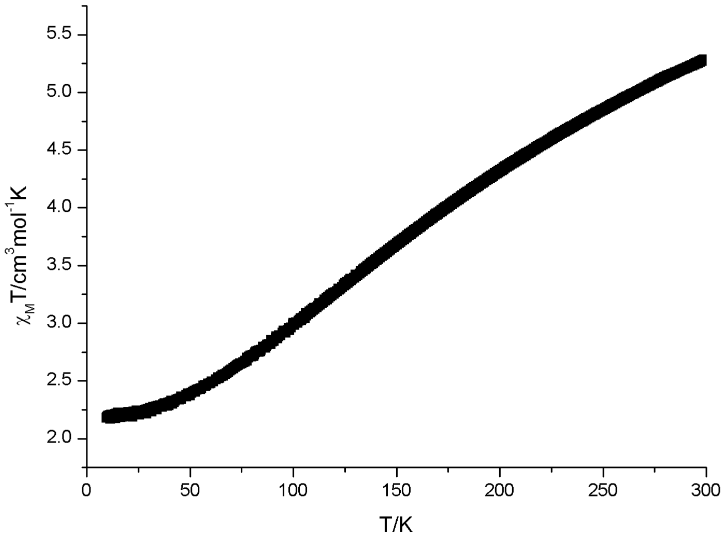

Figure 4.22
$\chi_M T$ *vs* T data for the bulk sample of **12**$(BF_4)_2$ CF_3CH_2OH. Collected at a scan rate of 2 K min^{-1} in sweep mode.

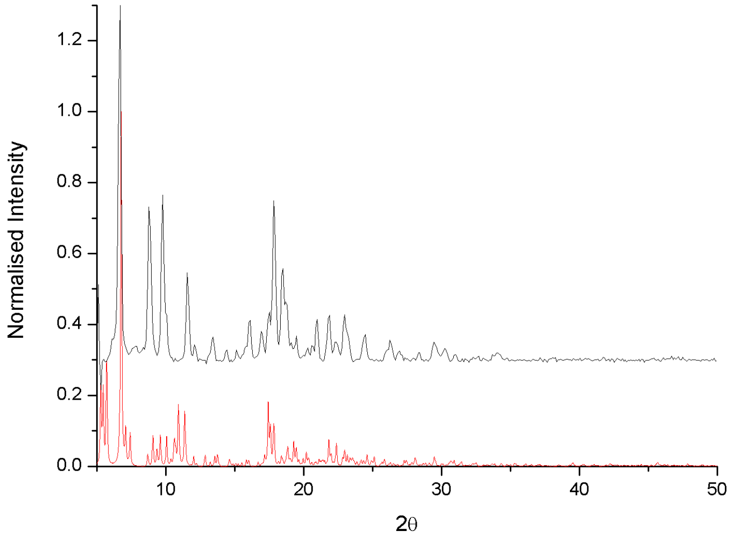

Figure 4.23
PXRD data for **12**$(BF_4)_2$ CF_3CH_2OH (black) compared with the powder pattern calculated from the crystal structure.

It was seen that in acetone solution **12**$(BF_4)_2$ stays fully HS from 320-220 K, then begins to undergo a gradual transition beginning at around 220 K (Figure 4.24). Because the main slope of the transition occurs outside the temperature range it is difficult to accurately extrapolate a value for $T_{1/2}$ to compare with the solid state measurements.

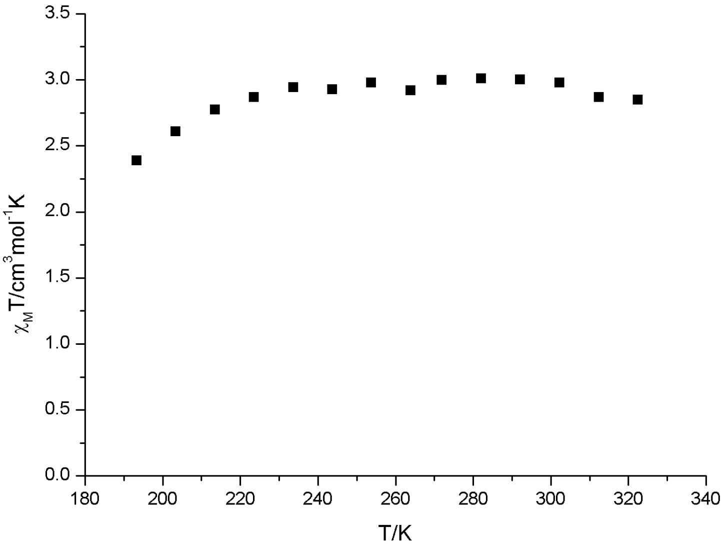

Figure 4.24
$\chi_M T$ *vs* T for **12**$(BF_4)_2$ in $(CD_3)_2CO$ solution via the Evans NMR method. Calculated using the shift in the acetone peak.

4.5. Complexes of Asymmetric Ligands $\mathbf{L^{14}}$ and $\mathbf{L^{15}}$

The ligands 2-(5-*tert*butyl-1*H*-pyrazol-3-yl)-6-(5-methyl-1*H*-pyrazol-3-yl)-pyridine (**L**^{14}) and 5-[6-(5-tert-Butyl-1*H*-pyrazol-3-yl)-pyridin-2-yl]-2*H*-pyrazol-3-ylamine (**L**^{15}) were both used to make their respective iron(II) salts. [Fe(**L**^{14})$_2$](BF$_4$)$_2$ (**14**(BF$_4$)$_2$) and [Fe(**L**^{15})$_2$](ClO$_4$)$_2$ (**15**(ClO$_4$)$_2$) were then screened for any spin crossover behaviour.

4.5.1. $\mathbf{[Fe(L^{14})_2](BF_4)_2 0.25CF_3CH_2OH{\cdot}2.6(C_2H_5)_2O}$ $\mathbf{(14(BF_4)_2 0.25CF_3CH_2OH{\cdot}2.6(C_2H_5)_2O)}$

Crystals of **14**$(BF_4)_2 0.25CF_3CH_2OH{\cdot}2.6(C_2H_5)_2O$ suitable for x-ray diffraction were obtained via slow vapour diffusion of diethyl ether into a trifluoroethanol solution to afford **14**$(BF_4)_2{\cdot}0.25CF_3CH_2OH{\cdot}2.6(C_2H_5)_2O$ which crystallised in the monoclinic space group $P2_1/c$ (a = 15.1739(5); b = 17.9832(6); c = 19.9978(7) Å, α = 90°, β = 95.117(1)°, γ = 90°, V = 5435.2(3) Å^3). The asymmetric unit contained one formula unit and four positions containing solvent molecules, two of which are partially occupied (Figure 4.25). The fully occupied solvent sites contain diethyl ether molecules with the oxygen forming a hydrogen bonding interaction with the pyrazolyl NH, H(16) and H(37) while the other pyrazolyl NH groups form hydrogen bonding interactions anions in the asymmetric unit (Table 4.10). These hydrogen bonds do not link adjacent dications and so do not form any long range hydrogen bonding networks. On this basis any spin transition which may occur in this solvate is expected to be gradual.

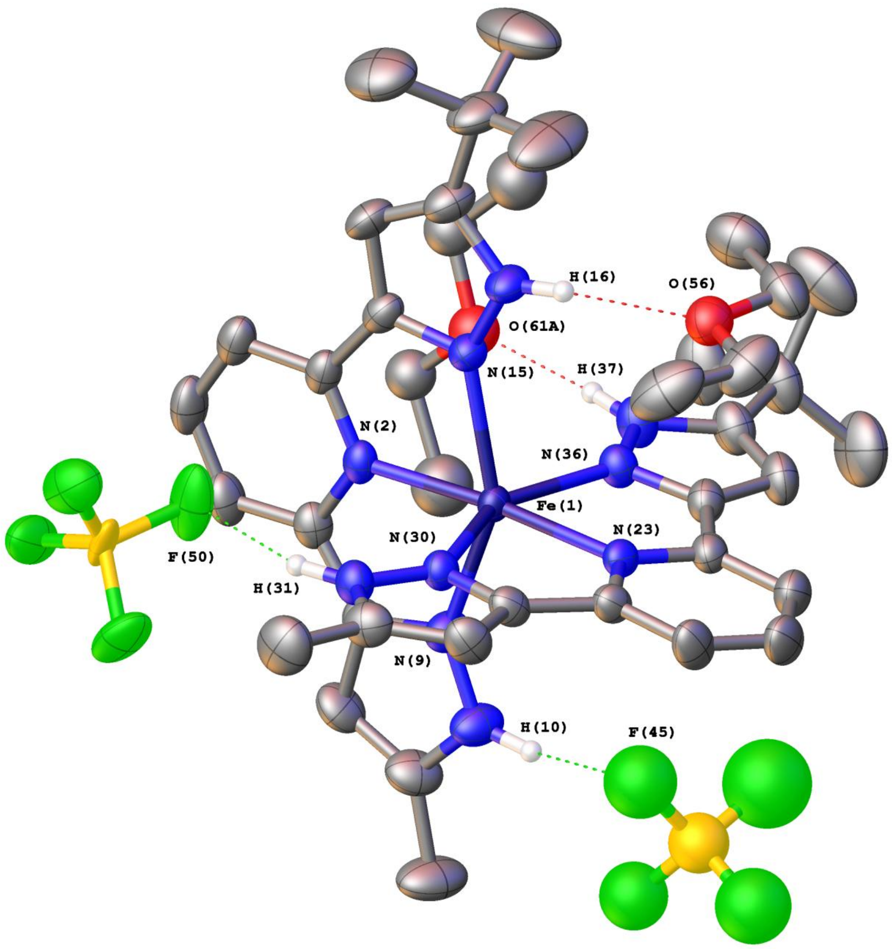

Figure 4.25
Asymmetric unit of **14**$(BF_4)_2 \cdot 0.25CF_3CH_2OH \cdot 2.6(C_2H_5)_2O$ showing hydrogen bonding motifs. Thermal ellipsoids are set to 50% probability. Solvent molecules and hydrogens not taking part in any interactions have been omitted, and only one position of disordered fragments are shown.

Table 4.10
Distances for hydrogen bonding interactions in **14**$(BF_4)_2 \cdot 0.25CF_3CH_2OH \cdot 2.6(C_2H_5)_2O$.

Interaction	Distance (Å)
N(10)-H(10)···F(45)	2.989(9)
N(16)-H(16)···O(56)	2.867(8)
N(31)-H(31)···F(50)	2.801(9)
N(37)-H(37)···O(61)	2.796(9)

Table 4.11
Selected geometric parameters for **14**$(BF_4)_2$·$0.25CF_3CH_2OH$·$2.6(C_2H_5)_2O$.

	14$(BF_4)_2$·$0.25CF_3CH_2OH$·$2.6(C_2H_5)_2O$
Fe-PyN (Å)	2.118(3)
Fe-PzN (Å)	2.186(3)
α(°)	149.0286(13)
θ(°)	88.7960(8)
ϕ(°)	174.3261(2)
Σ(°)	140.05
Θ(°)	343.83

It can be seen from the values of the Fe–N bond lengths and distortion parameters that this complex is HS at 110 K, although there is very little distortion in the *trans* angle, ϕ, and ligand plane twist angle, θ, unlike those seen in the complexes of $\mathbf{L^6}$ and $\mathbf{L^{12}}$ (Table 4.11). Variable temperature magnetic susceptibility measurements in the solid state recorded using a SQUID magnetometer in a field of 5 kG show a gradual, linear transition almost identical in form to that seen for **10**$(ClO_4)_2$ apart from reaching a higher value for $\chi_M T$ of 3.6 cm^{3}mol^{-1}K (Figure 4.26). $\chi_M T$ also only reaches a minimum value of 1.9 cm^{3}mol^{-1}K, suggesting that there is a HS phase impurity which is responsible for the zero field splitting at lower temperatures. An attempt at obtaining a powder pattern of the bulk sample used for the SQUID measurements showed that the material was amorphous and so is unlikely to be the same solvate as seen in the crystal structure. This was probably a result of the volatility of the diethyl ether and it was seen that single crystals of **14**$(BF_4)_2$·$0.25CF_3CH_2OH$·$2.6(C_2H_5)_2O$ lost their crystallinity if not placed under the cryostream promptly. The microanalysis for this complex also indicates that the bulk sample actually consists of **14**$(BF_4)_2 0.5CF_3CH_2OH$, suggesting a slightly different solvate which could have resulted from the loss of diethyl ether and some trifluoroethanol.

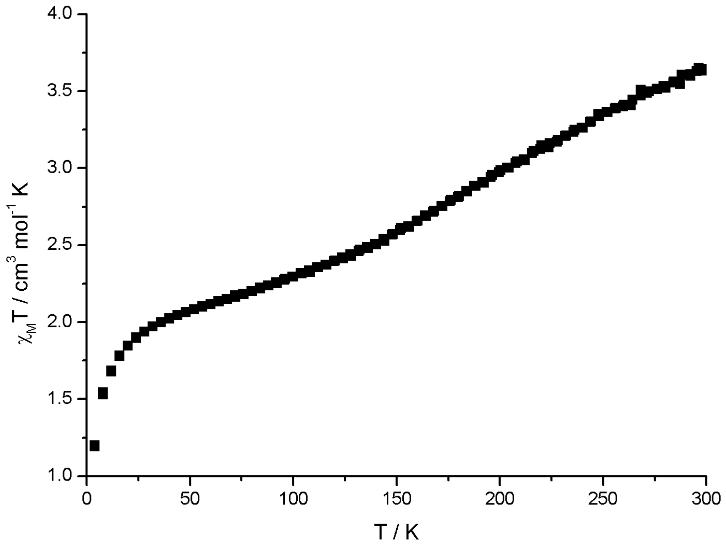

Figure 4.26
χ_MT *vs* T data for the bulk sample of **14**$(BF_4)_2 0.5CF_3CH_2OH$. Collected using a scan rate of 2 K min^{-1} in settle mode.

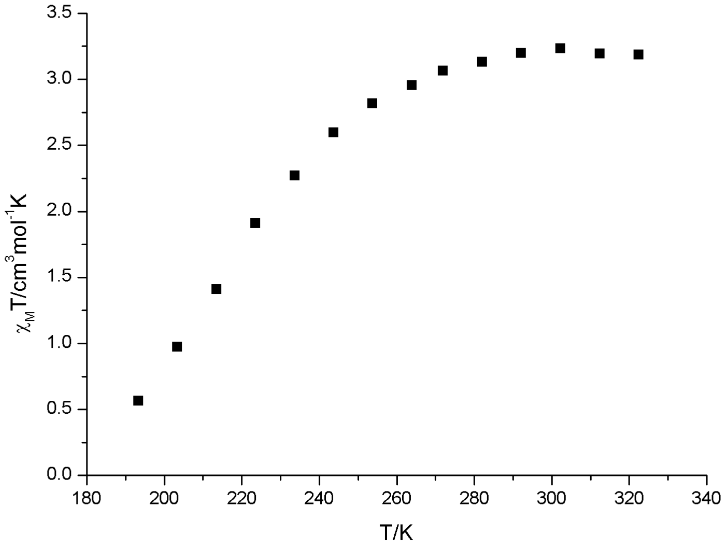

Figure 4.27
χ_MT *vs* T data for **14**$(BF_4)_2$ in $(CD_3)_2CO$ solution. Calculated using the shift in the TMS peak.

The magnetic susceptibility measurements in acetone solution via the Evans method show an almost complete and gradual transition centred around $T_{1/2}$ = 230 K (Figure 4.27). This is a much higher transition temperature than for **12**$(BF_4)_2$ which only just begins to switch at 220 K and this shows the importance of inductive effects of the groups on the pyrazolyl *C*5 position. The donation of additional electron density from the extra *tert*butyl group seems to help to stabilise the HS state in solution assuming that no interactions with the solvent are also contributing. This seems unlikely, however, as acetone is a good hydrogen bond acceptor and may form interactions with the pyrazolyl NH groups.

4.5.2. [Fe(**L**^{15})$_2$](ClO$_4$)$_2$·0.5C$_7$H$_8$ CH$_3$NO$_2$ (15(ClO$_4$)$_2$·0.5C$_7$H$_8$ CH$_3$NO$_2$)

Complexes of **L**^{15} proved difficult to isolate in sufficient purity as when the solvent was removed they had a tendency to form a viscous brown liquid, suggesting that some solvent remained. A solid was eventually isolated by sonication in toluene, although because of its low vapour pressure toluene could not be used in slow vapour diffusion and there was difficulty in obtaining crystals suitable for x-ray diffraction. Luckily an NMR sample which had been left for a few months appeared to contain small, pale yellow block like crystals which showed very strong diffraction, and a structure was obtained. It was found to crystallise in the triclinic space group *P*-1 (a = 12.8934(4); b = 14.9852(5); c = 16.5729(6) Å, α = 114.034(3)°, β = 99.858(3)°, γ = 95.295(3)°, V = 2834.19(19) Å^3). The asymmetric unit contained one formula unit of the expected complex and four acetone-*d*6 solvent molecules, two of which are accepting hydrogen bonds from *tert*butylpyrazole NH of separate ligands (Figure 4.28, Table 4.12). One of the aminopyrazolyl NH groups donates a hydrogen bond to a ClO$_4^-$ anion, although this interaction does not link adjacent complex dications. Unexpectedly when the structure is grown it can be seen that adjacent pairs of molecules interlock and the ligand molecules are covalently linked via the formation of a ring at the aminopyrazolyl groups of two adjacent dications. The two ligands in the asymmetric unit are similar but symmetrically inequivalent. Each ligand forms a 6 membered ring with its symmetrically inequivalent ligand in an adjacent molecule in an AB fashion, to give discrete pairs of complex dications linked by the formation of two of these rings (Figure 4.29, Figure 4.30). This modified ligand, **L**^{15a}, gives a dinuclear iron complex of the type [Fe$_2$(**L**^{15a})$_2$](ClO$_4$)$_4$·8(CD$_3$)$_2$CO.

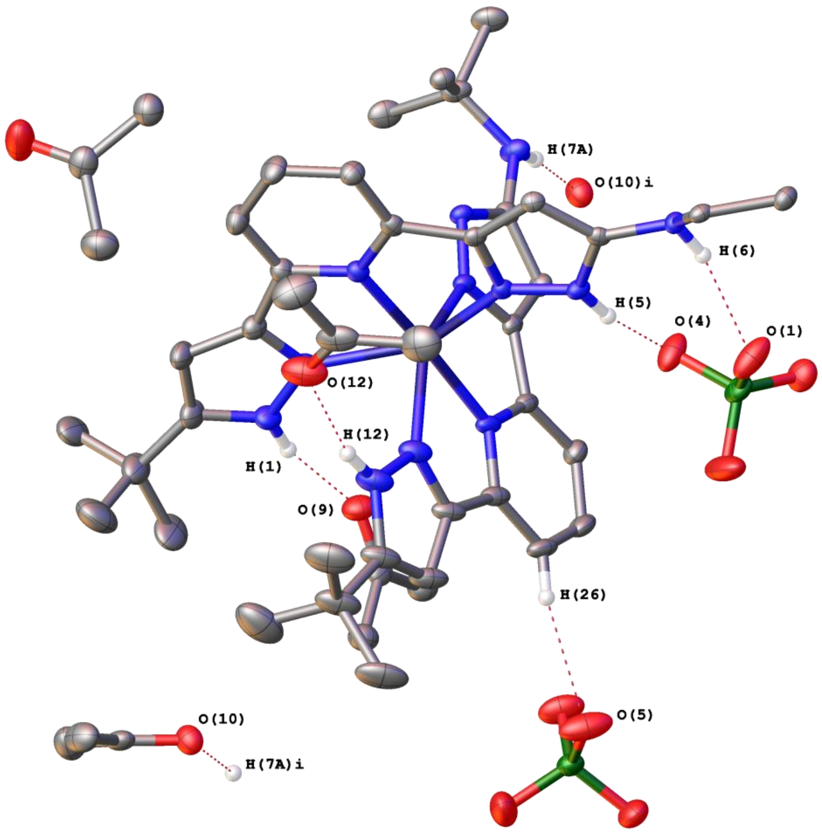

Figure 4.28
Asymmetric unit of $[Fe_2(\mathbf{L}^{15a})_2](ClO_4)_4 \cdot 8(CD_3)_2CO$ showing hydrogen bonding interactions. Thermal ellipsoids are set at 50% probability and hydrogens not taking part in any interactions have been omitted. Disordered *tert*butyl groups have only been shown in one orientation. Symmetry codes: (i) –*x*, -*y*, -*z*.

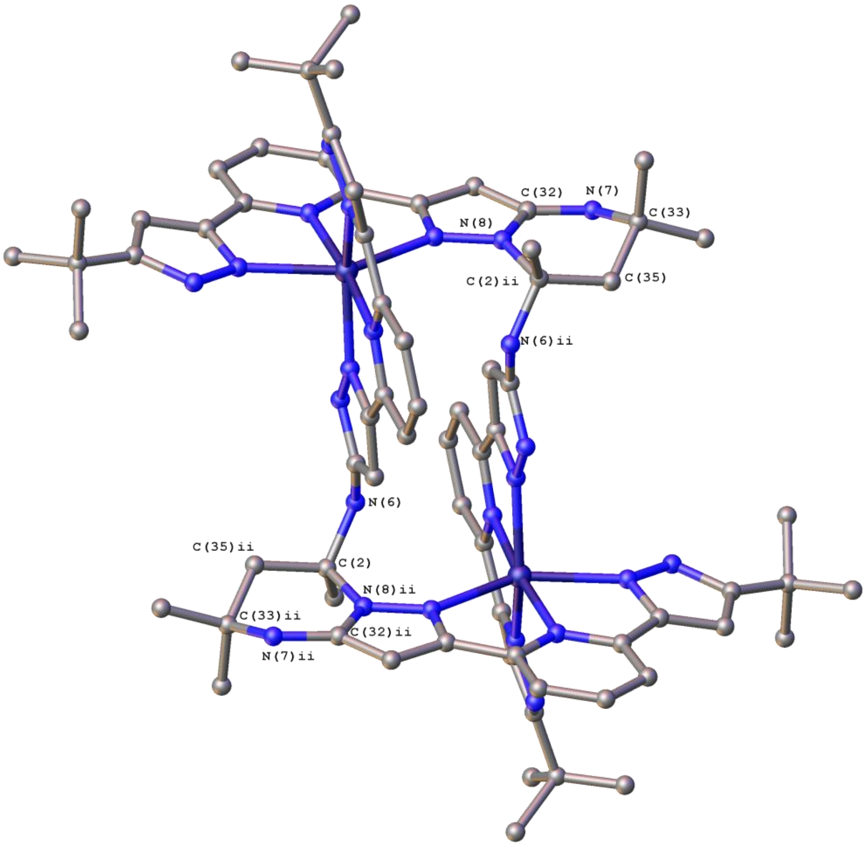

Figure 4.29
View of the covalent bonding between adjacent dication pairs in the structure of $[Fe_2(\mathbf{L}^{15a})_2](ClO_4)_4\cdot8(CD_3)_2CO$. Symmetry codes: (ii) –*x*, -*y*, 1-*z*.

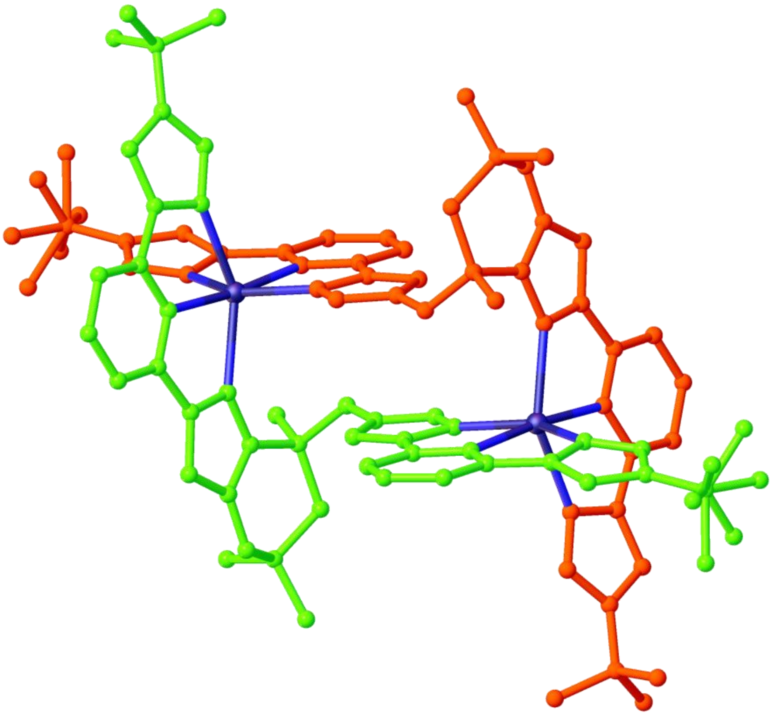

Figure 4.30
View of the structure of $[Fe_2(\mathbf{L}^{15a})_2](ClO_4)_4\cdot 8(CD_3)_2CO$ distinguishing the two separate covalently linked ligands.

Table 4.12
Distances for the hydrogen bonding interactions in the structure of $[Fe_2(\mathbf{L}^{15a})_2](ClO_4)_4\cdot 8(CD_3)_2CO$.

Interaction	**Distance (Å)**
N(1)-H(1)···O(9)	2.839(3)
N(5)-H(5)···O(4)	2.809(3)
N(6)-H(6)···O(1)	3.021(3)
N(7)-H(7)···O(10)	2.920(3)

Table 4.13
Selected geometric parameters for the iron centre in $[Fe_2(\mathbf{L}^{15a})_2](ClO_4)_4{\cdot}8(CD_3)_2CO$.

	$[Fe_2(L^{15a})_2](ClO_4)_4{\cdot}8(CD_3)_2CO$
Fe-PyN (Å)	2.126(2)
Fe-PzN (Å)	2.195(2)
α(°)	148.18(8)
θ(°)	80.26(2)
ϕ(°)	174.19(8)
Σ(°)	259.31
Θ(°)	343.93

It can be seen that the Fe–N bond lengths obtained from the crystal structure are of a length typical of a fully HS iron(II) complex. There is a particularly large value for the rhombic distortion parameter, Σ, which is significantly larger than that seen for complexes of $\mathbf{L}^{5}$, $\mathbf{L}^{6}$, $\mathbf{L}^{12}$ and $\mathbf{L}^{14}$ which are all below 200° and is a general indication of a distortion away from an octahedral geometry (Table 4.13).[21] Some of these distortions could be attributed to steric clashes of the *tert*butyl groups in this complex and could also the reason for disorder in one of these groups.

Each ring appears to have formed by a reaction involving two acetone molecules, but analysis on $[Fe_2(\mathbf{L}^{15a})_2](ClO_4)_4{\cdot}8(CD_3)_2CO$ formed is limited due to the sample size being so small. Further confirmation of the structure comes from the mass spectrum, which showed a peak at *m/z* 656.46 corresponding to the ligand $\mathbf{L}^{15a}$ with the new ring containing deuterium instead of hydrogen. Separate solutions of ligand and complex were made in acetone and monitored over a number of weeks via ES^+ mass spectrometry in order to determine whether this is a property of the ligand itself or if the iron facilitates the formation of these rings in some way. Although the spectra of both solutions did appear to get more convoluted over time, indicating that something is changing, no peaks were found that corresponded to $\mathbf{L}^{15a}$ or any chemically feasible intermediates to its formation. Attempts were also made to speed up the reaction by heating an acetone solution of $\mathbf{L}^{15}$ in the presence of a base (potassium *tert*butoxide) and the progress of the reaction was monitored via HPLC-MS. After 12 hours a mixture of products had formed with a major peak at *m/z* 381.2, which could correspond to an intermediate where a ring has formed on one side of $\mathbf{L}^{15}$. It is possible that the amino group on another ligand could attack and displace the hydroxyl group on the newly formed ring. This reaction would have to take place in the presence of catalytic amounts of H^+, and this could be the reason that none of **L^{15a}** was observed in this strongly basic reaction mixture, even after a four day reflux (Scheme 4.1). No single product was isolated from this mixture so unfortunately further analysis could not be carried out on this intermediate to unambiguously confirm its presence.

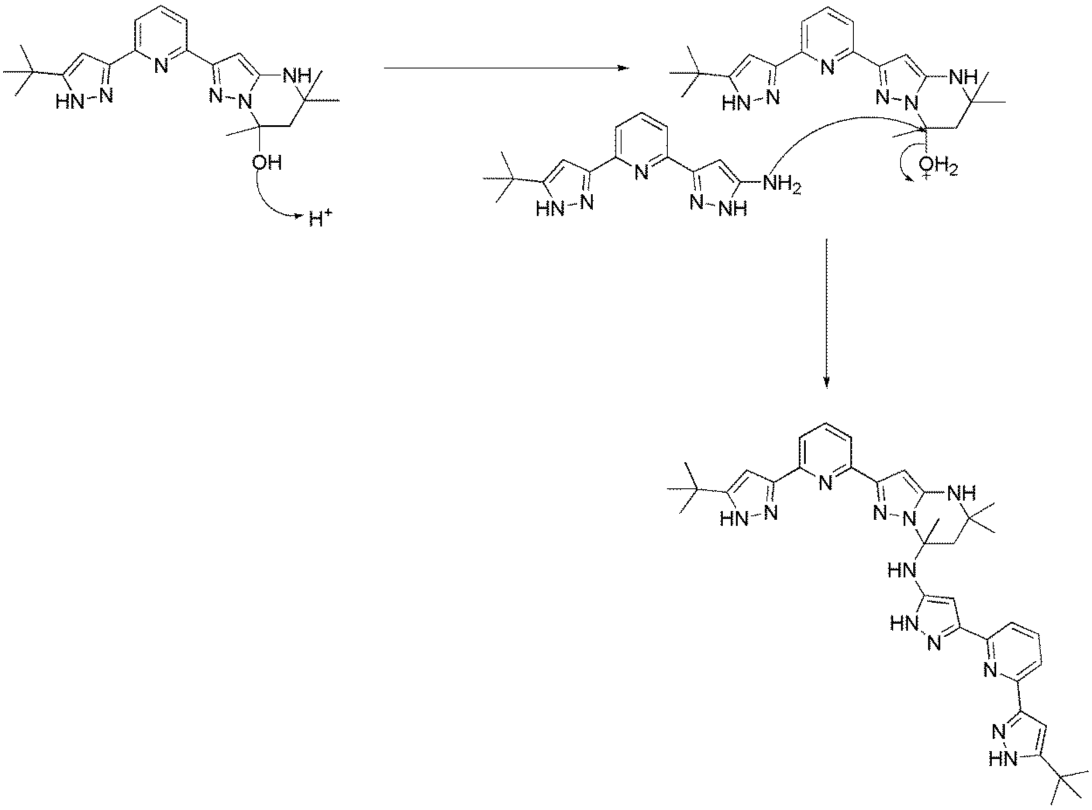

Scheme 4.1
Proposed mechanism for part of the formation of **L^{15a}**.

4.6. Complexes of 2,6-Di(1*H*-pyrazol-3-yl)pyridin-4-ylamine (L^{16})

The iron perchlorate complex of **L^{16}** (**16**$(ClO_4)_2$ was made by stirring **L^{16}** and iron perchlorate hydrate in methanol, and a precipitate was formed by addition of diethyl ether. Microanalysis indicated that the bulk sample of this complex is unsolvated, however the only crystals suitable for x-ray diffraction were obtained via slow vapour diffusion of diisopropyl ether into a pyridine solution. This complex crystallised in the monoclinic space group *I*2/*a* (a = 23.5787(9); b = 9.7022(4); c = 21.2623(10) Å, α = 90°, β = 101.235(4)°, γ = 90°, V = 4770.9(4) Å^3). The asymmetric unit contained half a molecular unit and two molecules of pyridine, giving the formula **16**$(ClO_4)_2{\cdot}4C_5H_5N$ (Figure 4.31). Each of the four pyridine molecules accept a hydrogen bond from the pyrazolyl NH groups of the dication, while the amino groups on the ligand backbone each donate one hydrogen bond to a ClO_4^- anion (Figure 4.31, Table 4.14). The iron centre lies on a 2-fold rotoinversion axis which runs along the crystallographic *c* axis and intersects the complex dication at 45° to each ligand in the equatorial plane.

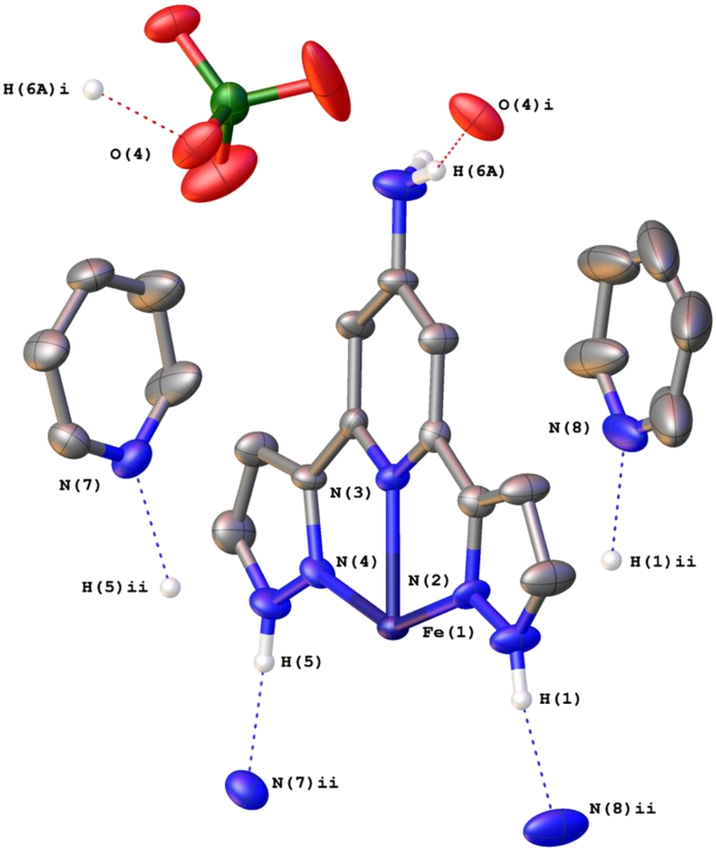

Figure 4.31
Asymmetric unit of **16**$(ClO_4)_2 \cdot 4C_5H_5N$ showing hydrogen bonding. Thermal ellipsoids are set at 50% probability and hydrogens not taking part in any interactions have been removed. Symmetry codes: (i) 1-*x*, 1/2+*y*, 3/2-*z*; (ii) 1/2-*x*, +*y*, 1-*z*.

Table 4.14
Distances for the hydrogen bonding interactions in the structure of **16**$(ClO_4)_2 \cdot 4C_5H_5N$.

Interaction	Distance (Å)
N(1)-H(1)···N(8)	2.769(7)
N(5)-H(5)···N(7)	2.822(6)
N(6)-H(6A)···O(4)	2.977(6)

Table 4.15
Selected geometric parameters for the iron centre in **16**(ClO_4)$_2$·4C_5H_5N.

	16(ClO_4)$_2$·4C_5H_5N
Fe-PyN (Å)	2.122(4)
Fe-PzN (Å)	2.226(4)
α(°)	147.38(14)
θ(°)	87.50(6)
ϕ(°)	179.3(2)
Σ(°)	148.32
Θ(°)	341.96

It can be seen from the Fe–N bond lengths that this complex in this particular tetrapyridine solvate is fully HS at 100 K however the other bond angle, especially the plane twist angle, θ, and the *trans* angle, ϕ, show very little deviation from the ideal octahedral geometry (Table 4.15). Variable temperature measurements of the bulk phase from methanol/diethyl ether shows a gradual transition where only approximately 70% of the iron centres reach their LS state at 10 K, and some differences in the gradient at around 250 K indicate that some structural changes may be taking place (Figure 4.32). The analogous 1-bpp complex does not show any interesting SCO behaviour, however this does not necessarily mean that the 3-bpp complex has no potential for SCO, as the added amino group offers additional hydrogen bond donors and an acceptor.[28] There may be a solvate or polymorph of this structure which undergoes a cooperative transition, although from multiple crystallisation attempts with different solvents the only structure obtained was the pyridine solvate.

It would have been interesting to further modify this pyridyl *C*4 position in order create new topologies and compare their SCO behaviour with their 1-bpp analogues, however due to the low yielding synthetic procedure for $\mathbf{L^{16}}$ this was not possible.

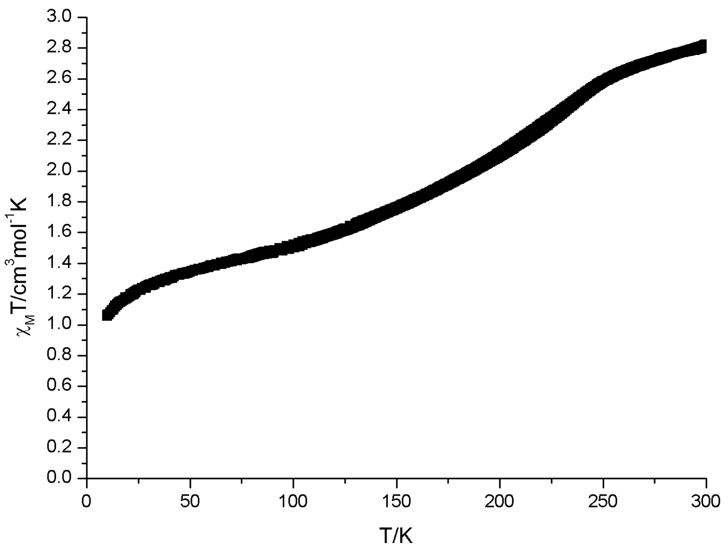

Figure 4.32
$\chi_M T$ *vs* T data for **16**(ClO_4)$_2$. Collected using a scan rate of 2 K min^{-1} in sweep mode.

4.7. Complexes of the Ligands 2,6-Di(4-chloro-1*H*-pyrazol-3-yl)-pyridine (L^{17}) and 2,6-Di(4-bromo-1*H*-pyrazol-3-yl)-pyridine (L^{18})

The iron(II) perchlorate complexes were made for both 2,6-di(4-chloro-1*H*-pyrazol-3-yl)-pyridine (**L**^{17}) and 2,6-di(4-bromo-1*H*-pyrazol-3-yl)-pyridine (**L**^{18}) were made by stirring the respective ligands in a methanol solution of iron(II) perchlorate hydrate. Crystals of [Fe(**L**^{18})$_2$](ClO_4)$_2$·2CH_3OH (**18**(ClO_4)$_2$·2CH_3OH) suitable for x-ray diffraction of each were obtained via slow vapour diffusion of diisopropyl ether into a methanol solution and were shown to be the dimethanol solvate. [Fe(**L**^{18})$_2$](ClO_4)$_2$·2CH_3OH (**18**(ClO_4)$_2$·2CH_3OH) was found to crystallise in the triclinic space group *P*-1 (a = 8.9025(4); b = 12.5712(6); c = 15.5796(7) Å, α = 78.555(4)°, β = 86.543(4)°, γ = 80.986(4)°, V = 1687.05(14) Å^3). The asymmetric unit contained one formula unit (Figure 4.33). On each ligand a pyrazolyl NH donates a hydrogen bond to the oxygen of a perchlorate anion, while the other donates a hydrogen bond to the oxygen of a methanol molecule (Table 4.16). The methanol molecules then donate a hydrogen bond to an adjacent perchlorate and so adjacent dication molecules are linked via MeOH···ClO_4^- linkages with the complex molecules interlocking to form a 1-D ladder type topology diagonally across the unit cell (Figure 4.34). The large bromine groups on the ligand backbone may prevent the ligands from getting close enough to one another to facilitate π-π interactions between the pyrazolyl groups, with the distance between the least square planes being 4.284(3) Å (Figure 4.35). To our knowledge there are no isostructural 1-bpp analogues of these complexes.

The Fe–N bond lengths are significantly shorter than those seen for the previous complexes and along with the smaller value for the rhombic distortion parameter, Σ, suggests that this complex is fully LS at 120 K in the solid state as this particular polymorph (Table 4.17). This accessible LS state together with the cooperative interactions described above make this complex a particularly interesting sample to study for SCO.

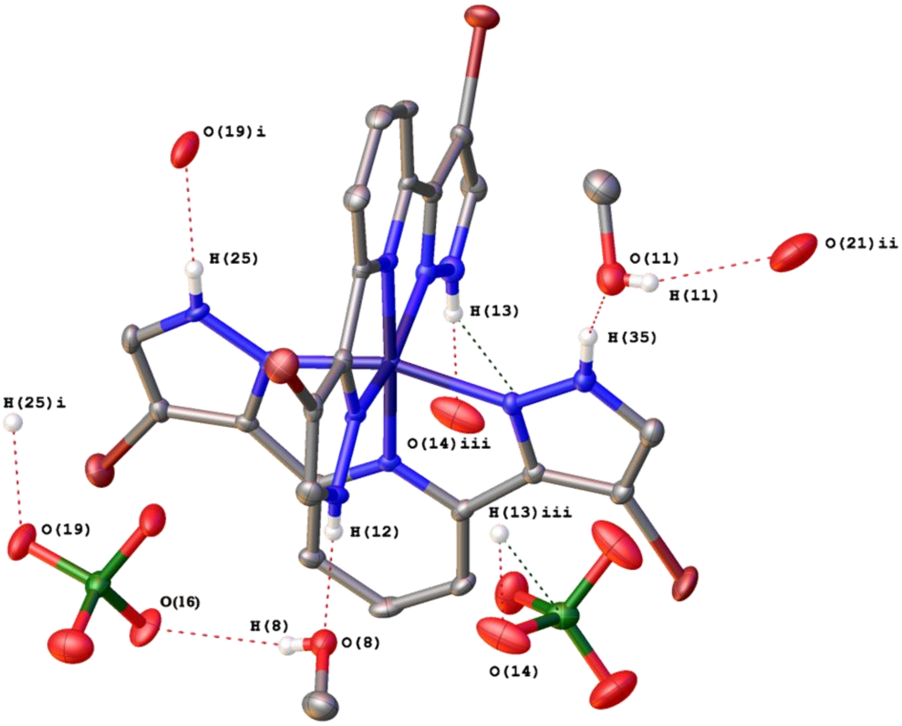

Figure 4.33
Asymmetric unit of **18**$(ClO_4)_2 \cdot 2CH_3OH$ showing hydrogen bonding interactions. Thermal displacement ellipsoids are set at 50% probability and hydrogens not participating in any interactions have been omitted. Symmetry codes: (i) -1-*x*, 2-*y*, -*z*; (ii) –*x*, 1-*y*, 1-*z*; (iii) -1+*x*, +*y*, +*z*.

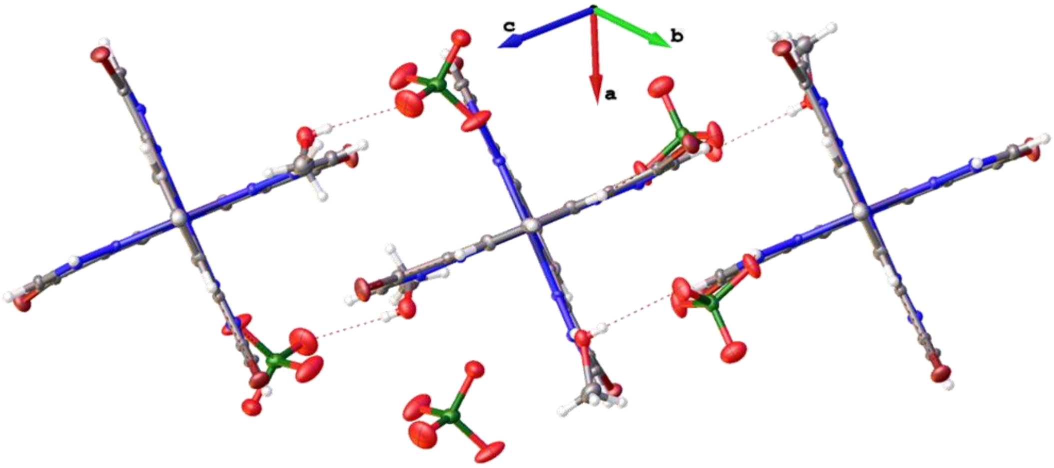

Figure 4.34
View of the chain forming hydrogen bonding interactions in the structure of **18**$(ClO_4)_2 \cdot 2CH_3OH$.

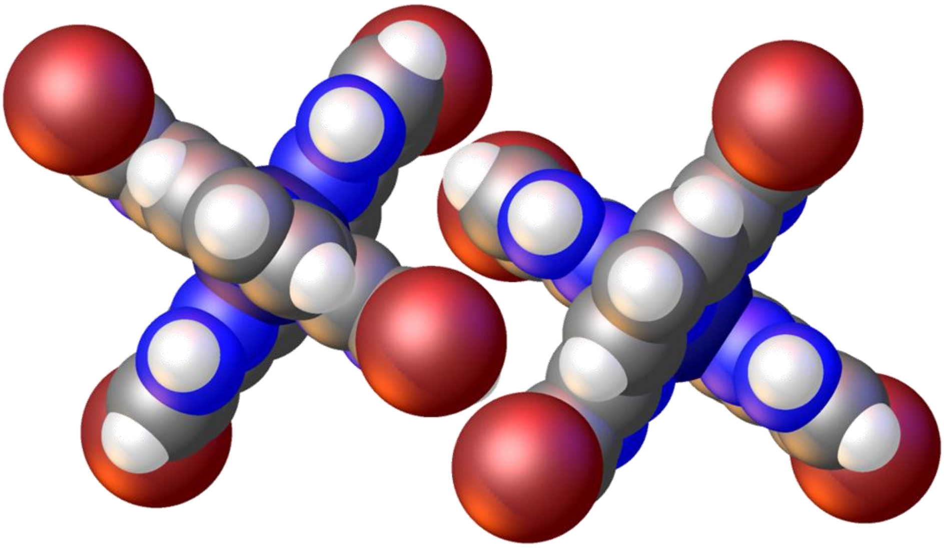

Figure 4.35
Spacefill view of the pseudo-terpyridine embrace in the structure of **18**$(ClO_4)_2 \cdot 2CH_3OH$.

Table 4.16
Distances for the hydrogen bonding interactions in the structure of **18**$(ClO_4)_2{\cdot}2CH_3OH$.

Interaction	**Distance (Å)**
O(8)-H(8)···O(16)	2.936(4)
O(11)-H(11)···O(21)	2.975(6)
N(12)-H(12)···O(8)	2.724(5)
N(13)-H(13)···O(14)	2.788(5)
N(25)-H(25)···O(19)	2.922(5)
N(35)-H(35)···O(11)	2.715(5)

Table 4.17
Selected geometric parameters for the iron centre in **18**$(ClO_4)_2{\cdot}2CH_3OH$.

	18$(ClO_4)_2{\cdot}2CH_3OH$
Fe-PyN (Å)	1.920(3)
Fe-PzN (Å)	1.968(3)
α(°)	158.66(13)
θ(°)	88.14(3)
ϕ(°)	177.77(12)
Σ(°)	93.17
Θ(°)	352.11

The bulk samples approximate as **17**$(ClO_4)_2$ and **18**$(ClO_4)_2{\cdot}CH_3OH$ via microanalysis. While there is no crystal structure to compare to **17**$(ClO_4)_2$, the loss of one equivalent of methanol in **18**$(ClO_4)_2{\cdot}CH_3OH$ could be due to exposure to the atmosphere.

Although the PXRD data for this sample are not particularly high resolution it can be seen that it is significantly different from the powder patter calculated from the crystal structure (Figure 4.36). This powder pattern was compared to that obtained for **17**$(ClO_4)_2$ to check for any similarities between the two structures but the pattern obtained showed that although the sample looked crystalline **17**$(ClO_4)_2$ was almost completely amorphous (Figure 4.37). One broad peak was resolved however and would indicate that these two samples are not isostructural.

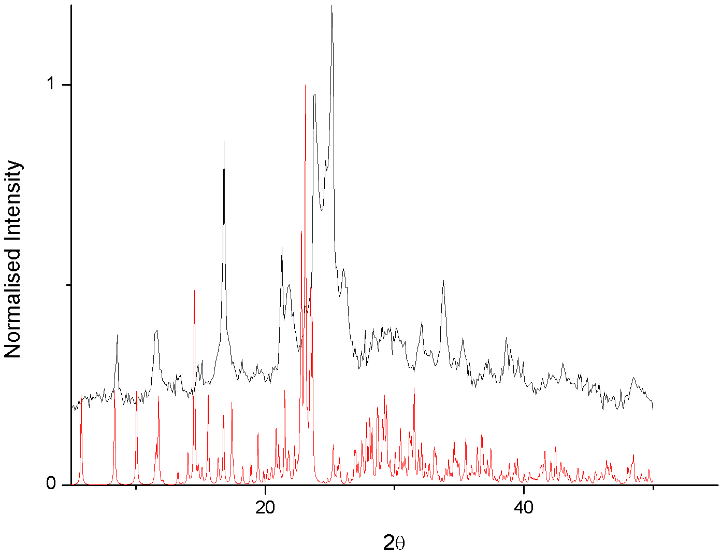

Figure 4.36
PXRD data for **18**$(ClO_4)_2{\cdot}CH_3OH$ (black) compared with the powder pattern calculated from the crystal structure.

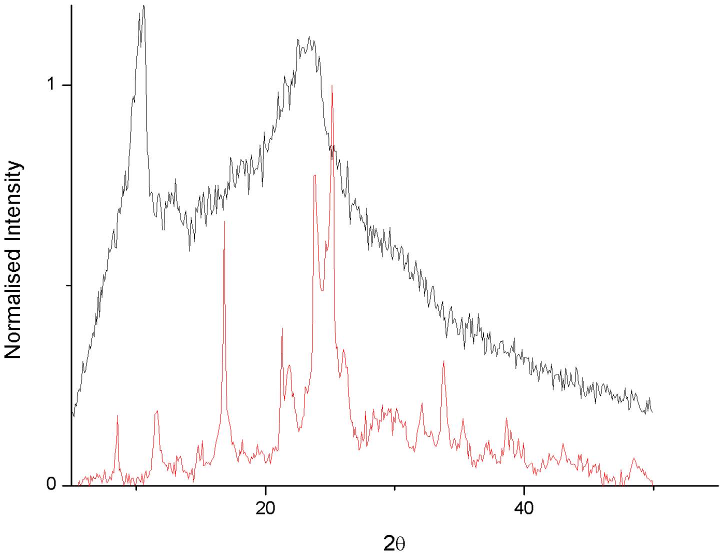

Figure 4.37
PXRD data obtained for **17**$(ClO_4)_2$ (black) and **18**$(ClO_4)_2{\cdot}CH_3OH$ (red).

The variable temperature magnetic susceptibility for this sample shows that it remains in the LS state from 3-350 K (Figure 4.38). A transition may occur at higher temperatures however the maximum temperature was limited by the SQUID magnetometer. The gradual increase in $\chi_M T$ observed with increasing temperature likely due to the sample not being properly centred in the magnetometer. This is common in diamagnetic samples, as the magnetometer centres the sample to the maximum signal which isn't obvious in diamagnetic samples. This diamagnetic character could be a result of the large bromide groups on the pyrazolyl backbone which may not accommodate a more highly distorted HS iron(II) centre.

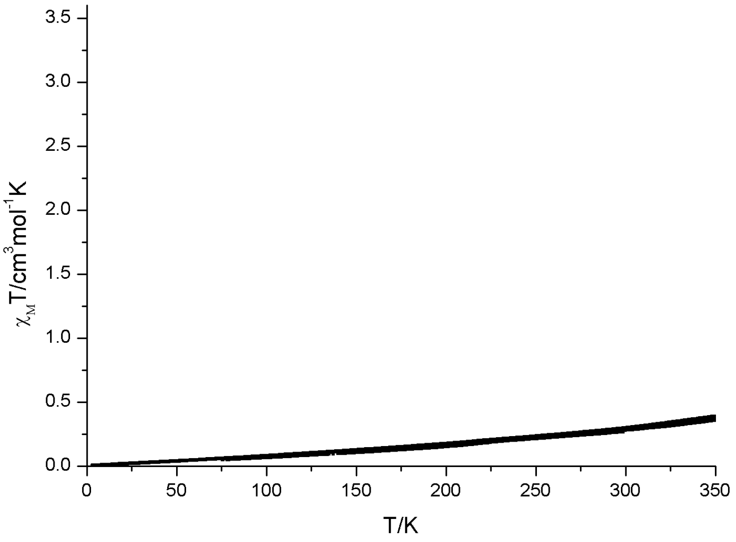

Figure 4.38
$\chi_M T$ *vs* T data for **18**$(ClO_4)_2 \cdot CH_3OH$. Collected using a scan rate of 2 K min^{-1} in sweep mode.

4.8. Conclusions

A series of complexes have been synthesised from novel ligands in an attempt to create cooperative SCO complexes with abrupt spin transitions and their structures have been analysed. The complexes of **L**^{5} show complex hydrogen bonding through both the pyrazolyl NH and amino substituents which connect to neighbouring dications through perchlorate anions that interosculate creating a 3-dimensional network similar to a fluorite topology. This hydrogen network does seem to be responsible for cooperativity and hysteresis in the bulk sample, however due to the unstable nature of this complex towards oxidation variable temperature magnetic measurements on a phase pure sample could not be obtained.

Converting the amino groups to secondary amides bearing alkyl substituents gives complexes which are much more stable towards oxidation, however the 3 dimensional hydrogen bonding networks are lost in complexes of **L^6** which give a 1 dimensional ladder type topology. This type of cooperativity may still have had an effect on the abruptness of the spin transition, however it was seen in the crystal structure that the bulky substituents on the pyrazolyl groups lead to a large distortion in the coordination sphere, one which favours the HS state. In order to access the LS state the complex would have to move to a more ideal octahedral geometry, a movement which would not be accommodated by the lattice and so a phase change would be necessary. In this case it seems that the energy barrier for this change is too high, therefore this complex remains trapped in the HS state.

Complexes of the alkylpyrazole ligands generally showed gradual spin transitions indicating a lack of cooperativity in the crystal lattice. While the crystal structure of the **12**$(BF_4)_2$ solvate showed extensive 3 dimensional hydrogen bonding networks the iron appears to remain LS at 150 K, probably due to similar steric constraints in the lattice as for **6**$(BF_4)_2$. Interestingly replacing a *tert*butyl group on one pyrazolyl arm of this ligand with a methyl group appears to stabilise the HS state by inductive effects, and raises the $T_{1/2}$ of the respective iron complex considerably in acetone solution. Similarly the addition of electron donating groups such as amino or alkyl groups appears to stabilise the HS state, compared to electron withdrawing groups such as in **L^6** which appear to stabilise the LS state (Figure 4.39). Based on the inductive effects of the substituents the opposite trend is expected and is observed in the 1-bpp series.[8] This effect remains unexplained and perhaps density functional calculations may shed light on this behaviour.

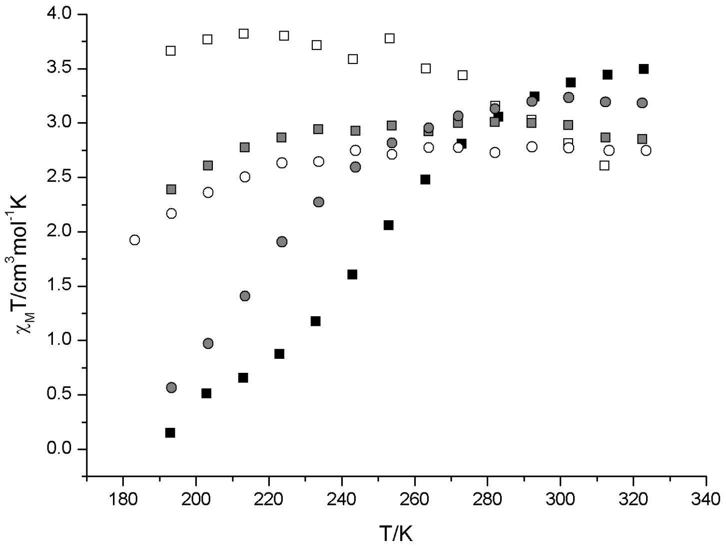

Figure 4.39
Comparison of the Evans data for $[Fe(3\text{-}bpp)_2]^{2+}$ (■), **14**$^{2+}$ (●), **15**$^{2+}$ (○), **12**$^{2+}$ (■) and **5**$^{2+}$ (□).

An interesting and unexpected reaction was observed in the iron complex of the unsymmetrical ligand **L**^{15} that appeared to involve a ring formation with two molecules of acetone at the NH and amino groups on the aminopyrazolyl moiety, giving pairs of complex dications linked by covalently bonded ligand dimers. Because only small amounts of this crystalline sample were obtained further analysis including variable temperature magnetic susceptibility could not be conducted, and attempts to make a bulk sample of this complex were unsuccessful. It was however shown that a possible intermediate in this reaction can be detected by refluxing the ligand in acetone in the presence of a base and this shows that the reaction can proceed in the absence of iron.

A crystal structure of a complex of the ligand **L**^{16} showed that the amino group on the pyrazolyl *C*4 position does not lead to any 3 dimensional hydrogen bonding networks and this complex shows a gradual, uncooperative spin transition. It would have been interesting to investigate the effect of a number of different substituents at this position however this was not possible due to synthetic problems with this type of ligand.

Finally the isostructural complexes of the 4-halopyrazole ligands were the only complexes in this chapter which were seen to be in their LS state at 150 K, and show 1-dimensional hydrogen bonding networks with an interlocking of adjacent cations. The variable temperature magnetic susceptibility of the 4-bromopyrazole complex shows that it remains fully LS between 3-350 K. This could be a steric effect of the large bromide atoms close to the coordination sphere.

All of the crystal structures obtained of these complexes have contained large amounts of lattice solvent, and it has proved difficult to replicate most of these in the bulk sample with PXRD measurements showing either a different phase or a completely amorphous material. In all but one of these complexes the solvent molecules form hydrogen bonding interactions and in some cases these lead to interesting topologies which extend throughout the lattice. The presence of absence of these interactions will affect the cooperativity of a spin transition and is one of the major hurdles when systematically searching for new SCO materials.

4.9. References

[1] T. D. Roberts, M. A. Little, L. J. Kershaw Cook, S. A. Barrett, F. Tuna and M. A. Halcrow, *Polyhedron* **2013**, *64*, 4-12.

[2] G. A. Craig, J. S. Costa, O. Roubeau, S. J. Teat and G. Aromí, *Chem. Eur. J.* **2012**, *18*, 11703-11715.

[3] K. A. Ali, *Arkivoc* **2010**, *11*, 55-63.

[4] Y. Zhou, W. Chen and D. Wang, *Dalton Trans.* **2008**, 1444-1453.

[5] T. M. Pfaffeneder, S. Thallmair, W. Bauer and B. Weber, *New J. Chem.* **2011**, *35*, 691-700.

[6] T. D. Roberts, F. Tuna, T. L. Malkin, C. A. Kilner and M. A. Halcrow, *Chem. Sci.* **2012**, *3*, 349-354.

[7] C. Carbonera, J. S. Costa, V. A. Money, J. Elhaïk, J. A. K. Howard, M. A. Halcrow and J. F. Létard, *Dalton Trans.* **2006**, 3058-3066.

[8] R. Pritchard, C. A. Kilner, S. A. Barrett and M. A. Halcrow, *Inorg. Chim. Acta* **2009**, *362*, 4365-4371.

[9] R. Pritchard, H. Lazar, S. A. Barrett, C. A. Kilner, S. Asthana, C. Carbonera, J. F. Létard and M. A. Halcrow, *Dalton Trans.* **2009**, 6656-6666.

[10] G. P. Shen, L. Qi, L. Wang, Y. Xu, J. J. Jiang, D. Zhu, X. Q. Liu and X. You, *Dalton Trans.* **2013**, *42*, 10144-10152.

[11] B. Weber, W. Bauer and J. Obel, *Angew. Chem., Int. Ed.* **2008**, *47*, 10098-10101.

[12] K. Takahashi, T. Kawakami, Z. Z. Gu, Y. Einaga, A. Fujishima and O. Sato, *Chem. Commun.* **2003**, 2374-2375.

[13] A. L. Allred, *J. Inorg. Nucl. Chem.* **1961**, *17*, 215-221.

[14] C. F. Sheu, S. M. Chen, G. H. Lee, Y. H. Liu, Y. S. Wen, J. J. Lee, Y. C. Chuang and Y. Wang, *Eur. J. Inorg. Chem.* **2013**, *2013*, 894-901.

[15] C. T. Brewer, G. Brewer, R. J. Butcher, E. E. Carpenter, A. M. Schmiedekamp and C. Viragh, *Dalton Trans.* **2007**, 295-298.

[16] M. Fondo, N. Ocampo, A. M. García-Deibe, M. Corbella, M. S. El Fallah, J. Cano, J. Sanmartín and M. R. Bermejo, *Dalton Trans.* **2006**, 4905-4913.

[17] M. C. Etter, *Acc. Chem. Res.* **1990**, *23*, 120-126.

[18] H. Chun, D. Kim, D. N. Dybtsev and K. Kim, *Angew. Chem., Int. Ed.* **2004**, *43*, 971-974.

[19] R. C. Weast, *CRC Handbook of Chemistry and Physics (62nd ed.)*, CRC Press, Boca Raton, FL, **1981**.

[20] M. Marchivie, P. Guionneau, J. F. Létard and D. Chasseau, *Acta Crystallogr., Sect. B: Struct. Sci.* **2005**, *B61*, 25-28.

[21] M. A. Halcrow, *Chem. Soc. Rev.* **2011**, *40*, 4119-4142.

[22] S. A. Barrett, C. A. Kilner and M. A. Halcrow, *Dalton Trans.* **2011**, *40*, 12021-12024.

[23] M. A. Halcrow, *Coord. Chem. Rev.* **2009**, *253*, 2493-2514.

[24] C. Reichardt, *Chem. Rev.* **1994**, *94*, 2319-2358.

[25] Y. Marcus, *Chem. Soc. Rev.* **1993**, *22*, 409-416.

[26] J. Catalán, C. Díaz, V. López, P. Pérez, P. J. L. G. De Paz and J. G. Rodríguez, *Liebigs Ann.* **1996**, 1785-1794.

[27] M. J. Kamlet, J. L. M. Abboud, M. H. Abraham and R. W. Taft, *J. Org. Chem.* **1983**, *48*, 2877-2887.

[28] L. J. Kershaw Cook in *Crystal Engineering and Bifunctionality in Spin-Crossover Materials*, *PhD* University of Leeds, **2013**.

Chapter 5

Iron(II) Complexes Incorporating 2,6-Di(5-methyl-1*H*-pyrazol-3-yl)pyridine and Resulting Perchlorate and Tetrafluoroborate Solid Solutions

5.1. Introduction

One particular 3-bpp derivative which has produced extremely interesting iron(II) complexes is 2,6-di(5-methyl-1*H*-pyrazol-3-yl)pyridine (**L**^{9}). Many of the novel ligands described in this thesis were made in an attempt to imitate and improve understanding of the factors which make **L**^{9} such a suitable ligand for iron(II) SCO complexes. Firstly the complex [Fe(**L**^{9})$_2$](BF$_4$)$_2$ (**9**(BF$_4$)$_2$) was synthesised and found to exist as either a dihydrate (**9**(BF$_4$)$_2$·2H$_2$O) or one of two dehydrated phases. One of these dehydrated phases was obtained by anhydrous crystallisation bearing a similar structural resemblance to **9**(BF$_4$)$_2$·2H$_2$O and the other was obtained by heating to 350 K under aerobic conditions.[1] All three of these structures showed a pseudo terpyridine embrace motif but single crystal and PXRD data show that each of these belong to different space groups. This is not uncommon as this type of lattice arrangement is known to exist in a number of different variations.[2-4]

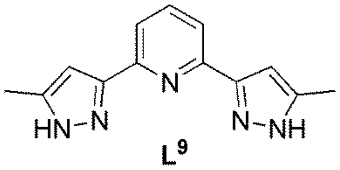

L^9

Figure 5.1
2,6-di(5-methyl-1*H*-pyrazol-3-yl)pyridine (**L**^{9})

Cooling **9**(BF$_4$)$_2$·2H$_2$O to 2 K and warming back to 300 K results in a roughly constant value for $\chi_M T$ of 1.7 cm^{3}mol^{-1}K which indicates a ratio of 1:1 HS:LS states in the sample, with a slight gradual increase when approaching 300 K. Warming the sample past 300 K gives an abrupt increase in $\chi_M T$ to 3.4 cm^{3}mol^{-1}K, a value which is consistent with a fully HS state. This thermally accessible HS state adopts a different phase to both the dihydrate and the dehydrate obtained by crystallisation. This new dehydrated phase then undergoes an abrupt spin transition to a fully LS state with a wide thermal hysteresis width of 65 K centred at 204 K (Figure 5.2). There are few examples of wider thermal hysteresis widths in the literature. Of these few examples the hysteresis widths range from 70 K to around 100 K under high pressure and are thought to be a result of the formation of metastable phases and high cooperativity owing to intermolecular hydrogen bonding networks.[5-8] In the case of **9**(BF$_4$)$_2$ the abruptness and hysteretic nature of the transition was believed to be due to a sequence of three phase changes elucidated via powder diffraction, with only one of these being the LS phase of the sample.

In **9**$(BF_4)_2$ the thermal hysteresis width appears to be dependent on the history of the sample and repeated thermal scanning causes increased abruptness and a narrowing of the hysteresis width from 65 K – 37 K without affecting the transition temperature. It is not unheard of for thermal cycling of SCO complexes to trigger a gradual change to a phase with different SCO properties. However in this case the proposed cause of this phenomenon is that the repeated thermal cycling and continuous phase changes results in more crystal defects, smaller domains and a truer powder.[9] This is also the reason why the hysteresis loop stabilises after a number of scans (Figure 5.3).

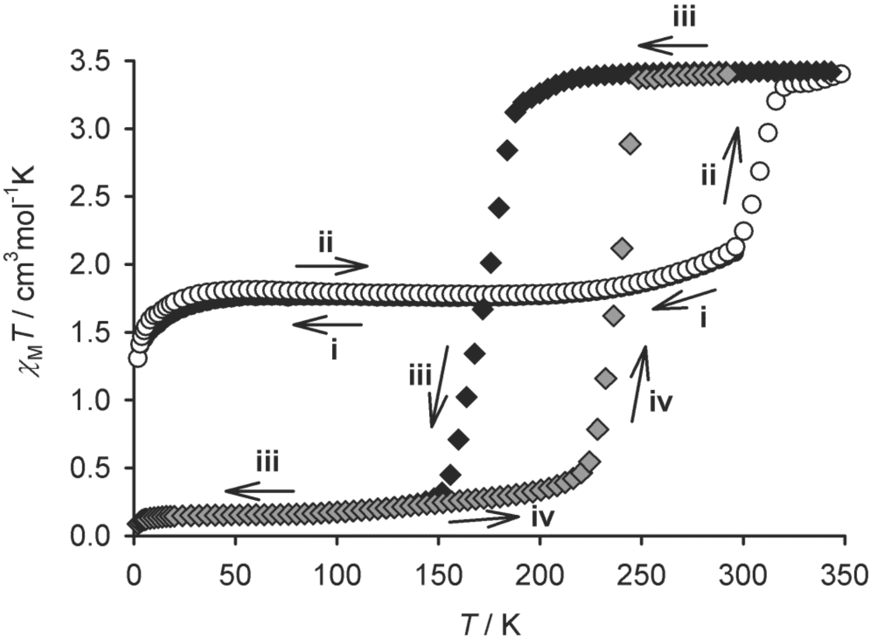

Figure 5.2
$\chi_M T$ *vs* T curves for **9**$(BF_4)_2{\cdot}2H_2O$ at a rate of 2 Kmin^{-1} in settle mode. (i) Cooling from 300-2 K; (ii) Warming from 2-350 K; (iii) Cooling from 350-2 K; (iv) Warming from 2-350 K.[1] Copyright © 2011, Royal Society of Chemistry.

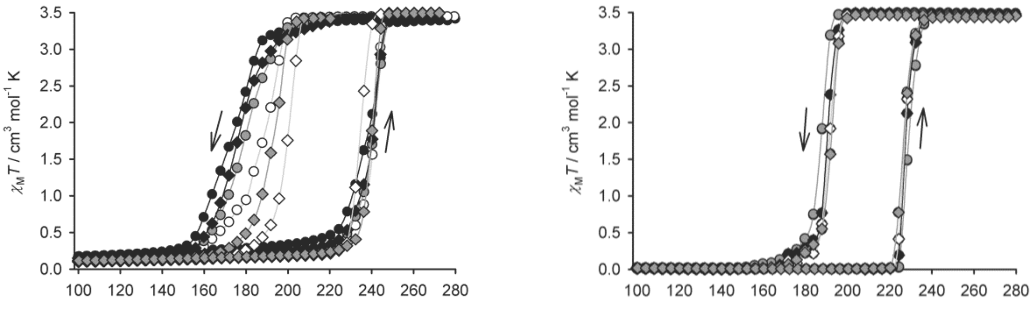

Figure 5.3
Repeated thermal scanning of a fresh sample (left) and a repeatedly dehydrated and rehydrated sample (right) at a scan rate of 2 Kmin^{-1} in settle mode. Scan 1 (●); scan 2 (○); scan 3 (●);scan 4 (■); scan 5 (◇); scan 6 (■).[1] Copyright © 2011, Royal Society of Chemistry.

Interestingly, crystal structures and powder diffraction data show that the perchlorate salt of this complex, **9**$(ClO_4)_2$, crystallises in isostructural hydrated and dehydrated phases to the tetrafluoroborate salt, however these phases show different magnetic behaviour.[10] While **9**$(BF_4)_2 \cdot 2H_2O$ formed by slow crystallisation from methanol/diethyl ether showed a 1:1 HS:LS ratio that remained unchanged from 2-300 K in cooling and warming modes, the isostructural perchlorate hydrate contains an ~85% HS fraction at 300 K and undergoes a complex hysteretic transition to afford a fully LS state at 110 K. In the cooling mode the sample undergoes an irregular decrease in $\chi_M T$ until a sudden drop at 265 K which is thought to be associated with a phase transition. $\chi_M T$ then continues to decrease irregularly until 120 K where an abrupt hysteretic transition to the fully LS state occurs (Figure 5.4). It is not clear from PXRD data whether or not a phase transition is responsible for the latter change in $\chi_M T$. Furthermore the isostructural dehydrated perchlorate and tetrafluoroborate salts obtained by thermal dehydration are both fully HS at 350 K, and both transition to isostructural HS phases between 295-303 K. However while the tetrafluoroborate undergoes two more phase changes below 295 K, the last of which leads to a fully LS phase, the perchlorate salt remains in the same fully HS phase over the entire temperature range and is devoid of any kind of spin transition.

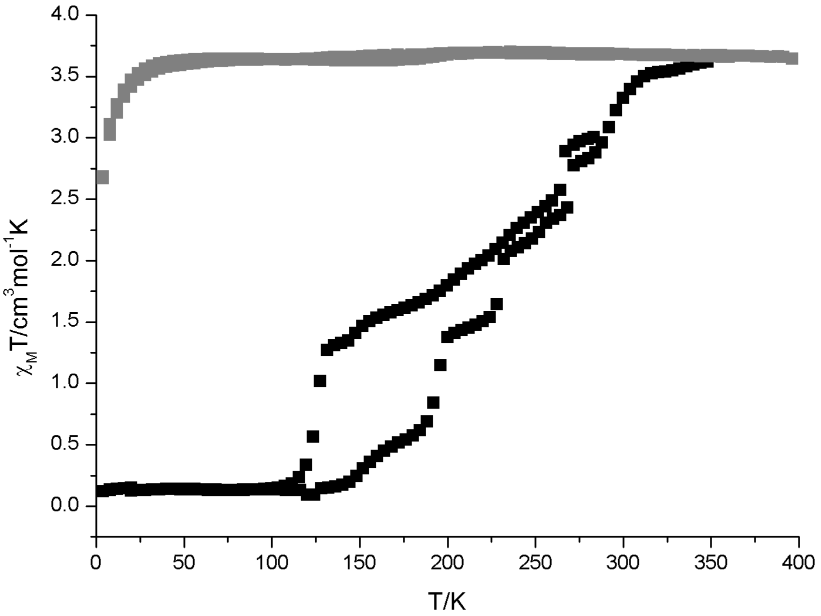

Figure 5.4
$\chi_M T$ *vs* T curves for **9**$(ClO_4)_2 \cdot 2H_2O$ (■) and **9**$(ClO_4)_2$ (■) recorded at a scan rate of 2 Kmin^{-1} in settle mode.[10] Copyright © 2011, Royal Society of Chemistry.

In light of these results it was in our interest to co-crystallise these two salts in differing proportions using the same recrystallisation methods. The behaviour of the crystalline mixed anion samples obtained was compared to the tetrafluoroborate and perchlorate salts previously described. In this vein it was hoped that light could be shed on the physical reasons for the discrepancy between the magnetic and phase behaviour of the two isostructural salts, or potentially create new phases with novel SCO behaviour.

5.2. Synthesis

The two salts **9**$(BF_4)_2$ and **9**$(ClO_4)_2$ were synthesised as previously described affording two red microcrystalline products.[1, 10] **9**$(BF_4)_2$ approximates as the dihydrate by microanalysis, whereas **9**$(ClO_4)_2$ was obtained as the dehydrate. These salts were then weighed out in molar proportions of 9:1, 3:1, 1:1 and 1:3 (all ratios in this work are quoted as BF_4^-:ClO_4^-) and dissolved fully in a small amount of methanol. These were then set up for slow vapour diffusion with diethyl ether to give large red plates, some of which were kept for structure determination via x-ray crystallography while the majority of the crystals were ground to make the bulk sample. It was on the bulk sample that variable temperature magnetic susceptibility measurements and powder diffraction data were obtained and the same sample was used for all the measurements to ensure consistency. A fresh sample of the 1:1 mixture was made for the repeated thermal scanning and scan rate study to ensure reproducibility. It was important when dissolving the salts in methanol that there was no solid remaining; if the solubility of the two salts differs slightly it could lead to inhomogeneity in the sample and molar proportions different to those intended.

It should be noted here that it is difficult to unambiguously confirm the existence of true solid solutions by most common bulk techniques. Microanalysis, thermogravimetric analysis (TGA) and powder diffraction would give the same results for a physical mixture of perchlorate and tetrafluoroborate crystals as they would for solid solutions. Probably the only available method to confirm the existence of solid solutions is single crystal x-ray diffraction as the anion site should give information about the composition; however these data are only available under certain circumstances. Even in the case that these data are available, as x-ray diffraction gives an average of the atomic positions there will be no information on possible domain structures within the crystal (domains consisting of exclusively perchlorate or tetrafluoroborate).

C,H,N and Cl microanalysis confirms that the complexes made are in the expected ratios and all of these mixtures approximate as their respective dihydrates. CHN analysis shows a difference between each of the complex mixtures and their parent salts, however this difference is quite small and could be caused by solvation by methanol and/or diethyl ether, however in each case Cl microanalysis shows the presence of chlorine from the perchlorate in the quantities expected. As these measurements were taken on the bulk sample, however, this is not evidence of co-crystallisation and the same results would be expected of a physical mixture of crystals.

Thermogravimetric analyses (TGA) were conducted on the bulk samples of 9:1, 3:1, 1:1 and 1:3 mixtures to determine the degree of solvation in the crystals (Figure 5.5). Initially all samples show an identical profile and gradually decrease in mass from ambient temperature until 100ºC, where the mass for each stabilises at around 95.5%. After this no further changes take place up until 300ºC, where the 9:1 mixture % weight gradually decreases due to decomposition and the % weight of the 1:3 mixture decreases abruptly to around 16%, indicating a perchlorate explosion. The 9:1, 3:1 and 1:1 mixtures were only taken up to a temperature of 300°C to avoid a perchlorate explosion. The initial decrease of around 4.5% in each case matches quite well with that calculated for the loss of two molecules of water per formula unit, showing that for each of these samples the expected dihydrate has been obtained (Table 5.1).

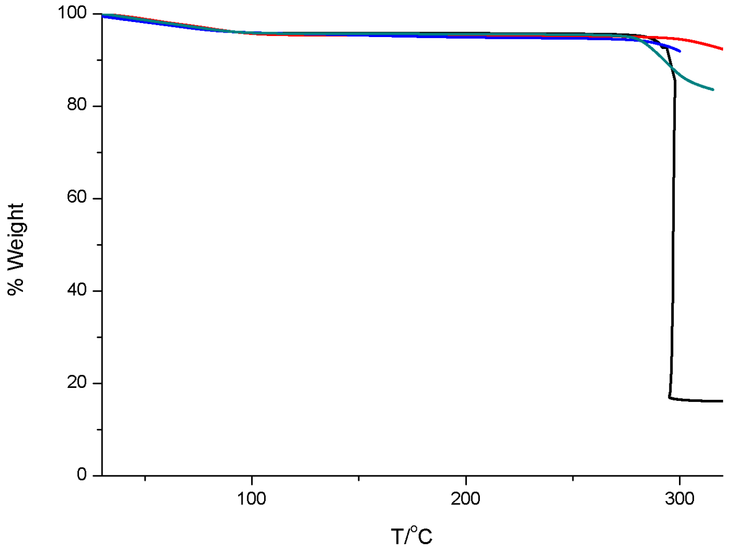

Figure 5.5
Thermogravimetric analysis of 9:1 (🟥), 3:1 (🟦), 1:1 (🟩) and 1:3 (⬛), mixtures of **9**$(BF_4)_x(ClO_4)_{2-x}\cdot H_2O$.

Table 5.1
Calculated % mass loss compared with experimental % mass loss obtained from thermogravimetric analysis of mixtures of **9**$(BF_4)_x(ClO_4)_{2-x}\cdot H_2O$.

Anion Ratio	Calculated Mass Loss (%)	Experimental Mass Loss (%)
1:3	4.86	4.22
1:1	4.66	4.32
3:1	4.80	4.90
9:1	4.78	4.66

5.3. Single Crystal X-Ray Diffraction Data

One of the few methods to unambiguously confirm co-crystallisation of the two salts is single crystal x-ray diffraction. A crystal structure of a mixed anion complex will also be useful to compare to the structures obtained for the isostructural tetrafluoroborate and perchlorate salts. Single crystal x-ray diffraction data were obtained for the 1:3, 3:1 and 9:1 mixtures of **9**$(BF_4)_x(ClO_4)_{2-x}$. In all these cases, however, the crystals used were weakly diffracting and gave poorly resolved data due to the large disorder in the anions. The data that gave the best solution was that of the 3:1 mixture at 290 K. This temperature was used because at lower temperatures a large proportion of the spots in the diffraction pattern did not match the suggested unit cell and this could be a result of cooling the sample too quickly in the cryostream, leading to an incomplete phase change.

The data were solved in the tetragonal space group $P4_2/n$ (a = 9.6249(16); b = 9.6249(16); c = 18.146(4) Å, $\alpha = \beta = \gamma$ = 90º, V = 1681.1(5) Å^3), and appears to be isostructural to the dehydrated phase of **9**$(BF_4)_2$ which was obtained by crystallisation in anhydrous solvents. This dehydration could be caused by running the crystal at a relatively high temperature under a stream of dry nitrogen as the microanalysis of the bulk sample approximates as the dihydrate, and the isostructural anhydrous tetrafluoroborate salt is known to readily take up atmospheric water.

Like the parent salt structures, the dication and anion sites are intersected by four-fold rotoinversion axes running parallel to the crystallographic c axis, and for the dication this runs down the length of the Fe–N$_{\text{pyridine}}$ bond resulting in an asymmetric unit containing quarter of a complex molecule (Figure 5.6). The disordered anion site lies on a C_2 axis and restraints were applied to the bonds. The occupancies of BF_4^- and ClO_4^- refine well as 0.75and 0.25 respectively, and it is possible to distinguish the two anion sites because of the significantly larger electron density of Cl compared to B. This serves to support the notion that this particular sample is a co-crystalline product containing both tetrafluoroborate and perchlorate anions within the crystal lattice, rather than a mixture of separate crystals. This structure exhibits the same terpyridine embrace packing motif which is usually associated with cooperative spin transitions (Figure 5.7). Therefore any discrepancy in the magnetic measurements and powder diffraction is likely to be caused by perturbations caused by the mixed anion sites.

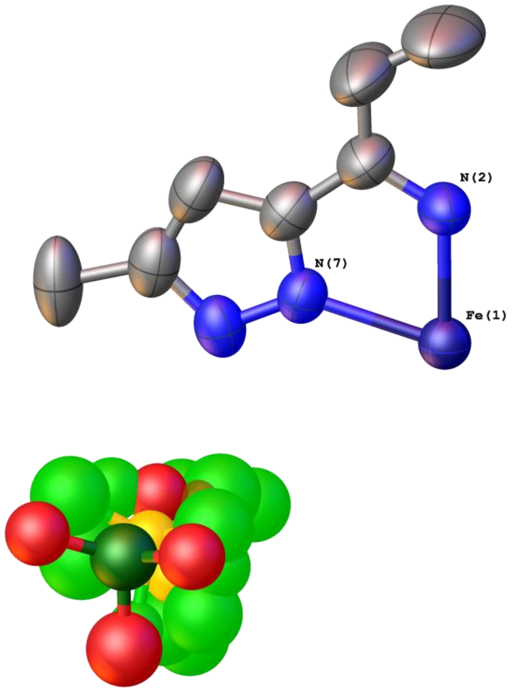

Figure 5.6
Crystal structure of the 3:1 mixture of **9**$(BF_4)_x(ClO_4)_{2-x}$. Thermal displacement ellipsoids are set at 50% probability and hydrogens have been omitted.

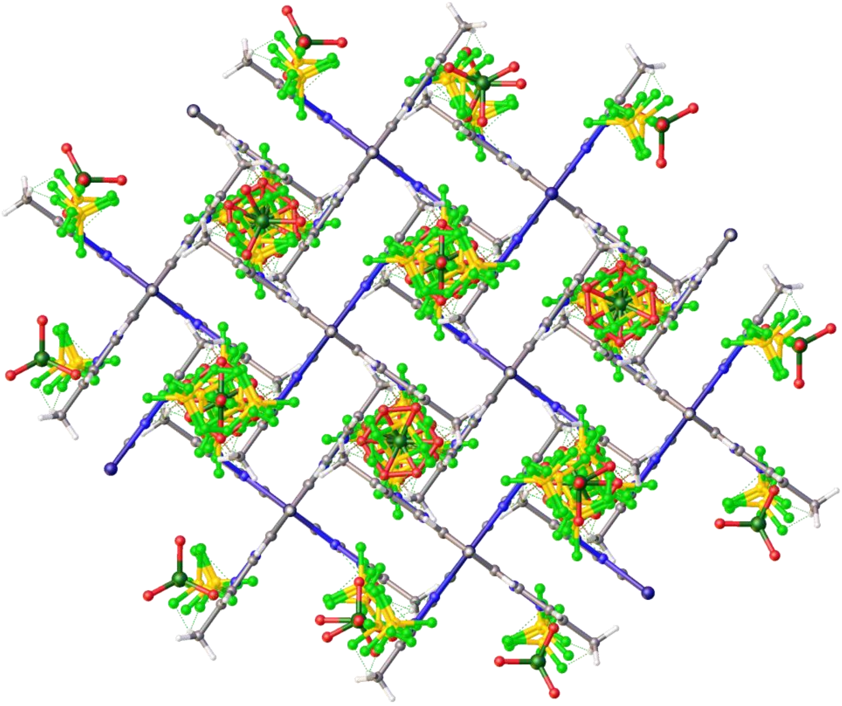

Figure 5.7
Packing diagram of the 3:1 mixture of **9**$(BF_4)_x(ClO_4)_{2-x}$.

Table 5.2
Selected geometric parameters of the iron centre in the 3:1 mixture of **9**$(BF_4)_x(ClO_4)_{2-x}$.

	9$(BF_4)_x(ClO_4)_{2-x}$ **(3:1)**
Fe-PyN (Å)	2.128(7)
Fe-PzN (Å)	2.195(5)
α(°)	147.0(3)
θ(°)	90.000(9)
ϕ(°)	180.00(17)
Σ(°)	150.72
Θ(°)	341.44

While this solution has low accuracy for the bond lengths and angles due to the poor quality of the data obtained, it can still be observed that the Fe–N bond lengths are in the range of those expected for a HS iron(II) complex and are well within the error (Table 5.2). This is also confirmed by the magnetic susceptibility measurements which will be discussed in detail in section **5.4**. The crystal structure shows that the HS state of this complex is very regular and shows a relatively low value for the rhombic distortion parameter, Σ, of 150.72º, indicating little deviation from an ideal octahedral geometry. The angle between the two ligand planes, θ, and the *trans* angle between the two $N_{pyridine}$–Fe–$N_{pyridine}$ bonds, ϕ, are exactly the ideal of 90º and 180º respectively, also indicating a more ideal octahedral coordination and the absence of any Jahn-Teller distortions. This ordered structure could be a result of the highly ordered terpyridine embrace structure as highly distorted complexes would not be able to interlock in such a manner.[4]

The terpyridine embrace motif extends in 2 dimensional layers in the *ab* crystallographic plane and is separated by layers of disordered anions which fit into the grooves formed by the perpendicular pyridine rings. The anions are then able to accept hydrogen bonds from the pyrazolyl NH groups. The distance between neighbouring pyrazolyl groups is 3.600(13) Å which is just outside the combined Van Der Waals radii of carbon, 3.4 Å, required for full π-π overlap and this could be a consequence of the methyl groups preventing closer proximity of the dications.

Although sufficient diffraction for full structure determination was only observed for the 3:1 mixture, data were also collected for the 1:3 and 9:1 mixtures. While the quality of the data were not sufficient to allow a full solution it did give accurate information about the unit cells and space group which could be used for comparison with the hydrated and anhydrous phases of the pure tetrafluoroborate and perchlorate salts (Table 5.3 and Table 5.4).

Table 5.3
Tabulated unit cell parameters for the different solvates of **9**$(BF_4)_2$ and **9**$(ClO_4)_2$.[1, 10]

	9$(BF_4)_2\cdot 2H_2O$	**9**$(BF_4)_2$	**9**$(ClO_4)_2$	**9**$(ClO_4)_2\cdot 2MeOH$
Crystal System	Tetragonal	Tetragonal	Tetragonal	Monoclinic
Space Group	$I4_1/a$	$P4_2/n$	$P4_2/n$	$P2_1/n$
a (Å)	13.7494(19)	9.7481(2)	9.7396(3)	13.6553(12)
b (Å)	13.7494(19)	9.7481(2)	9.7396(3)	19.7246(11)
c (Å)	35.336(3)	17.6848(5)	18.0080(8)	13.6951(15)
α (°)	90	90	90	90
β (°)	90	90	90	91.326(5)
γ (°)	90	90	90	90
V (Å^3)	6680.2(14)	1680.51(7)	1708.24(11)	3687.7(6)
T (K)	150(2)	150(2)	150(2)	150(2)

Table 5.4
Tabulated unit cell parameters for the mixed anion complexes **9**$(BF_4)_x(ClO_4)_{2-x}\cdot xH_2O$. ‡A good solution could not be found due to poor data, other possible space groups are *Pmmn* and $P2_12_12_1$.

	9$(BF_4)_x(ClO_4)_{2-x}\cdot xH_2O$ (1:3)	**9**$(BF_4)_x(ClO_4)_{2-x}\cdot xH_2O$ (3:1)	**9**$(BF_4)_x(ClO_4)_{2-x}\cdot xH_2O$ (9:1)
Crystal System	Tetragonal	Tetragonal	Orthorhombic
Space Group	$P4_2/n$	$P4_2/n$	$P112_1/n$‡
a (Å)	9.6422(13)	9.6249(16)	9.7152(3)
b (Å)	9.8269(19)	9.6249(16)	9.7152(3)
c (Å)	17.814(3)	18.146(3)	17.6363(8)
α (°)	90	90	90
β (°)	90	90	90
γ (°)	90	90	90
V (Å^3)	1687.93	1681.1(5)	1664.6
T (K)	110.0(2)	290.15	110.02(16)

From the data collected for the 1:3 complex, a solution was obtained for the dication but the disordered anion site could not be modelled. From this partial solution it was deemed likely that this complex is isostructural to both the 3:1 mixture, the dehydrated tetrafluoroborate and the dehydrated perchlorate (which was determined by comparison of the powder pattern), as the space group and unit cell dimensions are almost identical. The microanalysis of this complex approximates as the dihydrate and TGA shows a loss of mass consistent with the loss of two equivalents of water, however from this x-ray data the degree of hydration is not clear. Judging by the phase behaviour of the pure tetrafluoroborate this is more likely to be the dehydrated phase.

Data obtained for the 9:1 mixture was the poorest and it was not possible to solve a structure in any of the three most likely space groups. The data collected suggests this structure packs in an orthorhombic unit cell, unlike any of the other structures which are mainly tetragonal with the exception of the monoclinic structure of **9**$(ClO_4)_2{\cdot}2MeOH$. The methanol solvate was obtained from the perchlorate via the same slow vapour diffusion method from methanol/diethyl ether mixtures, but was preferentially formed when a higher concentration of the complex solution was used. In order to obtain crystals of the dihydrate, diethyl ether had to be diffused into a dilute solution of **9**$(ClO_4)_2$. In the case of the 9:1 mixture, although it is a different crystal system, the unit cell dimensions closely resemble those of the dehydrated forms and the structure is likely to be related. TGA and microanalysis support the assumption that this is the dihydrate, although it could have lost its water during the data collection. Because the data were so poor, however, there is no evidence to support this. If this mixture existed as the dimethanol solvate the expected mass loss in the TGA would be around 18.0%, much higher than the observed mass loss of 4.7% that correlates with the loss of two equivalents of water.

While the structure obtained for 3:1 mixture of **9**$(BF_4)_x(ClO_4)_{2-x}$ refines well using the expected ratios of BF_4^-:ClO_4^-, it is not certain whether this applies for the other mixtures as electron density in the anion site could not be assigned. It is possible that certain arrangements may crystallise preferentially regardless of the composition of the solution and that the bulk sample consists of a mixture of crystals which satisfy microanalysis. If this is the case it may become apparent in the magnetic susceptibility measurements as the magnetic behaviours of the two parent salts are known.

5.4. Magnetic Susceptibility

In order to investigate the effect of the anion doping on SCO behaviour variable temperature magnetic susceptibility measurements of the complex salt mixtures were recorded using a SQUID magnetometer. For these measurements there are two modes of temperature variation; sweep, in which the temperature is constantly varied and data points are measured at intervals, and settle where the temperature at each data point is stabilised before taking a measurement. It has been shown that kinetics can play a significant role in the shape of the χ_MT *vs* T curves and so the scan rate and mode of temperature variation become very important.[11] In the cases presented here a mixture of sweep and settle modes were used, however this was seen to have little effect on the spin curves and the scan rate appeared to be the more important factor. Where possible sweep mode was preferred as it was less time consuming and allowed more data to be collected. Firstly the magnetic susceptibility of the mixed anion complexes were obtained at a scan rate of 2 Kmin^{-1} and the shape of their χ_MT vs. T curves were compared to one another and their parent salts.

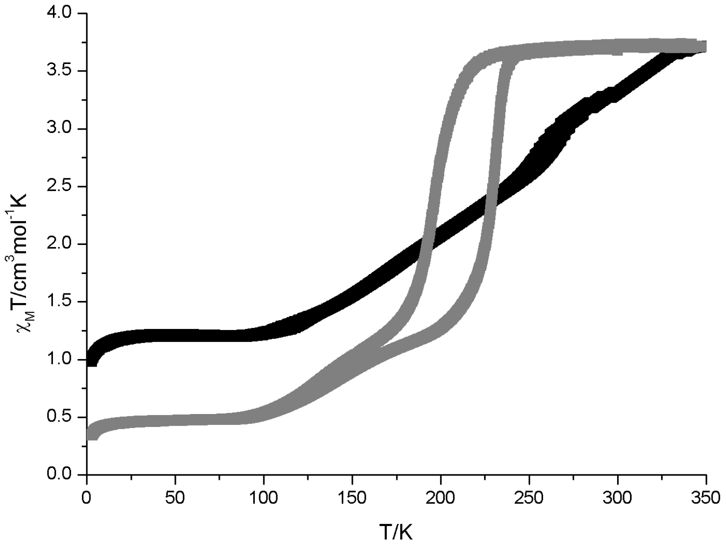

Figure 5.8
χ_MT *vs* T curves of the 1:3 mixture of **9**$(BF_4)_x(ClO_4)_{2-x}\cdot 2H_2O$. Temperature sequence: 300-2-350 K (■), 350-2-300 K (■). Scan rate 2 Kmin^{-1} in sweep mode.

To obtain the magnetic susceptibility for the 1:3 mixture the sample was first cooled at 2 Kmin^{-1} from 300 K to 2 K. From 300-250 K the curve resembles the gradual and irregular nature of **9**$(ClO_4)_2\cdot 2H_2O$ (Figure 5.8). Below 250 K the sample does not switch to the abrupt hysteretic transition seen in **9**$(ClO_4)_2\cdot 2H_2O$ and instead gradually decreases before levelling out below 100 K at an χ_MT value of 1.2 $cm^3mol^{-1}K$, corresponding to roughly 30% remaining HS centres. This implies that there could be a roughly 30% phase impurity which remains fully HS down to 2 K, and this phase could be similar to **9**$(ClO_4)_2$ which maintained a constant χ_MT value of 3.6 $cm^3mol^{-1}K$. The sample was then warmed from 2-350 K and followed the same path as the cooling cycle with χ_MT gradually continuing to increase past room temperature to a final value of 3.7 $cm^3mol^{-1}K$ expected for a fully HS complex. Warming to this temperature removes the lattice water and could cause a phase transition. As the sample is cooled it remains at a constant value of 3.7 $cm^3mol^{-1}K$ until 227 K where it decreases abruptly before becoming more gradual and eventually settles at a value of 0.5 $cm^3mol^{-1}K$ at 94 K. This value corresponds to approximately 14% of the iron centres remaining HS, which again could be a phase impurity. Heating the sample follows a similar pattern, except the abrupt part of the transition shows a hysteresis loop with a width of 32 K, similar to the hysteresis width for **9**$(BF_4)_2$ after repeated thermal cycling.

By comparison of the χ_MT *vs* T curves of the mixtures a transition towards the behaviour of **9**$(BF_4)_2{\cdot}2H_2O$ can be observed (Figure 5.9). The 1:3 and 1:1 mixtures follow a very similar profile to one another with the 1:1 mixture shifted 0.3 $cm^3mol^{-1}K$ lower and showing what appears to be a small hysteresis loop between 257 K and 314 K. The 3:1 and 9:1 mixtures show an increasing minimum χ_MT value which more closely resembles that of the pure tetrafluoroborate dihydrate which had a 50% HS fraction from 2-300 K. In these mixtures the onset of the χ_MT increase is raised to a higher temperature and becomes more abrupt, also suggesting a movement towards the behaviour of **9**$(BF_4)_2{\cdot}2H_2O$. These measurements were all recorded at a scan rate of 2 $Kmin^{-1}$, however the 1:3 and 9:1 mixtures were run in sweep mode and the 1:1 and 1:3 mixtures were run in settle mode.

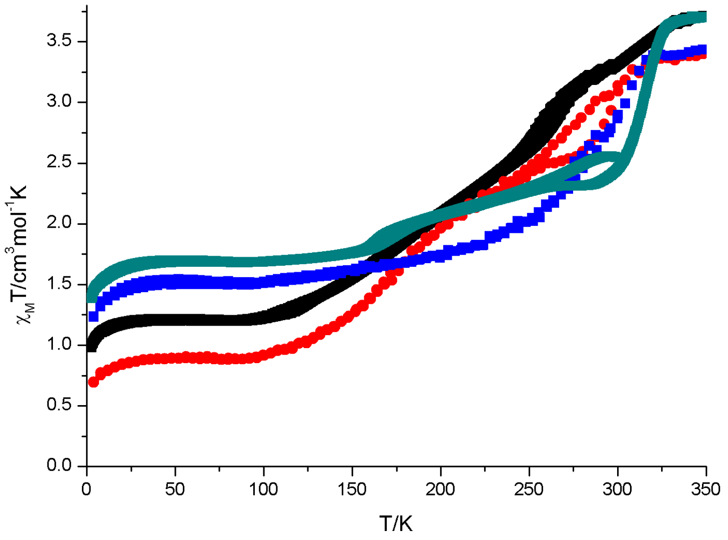

Figure 5.9
$\chi_M T$ *vs* T curves for the initial 300-2-350 K cycle for the mixtures of **9**$(BF_4)_x(ClO_4)_{2-x}\cdot 2H_2O$. Mixtures: 1:3 (■); 1:1 (●); 3:1 (■); 9:1 (■).

After being warmed to 350 K all four mixtures showed a change in their $\chi_M T$ *vs* T curves indicating that, like the parent salts, they have lost their lattice water and formed a new phase that undergoes an abrupt hysteretic spin transition. This transition is centred around 213 K and remains unchanged for the different mixtures and the maximum and minimum values for $\chi_M T$ are quite similar. None of the mixtures reach a minimum value of 0 $cm^3mol^{-1}K$ indicating that there may be some kind of phase impurity which does not reach a fully LS state, however this is much less apparent than for the dihydrate. There is a noticeable difference in the form of the hysteresis loop in the different mixtures. The 1:3 mixture has a hysteresis width of 32 K, and begins to lose its hysteresis becoming more gradual at the lower end of the loop, indicating a loss of cooperativity. For the 1:1 and 3:1 mixtures the hysteresis width is the same but the change in gradient is less pronounced and begins to look like that obtained for **9**$(BF_4)_2$ after repeated thermal cycling. Lastly for the 9:1 mixture the upper part of the hysteresis loop is quite similar to the other mixtures but as the temperature drops in the cooling mode the gradient changes twice, while the warming mode follows a more standard discontinuous transition. This widens the hysteresis width at the bottom to a maximum of 88 K, even wider than that recorded for a freshly prepared sample of **9**$(BF_4)_2$ and among the widest recorded in the literature for an iron complex at ambient pressure (Figure 5.10).

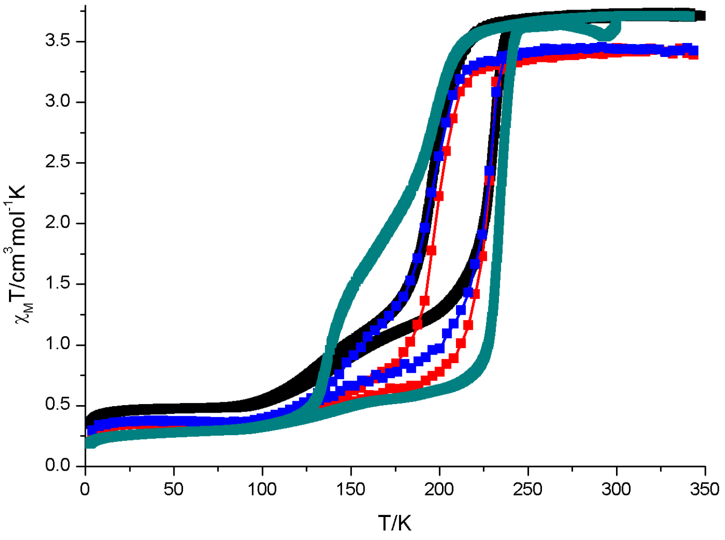

Figure 5.10

$\chi_M T$ *vs* T curves for the secondary 350-2-300 K cycle for the mixtures of **9**$(BF_4)_x(ClO_4)_{2-x}\cdot 2H_2O$. Mixtures: 1:3 (■); 1:1 (🟥); 3:1 (🟦); 9:1 (■). Data points have been connected with a spline curve for clarity.

5.4.1. The Effect of Thermal Cycling

The hysteresis width for these mixtures is around 32 K, which is similar to the 37 K observed for **9**$(BF_4)_2$ after repeated thermal scanning. The narrowing of the hysteresis is most likely due to the repeated phase changes which cause defects within the microcrystals and reduce the size of the domains in the crystal. It has been observed that reducing the domain size by mechanical grinding leads to narrower and less symmetric hysteresis loops.[12] It has long been known that hysteresis in a material requires the presence of some kind of domain formation proceeding through a nucleation event, which in the case of SCO would be a cluster of centres of one spin state existing in the metastable spin state.[13] Once these clusters reach a size where their energy is lower than that of the surrounding metastable phase, the new phase propagates through the crystal and this movement has even recently been observed in real time on a macroscopic scale.[14]

As the hysteresis loop of the mixed anion complexes was narrow and asymmetric it was predicted that the crystals contain more defects than a freshly prepared sample of **9**$(BF_4)_2$. If this is the case they already have a smaller domain size therefore repeated scanning will not have such a profound effect on the hysteresis loop.

Repeated thermal scanning of the 3:1 mixture at 2 Kmin^{-1} in settle mode shows that the sample begins with a χ_MT *vs* T curve that resembles **9**$(ClO_4)_2\cdot 2H_2O$, before gradually beginning to produce a typical abrupt hysteresis loop. The second scan produces an asymmetric hysteresis loop with a width of around 35 K and on the third scan this widens to 83 K, a similar width to the hysteresis of the 9:1 mixture at its widest point. On the cooling mode the χ_MT undergoes what looks similar to a two step spin transition with a plateau before an abrupt drop. This looks like a distorted version of the curve for the 9:1 mixture where the widened part of the loop is extended upward past 3.2 cm^{3}mol^{-1}K to give the majority of the hysteresis a width of 83 K (Figure 5.11).

After the fourth scan the material gives an almost symmetric hysteresis with a constant width of 50 K and the sample does not undergo further change on additional scans. This occurs more rapidly in this material than for **9**$(BF_4)_2$ which took over six thermal scans before it reached consistency. Interestingly the hysteresis observed for this 3:1 mixture after repeated thermal scans is both wider than that of the initial scan in Figure 5.10 and the aged sample of **9**$(BF_4)_2$, however it is important to note that these measurements were conducted on the same sample after the initial scans previously shown. It is possible that the strange shape of the first curve could be a result of full dehydration from the initial two scans followed by partial rehydration.

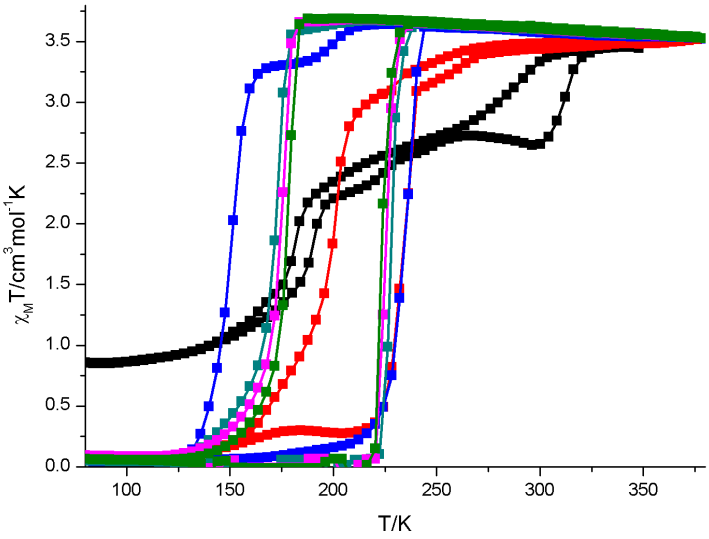

Figure 5.11
Repeated thermal scanning of the 3:1 mixture of **9**$(BF_4)_x(ClO_4)_{2-x}\cdot 2H_2O$ recorded at a scan rate of 2 Kmin^{-1} in settle mode. Scan 1 (■); scan 2(■); scan 3 (■); scan 4(■); scan 5 (■); scan 6 (■).

This was the behaviour which was expected of these complex salt mixtures on repeated thermal cycling, however the 1:1 mixture showed very different behaviour under these conditions. The first three scans look very similar and resemble that of **9**$(BF_4)_2{\cdot}2H_2O$, apart from the transition to the fully HS state shows some hysteresis. After the third scan the maximum temperature was increased from 350 K to 380 K which caused a sudden change in shape of the curves to something more closely resembling an abrupt hysteresis loop, although very asymmetric and showing undulations before the transition in the warming mode. The reason for these undulations are not clearly understood but may be a result of structural changes.[15] On the fifth thermal scan the onset of the hysteresis loop is abrupt and quite regular with a width of 30 K, and looks quite similar to those obtained for the dehydrated mixtures. In the cooling mode $\chi_M T$ levels out at 1.2 $cm^3mol^{-1}K$ at 190 K before dropping again at 128 K to a value of 0.5 $cm^3mol^{-1}K$ in what looks similar to a two step transition. In the warming mode at 128 K there is a small undulation and then $\chi_M T$ drops to 0.4 $cm^3mol^{-1}K$ and then begins to rise abruptly after 200 K giving an odd “L” shaped hysteresis loop (Figure 5.12).

On the sixth scan the cooling mode undergoes a similar two step decrease in $\chi_M T$ except with very different proportions and it comes to settle below 115 K at a much higher value of $\chi_M T$ = 2.4 $cm^3mol^{-1}K$. The warming mode of this scan is particularly interesting as at 124 K $\chi_M T$ decreases abruptly to a plateau with value of 0.5 $cm^3mol^{-1}K$ before increasing abruptly at 198 K back to the fully HS state. The seventh scan also shows this behaviour, except with a higher value for $\chi_M T$ below 115 K of 2.3 $cm^3mol^{-1}K$ and a lower plateau value of 0.3 $cm^3mol^{-1}K$ with more abrupt transitions in the warming mode (Figure 5.13). These hysteresis loops are extremely interesting because they show a very significant and abrupt decrease in $\chi_M T$ *vs* T caused by an increase in temperature, which is usually thermodynamically disfavoured in SCO systems. As the HS state has a higher electronic and vibrational entropy it is the favoured state at higher temperatures, and reverse spin transitions have been observed in Co(II) complexes which exhibit terpyridine embrace structures which is usually attributed to a large structural change.[16-18]

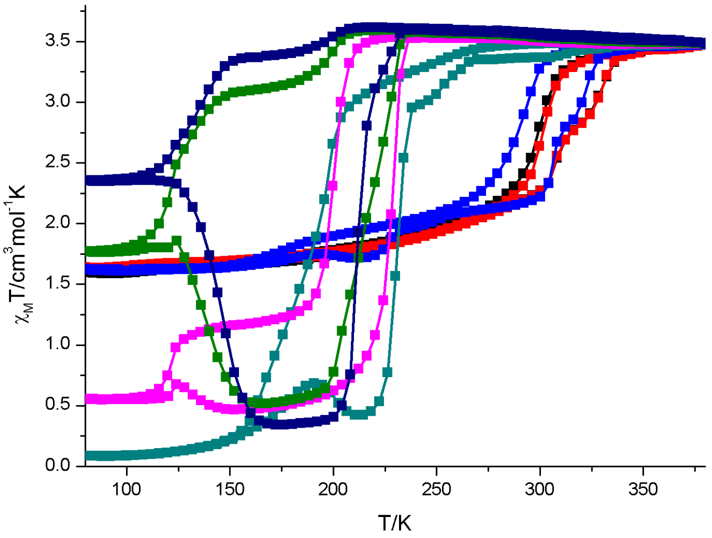

Figure 5.12
Repeated thermal scanning of the 1:1 mixture of **9**$(BF_4)_x(ClO_4)_{2-x}\cdot 2H_2O$ recorded at a scan rate of 2 Kmin^{-1} in settle mode. Scan 1 (■); scan 2(■); scan 3 (■); scan 4(■); scan 5 (■); scan 6 (■); scan 7 (■).

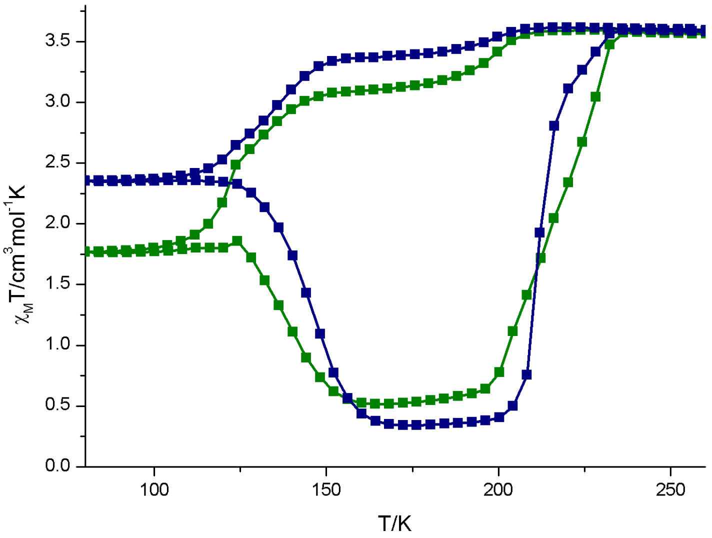

Figure 5.13
Expanded view of the $\chi_M T$ *vs* T curves for scan 6 (■) and scan 7 (■) of the 1:1 mixture of **9**$(BF_4)_x(ClO_4)_{2-x}\cdot 2H_2O$ at a scan rate of 2 Kmin^{-1}.

These data were then checked for reproducibility. A freshly prepared sample of the 1:1 mixture of **9**$(BF_4)_x(ClO_4)_{2-x}$ was placed in the sample tube used for the SQUID magnetometer and annealed at 80ºC overnight, then quickly sealed with sealing tape while still hot and placed in the magnetometer as quickly as possible. After heating overnight the sample goes from a red to a yellow colour indicating that dehydration has occurred. The magnetometer chamber is under vacuum so once the measurements are running it is unlikely that the sample will become rehydrated. This was confirmed after the measurements when the sample was still a yellow colour and remained as such for over a day showing that the tube was well sealed. The sample was annealed because it was hoped that the χ_MT *vs* T curve shown in Figure 5.13 could be attained much more quickly without numerous thermal cycles. It was also of concern that when the sample is dehydrated at the higher temperatures the water cannot easily escape the sample holder causing partial formation of the hydrate when the temperature is reduced.

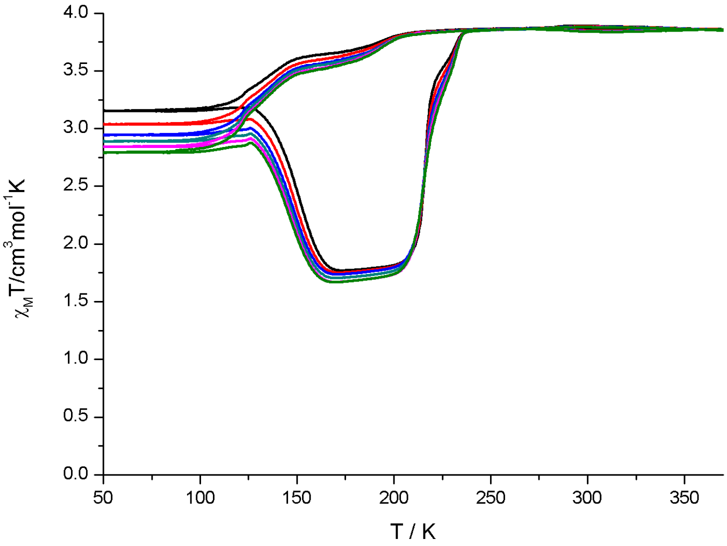

Figure 5.14
Repeated thermal scanning of the annealed 1:1 mixture of **9**$(BF_4)_x(ClO_4)_{2-x}\cdot 2H_2O$ recorded at a scan rate of 2 Kmin^{-1} in settle mode. Scan 1 (■); scan 2 (■); scan 3 (■); scan 4 (■); scan 5 (■); scan 6 (■). The curves are shown as lines for clarity.

The resulting χ_MT *vs* T curves for the annealed sample show more consistency than for the un-annealed sample and the χ_MT value for the plateau in the warming mode ranges from 1.7-1.8 cm^{3}mol^{-1}K compared with a minimum of 0.3 cm^{3}mol^{-1}K for the un-annealed sample (Figure 5.14). Although they are more consistent, these curves do show a small variation, the most significant being the decrease of the χ_MT value that the sample settles at below 115 K, which decreases in small increments for every scan. This contrasts with the un-annealed sample where this value increases significantly for every thermal scan. What should also be mentioned is that these measurements were recorded for a different sample on a different

SQUID magnetometer in sweep mode, whereas the data for the un-annealed sample were collected in settle mode.

5.4.2. The Effect of Thermal Scan Rate

It is already known that in some cases the thermal scan rate can greatly affect the nature SCO behaviours.[11, 19] In one instance the same material has been shown to contain two distinct hysteresis loops depending on whether it was cycled at 4 $Kmin^{-1}$ or 0.1 $Kmin^{-1}$, a difference which was attributed to slow kinetics of the HS→LS phase transition which leads to a freezing in of the metastable HS state at lower temperatures.[20] This example exhibits some of the undulations which are also observed in Figure 5.12. For this reason it was important to investigate the effect of the thermal scan rate on the 1:1 mixture of **9**$(BF_4)_x(ClO_4)_{2-x}$ in order to investigate whether this thermal trapping hypothesis can be applied to explain the bizarre behaviour observed in the magnetic moment. These measurements were recorded on the same sample and on the same magnetometer used for the results shown in Figure 5.14, and the sample was fully dehydrated by annealing at 80ºC overnight.

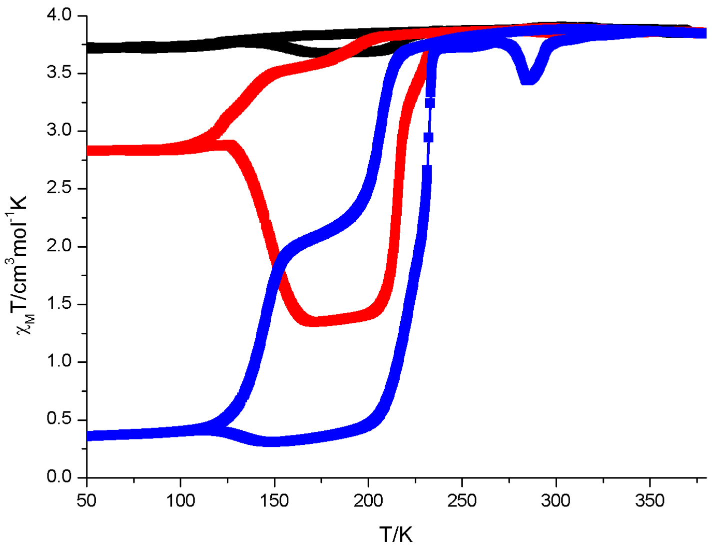

Figure 5.15
χ_MT *vs* T curve of the annealed 1:1 mixture of **9**$(BF_4)_x(ClO_4)_{2-x}\cdot 2H_2O$ at scan rates of 5 $Kmin^{-1}$ (■), 2 K min^{-1} (🟥) and 0.5 $Kmin^{-1}$ (🟦) in sweep mode.

These results show that the SCO behaviour of this sample is extremely dependant on the thermal scan rate. At the relatively fast scan rate of 5 Kmin^{-1} the sample remains in the fully HS state from 370-50 K and shows only a small drop in χ_MT between 150-236 K in the warming mode, indicating that the sample has remained trapped in its HS phase. Conversely, at a scan rate of 0.5 Kmin^{-1} the sample appears to show abrupt two step transitions in the cooling mode down to a χ_MT value which corresponds to only 16% HS iron centres and only a slight drop is observed at 120 K before an abrupt transition to the fully HS state. This behaviour could be due to the existence of two phases, one which remains fully HS and the other which undergoes a spin transition seen in the 0.5 Kmin^{-1} scan with a kinetically slow interconversion between the two. This is seen most clearly in the 2 Kmin^{-1} scan, which in the cooling mode shows a very similar two step decrease in χ_MT which only reaches a minimum value of 2.8 cm^{3}mol^{-1}K indicating that around 73% of the iron centres remain trapped in their metastable HS state (Figure 5.15). The abrupt drop in χ_MT after 125 K in the warming mode could follow a similar mechanism to that observed for the LIESST effect, where once the temperature is increased past a certain point tunnelling from the vibrational levels in the metastable HS state allow access to the more thermodynamically stable LS state.[21, 22]

5.5. Variable Temperature Powder Diffraction

Powder x-ray diffraction on these samples allows for a quick comparison of the different points in the magnetic profiles and can be used to easily distinguish the different phase changes which occur as the temperature is varied. Variable temperature powder x-ray diffraction (VTPXRD) data were collected for the 1:3 and the 9:1 mixtures as their magnetic behaviour showed the most considerable differences. When both samples were run it was noticed that under reduced pressure at room temperature the powders slowly transformed their phase over a few minutes, which is believed to be due to water escaping from the lattice and inducing a phase change. The mixtures were then heated to 350 K and then cooled at 2 Kmin^{-1} to the lowest temperature possible on the machine (usually 150 K) before being warmed back to 300 K in a similar manner to the experiment inside the SQUID magnetometer.

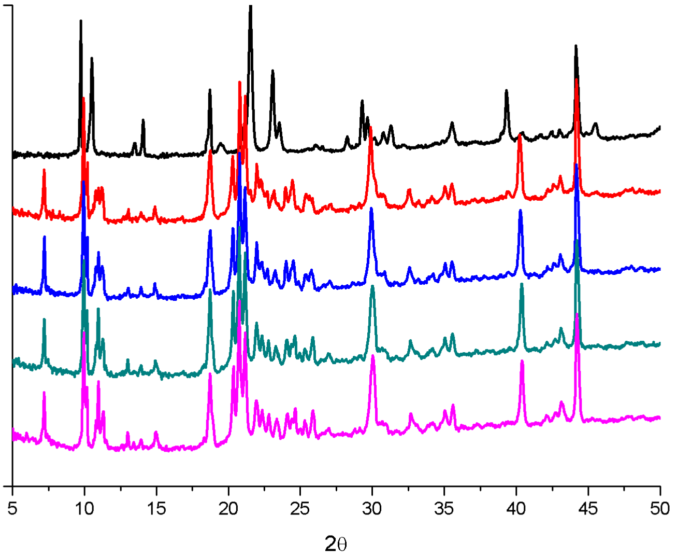

Figure 5.16
VTPXRD data for the cooling mode of the 1:3 mixture of **9**$(BF_4)_x(ClO_4)_{2-x}\cdot 2H_2O$ with a fixed slit correction applied. Temperatures: 353 K (■); 253 K (🟥); 231 K (🟦); 166 K (■); 149 K (■).

For the 1:3 mixture of **9**$(BF_4)_x(ClO_4)_{2-x}\cdot 2H_2O$ the data for the cooling cycle are almost identical to that obtained for the warming cycle (Figure 5.16). These data show that there is quite a clear phase change between 353 K and 253 K and then no subsequent phase changes. This is similar to the annealed perchlorate salt which undergoes a transition between these temperatures and the similar powder pattern at 353 K indicates that these are possibly isostructural. The second phase formed below 353 K, however, seems to show a different powder pattern not isostructural to any observed in the pure perchlorate.

The powder pattern at 353 K also matches well with the powder pattern calculated from the crystal structure obtained for the 3:1 mixture and shows that they are likely to be isostructural (Figure 5.17). The collected powder pattern does show a small number of additional peaks which might be evidence of a phase impurity and may have been avoided if the sample were annealed for longer at a higher temperature. Interestingly it is known that this sample undergoes a spin transition from the $\chi_M T$ *vs* T curves discussed in **5.4**, so it would seem that this abrupt, hysteretic spin transition the likes of which that are usually associated with structural changes occurs without a phase transition. This means that assuming the conditions in the diffractometer are the same as those in the SQUID magnetometer, this magnetic behaviour is more likely to be a result of a high degree of cooperativity in the lattice.

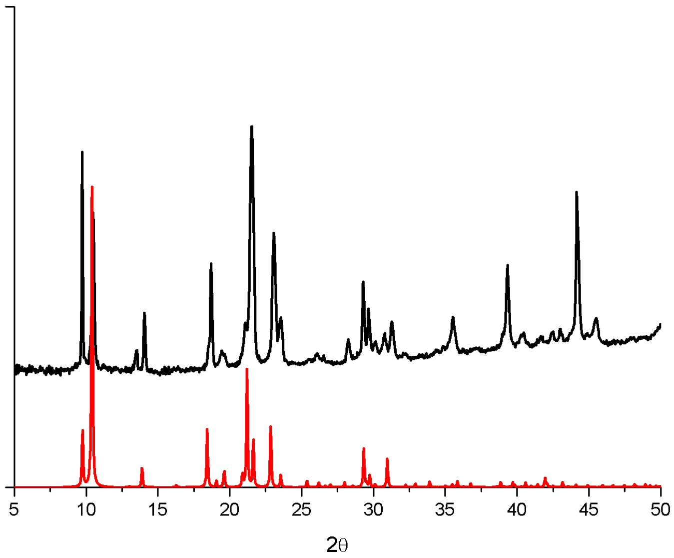

Figure 5.17
Comparison of the PXRD data obtained via experiment for the 1:3 mixture of **9**$(BF_4)_x(ClO_4)_{2-x}\cdot 2H_2O$ (■) with that calculated from the crystal structure of the 3:1 mixture of **9**$(BF_4)_x(ClO_4)_{2-x}\cdot 2H_2O$ (🟥).

When the experiment was repeated with the 9:1 mixture and the chamber was evacuated a sudden loss of solvent occurred which dispersed the sample up the vacuum line. This was unrecoverable however there was enough sample left to run VTPXRD measurements using a silicon chip. While the data are poorer it can still be used as a comparison to that already collected and calculated for other salts. The powder patterns show that there is a significant phase change when a vacuum is applied to the sample, which is probably due to the loss of lattice water (Figure 5.18). This is not a problem however because the new phase formed is isostructural to **9**$(BF_4)_2$ at 350 K and it is the dehydrated sample that has shown the most interesting behaviour. From the data obtained there are clearly two phase transitions, one between 353 K and 253 K, and the other between 231 K and 150 K (Figure 5.19). The warming cycle was identical to the cooling cycle and the patterns at each temperature match up perfectly so only the cooling cycle is shown in Figure 5.19. Although the powder patterns at different temperatures show some differences suggesting a change is taking place they still all show a number of common peaks suggesting that all the phases observed are very similar and probably another variant of the terpyridine embrace structure.

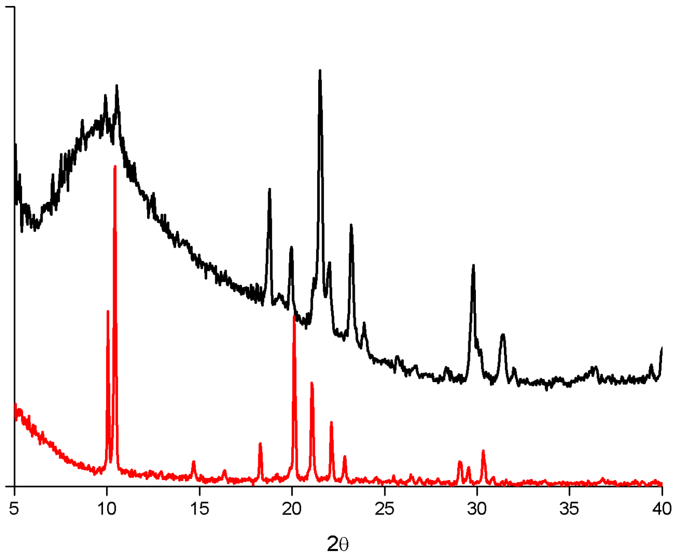

Figure 5.18
VTPXRD data for the 9:1 mixture of **9**$(BF_4)_x(ClO_4)_{2-x}\cdot 2H_2O$ at 300 K at 1 atm (🟥) and under an applied vacuum (⬛).

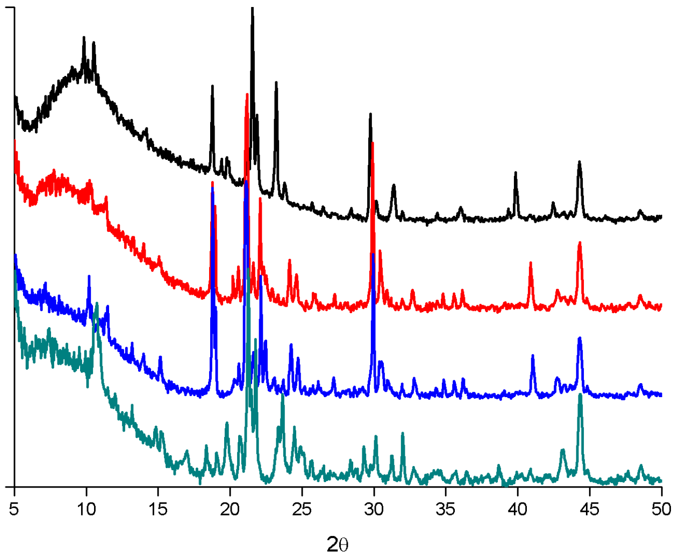

Figure 5.19
VTPXRD data for the cooling mode of the 9:1 mixture of **9**$(BF_4)_x(ClO_4)_{2-x}\cdot 2H_2O$ with a fixed slit correction applied. Temperatures: 353 K (⬛); 253 K (🟥); 231 K (🟦); 150 K (🟩).

This data was then compared to the PXRD data obtained for **9**$(BF_4)_2$ in order to ascertain whether any of these phases are isostructural at the given temperatures, which could give clues to the physical causes of the asymmetric shape of the hysteresis. In Figure 5.20 the powder diffraction pattern matches up very well with that of annealed **9**(BF_4)$_2$. Because the data for the mixture were recorded using only a small amount of sample on a silicon chip the background below 2θ = 15° is very high, however the two peaks at 9.6° and 10.5° can be still only just be seen.

When the powder pattern for the 9:1 mixture of **9**$(BF_4)_x(ClO_4)_{2-x}\cdot 2H_2O$ is compared with that of **9**(BF_4)$_2$at 253 K it can be seen that the two patterns share a lot of common peaks suggesting that they are very similar structures. The relative intensities of some of the peaks are slightly different, however. Due to the high background below 2θ = 15° the peaks in this region could not be unambiguously compared. At 150 K the powder pattern for **9**(BF_4)$_2$ remains the same but the 9:1 mixture of **9**$(BF_4)_x(ClO_4)_{2-x}\cdot 2H_2O$ changes substantially, such that there are barely any shared peaks indicating that the two samples are distinct phases (Figure 5.20, Figure 5.21 and Figure 5.22).

Of the temperatures used in this experiment 150 K and 231 K were chosen because they lie within the hysteresis loop, so it was expected that if the hysteresis is driven by phase changes that the cooling and warming modes might show different phases at the same temperature. This was not the case, however, but it is not direct proof that the hysteresis is not driven by phase changes. Ideally a powder pattern would be obtained below 100 K of the fully LS material however the lowest temperature of the diffractometer was limited to about 150 K.

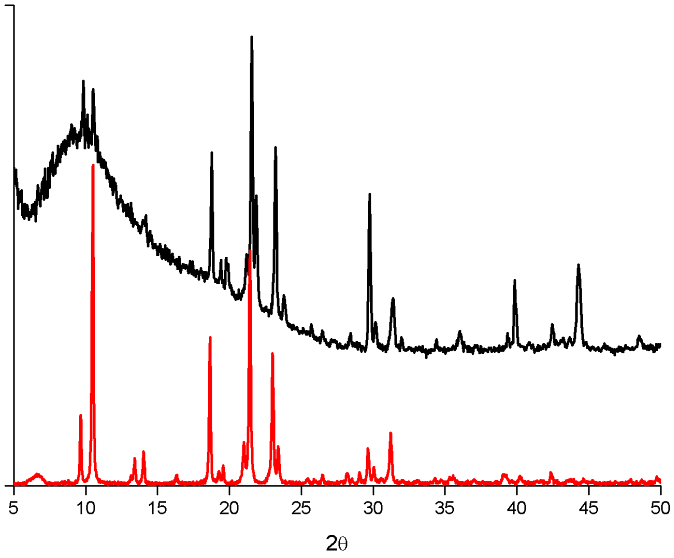

Figure 5.20
Comparison of the powder patterns of the 9:1 mixture of **9**$(BF_4)_x(ClO_4)_{2-x}\cdot 2H_2O$ (■) with **9**$(BF_4)_2\cdot 2H_2O$ (🟥) at 350 K.

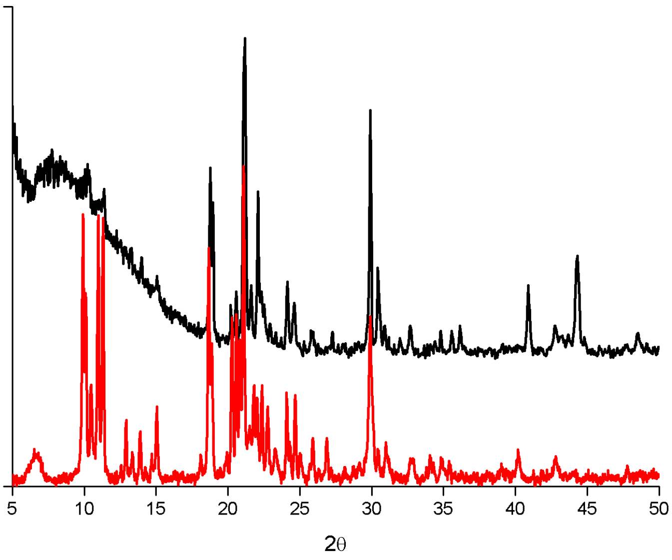

Figure 5.21
Comparison of the powder patterns of the 9:1 mixture of **9**$(BF_4)_x(ClO_4)_{2-x}\cdot2H_2O$ (■) with **9**$(BF_4)_2\cdot2H_2O$ at 253 K (🟥).

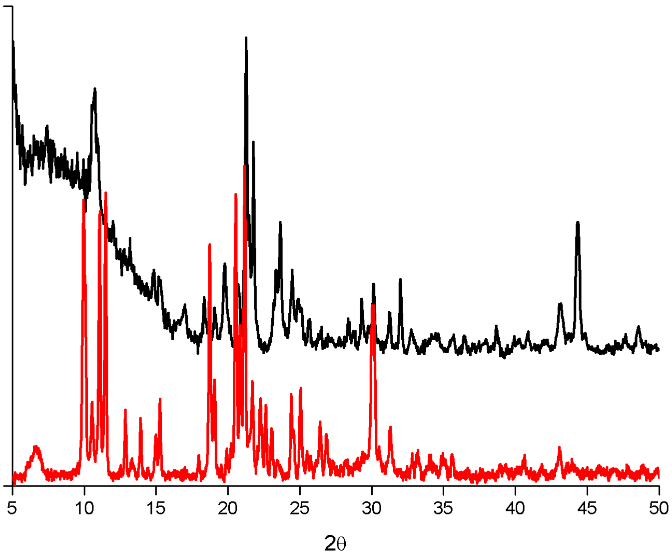

Figure 5.22
Comparison of the powder patterns of the 9:1 mixture of **9**$(BF_4)_x(ClO_4)_{2-x}\cdot2H_2O$ (■) with **9**$(BF_4)_2\cdot2H_2O$ at 150 K (🟥).

5.6. Conclusion

In conclusion mixtures were made in four different ratios of the salts **9**(BF_4)$_2$ and **9**(ClO_4)$_2$ to make mixed anion complexes of the type **9**$(BF_4)_x(ClO_4)_{2-x}\cdot 2H_2O$. It was shown by x-ray diffraction in the case where a structure could be fully resolved that that particular crystal contained both anions in a disordered site and that the two salts had co-crystallised together, rather than forming a mixture of separate crystals. Where full structures could not be fully resolved the unit cells were compared to those of the pure parent salts and found to be very similar to the phases formed upon loss of water. In all cases the mixed anion complexes approximated as the dihydrate in microanalysis and showed a loss of around 4.5% just over 300 K, corresponding to the expected mass loss for two equivalents of water.

Interestingly while the pure perchlorate remained fully HS through the entire temperature range, it was found that the substitution of only 25% of the perchlorate anions with tetrafluoroborate was enough to induce an abrupt hysteretic phase transition. However in all cases the hysteresis loops were asymmetric. Repeated thermal cycling of the 3:1 mixture showed that once the sample was fully dehydrated the hysteresis loop became more symmetric and abrupt with a constant width of 50 K which is still considerably large for a SCO complex. Repeated scanning of the 1:1 mixture showed seemingly bizarre SCO behaviour which turned out to be a result of the thermal scan rate dependence of this sample, and possibly involves the kinetically slow conversion to the fully LS phase which can only be properly accessed below a rate of 0.5 Kmin^{-1}. The sudden drop in $\chi_M T$ of this sample on warming at 2 Kmin^{-1} is probably the result of relaxation to the more thermodynamically stable LS state in a similar manner to that observed for the LIESST effect.

Variable temperature powder diffraction was employed on two of these mixtures to determine if any phase changes occur concomitantly with the hysteresis. For one of the mixtures this seems to not be the case and the abrupt hysteresis loop occurs without going through any phase changes. This contrasts to the pure annealed perchlorate which appears to remain trapped in the fully HS state due to inability to transition to another phase.

5.7. References

[1] T. D. Roberts, F. Tuna, T. L. Malkin, C. A. Kilner and M. A. Halcrow, *Chem. Sci.* **2012**, *3*, 349-354.

[2] J. McMurtrie and I. Dance, *Cryst. Eng. Comm.* **2005**, *7*, 230-236.

[3] J. McMurtrie and I. Dance, *Cryst. Eng. Comm.* **2010**, *12*, 2700-2710.

[4] M. L. Scudder, H. A. Goodwin and I. G. Dance, *New J. Chem.* **1999**, *23*, 695-705.

[5] B. Weber, W. Bauer and J. Obel, *Angew. Chem., Int. Ed.* **2008**, *47*, 10098-10101.

[6] B. Weber, W. Bauer, T. Pfaffeneder, M. M. Dîrtu, A. D. Naik, A. Rotaru and Y. Garcia, *Eur. J. Inorg. Chem.* **2011**, *2011*, 3193-3206.

[7] T. Nakamoto, A. Bhattacharjee and M. Sorai, *Bull. Chem. Soc. Jpn.* **2004**, *77*, 921-932.

[8] V. Ksenofontov, G. Levchenko, H. Spiering, P. Gütlich, J. F. Létard, Y. Bouhedja and O. Kahn, *Chem. Phys. Lett.* **1998**, *294*, 545-553.

[9] A. Bhattacharjee, V. Ksenofontov, K. H. Sugiyarto, H. A. Goodwin and P. Gütlich, *Adv. Funct. Mater.* **2003**, *13*, 877-882.

[10] T. D. Roberts, M. A. Little, F. Tuna, C. A. Kilner and M. A. Halcrow, *Chem. Commun. (Cambridge, U. K.)* **2013**, *49*, 6280-6282.

[11] R. G. Miller, S. Narayanaswamy, J. L. Tallon and S. Brooker, *New J. Chem.* **2014**, *38*, 1932-1941.

[12] E. W. Müller, H. Spiering and P. Gütlich, *J. Chem. Phys.* **1983**, *79*, 1439-1443.

[13] J. A. Enderby, *Trans. Faraday Soc.* **1955**, *51*, 835-848.

[14] M. Sy, F. Varret, K. Boukheddaden, G. Bouchez, J. Marrot, S. Kawata and S. Kaizaki, *Angew. Chem., Int. Ed.* **2014**, *53*, 7539-7542.

[15] S. Hayami, Y. Shigeyoshi, M. Akita, K. Inoue, K. Kato, K. Osaka, M. Takata, R. Kawajiri, T. Mitani and Y. Maeda, *Angew. Chem., Int. Ed.* **2005**, *44*, 4899-4903.

[16] M. Sorai in *Heat Capacity Studies of Spin Crossover Systems*, *Vol. 235* Springer Berlin Heidelberg, **2004**, p. 153-170.

[17] S. Hayami, D. Urakami, Y. Kojima, H. Yoshizaki, Y. Yamamoto, K. Kato, A. Fuyuhiro, S. Kawata and K. Inoue, *Inorg. Chem.* **2010**, *49*, 1428-1432.

[18] S. Hayami, Y. Komatsu, T. Shimizu, H. Kamihata and Y. H. Lee, *Coord. Chem. Rev.* **2011**, *255*, 1981-1990.

[19] R. Kulmaczewski, J. Olguin, J. A. Kitchen, H. L. C. Feltham, G. N. L. Jameson, J. L. Tallon and S. Brooker, *J. Am. Chem. Soc.* **2014**, *136*, 878-881.

[20] M. Seredyuk, M. C. Muñoz, M. Castro, T. Romero-Morcillo, A. B. Gaspar and J. A. Real, *Chemistry* **2013**, *19*, 6591-6596.

[21] A. Hauser, *Coord. Chem. Rev.* **1991**, *111*, 275-290.

[22] J. F. Létard, *J. Mater. Chem.* **2006**, *16*, 2550-2559.

Chapter 6

Ruthenium Transfer Hydrogenation Catalysts Based on 2,6-Di(1*H*-pyrazol-3-yl)pyridine Derivatives

6.1. Introduction

In addition to SCO complexes rigid tridentate NNN donors such as terpyridine, 2,6-di(pyrazol-1-yl)pyridine and 2,6-di(1*H*-pyrazol-3-yl)pyridine have been utilised in photo-luminescent complexes, photosensitizers, for actinide(III)/lanthanide(III) separation and catalysis.[1-3] Transfer hydrogenation catalysts utilising multidentate N donor ligands which form stable complexes with Ru(II) have been a popular alternative to more precarious methods involving pressurised hydrogen gas or harsh reducing agents.[4-7] A catalytic cycle for transfer hydrogenation is shown in Figure 6.1 and discussed in more detain in Chapter 1. The advantage of using 1-bpp ligands in these Ru catalysts is the same reason that makes these ligands so successful in the field of SCO; the relative ease of substitution at different positions allows for fine tuning of the sterics and electronics which are manifested in the properties of subsequent complexes.[8] The complex [$RuCl_2(PPh_3)(L)$] (L = 2,6-bis(3,5-dimethylpyrazol-1-yl)pyridine) has been structurally characterised and shown to efficiently catalyse hydrogenation of a wide range of substrates with yields ranging from 100-37% and with a final turnover frequency (TOF) of up to 6000 hr^{-1}.[9]

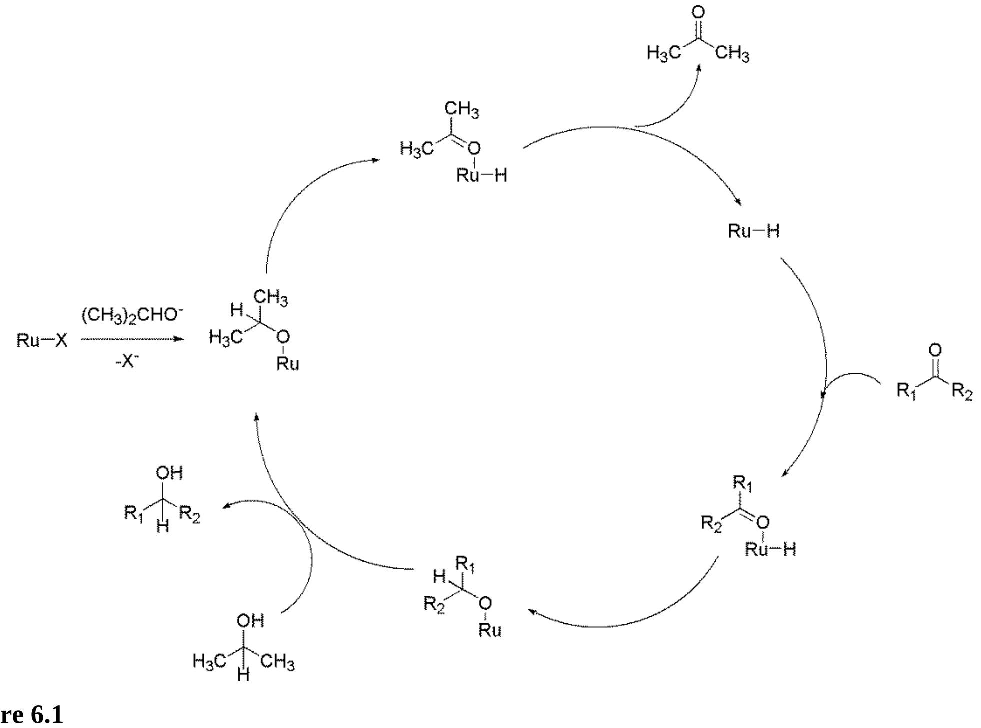

Figure 6.1
A general catalytic cycle for transfer hydrogenation.

Recently there has been much interest in using 3-bpp derivatives to make ruthenium pincer type complexes for transfer hydrogenation catalysts, since the rigid structure points the two pyrazolyl NH groups to the *trans* site of the Ru can act as proton donor to the substrate.[10] Pincer complexes of this type which contain two or more proton-donor groups are quite rare, but in some cases could be expected to increase the rate of hydrogenation reactions substantially.[11] There are limited examples of 3-bpp derivatives being used as a ligand in ruthenium pincer complexes of this type. The complexes [RuCl(3-bpp)(L)] where L = pyridine-2-carboxylate or quinoline-2-carboxylate gave 23-98% yields for the transfer hydrogenation of acetophenone derivatives. The yields were dependant on the substrate, with electron withdrawing substituents on the *para* position of the aryl ring favouring higher yields.[4] The efficiency of these catalysts were also dependent on L, with pyridine-2-carboxylate giving better yields than quinoline-2-carboxylate. However these 3-bpp complexes were less effective catalysts than analogues containing 2,6-di(benzimidazolyl)pyridine or pyridine-2,6-di(carbaldimine) as the tridentate ligand.

The complex [RuHL(PAr_3)$_2$]Cl where L = 2,6-di(1,5-diphenyl-1H-pyrazol-3-yl)pyridine) has been shown to be an effective catalyst with TOF's of up to 3534 hr^{-1} however the pyrazolyl NH groups in this complex have been removed so this behaviour exists in the absence of the proton delivery by the ligand and is dependent on the nature of the triarylphosphine groups.[12] A ruthenium complex has also been made using the ligand 2,6-di(5-*tert*but-1*H*-pyrazol-3-yl)pyridine (**L^{12}**), whose iron(II) complexes were discussed in Chapter 4. Complexes of the type [RuCl(**L^{12}**)(PPh_3)$_2$]Cl can be reversibly deprotonated at one or both pyrazolyl NH groups, which shows that these groups have potential as proton deliverers.[10] The two phosphine ligands are opposite one another in a *trans* arrangement and only one chloride ion is bound to the site *trans* to the 3-bpp ligand. This chloride dissociation occurs because of an increase in electron density at the metal centre making it a poorer π acceptor so weakening the M–Cl bond.[13] The remaining chloride site can then be substituted with more labile groups such as methanol, dioxygen or dinitrogen and this could give an easily accessible site that the substrate can *trans* to the 3-bpp ligand. It is in complexes of this type that catalysis mediated by the pyrazolyl NH groups would be most effective.

With this in mind this chapter is concerned with synthesising novel Ru(II) complexes of the type [RuCl(**L**)(PPh_3)$_2$]Cl using the novel ligands already synthesised and used to make novel SCO materials (Figure 6.2). These ligands have a variety of different substituents giving each unique steric and electronic factors which are important in this area of research. In addition to this asymmetrically substituted ligands offer potential to improve the enantiomeric selectivity of the transfer hydrogenation catalysts.

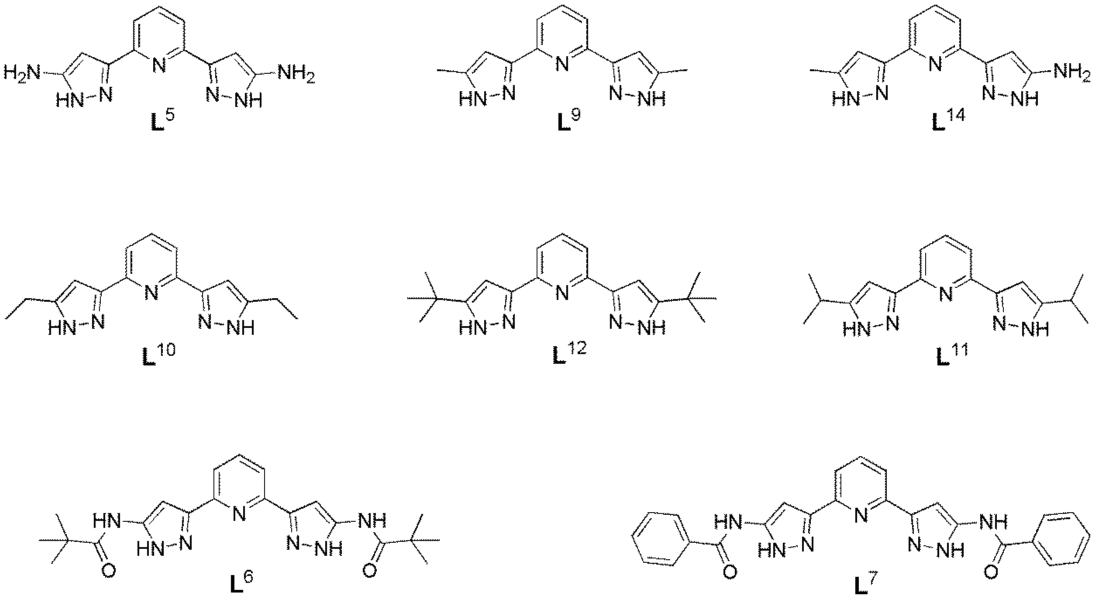

L^{5} **L**^{9} **L**^{14} **L**^{10} **L**^{12} **L**^{11} **L**^{6} **L**^{7}

Figure 6.2
Structures of the ligands discussed in this chapter.

Table 6.1
List of complexes discussed in this chapter. Any solvation present is denoted throughout.

Complex
[Ru(**L**^{6})(PPh$_3$)$_2$]Cl$_2$
[Ru(**L**^{7})(PPh$_3$)$_2$]Cl$_2$
[RuCl(**L**^{9})(PPh$_3$)$_2$]Cl
[Ru(**L**^{10})(PPh$_3$)$_2$]Cl$_2$
[Ru(OH$_2$)(**L**^{12})(PPh$_3$)$_2$]Cl$_2$
[Ru(OH$_2$)(**L**^{12})(PPh$_3$)$_2$](PF)$_2$

6.2. Synthesis

The general synthetic procedure for these complexes first involved synthesising [$RuCl_2(PPh_3)_3$] using the standard literature procedure, forming a brown/dark red microcrystalline solid.[14] This was then suspended in dichloromethane and stirred with 1 equivalent of the relevant 3-bpp derivative for 3 hours at room temperature, before reducing the solvent and precipitating with diethyl ether.[11] This yielded complexes with varying degrees of hydration, as determined via microanalysis. As the catalytic reaction takes place in solution solvation of these complexes in the solid state are not so important as in spin crossover, and a number of different solvates are discussed in this chapter.

It was essential to thoroughly wash the product with diethyl ether in order to remove the free triphenylphosphine that is liberated upon coordination of the 3-bpp ligand. When this reaction was performed using ligands with an amino group at the pyrazolyl *C*5 position it was found that, like their iron complexes, the resultant products are air sensitive. After a few days the orange/brown solid products turned to a dark green/blue, and this process was greatly accelerated to just a few minutes in chloroform solution. This is quite possibly some kind of oxidation process to a ruthenium(III) complex, however because no structure of this product was obtained this cannot be confirmed. Where $\mathbf{L^5}$ was used, the orange product's ^{1}H NMR showed broadened multiplets between 6.7-7.7 ppm, with overlapping triphenylphosphine and $\mathbf{L^5}$ hydrogen environments that cannot be assigned fully. This could be a result of the apparent instability of the complex in chloroform and this ^{1}H NMR spectrum could be a mixture of the orange and green products. Indeed after the spectrum was collected the solution in the NMR tube had darkened, indicating that formation of the green product had taken place.

ES$^+$ mass spectrometry of these complexes in some cases did not show the expected peak for the [RuCl($\mathbf{L}$)$(PPh_3)_3$]$^+$ cations, even for some complexes which were otherwise well characterised. In the cases where the ligand used was $\mathbf{L^9}$, $\mathbf{L^{10}}$ or $\mathbf{L^{12}}$ the expected mass peaks were found. In the case of $\mathbf{L^9}$ the mass corresponded to the cation [RuCl($\mathbf{L^9}$)(PPh_3)]$^+$, indicating a loss of one triphenylphosphine while the complexes of $\mathbf{L^{10}}$ and $\mathbf{L^{12}}$ were both seen to retain both of their triphenylphosphine ligands. In all these cases the masses and isotopic patterns show that each cationic fragment contains ruthenium and a single chlorine, supporting the prediction that one chlorine would dissociate due to the increased electron density at the metal centre.

It was noted that two isomers of these complexes can be formed in this reaction with *trans* or *cis* triphenylphosphine ligands (Figure 6.3). These two isomers can be distinguished by ^{31}P{^{1}H} NMR, as due to the C_2 symmetry of the complex cation the phosphorous environments in the *trans* isomer are identical and we expect a single peak in the spectrum.

Conversely for the *cis* isomer the complex molecule is not symmetric and so would be expected to show an AB type pair of doublets in the $^{31}P\{^{1}H\}$ NMR spectrum.[13] In addition the *trans* isomer is expected to have a dipole moment equal or close to zero, making it less soluble than the corresponding *cis* isomer and this property could be used as a means to separate the two.[15]

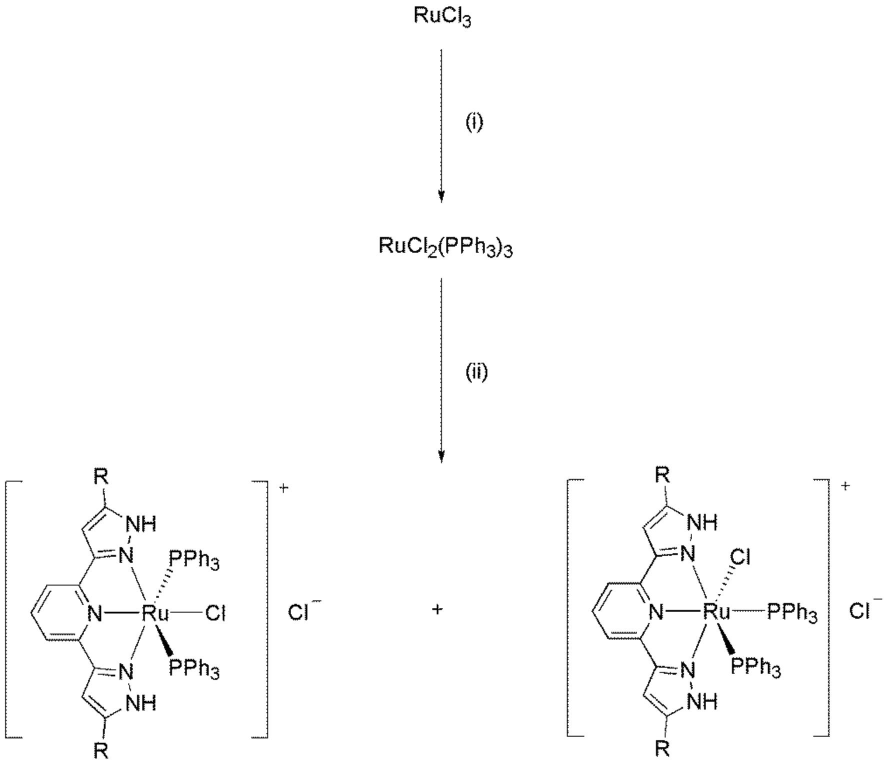

Figure 6.3
Synthetic pathway towards ruthenium(II) complexes of the type $[RuCl(\mathbf{L})(PPh_3)_2]Cl$ where **L** is a 3-bpp derivative. Reagents: (i) PPh_3; (ii) **L**.

The existence of these two isomers proved to be a problem during purification. Generally the method for separation was to add diethyl ether to the dichloromethane solution obtained after (ii) (Figure 6.3) until an orange precipitate cleanly forms. This was then removed from the reaction mixture via filtration and washed thoroughly with diethyl ether. This orange crystalline material was found to be the less soluble *trans* isomer and this was confirmed via $^{31}P\{^{1}H\}$ NMR spectroscopy which showed a single peak in the region of 23-36 ppm corresponding to the two identical triphenylphosphine ligands (Figure 6.4). The exact value of this shift seemed to be dependent on electronic nature of the ligand. For the sample of $[RuCl(\mathbf{L^9})(PPh_3)_2]Cl$ a peak was observed at 24.4 ppm, with additional peaks downfield which may be related to the formation of the green species in solution. The shifts observed for the diamido 3-bpp complexes of $\mathbf{L^6}$ and $\mathbf{L^7}$ were slightly higher at 34.8 and 36.5 ppm respectively while those for the ligands bearing alkyl substituents **L^9**, **L^{10}** and **L^{12}** the phosphorous shifts were 24.4, 24.4 and 23.7 ppm respectively. This trend follows the trend of electron withdrawing capabilities of the pyrazolyl substituents and for the amino and amido ligands there will be less electron density available at the coordinating pyrazolyl nitrogen atoms. This in turn will reduce the amount of electron density at the metal available for π backbonding, and as the phosphine ligands are strong π acceptors this will cause a deshielding of the ^{31}P nucleus and cause a downfield shift in the ^{31}P{^{1}H} NMR spectrum.[16]

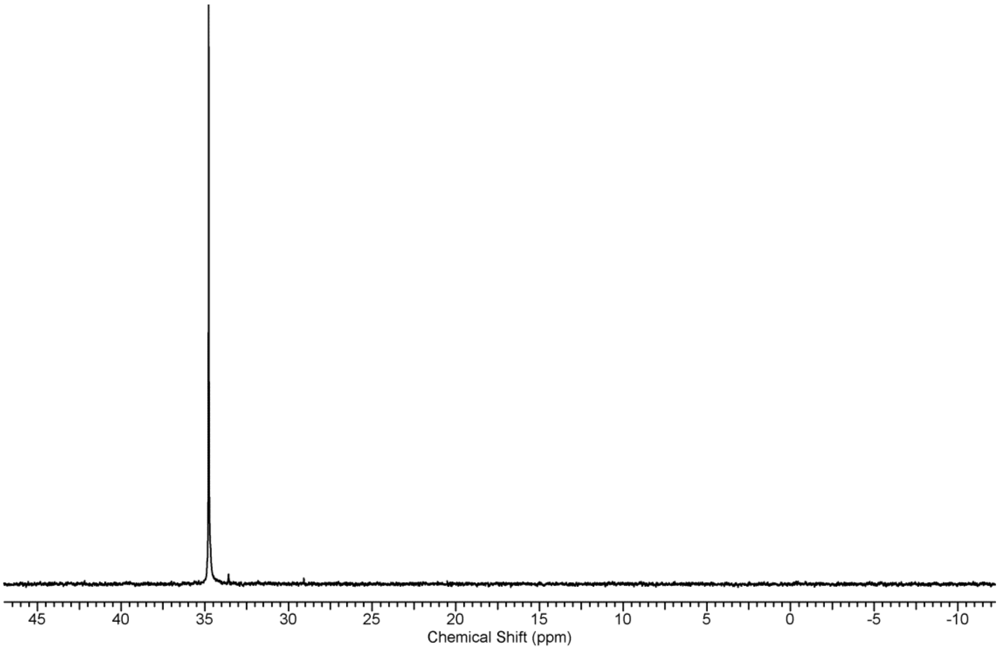

Figure 6.4
^{31}P{^{1}H} NMR spectrum of the *trans* isomer of [RuCl(**L^6**)(PPh$_3$)$_2$]Cl referenced to 85% aqueous H_3PO_4.

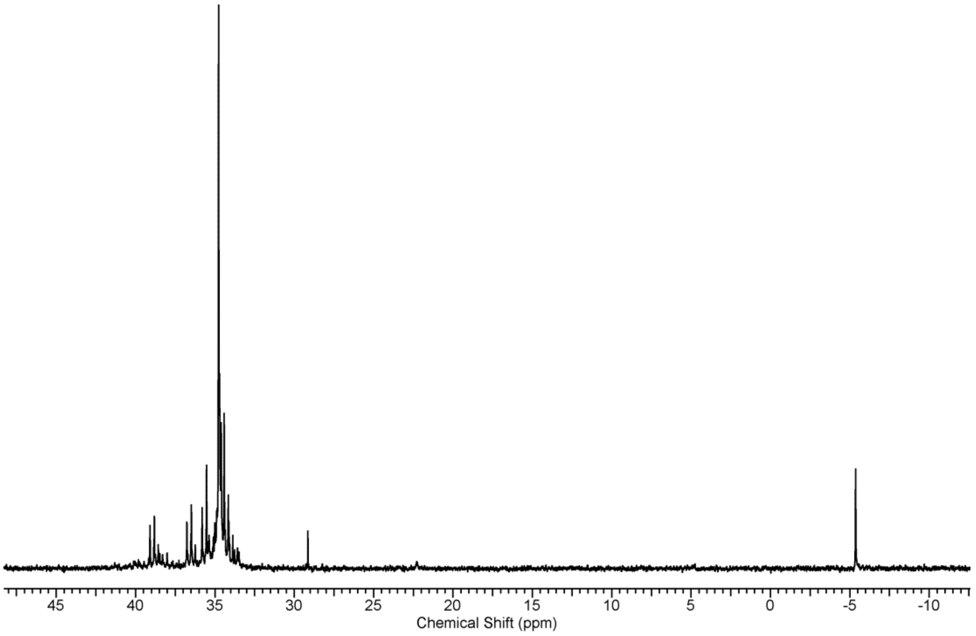

Figure 6.5
$^{31}P\{^{1}H\}$ NMR spectrum of a poorly separated product of $[RuCl(\mathbf{L^6})(PPh_3)_2]Cl$ referenced to 85% aqueous H_3PO_4.

The filtrate from this separation was usually a mixture of some *trans* product, free triphenylphosphine (seen as a peak in the $^{31}P\{^{1}H\}$ NMR at around -5 ppm) and a mixture of other products which are likely to contain the *cis* product. The filtrate was a green colour similar to the complex of $\mathbf{L^5}$ which suggests that the filtrate could contain a related species and the *cis* product itself could not be isolated from this mixture. The efficacy of this method of separation seemed dependent on the ligand used and could be unreliable, meaning that very low yields of the desired *trans* product were obtained. The purity of the isomers was checked by $^{31}P\{^{1}H\}$ NMR, as a poor separation resulted in additional peaks in the spectrum (Figure 6.5). In an attempt to improve the yield the reaction mixture was heated in the hope of changing the proportions of the *cis* and *trans* product formed but little change was observed in the phosphorous NMR.

In the interests of making a more efficient catalyst the chloride ligand and anion were exchanged with hexafluorophosphate by addition of silver hexafluorophosphate. The reason for this is that the hexafluorophosphate is bulkier and less basic than the chloride, and won't be able to coordinate to the ruthenium centre. This would leave a vacant site opposite the 3-bpp ligand where a substrate can attach and could possibly improve the efficiency of the catalyst. Where attempted this resulted in a brown solution with a small amount of extremely fine white silver chloride as a precipitate. This precipitate was so fine that it went through most filters and filtering through a plug of celite resin was the most effective way of removing this by-product. The resulting brown solution was evaporated to leave a brown solid, and microanalysis was used to determine the effectiveness of the salt exchange. In the case of [RuCl(**L^{12}**)(PPh_3)$_2$]Cl the microanalysis showed CHN values which closely match those predicted for the hexafluorophosphate salt and also shows a complete absence of chlorine.

This salt exchange was also attempted with [RuCl(**L^7**)(PPh_3)$_2$]Cl, which was determined as the isomerically pure *trans* isomer via $^{31}P\{^1H\}$ NMR (Figure 6.6). After stirring at room temperature for 20 hours in dichloromethane the resulting solution was shown to contain a mixture of isomers again (Figure 6.7), which could not be separated by their differences in solubility.

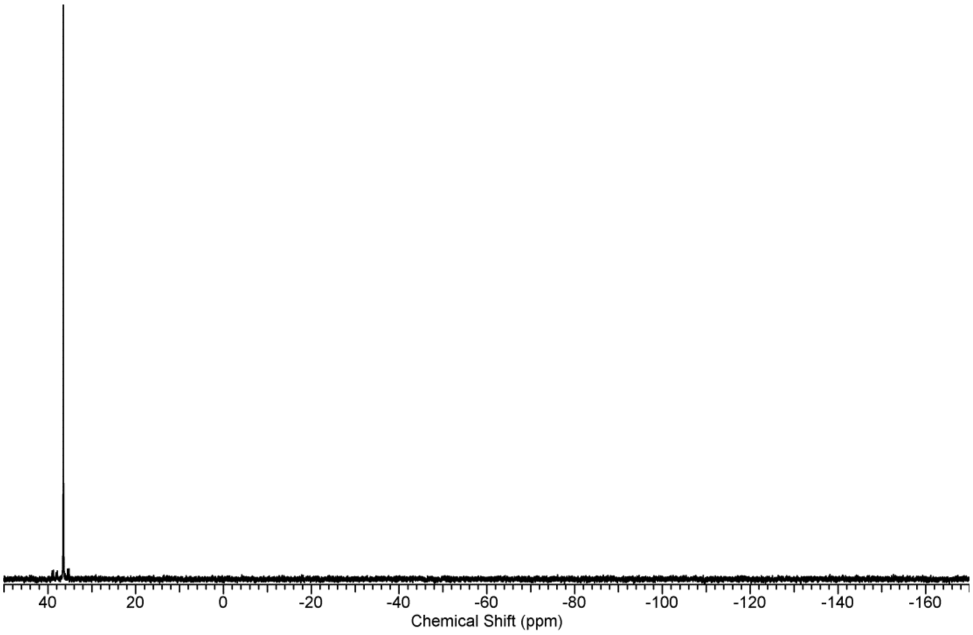

Figure 6.6
$^{31}P\{^1H\}$ NMR spectrum of the *trans* isomer of [RuCl(**L^7**)(PPh_3)$_2$]Cl referenced to 85% aqueous H_3PO_4.

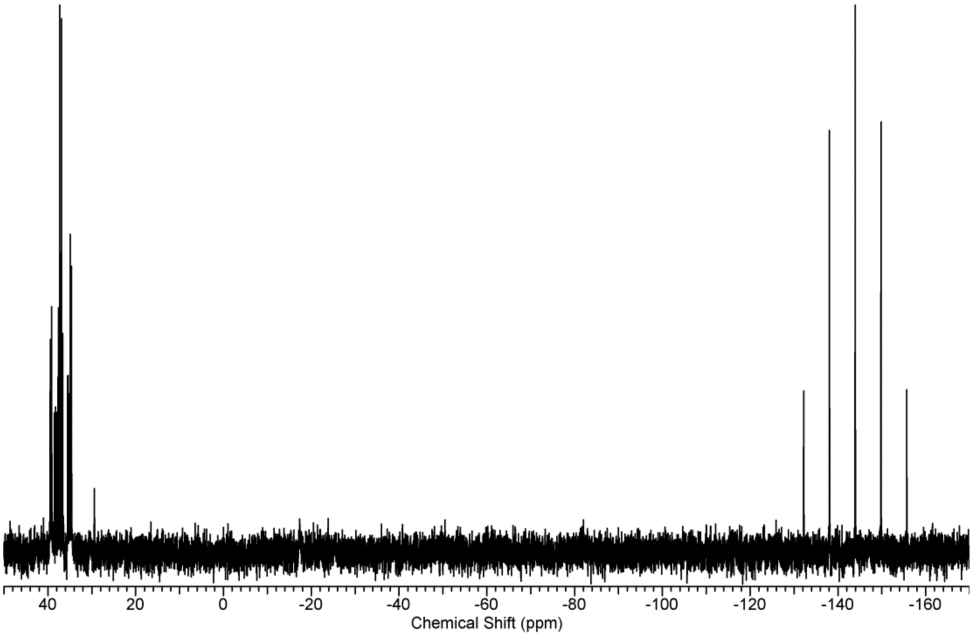

Figure 6.7
$^{31}P\{^1H\}$ NMR spectrum of [RuCl($\mathbf{L}^7$)(PPh_3)$_2$]Cl after salt exchange with $AgPF_6$. Referenced to 85% aqueous H_3PO_4.

6.3. Crystal Structures

Crystal structures were obtained for $[RuCl(\mathbf{L}^{\mathbf{9}})(PPh_3)_2]Cl{\cdot}CH_3OH$, $[RuCl(\mathbf{L}^{\mathbf{12}})(PPh_3)_2]Cl{\cdot}2CHCl_3$ and $[Ru(\mathbf{L}^{\mathbf{12}})(OH_2)(PPh_3)_2](PF_6)_2$. The geometry of these structures was analysed, particularly that of the pyrazole rings as abnormalities can indicate deprotonation of the pyrazolyl NH group.

6.3.1. $[RuCl(L^9)(PPh_3)_2]Cl{\cdot}CH_3OH$

Crystals suitable for x-ray diffraction were obtained via slow vapour diffusion of diisopropyl ether into a solution of $[RuCl(\mathbf{L}^{\mathbf{9}})(PPh_3)_2]Cl$ in methanol. The structure of the methanol solvate was collected in the triclinic space group *P*-1 (a = 11.9552(4); b = 12.4611(4); c = 16.7064(6) Å, α = 79.906(3)°, β = 78.741(3)°, γ = 64.853(3)°, V = 2197.63(14) $Å^3$) and the asymmetric unit contains one complete formula unit (Figure 6.8). The structure clearly shows the two triphenylphosphine groups are opposite one another in the *trans* position, while the site opposite $\mathbf{L}^{\mathbf{9}}$ is occupied by a chlorido ligand. The other chloride anion is not bound to the ruthenium but accepts hydrogen bonds from a pyrazolyl NH (N(15)) and a methanol OH group. The other pyrazolyl NH group (N(3)) donates a hydrogen bond to the bound chlorine (Cl(58)) on another complex molecule. This serves to link complex molecules together in discreet pairs which are symmetry related by an inversion centre (Figure 6.9). This structure is similar to the dimers of ruthenium pincer complexes obtained in the literature where the ligands used are 2,6-di(5-butylpyrazol-3-yl)pyridine and 2,6-di(5-*tert*butylpyrazol-3- yl)pyridine ($\mathbf{L}^{\mathbf{12}}$).[10, 11] Both of these literature structures are isostructural and crystallise in the monoclinic space group $P2_1/c$.

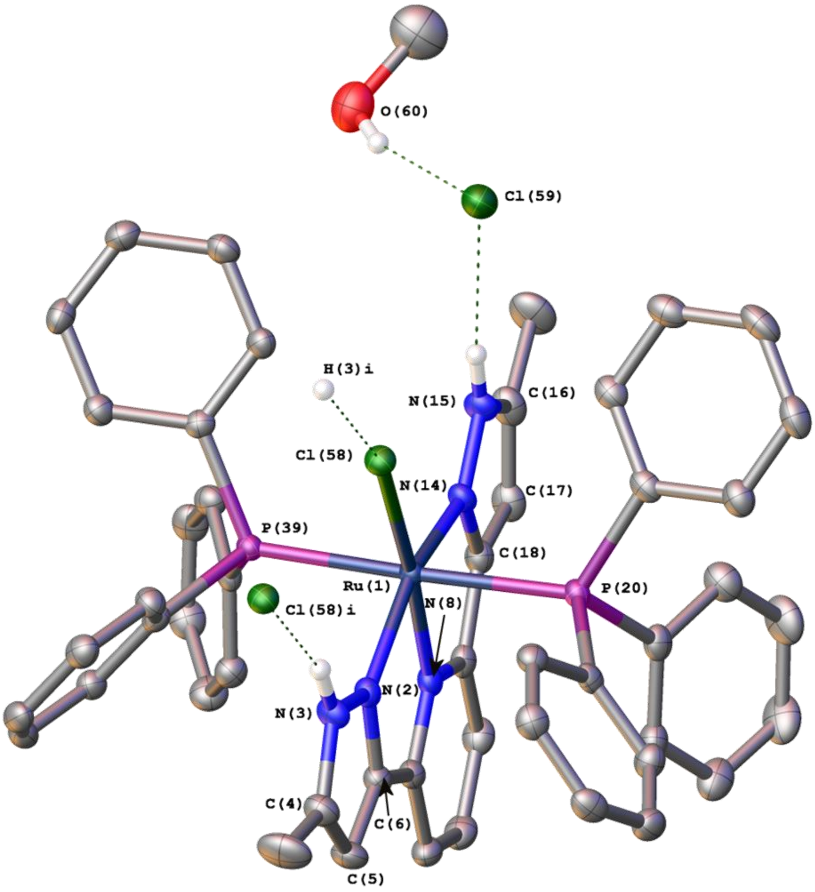

Figure 6.8
The asymmetric unit of [RuCl(**L**^{9})(PPh$_3$)$_2$]Cl·CH$_3$OH showing hydrogen bonding interactions. Thermal displacement ellipsoids are set at 50% probability and hydrogen atoms not taking part in any interactions have been omitted. Symmetry code: (i) 1-*x*, 1-*y*, 1-*z*.

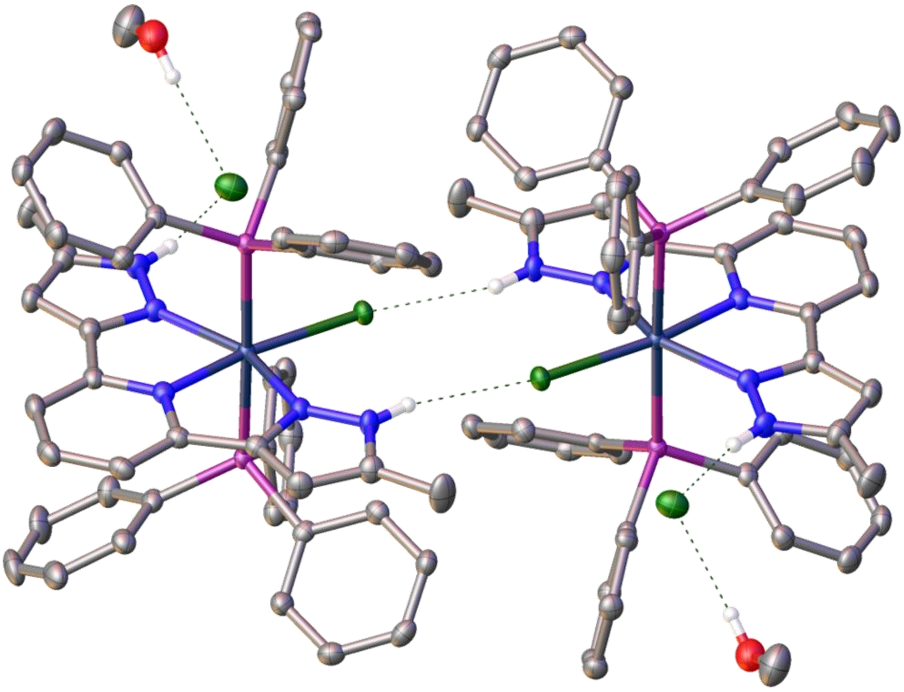

Figure 6.9
Hydrogen bonding interactions in the structure of [RuCl(**L**^{9})(PPh$_3$)$_2$]Cl·CH$_3$OH. Thermal displacement ellipsoids are set at 50% probability and hydrogen atoms not taking part in any interactions have been omitted.

Table 6.2
Tabulated distances for the hydrogen bonding interactions in the structure of [RuCl(**L**^{9})(PPh$_3$)$_2$]Cl·CH$_3$OH.

Interaction	Distance (Å)
N(3)-H(3)···Cl(58)	3.317(2)
N(15)-H(15)···Cl(59)	3.118(2)
O(60)-H(60)···Cl(59)	3.130(2)

Table 6.3
Selected bonding distances in the structure of [RuCl(**L**^{9})(PPh$_3$)$_2$]Cl·CH$_3$OH.

	Distance (Å)
Ru(1)-N(8)	1.9857(19)
Ru(1)-Cl(58)	2.4719(6)
Ru(1)-P(20)/Ru(1)-P(39)	2.3913(6)/2.3657(6)
Ru(1)-N(2)/Ru(1)-N(14)	2.0556(18)/2.1111(18)
N(2)-N(3)/N(14)-N(15)	1.339(3)/1.350(3)
N(3)-C(4)/N(15)-C(16)	1.354(3)/1.353(3)
C(4)-C(5)/C(16)-C(17)	1.375(4)/1.373(4)
C(5)-C(6)/C(17)-C(18)	1.405(3)/1.396(3)
C(6)-N(2)/C(18)-N(14)	1.351(3)/1.353(3)

Table 6.4
Selected bond angles in the structure of [RuCl(**L**^{9})(PPh$_3$)$_2$]Cl·CH$_3$OH.

	Angle (°)
N(8)-Ru(1)-Cl(58)	170.58(6)
P(20)-Ru(1)-P(39)	177.287(18)
N(2)-Ru(1)-N(8)/N(14)-Ru(1)-N(8)	78.45(8)/77.69(7)
N(2)-N(3)-C(4)/N(14)-N(15)-C(16)	112.1(2)/111.2(2)
N(3)-C(4)-C(5)/N(15)-C(16)-C(17)	106.6(2)/107.7(2)
C(4)-C(5)-C(6)/C(16)-C(17)-C(18)	105.9(2)/105.2(2)
C(5)-C(6)-N(2)/C(17)-C(18)-N(14)	109.5(2)/110.5(2)
C(6)-N(2)-N(3)/C(18)-N(14)-N(15)	105.94(18)/105.42(18)

The hydrogen bond which holds the two complex molecules together has a length of 3.317(2) Å (Table 6.2), similar to that observed in Thiel's complex [RuCl(L)(PPh$_3$)$_2$]Cl (where L = 2,6-di(5-butylpyrazol-3- yl)pyridine).[11]

The geometry around the ruthenium is a distorted octahedron with an octahedral distortion of 35.34(5)º. The coordinating chlorido ligand is bent in the plane of $\mathbf{L}^{9}$ giving the N(8)–Ru(1)–Cl(58) bond angle of 170.58(6)°. This distortion probably avoids steric clashes with the methyl groups on the pyrazolyl *C*5 position and allows the chlorido ligand to form a stronger hydrogen bonding interaction with the neighbouring complex molecule. By examination of the bond lengths and bond angles in the pyrazolyl rings it can be deduced that they are both protonated (Table 6.3 and Table 6.4). The N(2)–N(3)–C(4)/N(14)–N(15)–C(16) bond angles are around 111º, and if deprotonation had occurred this angle would be expected to be around 106º due to the increased *s* character of the pyrazolyl *N*1 atom.[17] This is based on cases where structures of pyrazole and pyrazolato complexes have been obtained.[18, 19]

6.3.2. $[Ru(OH_2)(L^{12})(PPh_3)_2]Cl_2{\cdot}2CHCl_3$

Crystals of $[Ru(OH_2)(\mathbf{L}^{12})(PPh_3)_2]Cl_2{\cdot}2CHCl_3$ were obtained from a saturated chloroform solution overnight. This complex was found to crystallise in the monoclinic space group *P*2/*n* (a = 12.1641(5); b = 10.8190(4); c = 25.7429(10) Å, α = 90°, β = 91.863(3)°, γ = 90°, V = 3386.1(2) Å^3) and the asymmetric unit contained half a complex dication, one chloride anion and two chloroform molecules (Figure 6.10). The complex dication lies on a C_2 crystallographic rotation axis which intersects through the ruthenium along the central pyridine N–Ru bond while the chloroform molecules are symmetry related by inversion centres. Though this complex was synthesised in the same manner as Kuwata *et al*. the structure is very different. [10] While Kuwata's complex exhibits a similar structure to $[RuCl(\mathbf{L}^{9})(PPh_3)_2]Cl{\cdot}CH_3OH$ described in **6.3.1** the structure of $[Ru(OH_2)(\mathbf{L}^{12})(PPh_3)_2]Cl_2{\cdot}2CHCl_3$ does not show the same hydrogen bonded dimer motif. Instead of having one coordinating chlorido ligand and one free chloride anion this structure shows that both chlorides are free and the position trans to the ligand $\mathbf{L}^{12}$ has been occupied by a water molecule. This water molecule donates one hydrogen bond to each chloride anion, which in turn accepts hydrogen bonds from one pyrazolyl NH group, two chloroform CH groups and an aryl CH group on a triphenylphosphine ligand (Figure 6.11, Table 6.5). This hydrogen bonding makes a very stable structure but does not extend beyond the complex cation to link adjacent complex molecules.

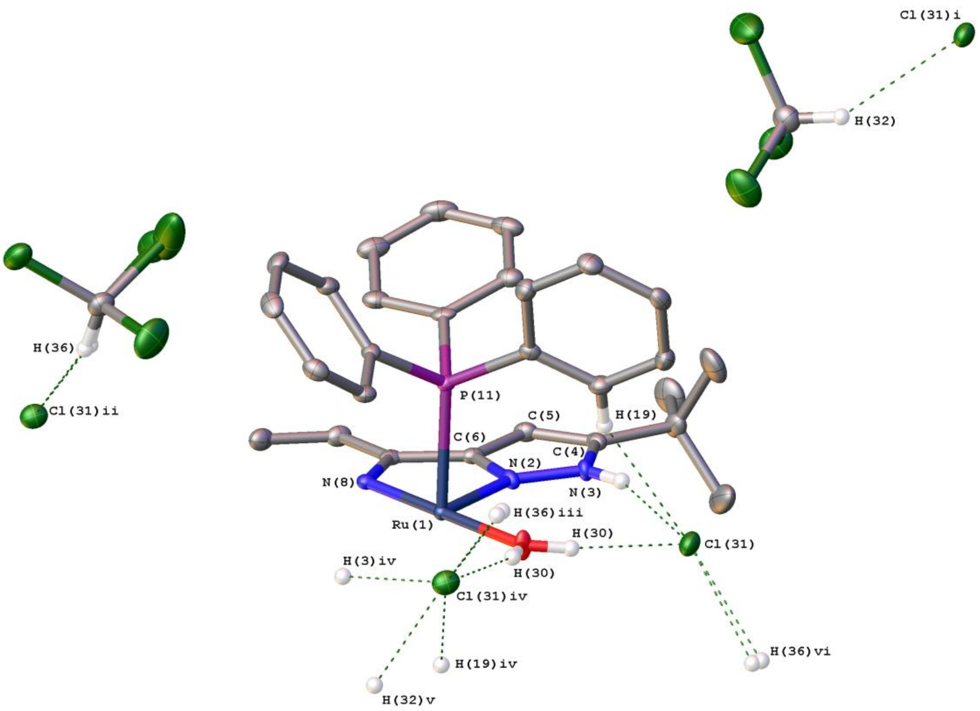

Figure 6.10
The asymmetric unit of $[\mathrm{Ru(OH_2)}(\mathbf{L}^{12})(\mathrm{PPh_3})_2]\mathrm{Cl_2}\cdot 2\mathrm{CHCl_3}$ showing hydrogen bonding interactions. Thermal displacement ellipsoids are set at 50% probability and hydrogen atoms not taking part in any interactions have been omitted. Symmetry codes: (i) 1-*x*, 1-*y*, 1-*z*; (ii) 1/2-*x*, -1+*y*, 1/2-*z*; (iii) +*x*, 1+*y*, +*z*; (iv) 1/2-*x*, +*y*, 1/2-*z*; (v) -1/2+*x*, 1-*y*, -1/2+*z*; (vi) 1/2-*x*, 1+*y*, 1/2-*z*.

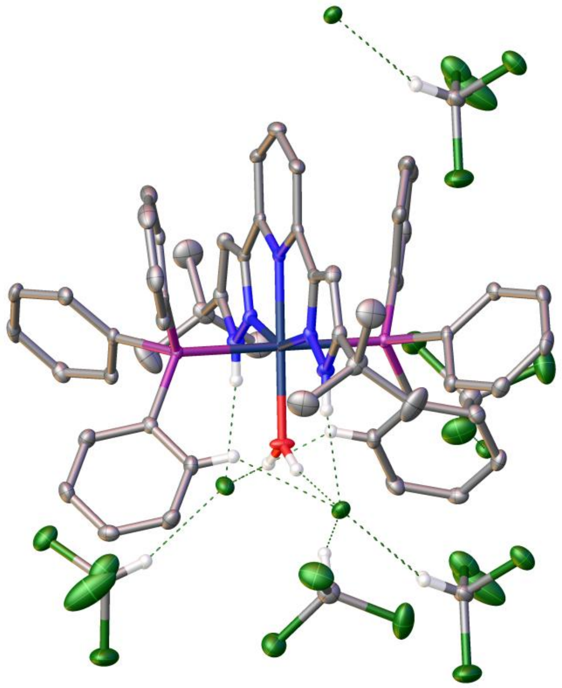

Figure 6.11
Hydrogen bonding interactions in the structure of $[\mathrm{Ru(OH_2)}(\mathbf{L}^{12})(\mathrm{PPh_3})_2]\mathrm{Cl_2}\cdot 2\mathrm{CHCl_3}$.

Table 6.5
Tabulated distances for the hydrogen bonding interactions in the structure of $[Ru(OH_2)(\mathbf{L}^{12})(PPh_3)_2]Cl_2{\cdot}2CHCl_3$.

Interaction	Distance (Å)
N(3)-H(3)···Cl(31)	3.149(3)
O(30)-H(30)···Cl(31)	3.1329(14)
C(19)-H(19)···Cl(31)	3.398(3)
C(32)-H(32)···Cl(31)	3.462(4)
C(36)-H(36)···Cl(31)	3.343(4)

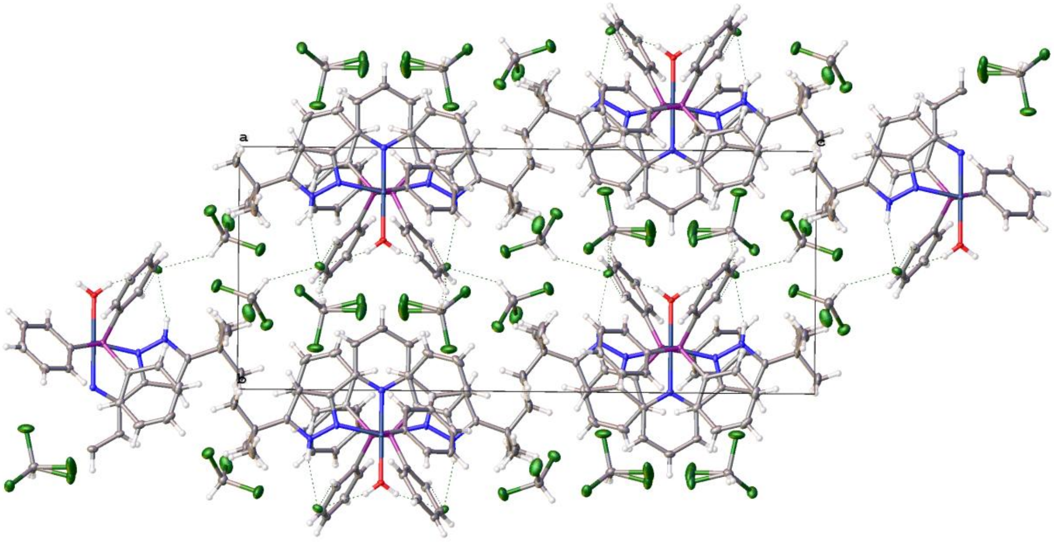

Figure 6.12
View of the structure of $[Ru(OH_2)(\mathbf{L}^{12})(PPh_3)_2]Cl_2{\cdot}2CHCl_3$ down the *a* axis.

The structure packs in ABAB type layers down the length of the *c* crystallographic axis. The layers consist of ordered complex molecules which are arranged in the same orientation through the *ab* crystallographic plane along their C_2 axes. In the next layer the orientation of the complex cations are inverted and the layers repeat in an ABAB fashion (Figure 6.12).

Table 6.6
Selected bonding distances in the structure of [Ru(OH$_2$)(**L**^{12})(PPh$_3$)$_2$]Cl$_2$·2CHCl$_3$.

	Distance (Å)
Ru(1)-N(8)	1.985(4)
Ru(1)-O(30)	2.135(3)
Ru(1)-P(11)	2.4110(7)
Ru(1)-N(2)	2.066(3)
N(2)-N(3)	1.347(4)
N(3)-C(4)	1.360(4)
C(4)-C(5)	1.567(5)
C(5)-C(6)	1.407(5)
C(6)-N(2)	1.352(4)

Table 6.7
Selected bond angles in the structure of Ru(OH$_2$)(**L**^{12})(PPh$_3$)$_2$]Cl$_2$·2CHCl$_3$. Symmetry code: (iv) 1/2-*x*, +*y*, 1/2-*z*.

	Angle (°)
N(8)-Ru(1)-O(30)	180.0(3)
P(11)-Ru(1)-P(11)^{iv}	179.80(5)
N(2)-Ru(1)-N(8)	77.84(8)
N(2)-N(3)-C(4)	111.6(3)
N(3)-C(4)-C(5)	106.9(3)
C(4)-C(5)-C(6)	106.1(3)
C(5)-C(6)-N(2)	109.5(3)
C(6)-N(2)-N(3)	105.9(3)

The selected bond lengths in the structure of [Ru(OH$_2$)(**L**^{12})(PPh$_3$)$_2$]Cl$_2$·2CHCl$_3$ are almost identical to those seen in the structure of [RuCl(**L**^{9})(PPh$_3$)$_2$]Cl·CH$_3$OH (Table 6.6). The most noticeable difference between the two is that the C(4)–C(5) bond length is significantly longer in [Ru(OH$_2$)(**L**^{12})(PPh$_3$)$_2$]Cl$_2$·2CHCl$_3$, 1.567(5) Å, compared to that seen in [RuCl(**L**^{9})(PPh$_3$)$_2$]Cl·CH$_3$OH, 1.374(4) Å (average). The N(2)–N(3)–C(4) bond angle of 111.6(3) does indicate that the pyrazolyl NH has not been deprotonated and so this is not the reason for this difference in bond length (Table 6.7). From the selected bond angles shown in Table 6.7 it can be seen that the pyridine N–Ru–O angle is exactly 180° and does not show the significant deviation from the octahedral ideal seen in the coordination sphere of [RuCl(**L**^{9})(PPh$_3$)$_2$]Cl·CH$_3$OH. This is due to the monomeric structure of [Ru(OH$_2$)(**L**^{12})(PPh$_3$)$_2$]Cl$_2$·2CHCl$_3$ in which the coordinating water does not have to move in order to relieve steric conflict between the neighbouring cation. The coordinating water is also forming two symmetric hydrogen bonding interactions with the chloride anions and so a more central position allows these interactions to occur simultaneously. The octahedral distortion observed for the coordination sphere of [Ru(OH$_2$)(**L**^{12})(PPh$_3$)$_2$]Cl$_2$·2CHCl$_3$ is 48.06(8)°, larger than the 35.34(5)° that was calculated for [RuCl(**L**^{9})(PPh$_3$)$_2$]Cl·CH$_3$OH.

The coordinating water in this complex has implications for its catalytic activity. As water is a more labile ligand than chlorido it is possible that this position *trans* to the ligand **L**^{12} could be more easily exchanged for a substrate molecule. This will poise the complex in an ideal way for **L**^{12} to act as a proton deliverer and potentially speed up the transfer hydrogenation reaction. It is difficult to say, however, whether this structure will be present in the reaction mixture or the chlorido ligand will replace the coordinated water. It could be the case that the hydrogen bonding and packing effects stabilise this particular structure and the chlorido ligand may be the more favoured in solution. This is the reason for exchanging chloride for hexafluorophosphate. Hexafluorophosphate is expected to be too bulky to coordinate to the ruthenium centre thus leaving the position *trans* to the 3-bpp ligand coordinated by a more weakly bound solvent molecule. It is hoped that this solvent molecule could be more easily exchanged for a substrate molecule and so increase the catalytic activity of the dihexafluorophosphate complex when compared to its dichloride equivalent.

6.3.3. $[Ru(OH_2)(L^{12})(PPh_3)_2](PF_6)_2$

In this case crystals of the orange solid were obtained from methanol via slow vapour diffusion of diisopropyl ether. $[Ru(OH_2)(\mathbf{L}^{12})(PPh_3)_2](PF_6)_2$ was found to crystallise in the monoclinic space group *C*2/*c* (*a* = 41.2140(9); *b* = 12.9493(3); *c* = 21.7724(4) Å, α = 90°, β = 96.056(2)°, γ = 90°, *V* = 11554.9(4) $Å^3$) and the asymmetric unit contains one complete formula unit with no lattice solvent (Figure 6.13). One of the hexafluorophosphate anions is disordered over two positions in a 1:1 ratio, and two of the phenyl rings on the same triphenylphosphine ligand are each disordered in a ratio of 1:1 over two positions. The disorder in the triphenylphosphine is the result of a steric clash between adjacent complex molecules where one position of the phenyl rings cannot be occupied by both molecules simultaneously (Figure 6.14). Adjacent molecules are symmetry related by C_2 rotation axes which run parallel to the *b* crystallographic axis, one of which runs through the space between the disordered triphenylphosphine groups. These rotation axes do not intersect any atomic coordinates. The complex packs in an analogous manner to the structure of $[Ru(OH_2)(\mathbf{L}^{12})(PPh_3)_2]Cl_2{\cdot}2CHCl_3$ where complex dications align in alternating layers along the *bc* crystallographic plane. In this case the complex dications are separated by hexafluorophosphate anions rather than chloroform solvent molecules however.

The position trans to the ligand $\mathbf{L}^{12}$ was assigned as a coordinating water but this assignment is quite ambiguous. There is more electron density around this position which couldn't be assigned to a fully occupied atomic position and this gives the largest unassigned peak in the structure a value of 2.83 *e* $Å^{-3}$. It is possible that this position is not occupied uniformly throughout the structure and that a number of different molecules could coordinate. In additional to methanol and water there is also a possibility that a molecule of dinitrogen could coordinate to this position in a similar manner to that observed by Kuwata *et al*.[10] In this paper molecules of dioxygen were also capable of coordinating to the ruthenium although in a side on conformation which doesn't fit the remaining Q peaks in the structure.

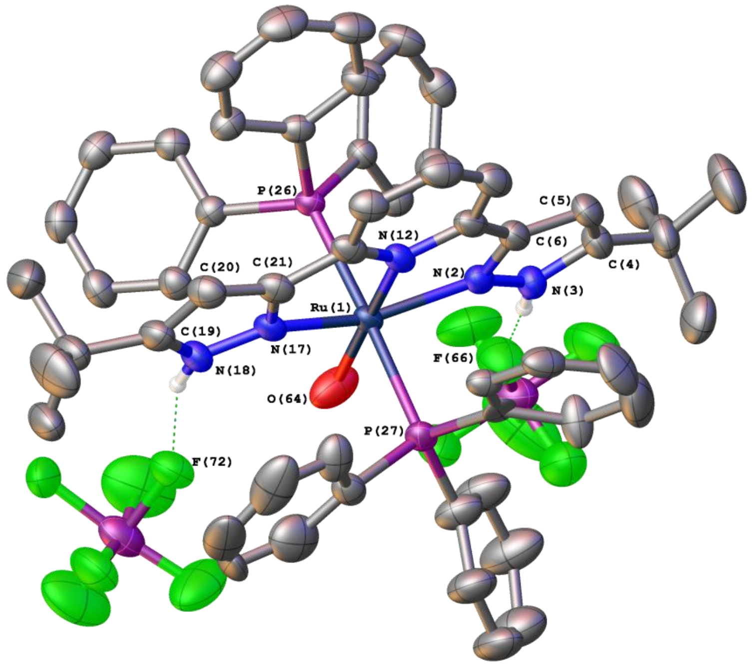

Figure 6.13
The asymmetric unit of $[Ru(OH_2)(\mathbf{L}^{12})(PPh_3)_2](PF_6)_2$ showing hydrogen bonding interactions. Thermal displacement ellipsoids are set at 50% probability and hydrogen atoms not taking part in any interactions have been omitted. Disordered phenyl rings and anion have only been shown in one position.

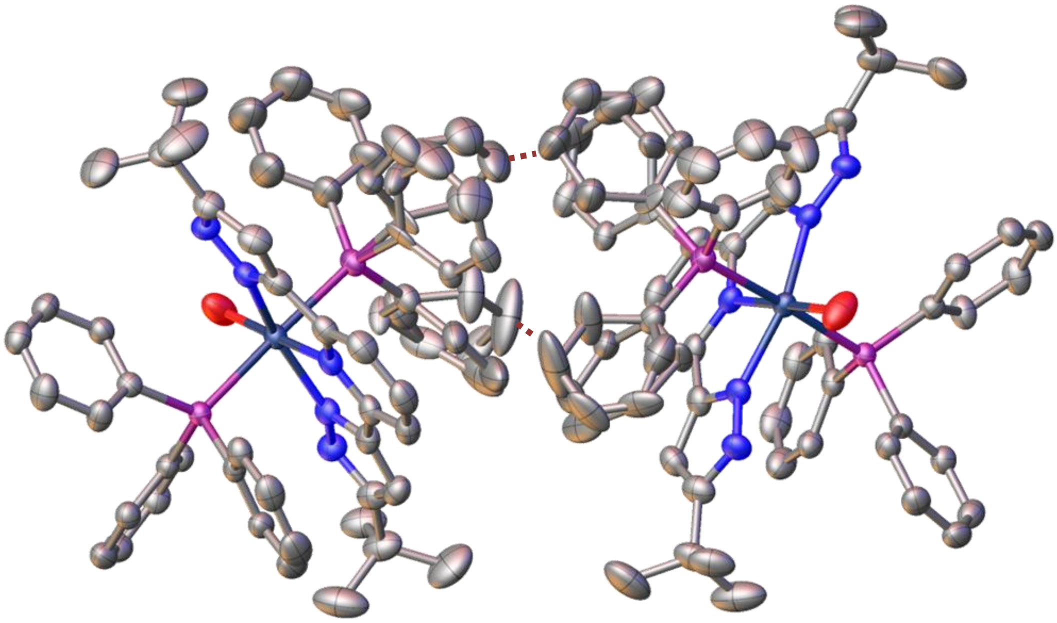

Figure 6.14
View of the steric clash between adjacent molecules in $[Ru(OH_2)(\mathbf{L}^{12})(PPh_3)_2](PF_6)_2$. Thermal displacement ellipsoids are set at 50% probability and hydrogen atoms have been omitted.

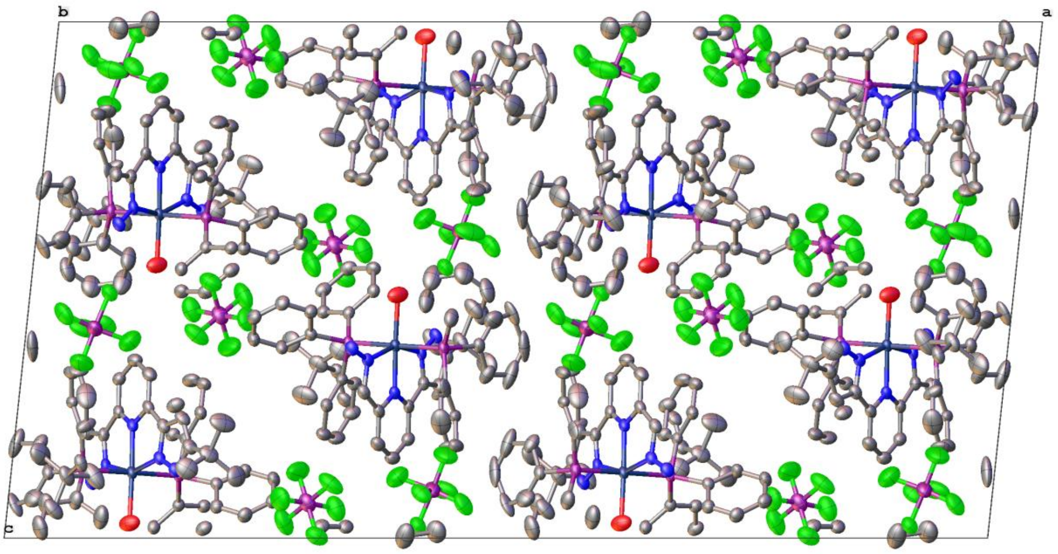

Figure 6.15
View of the structure of [Ru(OH$_2$)(**L**^{12})(PPh$_3$)$_2$](PF$_6$)$_2$ down the *b* crystallographic axis.

The hydrogen bonding in this structure is limited to the two unique hexafluorophosphate anions which each accept a hydrogen bond from each of the two pyrazole NH groups on **L**^{12} (Figure 6.10). These interactions are localised and so do not extend throughout the crystal linking adjacent molecules. The bond lengths and angles for the ruthenium coordination sphere and the pyrazolyl rings are very similar to those already observed in the structure of [RuCl(**L**^{9})(PPh$_3$)$_2$]Cl·CH$_3$OH (Table 6.9 and Table 6.10). The major difference between these two structures is that the N(12)–Ru(1)–O(64) angle is much closer to 180° in the structure of [Ru(OH$_2$)(**L**^{12})(PPh$_3$)$_2$](PF$_6$)$_2$ and this could reflect the non-dimeric nature of this structure. The angles of the N(2)–N(3)–C(4) and N(17)–N(18)–C(19) bonds in the pyrazolyl rings are 113.0(4)° and 112.0(4)° respectively, so indicates that these pyrazolyl NH groups are protonated as expected.

Table 6.8
Tabulated distances for the hydrogen bonding interactions in the structure of [Ru(OH$_2$)(**L**^{12})(PPh$_3$)$_2$](PF$_6$)$_2$.

Interaction	**Distance (Å)**
N(3)-H(3)···F(66)	3.022(6)
N(18)-H(18)···F(72)	2.997(6)

Table 6.9
Selected bonding distances in the structure of [Ru(OH$_2$)(**L**^{12})(PPh$_3$)$_2$](PF$_6$)$_2$.

	Distance (Å)
Ru(1)-N(12)	1.996(4)
Ru(1)-O(64)	2.137(5)
Ru(1)-P(26)/Ru(1)-P(27)	2.4095(12)/2.4086(13)
Ru(1)-N(2)/Ru(1)-N(17)	2.094(4)/2.097(4)
N(2)-N(3)/N(17)-N(18)	1.353(6)/1.358(6)
N(3)-C(4)/N(18)-C(19)	1.357(6)/1.356(7)
C(4)-C(5)/C(19)-C(20)	1.380(8)/1.376(8)
C(5)-C(6)/C(20)-C(21)	1.401(7)/1.385(8)
C(6)-N(2)/C(21)-N(22)	1.360(6)/1.353(6)

Table 6.10
Selected bond angles in the structure of [Ru(OH$_2$)(**L**^{12})(PPh$_3$)$_2$](PF$_6$)$_2$.

	Angle (°)
N(12)-Ru(1)-O(64)	178.12(17)
P(26)-Ru(1)-P(27)	177.61(4)
N(2)-Ru(1)-N(12)/N(17)-Ru(1)-N(12)	77.73(16)/77.12(16)
N(2)-N(3)-C(4)/N(17)-N(18)-C(19)	113.0(4)/112.0(4)
N(3)-C(4)-C(5)/N(18)-C(19)-C(20)	106.0(5)/106.6(5)
C(4)-C(5)-C(6)/C(19)-C(20)-C(21)	106.1(5)/105.8(5)
C(5)-C(6)-N(2)/C(20)-C(21)-N(22)	110.5(5)/111.3(5)
C(6)-N(2)-N(3)/C(21)-N(22)-N(17)	104.4(4)/104.3(4)

In addition to the orange solid determined to be the *trans* isomer, the green solid thought to contain the *cis* isomer was also set up for crystallisation in an attempt to identify what substances were present. If the species in the green product were known it could have been used to increase the efficiency of the purification of the desired *trans* isomer. The green solid was dissolved in methanol and crystallised by the diffusion of diisopropyl ether. This yielded a green solution with small colourless crystals. The data collected using these crystals are only 30% complete to a 2θ of 133º and so a full structure could not be determined. The unit cell was determined to be trigonal and the space group that gave the best solution was *R*3 (a = 14.2825(10); b = 14.2825(10); c = 51.084(6) Å, α = 90°, β = 90°, γ = 120°, V = 9024.5(13) Å^3). A crude solution of this data indicates that the crystal consists of $[RuH(PPh_3)_4](PF_6)$, which is a known complex.[20] The hydride is not visible in the structure, which is expected due to the lack of electron density around the hydride and the two PF_6 sites are only partially occupied, suggesting only 1 PF_6 anion per formula unit. This structure is also supported by the similarity of the unit cell to the complex $[Ag(PPh_3)_4](SbF_6)$, for which the crystal structure has already been published.[21] The colourless appearance of these crystals suggests that this is not the only component of the green fraction but explains why the phosphorous NMR is more complicated than that expected for just the *cis* isomer of $[Ru(OH_2)(\mathbf{L^{12}})(PPh_3)_2](PF_6)_2$.

6.4. Catalytic Activity

The complexes whose pure *trans* isomer was obtained in sufficient yields were then screened for catalytic activity in the transfer hydrogenation of acetophenone derivatives. The general procedure for the transfer hydrogenation of acetophenone derivatives was adapted from the literature procedures.[4, 22] A mixture of ketone and catalyst was suspended in isopropanol and heated to 80ºC before a solution of potassium isopropoxide was added to initiate the reaction. At time increments a sample was taken and decane was added which acted as a standard for the GC measurements. Decane was not used as an internal standard because of concerns that it may somehow interfere with the catalytic reaction. Unlikely as this is, the decane standard was added after the aliquot was taken as a precaution.

The GC was calibrated for the acetophenone derivatives and their corresponding alcohols in the same solution composition as the reaction mixture. The response factors calculated from these calibrations were then used to determine the amount of product and starting material that was present in each of the sample mixtures. Once a carefully measured amount of decane was added to each aliquot the samples were filtered through a plug of celite into GC vials and the samples were run as quickly as possible.

Acetophenone overlapped with the phenylethanol product in the GC chromatogram and so the temperature ramp was halved from 20ºCmin^{-1} to 10ºCmin^{-1} which increased running time but allowed the resolution of these peaks. The reaction mixtures where 3,4-dihydroxyacetophenone and 4-nitroacetophenone were used as substrate were run with a temperature ramp of 20ºCmin^{-1}. Aside from these differences the other parameters used in these methods were identical.

Due to the poor yields of the pure complexes a full optimisation of the reaction could not take place. As the reaction conditions had been adapted from those which had already been optimised in the literature for similar complexes the only optimisation which took place was for the catalyst loading. In this way it was intended that the results obtained using the same method for each complex could be compared to one another and trends relating to the structure of catalyst and substrate identified. Three catalyst loadings of 0.2, 0.5 and 1.0 mol% were initially screened using $[Ru(OH_2)(\mathbf{L^{12}})(PPh_3)_2]Cl_2$ as the catalyst because it was obtained in the highest yield. In the literature pincer complexes of this type have been shown to be effective in loadings from 0.05-1 mol%.[12, 22] In our case 1 mol% was chosen as the maximum loading in order to ensure multiple reactions using each complex were possible and acetophenone was used as the substrate.

The results of the catalyst loading experiment show that even with 1 mol% of catalyst after 20 hours at 80ºC the reaction is only 83.6% complete (Table 6.11). Conversely using 0.2 mol% of catalyst resulted in no product formed whatsoever. In all cases the starting material and product combined do not equal 100%, indicating possibly a side reaction generating a product which is either invisible to the detector or removed during the celite filtration. This could also be the reason for the 0.5% catalyst loading showing no starting material or product.

Table 6.11
Results for different loadings of the complex $[Ru(OH_2)(\mathbf{L}^{12})(PPh_3)_2]Cl_2$ in the transfer hydrogenation reaction of acetophenone. Conditions: ^{i}PrOH, ^{i}PrOK, 80°C.

Catalyst	Starting Material (%)		Product (%)	
	1 hr	20 hrs	1 hr	20 hrs
0.2%	26.5	38.4	0.0	0.0
0.5%	0.0	0.0	0.0	47.5
1.0%	22.6	0.0	0.0	83.6

For the catalytic reactions 1 mol% of catalyst was chosen as the standard loading by which the performance of each complex as a transfer hydrogenation catalyst would be compared. First the catalytic activity of each complex was tested in the transfer hydrogenation reaction of acetophenone in order to identify any relation of ligand structure to catalytic activity. From these results it seems that $[Ru(OH_2)(\mathbf{L}^{12})(PPh_3)_2](PF_6)_2$ is the most catalytically active complex achieving an 80% conversion after only 4 hours (Table 6.12). The fluctuations after 4 hours indicate the error in this measurement which could be due to human error in the aliquot measurements or a loss of solvent due to evaporation affecting the concentrations. Ideally each reaction would be repeated three times and an average value taken, however this was not possible due to only a small amount of each catalyst being available.

The $[Ru(\mathbf{L})(PPh_3)_2]Cl_2$ complexes of ligands $\mathbf{L}^{6}$, $\mathbf{L}^{10}$ and $\mathbf{L}^{12}$ all show no catalytic activity during the first 8 hours of the reaction, and between 8-24 hours give conversions between 52-80%. $[Ru(\mathbf{L}^{13})(PPh_3)_2]Cl_2$ only gives a final conversion of 64% of the substrate but shows catalytic activity after only two hours

Table 6.12
Results for transfer hydrogenation of acetophenone for complexes of the type [Ru(**L**)$(PPh_3)_2$]$\mathbf{X}_2$. Conditions: ^iPrOH, ^iPrOK, 80ºC.

L	X⁻	Product (%)				
		2 hrs	4 hrs	6 hrs	8 hrs	24 hrs
$\mathbf{L^6}$	Cl⁻	0.0	0.0	0.0	0.0	51.7
$\mathbf{L^{10}}$	Cl⁻	0.0	0.0	0.0	0.0	79.6
$\mathbf{L^{12}}$	Cl⁻	0.0	0.0	0.0	0.0	80.5
$\mathbf{L^{12}}$	PF_6^-	59.0	79.9	88.3	79.8	86.2
$\mathbf{L^{13}}$	Cl⁻	19.1	28.1	30.0	32.4	64.0

Acetophenone, 3,4-dimethoxyacetophenone and 4-nitroacetophenone were used as substrates for transfer hydrogenation. 3,4-dimethoxyacetophenone and 4-nitroacetophenone were used to compare the effect of electron donating and electron withdrawing groups on the phenyl ring and whether they affect the productivity of the catalyst when compared to acetophenone. For the complex $[Ru(OH_2)(\mathbf{L^{12}})(PPh_3)_2]Cl_2$ it seems that catalytic activity is increased when 3,4-dimethoxyacetophenone is used and decreased when 4-nitroacetophenone is used as a substrate (Table 6.13).

Table 6.13
Results for the catalytic activity of $[Ru(OH_2)(\mathbf{L^{12}})(PPh_3)_2]Cl_2$ on different acetophenone derivatives. Conditions: ^iPrOH, ^iPrOK, 80ºC.

Substrate	Product (%)				
	2 hrs	4 hrs	6 hrs	8 hrs	24 hrs
3,4-dimethoxyacetophenone	4.2	6.5	7.5	10.9	29.5
acetophenone	0.0	0.0	0.0	0.0	80.5
4-nitroacetophenone	0.0	0.0	3.4	4.5	3.8

For the complex $[Ru(OH_2)(\mathbf{L^{10}})(PPh_3)_2]Cl_2$ there was a large discrepancy between the three substrates (Table 6.14). While acetophenone showed around 80% of phenylethanol after 24 hours after the same time there was a complete absence of 4-nitrophenylethanol when 4-nitroacetophenone was used as a substrate. There is a small anomaly observed after 4 hours however this is within experimental error. Conversely this catalyst shows a higher activity towards 3,4-dimethoxyacetophenone and 3,4-dimethoxyacetophenone was produced after only two hours. The final value for the percentage of 3,4-dimethoxyacetophenone produced is 175% which is of course not a true value. This value was also obtained after the instrument was recalibrated and suggests that something could be happening in the reaction mixture that changes the response factor of the detector towards 3,4-dimethoxyacetophenone.

Table 6.14
Results for the catalytic activity of $[Ru(OH_2)(\mathbf{L}^{10})(PPh_3)_2]Cl_2$ on different acetophenone derivatives. Conditions: ^iPrOH, ^iPrOK, 80ºC.

Substrate	**Product (%)**				
	2 hrs	4 hrs	6 hrs	8 hrs	24 hrs
3,4-dimethoxyacetophenone	11.5	16.8	16.9	19.7	175.4
acetophenone	0.0	0.0	0.0	0.0	79.6
4-nitroacetophenone	0.0	2.9	0.0	0.0	0.0

While these two complexes suggest an increased activity towards transfer hydrogenation of 3,4-dimethoxyacetophenone compared to acetophenone, the complex $[Ru(\mathbf{L}^7)(PPh_3)_2]Cl_2$ shows an apparent decrease in activity (Table 6.15). The activity is still higher than when 4-nitroacetophenone is used as a substrate however, which shows no formation of product even after 24 hours.

Table 6.15
Results for the catalytic activity of $[Ru(\mathbf{L}^7)(PPh_3)_2]Cl_2$ on different acetophenone derivatives. Conditions: ^iPrOH, ^iPrOK, 80ºC.

Substrate	**Product (%)**				
	2 hrs	4 hrs	6 hrs	8 hrs	24 hrs
3,4-dimethoxyacetophenone	0.0	0.0	0.0	0.0	26.9
acetophenone	19.1	28.1	30.0	32.4	64.0
4-nitroacetophenone	0.0	0.0	0.0	0.0	0.0

6.5. Conclusion

In total five ruthenium complexes of the type [Ru(**L**)$(PPh_3)_2]X_2$ (where L = **L**^{6}, **L**^{7}, **L**^{9}, **L**^{10}, **L**^{12} and X = Cl, PF_6) were obtained. The separation of the isomers proved troublesome and resulted in poor yields however, restricting the scope of catalytic activity measurements. Crystal structures of the complexes [RuCl(**L**^{9})$(PPh_3)_2$]Cl·CH_3OH, [RuCl(**L**^{12})$(PPh_3)_2$]Cl·2$CHCl_3$ and [Ru(**L**^{12})$(OH_2)(PPh_3)_2](PF_6)_2$ were obtained and show that it is possible to exclude chlorido ligands from the ruthenium coordination sphere. It is possible that by replacing this site with a more labile ligand, such as water, catalytic activity could be increased by allowing the substrate to more easily bind.

In one case a salt exchange was successfully carried out to make the hexafluorophosphate complex salt [Ru(**L**^{12})$(OH_2)(PPh_3)_2](PF_6)_2$ with the intention of improving catalytic activity by freeing the site *trans* to the ligand **L**^{12} of chloride so a substrate can coordinate more easily. This appears to have been successful as [Ru(**L**^{12})$(OH_2)(PPh_3)_2](PF_6)_2$ exhibited the highest catalytic activity, converting around 80% of acetophenone to phenylethanol after only 4 hours. Similar complexes where L = 2,6-di(1*H*-pyrazol-3-yl)pyridine in the literature have been shown to achieve 93% conversion after only 1 hour however, and ruthenium complexes containing 2,6-di(1-pyrazolyl)pyridine derivatives have shown up to 97% conversion after only 10 minutes.[4, 23]

Further optimisation for the complexes in this chapter may have been achieved had higher yields of the complexes been obtained, but the activity recorded for these complexes using the same method are comparable to one another. Out of the chloride salts the complex with the highest initial activity towards transfer hydrogenation of acetophenone was [Ru(**L**^{7})$(PPh_3)_2]Cl_2$ however this did not give the highest conversion after 24 hours.

The initial rate of transfer hydrogenation of the acetophenone derivatives in most cases appears to decrease in the order 3,4-dimethoxyacetophenone > acetophenone > 4-nitroacetophenone. This corresponds to the pattern of decreasing electron density at the phenyl ring, consistent with that observed in the literature and is related to electron density available at the C=O which determines the ease of activation.[24-26] Final % conversions after 24 hours, however, show that these TH catalysts are most active towards unsubstituted acetophenone. In the case of the catalysts [Ru(OH_2)(**L**^{10})$(PPh_3)_2]Cl_2$ and [Ru(OH_2)(**L**^{12})$(PPh_3)_2]Cl_2$ no acetophenone is converted to phenylethanol until after 8 hours at 80°C, but after 24 hours there is a 79.6% and 80.5% conversion respectively.

These ligands have shown potential use in ruthenium transfer hydrogenation catalysts. Scope for further work includes refining the efficiency of the isomer separation of these pincer complexes. This will also allow further optimisation of the catalytic reaction conditions and study of the effects of a wider range of substrates, as well as determining whether the results obtained here are reproducible.

6.6. References

[1] J. P. Sauvage, J. P. Collin, J. C. Chambron, S. Guillerez, C. Coudret, V. Balzani, F. Barigelletti, L. De Cola and L. Flamigni, *Chem. Rev.* **1994**, *94*, 993-919.

[2] A. Bremer, C. M. Ruff, D. Girnt, U. Müllich, J. Rothe, P. W. Roesky, P. J. Panak, A. Karpov, T. J. J. Müller, M. A. Denecke and A. Geist, *Inorg. Chem.* **2012**, *51*, 5199-5207.

[3] L. L. Miao, H. X. Li, M. Yu, W. Zhao, W. J. Gong, J. Gao, Z. G. Ren, H. F. Wang and J. P. Lang, *Dalton Trans.* **2012**, *41*, 3424-3430.

[4] O. Dayan, N. Özdemir, Z. Şerbetci, M. Dinçer, B. Çetinkaya and O. Büyükgüngör, *Inorg. Chim. Acta* **2012**, *392*, 246-253.

[5] J. X. Gao, T. Ikariya and R. Noyori, *Organometallics* **1996**, *15*, 1087-1089.

[6] S. Hashiguchi, A. Fujii, J. Takehara, T. Ikariya and R. Noyori, *J. Am. Chem. Soc.* **1995**, *117*, 7562-7563.

[7] T. Ohkuma, H. Ooka, T. Ikariya and R. Noyori, *J. Am. Chem. Soc.* **1995**, *117*, 10417-10418.

[8] D. L. Jameson, J. K. Blaho, K. T. Kruger and K. A. Goldsby, *Inorg. Chem.* **1989**, *28*, 4312-4314.

[9] H. Deng, Z. Yu, J. Dong and S. Wu, *Organometallics* **2005**, *24*, 4110-4112.

[10] A. Yoshinari, A. Tazawa, S. Kuwata and T. Ikariya, *Chem. - Asian J.* **2012**, *7*, 1417-1425.

[11] T. Jozak, D. Zabel, A. Schubert, Y. Sun and W. R. Thiel, *Eur. J. Inorg. Chem.* **2010**, 5135-5145.

[12] L. Wang, H. R. Pan, Q. Yang, H. Y. Fu, H. Chen and R. X. Li, *Inorg. Chem. Commun.* **2011**, *14*, 1422-1427.

[13] N. J. Beach and G. J. Spivak, *Inorg. Chim. Acta* **2003**, *343*, 244-252.

[14] M. A. Fox, J. E. Harris, S. Heider, V. Pérez-Gregorio, M. E. Zakrzewska, J. D. Farmer, D. S. Yufit, J. A. K. Howard and P. J. Low, *J. Organomet. Chem.* **2009**, *694*, 2350-2358.

[15] O. A. Osipov, A. D. Garnovskii and V. I. Minkin, *J. Struct. Chem.* **1967**, *8*, 817-828.

[16] M. Gerloch and L. R. Hanton, *Inorg. Chem.* **1981**, *20*, 1046-1050.

[17] S. Kuwata and T. Ikariya, *Chem. Eur. J.* **2011**, *17*, 3542-3556.

[18] B. Bovio, G. Banditelli and A. L. Bandini, *Inorg. Chim. Acta* **1985**, *96*, 213-223.

[19] F. Bonati, *Gazz. Chim. Ital.* **1989**, *119*, 291-300.

[20] J. R. Sanders, *J. Chem. Soc., Dalton Trans.* **1973**, 743-747.

[21] Z. Ma, Y. Lin and Z. N. Chen, *Jiegou Huaxue* **2004**, *23*, 1277-1281.

[22] M. T. Reetz and X. Li, *J. Am. Chem. Soc.* **2006**, *128*, 1044-1045.

[23] W. Du, Q. Wang, L. Wang and Z. Yu, *Organometallics* **2014**, *33*, 974-982.

[24] M. Aydemir, F. Durap, A. Baysal, N. Meric, A. Buldağ, B. Gümgüm, S. Özkar and L. T. Yildirim, *J. Mol. Catal. A: Chem.* **2010**, *326*, 75-81.

[25] J. W. Faller and A. R. Lavoie, *Organometallics* **2001**, *20*, 5245-5247.

[26] P. Pelagatti, M. Carcelli, F. Calbiani, C. Cassi, L. Elviri, C. Pelizzi, U. Rizzotti and D. Rogolino, *Organometallics* **2005**, *24*, 5836-5844.

Chapter 7

Experimental

7.1. General Experimental Considerations

Elemental microanalyses were performed by the University of Leeds School of Chemistry microanalytical service. Electrospray mass spectra (ESMS) were obtained by the author and T. Marinko-Covell on a Bruker MicroTOF spectrometer, from MeCN feed solutions. All mass peaks have the correct isotopic distributions for the proposed assignments. Thermogravimetric analyses were run by A. Kazlauciunas at the University of Leeds using a TA instruments TGA 2050 analyser.

NMR spectra were run by the author on a Bruker Avance DPX 300 or Bruker Avance DRX 500 LC NMR at 298 K. Chemical shifts were quoted relative to residual solvent protons for ^{1}H and ^{13}C, and ^{31}P NMR chemical shifts are quoted relative to 85% aqueous phosphoric acid.

Magnetic susceptibility measurements were performed by F. Tuna, L. J. Kershaw Cook or R. Kulmaczewski on a Quantum Design VSM SQUID magnetometer, in an applied field of 5000 G. A diamagnetic correction for the sample was estimated from Pascal’s constants; a diamagnetic correction for the sample holder was also measured, and applied to the data. Variable temperature magnetic susceptibility in solution via the Evans method were performed by S. Barrett on a Bruker DRX 500 spectrometer at a frequency of 500.13 MHz.[1, 2] A diamagnetic correction for the solvent, and a correction for the change in density of the solvent with temperature, were applied to these data.[3]

Fixed temperature powder diffraction measurements were carried out by the author at ambient temperature on a Bruker D2 Phaser equipped with a LynxEye detector using Long Fine Focused Cu radiation ($\lambda° = 1.54060$ Å) and data workup was performed using Bruker DIFFRAC Suite software. Variable temperature powder diffraction measurements were obtained by T. Comyn at the University of Leeds School of Chemical and Process Engineering using a Panalytical Xpert MPD diffractometer with an Anton Par TTK 450 stage.

Diffraction data were measured by the author, M. A. Little or L. J. Kershaw Cook using one of the following: (i) Bruker X8 Apex II diffractometer fitted with an Oxford Cryostream low temperature device, using graphite monochromated Mo-K_{α} radiation ($\lambda = 0.71073$ Å) generated by a rotating anode, (ii) Agilent SuperNova diffractometer equipped with an Atlas CCD detector and connected to an Oxford Cryostream low temperature device using monochromated Cu K_{α} radiation ($\lambda = 1.54184$ Å) / Mo K_{α} radiation ($\lambda = 0.7107$ Å) from a Microfocus Nova/Mova X-ray source. Structures were solved by M. A. Halcrow, or the author. Structure solution by Direct and Patterson methods was achieved through the use of SHELXS86 program and the structural model refined by full matrix least squares on F^2 using SHELXL97.[4] Editing of crystallographic information files was carried out using

Platon.[5] Molecular graphics and geometric information were calculated by the Olex 2 program.[6]

Dry solvents were obtained from the University of Leeds solvent purification service.

GC analyses were performed using a Bruker 430-GC equipped with a CP-8400 autosampler. Separation was achieved using a BR-5 column (30 m x 0.25 mm (ID) x 0.25 µm film thickness) with carrier gas flow rate of 2.0 $\mathrm{mLmin^{-1}}$. The temperature ramp from 50 to 310 ^{o}C for reactions involving 3,4-dimethoxyacetophenone and 4-nitroacetophenone was 20 $^{o}\mathrm{Cmin^{-1}}$ and 10$^{o}\mathrm{Cmin^{-1}}$ for those involving acetophenone. The injection volume was 1 µL with a split ratio of 10. The response factors for the standard, substrate and product were calculated using an appropriate calibration for this GC and column.

7.2. Chapter 3:
Iron(II) Complexes of 2,6-Di(1-alkylpyrazol-3-yl)pyridine Derivatives

7.2.1. 2,6-Di[(N,N-dimethylamino)-1-oxoprop-2-en-1-yl]pyridine[7]

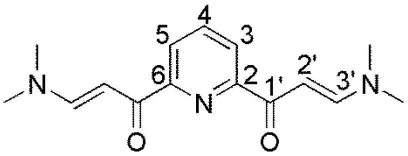

2,6-Diacetyl pyridine (5 g, 30 mmol) was dissolved in neat N,N-dimethylformamide dimethylacetal (25 g, 171 mmol) to give a clear solution. The solution was then heated at reflux (110℃) for 6 hours after which an orange precipitate had formed and the solution turned brown. The precipitate was filtered off and thoroughly washed with acetone. Yield 5.48 g, 66.8 %.

CHN analysis: Calcd. from $C_{15}H_{19}O_2N_3$ C, 65.91; H, 7.00; N, 15.37 %. Found C, 65.70; H, 7.00; N, 15.45 %.

ES$^+$ mass spectrum: Calcd. from $C_{15}H_{19}O_2N_3 \cdot H^+$ 274.2 g mol^{-1}. *m/z* 274.2.

^{1}H-NMR δ_H (500 MHz, METHANOL - *d*4): 3.08 (s, 6 H, C*H*$_3$), 3.28 (s, 6H, C*H*$_3$), 6.66 (s, 2 H, COHC=C*H*), 8.01 (d, *J*=9 Hz, 2 H, CO*H*C=CH), 8.02 (t, *J*=7.7 Hz, 1 H, Py *H*^{4}), 8.14 (d, J=7.4 Hz, 2 H, Py *H*^{3}).

^{13}C{^{1}H}-NMR δ_C (126 MHz, METHANOL - *d*4): 30.7 (*C*H$_3$), 37.7 (*C*H$_3$), 45.7 (*C*H$_3$), 92.2 (*C*$^{2`}$), 124.4 (Py *C*$^3$), 139.0 (Py *C*$^4$), 156.2 (Py *C*$^2$), 157.0 (*C*$^{3`}$), 210.0 (*C*=O).

IR mid: $\nu(\text{C–H})_{\text{alkene}}$ = 3102 cm^{-1} (m), $\nu(\text{C–H})_{\text{aromatic}}$ = 3025 cm^{-1} (m), $\nu(\text{C–H})_{\text{aliphatic}}$ = 2916 cm^{-1} (m), $\nu(\text{C=O})$ = 1644 cm^{-1} (s).

7.2.2. 2,6-Di(1*H*-pyrazol-3-yl)pyridine[8]

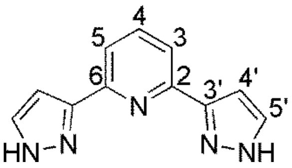

Hydrazine hydrate (6.0 g, 200 mmol) was added to a stirred suspension of 2,6-*bis*[(N,N`-dimethylamino)-1`-oxoprop-2`-en-1`-yl]pyridine (5.0 g, 18 mmol) in ethanol (75 ml) and then heated to reflux for 20 hours, after which the orange suspension had turned to a pale yellow solution. The solution was allowed to cool and water added until a white precipitate formed which was filtered and recrystallised from chloroform to give a colourless crystalline solid. Yield 3.12 g, 81.2 %.

CHN analysis: Calc. from $C_{11}H_9N_5$ C, 62.59; H, 4.30; N, 33.16 %. Found C, 62.25; H, 4.25; N, 33.50 %.

EI$^+$ mass spectrum: Calc. from $C_{11}H_9N_5$ 211.1 g mol^{-1}. *m/z* 211.1.

^{1}H-NMR δ_H (300 MHz, DMSO *d*6): 6.90 - 8.00 (br. m, 7 H, Py $H^{3/4/5}$ Pz $H^{3'/4'/5'}$), 13.02 (s, 1 H, N*H*), 13.49 (s, 1 H, N*H*).

^{13}C{^{1}H}-NMR δ_C (126 MHz, DMSO *d*6) 103.5 (Pz $C^{4'}$), 117.7 (Py C^3), 129.7 (Pz $C^{5'}$), 140.3 (Py C^4), 147.2 (Pz $C^{3'}$ or Py C^2), 151.1 (Pz $C^{3'}$ or Py C^2).

7.2.3. 2,6-Di(1-methylpyrazol-3-yl)pyridine (L^1)[9]

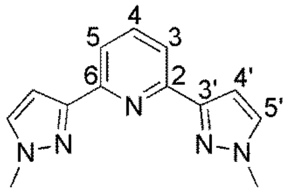

Iodomethane (2.80 g, 20.0 mmol) was added to a stirred solution of 2,6-di(1*H*-pyrazol-3-yl)pyridine (1.50 g, 7.1 mmol) and sodium methoxide (1.08 g, 20 mmol) in dry THF and the mixture was heated at reflux for 48 hours. The solvent was then evaporated to leave a pale yellow solid. The product was then dissolved in chloroform and washed with water (3 x 30 mL). The solvent was then evaporated to leave a white crystalline solid. 0.83 g, 48.8 %.

CHN analysis: Calcd. from $C_{13}H_{13}N_5$ C, 65.25; H, 5.48; N, 29.27 %. Found C, 64.65; H, 5.45; N, 29.50 %.

ES$^+$ mass spectrum: Calcd. from $C_{13}H_{13}N_5\cdot Na^+$ 262.1 g mol^{-1}. *m/z* 262.1.

^{1}H-NMR δ_H (500 MHz, CHLOROFORM-*d*): 3.63 (s, 6 H, CH_3), 6.76 (d, *J*=2.3 Hz, 2 H, Pz $H^{4''}$), 7.38 (d, *J*=2.3 Hz, 2 H, Pz $H^{5'}$), 7.63 (d, *J*=7.8 Hz, 2 H, Py $H^{3'}$), 7.79 (t, *J*=7.8 Hz, 1 H, Py H^4).

^{13}C{^{1}H}-NMR δ_C (126 MHz, CHLOROFORM-*d*): 39.0 (CH_3), 104.2 ($C^{4'}$), 119.0 (C^3), 132.6 ($C^{5'}$), 138.8 (C^4), 150.3 (C^2 or $C^{3'}$), 150.9 (C^2 or $C^{3'}$).

IR mid: ν(C–H)$_{aromatic}$ = 3093 cm^{-1} (s), ν(C–H)$_{aliphatic}$ = 2939 cm^{-1} (s), ν(C=C)$_{aromatic}$ = 1603 cm^{-1} (m).

7.2.4. 2,6-Di(1-*iso*propylpyrazol-3-yl)pyridine (L^2)[9]

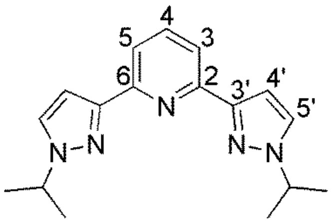

2,6-Di(1*H*-pyrazol-3-yl)pyridine (2.00 g, 9.5 mmol) and lithium hydride (0.22 g, 28.4 mmol) were suspended in dry THF and 2-iodopropane (4.83 g, 28.4 mmol) was added. The mixture was then heated at reflux for 3 days after which a white precipitate had formed. This was collected via filtration, washed with water and thoroughly dried under high vacuum. 2.67 g, 95.3 %.

ES^+ mass spectrum: Calcd. from $C_{17}H_{21}N_5 \cdot Na^+$ 318.2 g mol^{-1}. *m/z* 318.2.

^1H NMR δ_H (500 MHz, DMSO-*d*6): 1.47 (d, *J*=6.7 Hz, 12 H, CH_3) 4.57 (*sept*, *J*= 6.6 Hz, 2 H, C*H*(CH_3)$_2$) 6.92 (d, *J*=2.1 Hz, 2 H, Pz $H^{4'}$), 7.83 (s, 2 H, Pz $H^{5'}$), 7.84 (s, 2 H, Py $H^{3/5}$), 7.84 (s, 1 H, Py H^4).

$^{13}C\{^1H\}$-NMR δ_C (300 MHz, DMSO *d*6): 22.2 (*C*H_3), 54.3 (*C*H(CH_3)$_2$), 104.0 (Pz $C^{4`}$), 119.3 (Py $C^3$), 128.9 (Pz $C^{5`}$), 139.0 (Py C^4), 149.6 (Py C^2 or Pz $C^{3`}$), 151.0 ((Py $C^2$ or Pz $C^{3`}$).

IR mid: ν(C–H)$_{aromatic}$ = 3094 cm^{-1} (m), ν(C–H)$_{alkane}$ = 2934 cm^{-1} (s), ν(C–H)$_{alkane}$ = 2875 cm^{-1} (m), ν(C=C)$_{aromatic}$ = 1574 cm^{-1} (m).

7.2.5. 2,6-Di(1-allylpyrazol-3-yl)pyridine (L^3)

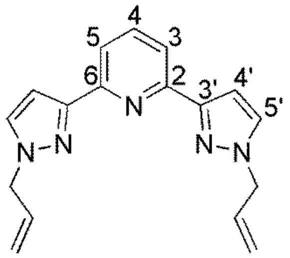

2,6-Di(1*H*-pyrazol-3-yl)pyridine (2.00 g, 9.5 mmol) and lithium hydride (0.22 g, 28.4 mmol) were suspended in anhydrous THF and stirred until effervescence ceased. Allyl bromide (3.43 g, 28.4 mmol) was then added and the mixture was heated at reflux for 16 hours. The solvent was then evaporated and the resulting solid was then suspended in water and extracted with chloroform. The organic layer was dried with magnesium sulphate and the solvent evaporated, which left an orange oily substance. This was then frozen using liquid nitrogen and placed under high vacuum to remove the last solvent residue, leaving apale yellow crystalline solid. 1.48 g, 53.5 %.

CHN analysis: calcd from $C_{17}H_{17}N_5$ C, 70.08; H, 5.88; N, 24.04 %. Found C, 69.45; H, 5.90; N, 23.90 %.

ES^+ mass spectrum: Calcd from $C_{17}H_{18}N_5^+$ 292.16 g mol^{-1}, *m/z* 292.15.

^1H NMR δ_H (500 MHz, CHLOROFORM-*d*): 4.75 (d, *J*=5.95 Hz, 21 H, CH_2) 5.18 (ddd, *J*=16.78, 6.1, 1.1 Hz, 4 H, CH=CH_2) 6.00 (ddt, *J*=16.8, 10.5, 5.9, 5.9 Hz, 2 H, C*H*=CH_2) 6.97 (d, *J*=2.3 Hz, 2 H, Pz $H^{4'}$) 7.38 (d, *J*=2.3 Hz, 2 H, Pz $H^{5'}$) 7.65 (t, *J*=7.8 Hz, 1 H, Py H^4)

7.80 (d, J=7.8 Hz, 2 H, Py$H^{3/5}$).

^{13}C NMR δ_C (500 MHz, CHLOROFORM-d): 54.9 (CH$_2$), 105.0 (Pz $C^{4'}$), 118.5 (Py C^3), 118.6 (CH=CH$_2$), 130.3 (Pz $C^{5'}$), 132.9 (CH=CH$_2$), 137.0 (Py C^4), 151.8 – 152.2 (Py C^2, Pz $C^{3'}$).

7.2.6. 2,6-Di(1-benzylpyrazol-3-yl)pyridine (L^4)[9]

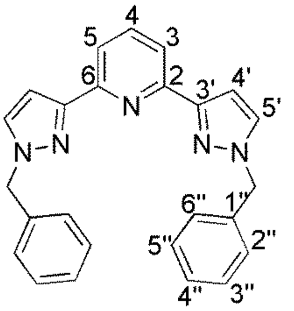

2,6-Di(1H-pyrazol-3-yl)pyridine (2.00 g, 9.5 mmol) and lithium hydride (0.22 g, 28.4 mmol) were suspended in dry THF and benzyl bromide (4.86 g, 28.4 mmol) was added. The mixture was then heated at reflux for 44 hours under a nitrogen atmosphere. The resulting white precipitate was removed via filtration and washed with water. The solid was then recrystallised from chloroform and thoroughly dried under high vacuum. 1.67 g, 44.8 %.

EI$^+$ mass spectrum: Calcd. from $C_{25}H_{21}N_5$ 391.2 g mol^{-1}, m/z 391.2.

^{1}H-NMR δ_H (500 MHz, CHLOROFORM-d): 5.15 (s, 4 H, CH_2), 6.86 (s, 2 H, Pz$H^{4'}$), 6.90 – 7.20 (m, 10 H, Bz H), 7.30 (d, J=2.3 Hz, 2 H, Pz $H^{5'}$), 7.66 (t, J=5.0 Hz, 1 H, Py H^4), 7.71 (s, 2 H, Py$H^{3/5}$).

^{13}C{^{1}H}-NMR δ_C (126 MHz, CHLOROFORM-d): 56.2 (CH$_2$), 105.2 (Pz $C^{5'}$), 118.6 (Py C^3), 127.0 – 129.0 (Bz $C^{2''/6''}$, $C^{3''/5''}$, $C^{4''}$)130.9 (Pz $C^{4'}$), 136.4 (Bz $C^{1''}$), 137.3 (Py C^4), 151.7 (Py C^2).

IR mid: ν(C–H)$_{\text{aromatic}}$ = 3032 cm^{-1} (s), ν(C–H)$_{\text{alkane}}$ = 2925 cm^{-1} (m), ν(C=C)$_{\text{aromatic}}$ = 1602 cm^{-1} (s).

7.2.7. 2,6-Di(1-phenylpyrazol-3-yl)pyridine (Attempted Synthesis)

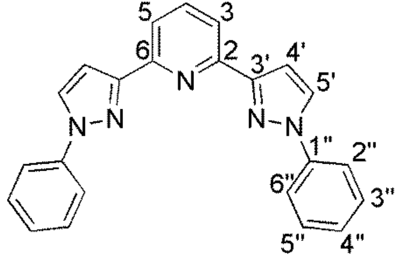

2,6-Di[(N,N-dimethylamino)-1-oxoprop-2-en-1-yl]pyridine (84.4 mg, 0.3 mmol) was suspended in an ethanol/acetic acid mixture (7:3, 50 mL) and phenylhydrazine (90 µL, 0.9 mmol) and the mixture was stirred at room temperature for 20 hours. The mixture was then neutralised with saturated sodium carbonate solution, forming an orange oil which was separated and dried under vacuum. LCMS shows 3 peaks with *m/z* 364.2 $[MH]^+$.

7.2.8. $[Fe(L^1)_2](BF_4)_2$[10]

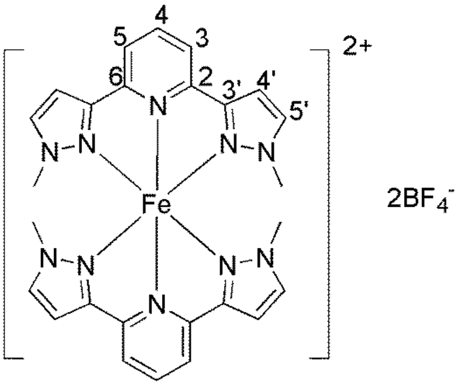

Iron(II) tetrafluoroborate hexahydrate (0.14 g, 0.4 mmol) was added to a stirred solution of 2,6-di(1-methylpyrazol-3-yl)pyridine (0.20 g, 0.8 mmol) in nitromethane (15mL) and the resulting yellow solution was stirred for a further 30 minutes. Diethyl ether was then added until a yellow precipitate formed which was collected via filtration. The product was then recrystallised from methanol/diethyl ether to give a yellow crystalline solid. 0.51 g, 53.7 %. CHN analysis: Calcd. from $C_{26}H_{26}B_2F_8FeN_{10}$ C, 44.11; H, 3.70; N, 19.78 %. Found C, 43.95; H, 3.65; N, 19.65 %.

ES^+ mass spectrum: calcd. from $C_{26}H_{26}FeN_{10}^{2+}$ 534.2 g mol^{-1}. Found *m/z* 267.1 $[\mathbf{1}]^{2+}$.

^{1}H-NMR δ_H (300 MHz, METHANOL - *d*3): 2.2 (12 H, CH_3), 22.6 (2H, Py H^4), 48.5 (4 H, Pz $H^{3'}$), 57.1 (4 H, Py $H^{3/5}$ or Pz $H^{3'}$), 62.0 (4H, Py $H^{3/5}$ or Pz $H^{5'}$).

IR mid: ν(C–H)$_{aromatic}$ = 3149 cm^{-1} (s), ν(C=C)$_{aromatic}$ = 1616 cm^{-1} (m), ν(B–F) = 1047 cm^{-1} (vs).

7.2.9. [Fe(L^1)$_2$](ClO$_4$)$_2$[10]

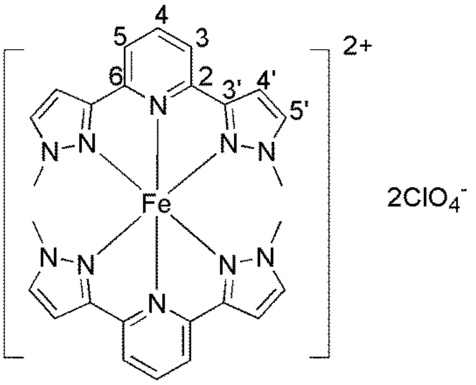

Iron(II) perchlorate hydrate (0.11 g, 0.4 mmol) was added to a stirred solution of 2,6-di(1-methylpyrazol-3-yl)pyridine (0.20 g, 0.8 mmol) in nitromethane (15mL) and the resulting orange solution was stirred for a further 30 minutes. Diethyl ether was then added and put in the freezer for 2 hours until a yellow precipitate formed which was collected via filtration. The product was then recrystallised from methanol/diethyl ether to give a yellow crystalline solid. 0.11 g, 37.5 %.

CHN analysis: Calcd. from $C_{26}H_{26}Cl_2FeN_{10}O_8$ C, 42.59; H, 3.57; N, 19.10 %. Found C, 42.60; H, 3.50; N, 19.05 %.

ES$^+$ mass spectrum: calcd. from $C_{26}H_{26}FeN_{10}^{2+}$ 534.2 g mol^{-1}. Found *m/z* 267.1 [**1**]$^{2+}$.

^{1}H-NMR δ_H (300 MHz, METHANOL - *d*3): 2.2 (12 H, CH_3), 22.6 (2 H, Py H^4), 48.5 (4 H, Pz $H^{3'}$), 57.1 (4 H, Py $H^{3/5}$ or Pz $H^{3'}$), 62.0 (4 H, Py $H^{3/5}$ or Pz $H^{5'}$).

IR mid: $\nu(C–H)_{aromatic}$ = 3132 cm^{-1} (m), $\nu(C=C)_{aromatic}$ = 1615 cm^{-1} (m), $\nu(Cl–O)$ = 1097 cm^{-1} (vs).

7.2.10. [Fe(L^1)$_2$](PF$_6$)$_2$[10]

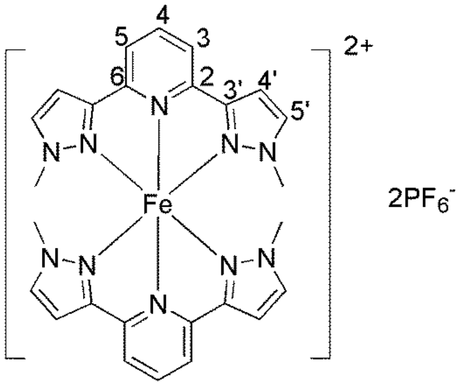

Iron(II) chloride tetrahydrate (0.08 g, 0.4 mmol) was added to a stirred suspension of 2,6-di(1-methylpyrazol-3-yl)pyridine (0.20 g, 0.8 mmol) in water (15 mL). The mixture was stirred for 30 minutes and the mixture was filtered and saturated ammonium hexafluorophosphate aqueous solution (10 mL) was added causing precipitation of a yellow solid which was collected via filtration. The product was recrystallised from methanol/diethyl ether to give a yellow crystalline solid. 0.23 g, 70.4 %.

CHN analysis: Calcd. from $C_{26}H_{26}F_{12}FeN_{10}P_2$ C, 37.88; H, 3.18; N, 16.99 %. Found C, 37.80; H, 3.10; N, 17.05 %.

ES^+ mass spectrum: calcd. from $C_{26}H_{26}FeN_{10}{}^{2+}$ 534.2 g mol^{-1}. Found *m/z* 267.1 $[\mathbf{1}]^{2+}$.

^{1}H-NMR δ_H (300 MHz, METHANOL - *d*3): 2.2 (12 H, CH_3), 22.6 (2 H, Py H^4), 48.5 (4 H, Pz $H^{3'}$), 57.1 (4 H, Py $H^{3/5}$ or Pz $H^{3'}$), 62.0 (4 H, Py $H^{3/5}$ or Pz $H^{5'}$).

IR mid: ν(C–H)$_{aromatic}$ = 3149 cm^{-1} (s), ν(C=C)$_{aromatic}$ = 1616 cm^{-1} (m), ν(P–F) = 834 cm^{-1} (vs).

7.2.11. $[Fe(L^2)_2](BF_4)_2 \cdot H_2O$[10]

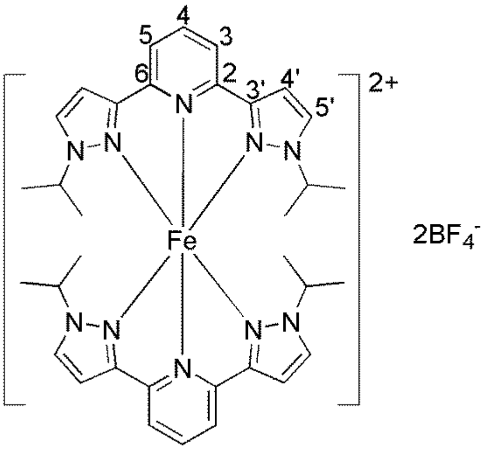

Iron(II) tetrafluoroborate hexahydrate (0.11 g, 0.3 mmol) was added to a stirred solution of 2,6-di(1-isopropylpyrazol-3-yl)pyridine (0.20 g, 0.7 mmol) in methanol (15 mL). The mixture was stirred for a further 45 minutes before the yellow precipitate was removed via filtration and washed with diethyl ether. 0.17 g, 54.8 %. Crystals suitable for XRD were obtained via slow vapour diffusion from acetonitrile/diisopropyl ether.

CHN analysis: calcd. from $C_{34}H_{42}B_2F_8FeN_{10} \cdot H_2O$ C, 48.72; H, 5.29; N, 16.71 %. Found C, 48.90; H, 4.95; N, 16.70 %.

ES^+ mass spectrum: calcd. from $C_{34}H_{42}FeN_{10}$ 646.3 g mol^{-1}. m/z 323.2 $[\mathbf{2}]^{2+}$.

^{1}H NMR δ_H (500 MHz, ACETONITRILE-*d*3): 2.2 (24 H, CH(CH_3)$_2$) 4.7 (4 H, C*H*(CH$_3$)$_2$), 21.1 (2 H, Py H^4), 45.8 (4H, Pz $H^{5'}$), 60.8 (4 H, Pz $H^{4'}$ or Py $H^{3/5}$), 61.6 (4 H, Pz $H^{4'}$ or Py $H^{3/5}$).

IR mid: ν(C–H)$_{aromatic}$ = 3146, 3085 cm^{-1} (m), ν(C – H)$_{alkane}$ = 2981, 2940, 2882 cm^{-1}, ν(C=C)$_{aromatic}$ = 1614 cm^{-1} (s), ν(B–F) = 1055 cm^{-1} (vs).

7.2.12. $[Fe(L^2)_2](ClO_4)_2$[10]

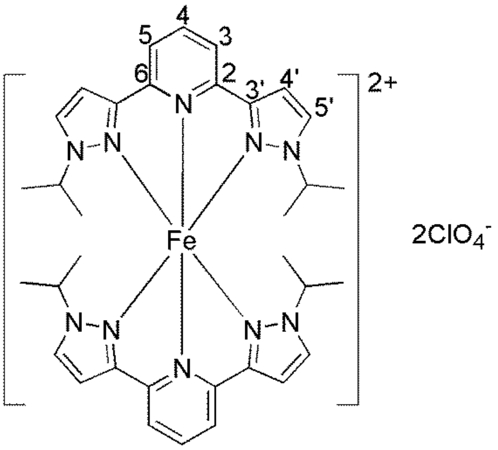

Iron(II) perchlorate hydrate (0.09 g, 0.4 mmol) was added to a stirred solution of 2,6-di(1-isopropylpyrazol-3-yl)pyridine (0.20 g, 0.7 mmol) in methanol (20 mL). The mixture was stirred for a further 45 minutes before the yellow precipitate was removed via filtration and washed with diethyl ether. 0.15 g, 45.8%. Crystals suitable for XRD were obtained via slow vapour diffusion from acetonitrile/diisopropyl ether.

CHN analysis: calcd from $C_{34}H_{42}Cl_2FeN_{10}O_8{\cdot}H_2O$ C, 47.29; H, 5.14; N, 16.22 %. Found C, 47.50; H, 4.95; N, 16.15 %.

ES$^+$ mass spectrum: calcd. from $C_{34}H_{42}FeN_{10}$ 646.3 g mol^{-1}. m/z 323.2 $[\mathbf{2}]^{2+}$.

^{1}H NMR δ_H (500 MHz, ACETONITRILE-*d*3): 2.1, 2.2 (24 H, $CH(CH_3)_2$), 4.7 (4 H, $CH(CH_3)_2$), 21.1 (2 H, Py H^4), 45.8 (4 H, Pz $H^{5'}$), 60.8 (4 H, Pz $H^{4'}$ or Py $H^{3/5}$), 61.6 (4 H, Pz $H^{4'}$ or Py $H^{3/5}$).

IR mid: $\nu(C–H)_{aromatic}$ = 3135, 3085 cm^{-1} (m), $\nu(C – H)_{alkane}$ = 2981, 2938, 2880 cm^{-1}, $\nu(C=C)_{aromatic}$ = 1614 cm^{-1} (s), $\nu(Cl – O)$ = 1084 cm^{-1} (vs).

7.2.13. $[Fe(L^2)_2](PF_6)_2$[10]

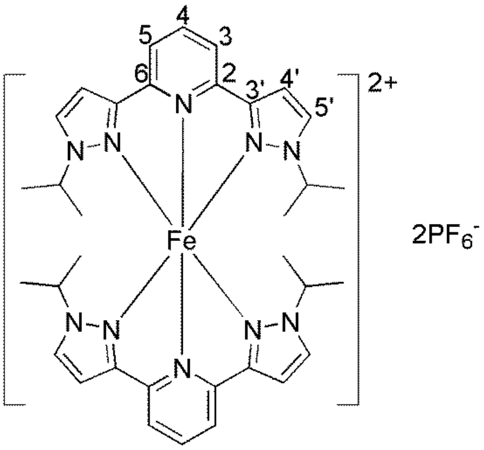

Ferrous chloride tetrahydrate (0.07 g, 0.3 mmol) was added to a stirred solution of 2,6-di(1-isopropylpyrazol-3-yl)pyridine (0.20 g, 0.7 mmol), and then a saturated solution of ammonium hexafluorophosphate in water (10 mL) was added. The yellow precipitate which formed was collected via filtration. 0.26 g, 81.0 %. Crystals suitable for XRD were obtained via slow vapour diffusion from acetonitrile/diisopropyl ether.

CHN analysis: calcd from $C_{34}H_{42}F_{12}FeN_{10}P_2$ C, 43.60; H, 4.52; N, 14.96 %. Found C, 43.15; H, 4.40; N, 14.90 %.

ES^+ mass spectrum: calcd. from $C_{34}H_{42}FeN_{10}$ 646.3 g mol^{-1}. m/z 323.2 $[\mathbf{2}]^{2+}$.

^{1}H NMR δ_H (500 MHz, ACETONITRILE-*d*3):2.1, 2.2 (24 H, CH(C*H*$_3$)$_2$), 4.7 (4 H, C*H*(CH$_3$)$_2$), 21.1 (2 H, Py H^4), 45.8 (4 H, Pz $H^{5'}$), 60.8 (4 H, Pz $H^{4'}$ or Py $H^{3/5}$), 61.6 (4 H, Pz $H^{4'}$ or Py $H^{3/5}$).

IR mid: $\nu(C–H)_{aromatic}$ = 3151 cm^{-1} (m), $\nu(C – H)_{alkane}$ = 2980, 2937, 2882 cm^{-1}, $\nu(C=C)_{aromatic}$ = 1614 cm^{-1} (s), $\nu(P – F)$ = 841 cm^{-1} (vs).

7.2.14. $[Fe(L^3)_2](BF_4)_2$[10]

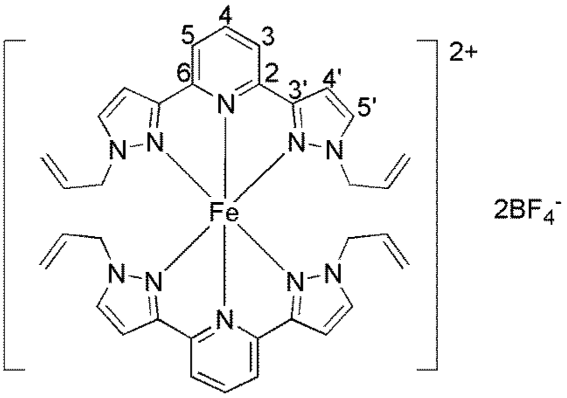

2,6-Di(1-allylpyrazol-3-yl)pyridine (0.20 g, 0.7 mmol) was dissolved in methanol (15 mL) and iron(II) tetrafluoroborate hexahydrate (0.12 g, 0.3 mmol) was added. The mixture was then stirred for a further 30 minutes after which a yellow precipitate had formed. The precipitate was removed via filtration. 0.218 g, 78.9 %.

CHN analysis: Calcd. from $C_{34}H_{34}B_2F_8FeN_{10}$ C, 50.28; H, 4.22; N, 17.25 %. Found C, 50.10; H, 4.15; N, 16.95 %.

ES$^+$ mass spectrum: Calcd from $C_{34}H_{34}FeN_{10}^{2+}$ 319.12 g mol^{-1}, found *m/z* 319.12.

^{1}H NMR δ_H (500 MHz, ACETONITRILE-*d*3): -0.6 (8 H, C$H_{2(alkyl)}$), 2.1 (8 H, C$H_{2(allyl)}$), 2.2 (4 H, C$H_{(allyl)}$), 21.7 (2 H, Py H^4), 46.8 (4 H, Pz $H^{5'}$), 58.9 – 61.8 (Py $H^{3/5}$, Pz $H^{4'}$).

IR mid: ν(C–H) = 3126, 2987 cm^{-1} (m), $\nu(C{=}C)_{alkene}$ = 1645 cm^{-1} (w), $\nu(C{=}C)_{aromatic}$ = 1614 cm^{-1} (s), ν(B – F) = 1050 cm^{-1} (vs).

7.2.15. $[FeL^4)_2](BF_4)_2$[10]

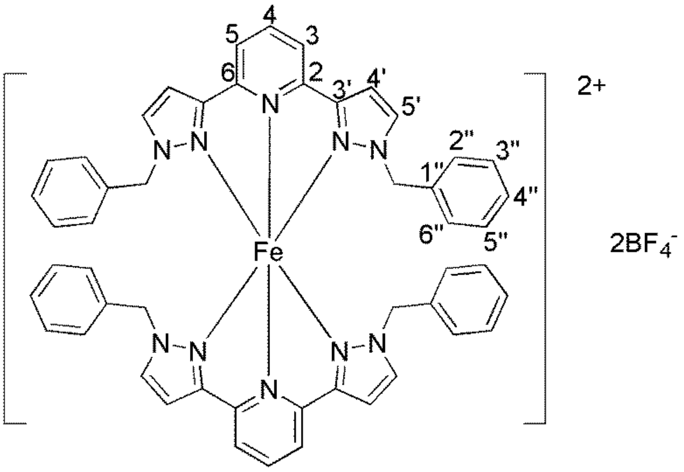

Iron(II) tetrafluoroborate hexahydrate (0.09 g, 0.2 mmol) was added to a stirred solution of 2,6-di(1-benzylpyrazol-3-yl)pyridine(0.2 g, 0.5 mmol) in methanol (15 mL) and stirred for a further hour. Diethyl ether was added and the resulting precipitate was removed via filtration. 0.17 g, 66.4 %.

CHN analysis: calcd. from $C_{50}H_{42}B_2F_8FeN_{10}$ C, 59.32; H, 4.18; N, 13.84 %. Found C, 58.75, H, 4.10; N, 13.75 %.

ES^+ mass spectrum: calcd. from $C_{50}H_{42}FeN_{10}$ 838.8 g mol-1. m/z 419.2 [**4**]$^{2+}$.

^{1}H NMR spectrum δH (500 MHz, ACETONITRILE-*d*3): -0.5 (8 H, CH_2), 2.2 (8 H, Bz $H^{2''/6''}$), 5.5 (8 H, Bz $H^{3''/5''}$), 6.4 (4 H, Bz $H^{4''}$), 20.8 (2 H, Py H^{4}), 46.0 (4 H, Pz $H^{5'}$), 59.5 (4 H, Pz $H^{4'}$ or Py $H^{3/5}$), 60.9 (4 H, Pz $H^{4'}$ or Py $H^{3/5}$).

IR mid: ν(C–H)$_{\text{aromatic}}$ = 3145, 3034 cm^{-1} (m), ν(C=C)$_{\text{aromatic}}$ = 1610 cm^{-1} (s), ν(B – F) = 1052 cm^{-1} (vs).

7.3. Chapter 4:
Substitution of 2,6-Di(1*H*-pyrazol-3-yl)pyridine at the Pyrazolyl *C*4, *C*5 Positions and the Pyridyl *C*4 Position and Implications on Spin Crossover

7.3.1. 2,6-Di(3-oxo-3-propanenitrile)pyridine[11]

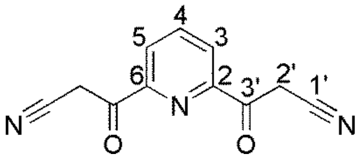

2,6-pyridine dicarboxylic methyl ester (25.0 g, 128 mmol) and acetonitrile (13.5 ml, 320 mmol) were dissolved in dry THF (300 ml) and sodium hydride (21.0 g) was added. The mixture was then heated at reflux for 2 hours and then the pale yellow solid was filtered off. This was re-dissolved in water (400 ml) and acidified to ~pH 5. The solid which precipitated was filtered, washed with water, dried and re-crystallised from ethanol/dioxane to give an orange solid. Yield 9.4 g, 34.4 %.

CHN analysis: Calcd. for $C_{11}H_7O_2N_3$ C, 61.97; H, 3.31; N, 19.71 %. Found C, 62.10; H, 3.30; N, 19.55 %.

ES^+ mass spectrum: Calcd. for $C_{11}H_7O_2N_3Na^+$ 236.2 g mol^{-1}. m/z 236.1.

^{1}H-NMR δ_H (500 MHz, ACETONE-*d*6): 4.84 (s, 4 H, CH_2), 8.38 (s, 3 H, Py $H^{3/5}$, Py H^4).

^{13}C{^{1}H}-NMR δ_C (126 MHz, ACETONE-*d*6): 28.6 (*C*H$_2$), 114.8 (*C*≡N), 125.8 (Py *C*), 139.4 (Py *C*), 150.0 (Py *C*), 189.3 (*C*=O).

7.3.2. 2,6-Di(5-amino-1*H*-pyrazol-3-yl)pyridine (L^5)[12]

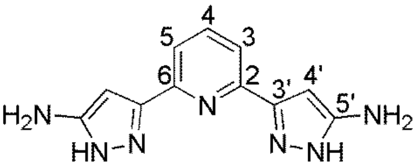

Hydrazine hydrate (9.00 g, 180 mmol) was added to a suspension of pyridine-2,6-bis-(3-oxo-3-propanenitrile) (8.00 g, 37 mmol) in ethanol absolute (100 ml) and the mixture refluxed for 20 hours, after which a beige precipitate formed. The solvent was reduced and then diethyl ether (225 ml) was added. The precipitate was then filtered, washed with pentane and dried under vacuum. Rapidly loses mass when heated, possibly holding solvent. Explains poor CHN results. Yield 5.18 g, 57.2 %.

CHN analysis: Calcd. from $C_{11}H_{11}N_7{\cdot}H_2O$ C, 50.96; H, 5.05; N, 37.82 %. Found C, 50.10; H, 4.95; N, 37.25 %.

ES^+ mass spectrum: Calcd. from $C_{11}H_{11}N_7{\cdot}H^+$ 242.1 g mol^{-1}. m/z 242.1.

^{1}H-NMR δ_H (500 MHz, DMSO-*d*6): 4.69 (s, 4 H, N*H*$_2$), 6.09 (s, 2 H, Pz $H^{4'}$), 7.55 (s, 2 H, Py $H^{3/5}$), 7.82 (s, 1 H, Py H^4), 12.16 (s, 2 H, Pz N*H*).

^{13}C-NMR δ_C (126 MHz, DMSO-*d*6): 90.0 (Pz $C^{4'}$), 117.4 (Py C^3), 138.3 (Py C^4), 141.2 (Pz $C^{3'}$ or Pz $C^{5'}$), 147.3 (Pz $C^{3'}$ or Pz $C^{5'}$), 156.5 (Py C^2).

7.3.3. 2,6-Di(5-*tert*butylamido-1*H*-pyrazol-3-yl)pyridine hydrochloride[12]

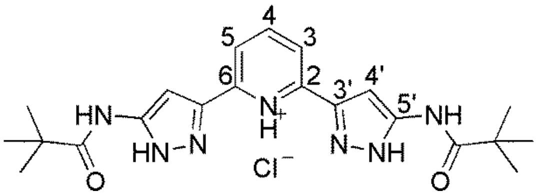

Trimethylacetyl chloride (4.00 g, 33.2 mmol) was added to a stirred suspension of 2,6-Bis(5-amino-1*H*-pyrazol-3-yl)pyridine (2.00 g, 8.3 mmol) in dry acetonitrile (90 mL) under a nitrogen atmosphere. The mixture was then heated at reflux under nitrogen for 48 hours, after which a white precipitate had formed and was removed via filtration. 2.78 g, 75.1 %.

CHN analysis: Calcd. from $C_{21}H_{28}ClN_7O_2$ C, 56.56; H, 6.33; N, 21.99; Cl, 7.95 %. Found C, 56.25; H, 6.35; N, 22.15; Cl, 8.10 %.

ES^+ mass spectrum: Calcd. From $C_{21}H_{27}N_7O_2{\cdot}Na^+$ 432.2g mol^{-1}. m/z 432.2.

^{1}H-NMR δ_H (300 MHz, DMSO-*d*6): 1.23 (s, 18H, C*H*$_3$), 7.16 (s, 2 H, Pz $H^{4'}$), 7.73 (d, 7.8 Hz, 2 H, Py $H^{3/5}$), 7.93 (t, 7.5 Hz, 1 H, Py H^4), 9.98 (s, 2 H, Pz N*H*).

^{13}C-NMR δ_C (126 MHz, DMSO-*d*6): 27.1 (*C*H$_3$), 30.7 (*C*(CH$_3$)$_3$), 95.4 (Pz $C^{4'}$), 118.3 (Py $C^{3/5}$), 138.8 (Py C^4), 141.4-148.0 (Py $C^{2/6}$, Pz $C^{3'}$ and Pz $C^{5'}$), 175.9 (*C*=O).

7.3.4. 2,6-Di(5-*tert*butylamido-1*H*-pyrazol-3-yl)pyridine (L^6)[12]

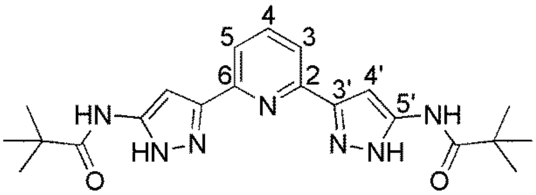

Saturated sodium carbonate solution (150 mL) was added to a suspension of 2,6-di(5-*tert*butylamido-1*H*-pyrazol-3-yl)pyridine hydrochloride (2.50 g, 5.6 mmol) in chloroform (150 mL) and the mixture was heated at reflux for 72 hours. The resulting two phase solution was allowed to cool and then separated. The aqueous layer was then extracted with dichloromethane (2 x 30 mL), the organic fractions combined and evaporated to leave a white solid. Approximates as the 0.5 methanol solvate. 1.62 g, 70.7 %.

CHN analysis: Calcd. from $C_{21}H_{27}N_7O_2$·0.5MeOH C, 60.69; H, 6.87; N, 23.04 %. Found C, 60.55; H, 6.65; N, 23.25 %.

ES^+ mass spectrum: Calcd. From $C_{21}H_{27}N_7O_2\cdot Na^+$ 432.2 g mol^{-1}. m/z 432.2.

^{1}H-NMR δ_H (300 MHz, CHLOROFORM-*d*): 1.27 (s, 18 H, CH_3), 7.19 (s, 2 H, Pz $H^{4'}$), 7.31 (s, 2 H, CON*H*), 7.46 (d, *J*=7.8 Hz, 2 H, Py $H^{3/5}$), 7.71 (t, *J*=6.0 Hz, 1 H, Py H^4) 8.86 (s, 2 H, Pz N*H*), 12.41 (s, 2 H, Pz N*H*).

^{13}C-NMR δ_C (126 MHz, CHLOROFORM-*d*): 26.5 (*C*H_3), 94.7 (Pz $C^{4'}$), 118.7 (Py $C^{3/5}$), 137.2 (Py C^4), 141.2 – 148.5 (Py $C^{2/6}$, Pz $C^{3'}$, Pz $C^{5'}$), 175.58 (NH*C*=O).

IR mid: $\nu(N–H)_{amide}$ = 3386 cm^{-1} (w), $\nu(C–H)_{aliphatic}$ = 2969 cm^{-1} (m), $\nu(C=O)_{amide}$ = 1671 cm^{-1} (s).

7.3.5. 2,6-Di(5-benzylamido-1*H*-pyrazol-3-yl)pyridine hydrochloride[12]

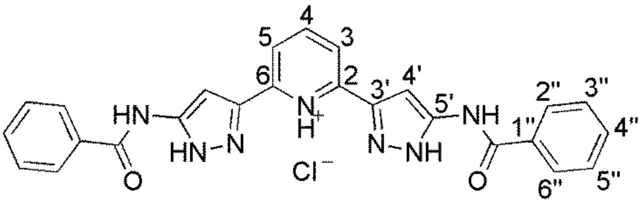

2,6-Di(5-amino-1*H*-pyrazol-3-yl)pyridine (2.00 g, 8.3 mmol) was suspended in dry acetonitrile (90 mL) under nitrogen and benzoyl chloride (4.00 g, 28.4 mmol) was added. The mixture was then heated at reflux for 48 hours after which the suspension had turned an off-white colour. The solid was then collected via filtration. 3.71 g, 92.0 %.

ES^+ mass spectrum: Calcd. from $C_{25}H_{19}N_7O_2Na$ 472.2 g mol^{-1}. *m/z* 472.2

^{1}H-NMR δ_H (500 MHz, DMSO-*d*6) 7.71 (s, 2 H, Pz $H^{4'}$), 7.54 (t, *J*=7.5 Hz, 4 H, Bz $H^{3''/5''}$), 7.60 (t, *J*=7.5 Hz, 2 H, Bz$H^{4''}$), 7.83 (d, *J*=7.8 Hz, 2 H, Py $H^{3/5}$), 7.98 (t, *J*=7.5 Hz, 1 H, Py H^4), 8.08 (d, *J*=7.5 Hz, 4 H, Bz $H^{2''/6''}$), 11.00 (s, 2 H, Pz N*H*).

^{13}C-NMR δ_C (126 MHz, DMSO-*d*6) 95.8 (Pz $C^{4'}$), 118.5 (Py $C^{3/5}$), 127.8 (Bz $C^{2''/6''}$), 128.3

(Bz $C^{3''/5''}$), 131.6 (Bz $C^{4''}$), 134.0 (Bz $C^{1''}$), 138.8 (Py C^{4}), 141.5-147.97 (Py $C^{2/6}$, Pz $C^{3'}$ and Pz $C^{5'}$), 164.60 (C=O).

IR mid: $\nu(\text{N–H})_{\text{amide}}$ = 3386 cm^{-1} (w), $\nu(\text{C–H})_{\text{aliphatic}}$ = 2957 cm^{-1} (m), $\nu(\text{C=O})_{\text{amide}}$ = 1691 cm^{-1} (s).

7.3.6. 2,6-Di(5-benzylamido-1*H*-pyrazol-3-yl)pyridine[12] (L^7)

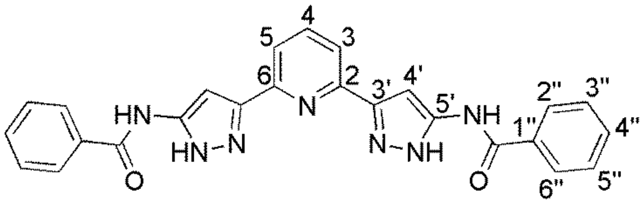

A mixture of 2,6-Bis(5-{benzylamide}-1*H*-pyrazol-3-yl)pyridine hydrochloride (3.00 g, 6.2 mmol) in chloroform (140 mL) and saturated sodium carbonate solution (140 mL) was heated at reflux for 2 days. The product was a white precipitate in the aqueous layer, and was filtered, washed with acetone and dried. Yield 0.92 g, 33.0 %.

ES^+ mass spectrum: Calcd. from $C_{25}H_{19}N_7O_2Na$ 472.2 g mol^{-1}. *m/z* 472.2.

^{1}H-NMR δ_H (500 MHz, DMSO-*d*6) 7.35 (s, 2 H, Py H^4), 7.49 – 7.61 (m, 6 H, Bz $H^{3''/5''}$, Bz $H^{4''}$), 7.81 (d, 7.7 Hz, 2H, PyH^3), 7.97 (t, *J*=7.7 Hz, 1 H, Py H^4), 8.05 (d, *J*=6.0 Hz, 4 H, Bz $H^{2''/6''}$).

^{13}C-NMR δ_C (126 MHz, DMSO-*d*6) 95.8 (Pz$C^{4'}$), 118.4 (Py$C^{3/5}$), 127.7-128.3 (Bz$C^{2''/6''}$ or Bz $C^{3''/5''}$), 131.6 (Bz $C^{4''}$), 134.0 (Pz$C^{3'}$), 138.8 (Py C^4), 141.6 (Bz $C^{1''}$), 147.3 (Py$C^{2/6}$ or Pz$C^{5'}$), 148.0 (Py$C^{2/6}$ or Pz$C^{5'}$), 164.7 (C=O).

IR mid: $\nu(\text{N–H})_{\text{amide}}$ = 3458 cm^{-1} (m), $\nu(\text{C–H})_{\text{aromatic}}$ = 3293 cm^{-1} (s), $\nu(\text{C=O})_{\text{amide}}$ = 1672 cm^{-1} (vs).

7.3.7. 2,6-Di(5-(methylthiourea)-1*H*-pyrazol-3-yl)pyridine[12] (L^8)

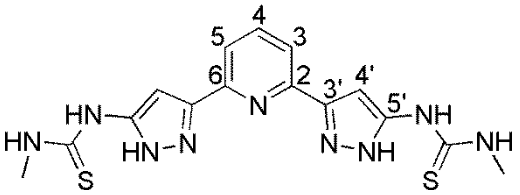

Methyl isothiocyanate (0.71 g, 9.6 mmol) was added to a suspension of 2,6-Bis(5-amino-1*H*-pyrazol-3-yl)pyridine (1.16 g, 4.8 mmol) in acetonitrile (70 mL) and the mixture was then heated at reflux for 18 hours. Mass spectrum showed that some starting material was present so an excess of methyl isothiocyanate was added and the mixture heated at reflux for a further 18 hours. The resulting white precipitate was then filtered and washed with chloroform. Yield 0.93 g, 50.0 %.

Found C, 46.60; H, 4.35; N, 32.85; S, 16.20 %.calcd. from $C_{15}H_{17}N_9S_2$ C, 46.49; H, 4.42; N, 32.53; S, 16.55 %.

Mass spectrum: Calcd. from $C_{15}H_{17}N_9S_2Na^+$ 410.1. *m/z* 410.1.

^{1}H-NMR δ_H (500 MHz, DMSO-*d*6) 3.11 (s, 6 H, C*H*$_3$), 7.55 (s, 2 H, Pz *H*$^{4'}$), 7.97 (t, *J*=9.0 Hz, 1 H, Py *H*^{4}), 8.14 (d, *J*=9.0 Hz, 2 H, Py *H*$^{3/5}$), 12.15 (s, 2 H, Pz N*H*).

^{13}C-NMR δ_C (126 MHz, DMSO-*d*6) 30.6 (*C*H$_3$), 86.6 (Pz *C*$^{4'}$), 120.2 (Py *C*$^{3/5}$), 137.1 (Py *C*^{4}), 150.8-175.9 (Py *C*$^{2/6}$ or Pz *C*$^{3'}$ and Pz *C*$^{5'}$), 206.64 (*C*=S).

IR mid: ν(N-H) = 3356, 3320 cm^{-1} (s), ν(C-H) = 2994 cm^{-1} (w), ν(C=C)$_{\text{aromatic}}$ = 1610 cm^{-1} (s), ν(C=S) = 1350 cm^{-1} (s).

7.3.8. 2,6-Di(3-oxo-pentanoyl)pyridine[13]

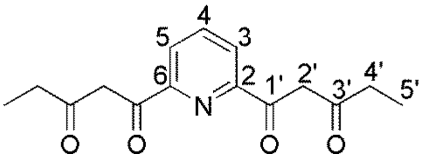

Dimethylpyridine-2,6-dicarboxylate (1.48 g, 7.6 mmol) and sodium methoxide (1.03 g, 19.0 mmol) was suspended in dry toluene (50 mL) under a dry nitrogen atmosphere and but-2-one (1.37 g, 19.0 mmol) was added. The mixture was stirred for 15 minutes at room temperature before being heated at 60 ºC for 12 hours. The resulting yellow suspension was evaporated and the residue added to a mixture of acetic acid (15 mL) water (25 mL) and ice (25 g). When the ice melted the resulting yellow precipitate was removied via filtration and dried. 1.37 g, 65.5 %.

CHN analysis: Calcd. from $C_{15}H_{17}NO_4$ C, 65.44; H, 6.22; N, 5.09 %. Found C, 65.80; H, 6.30; N, 5.15 %.

ES$^+$ mass spectrum: Calcd. from $C_{15}H_{17}NNaO_4$ 298.1 g mol^{-1}. Found *m/z* 298.1.

^{1}H-NMR δ_H (300 MHz, CHLOROFORM-*d*) 0.93 - 1.37 (m, 6 H, C*H*$_3$), 2.35 - 2.78 (m, 4 H, C*H*$_2$CH$_3$), 7.92 (q, *J*=8.1 Hz, 1 H, Py *H*^{4}) 8.01 - 8.26 (m, 2 H, Py *H*$^{3/5}$).

^{13}C-NMR δ_C (126 MHz, CHLOROFORM-*d*) 9.5 (*C*H$_3$), 32.7 (*C*H$_2$CH$_3$), 96.1 (CO*C*H$_2$CO), 124.1 (Py *C*$^{3/5}$), 138.1 (Py *C*^{4}), 151.8 (Py *C*$^{2/6}$), 172.0 (*C*$^{3'}$=O), 199.2 (*C*$^{1'}$=O).

7.3.9. 2,6-Di(5-ethyl-1*H*-pyrazol-3-yl)pyridine (L^{10})

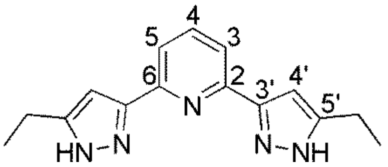

2,6-Di(3-oxo-pentanoyl)pyridine (1.00 g, 3.6 mmol) was dissolved in an ethanol/acetic acid mixture (7:3, 50 mL) and hydrazine monohydrate (0.54 g, 10.7 mmol) was added. The solution was stirred at room temperature for 20 hours. The ethanol was removed and saturated sodium carbonate solution was added. The resulting mixture was extracted with chloroform and the washed with brine before being dried (Na_2SO_4) and evaporated to leave a pale yellow solid. 0.62 g, 64.4 %.

CHN analysis: Calcd. from $C_{15}H_{19}N_5O\cdot H_2O$ C, 63.14; H, 6.71; N, 24.54%. Found C, 62.70; H, 6.00; N, 23.60%.

ES^+ mass spectrum: Calcd. from $C_{15}H_{17}N_5Na$ 290.1 g mol^{-1}. Found *m/z* 290.1.

^{1}H NMR δ_H (500 MHz, CHLOROFORM-*d*) 1.06 (t, *J*=7.32 Hz, 6 H, CH_3), 6.19 (s, 2 H, Pz$H^{4'}$), 2.50 (q, *J*=7.3 Hz, 4 H, CH_2), 7.11 (s, 2 H, Py$H^{3/5}$), 7.37 (t, *J*=7.78 Hz, 1 H, PyH^4).

^{13}C NMR δ_C (126 MHz, CHLOROFORM-*d*) 13.5 (CH_3), 20.9 (CH_2), 100.9 (Pz$C^{4'}$), 117.7 (Py$C^{3/5}$), 137.1 (PyC^4), 143.8 (PyC^6 and Pz$C^{3'}$), 148.1 (PyC^6 and Pz$C^{3'}$), 154.5 (PyC^2).

7.3.10. 2,6-Di(4-methyl-3-oxo-pentanoyl)pyridine[13]

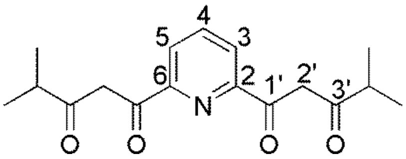

Dimethylpyridine-2,6-dicarboxylate (1.66 g, 8.5 mmol) and sodium methoxide (1.15 g, 21.3 mmol) were suspended in dry tetrahydrofuran under nitrogen. 3-methylbutan-2-one was then added and the mixture was heated at 65 °C for 20 hours. The mixture was allowed to cool before being reduced and added to water (70 mL). The solution was then neutralised with conc. hydrochloric acid and extracted with chloroform. The chloroform layer was dried (Na_2SO_4) and evaporated to leave an orange oil. 1.81 g, 70.2 %

ES^+ mass spectrum: calcd. from $C_{17}H_{22}NO_4^+$ 304.15 g mol^{-1}. Found *m/z* 304.15.

^{1}H NMR δ_H (500 MHz, CHLOROFORM-*d*) 1.18 (s, 6 H, CH_3), 1.19 (s, 6 H, CH_3), 2.64 (spt, *J*=7.0 Hz, 2 H, $CH(CH_3)_2$), 3.67 (s, 2 H, $COCH_2CO$), 6.84 (s, 2 H, COH=C*H*CO), 7.91 (t, *J*=8.0 Hz, 2 H, Py H^4), 8.10 (d, *J*=7.7 Hz, 2 H, Py $H^{3/5}$)

^{13}C NMR δ_C(126 MHz, CHLOROFORM-*d*) 19.3 (CH_3), 37.6 ($CH(CH_3)_2$), 67.9 ($COCH_2CO$), 94.7 (COH*C*H=CO), 124.1 (Py $C^{3/5}$), 138.2 (Py C^4), 151.8 (Py $C^{2/6}$), 181.2 ($COCH_2CO^iPr$), 201.8 ($COCH_2CO^iPr$).

7.3.11. 2,6-Di(5-*iso*prop-1*H*-pyrazol-3-yl)pyridine (L[11])

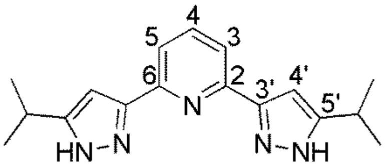

2,6-Di(4-methyl-3-oxo-pentanoyl)pyridine (1.81 g, 6.0 mmol) was dissolved in a mixture of ethanol and acetic acid (7:3, 50 mL) and hydrazine monohydrate (1.28 g, 25.5 mmol) was added. The mixture was stirred at room temperature for 20 hours and saturated sodium carbonate solution was added until effervescence ceased. Diethyl ether was then added and evaporated to remove the last traces of acetic acid, and the mixture was filtered to leave a white solid. 1.05 g, 59.3 %.

CHN analysis: calcd. from $C_{17}H_{21}N_5$ C, 69.12; H, 7.17; N, 23.71 %. Found C, 68.60; H, 7.20; N, 23.90 %.

ES^+ mass spectrum: calcd. from $C_{17}H_{22}N_5^+$ 296.19 g mol^{-1}. Found *m/z* 296.19.

^{1}H NMR δ_H (500 MHz, DMSO-d_6) 1.28 (s, 6 H, CH_3), 1.30 (s, 6 H, CH_3), 3.01 (spt, *J*=6.8 Hz, 2 H, C*H*(CH_3)$_2$), 6.80 (s, 2 H, Pz H^4), 7.75 (d, *J*=6.3 Hz, 2 H, Py $H^{3/5}$), 7.84 (t, *J*=7.5 Hz, 1 H, Py H^4), 12.80 (broad s, 2 H, Pz N*H*).

^{13}C NMR δ_C (126 MHz, DMSO-d_6) 22.6 (CH_3), 25.6 (CH(CH_3)$_2$), 100.1 (Pz C^4), 117.5 (Py $C^{3/5}$), 137.4 (Py C^4).

7.3.12. 2,6-Di(4-dimethyl-3-oxo-pentanoyl)pyridine[13].

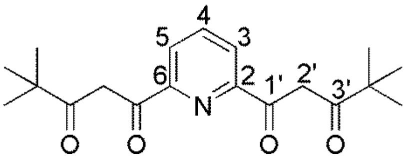

Sodium ethoxide was freshly prepared by stirring sodium (0.77 g, 33.4 mmol) in ethanol (15 mL) until consumed and then removing the solvent under vacuum. Toluene (30 mL) and pinacolone (3.86 g, 38.5 mmol) was added before dimethylpyridine-2,6-dicarboxylate (2.50 g, 12.8 mmol) was added. The mixture was then stirred for 8 hours before being stirred at 60° C for 4 hours. The red solution was then evaporated and the resulting solid added to a mixture of acetic acid (15 mL), water (25 mL) and ice (50 g) and stirred. The mixture was then filtered, dried and dissolved in dichloromethane. The solution was then washed with sat. sodium carbonate solution (2 x 30 mL) and water (30 mL) before being dried ($MgSO_4$) and the solvent evaporated to leave an orange solid. 1.42 g, 33.6 %. Analysis shows a mixture of products containing the desired product and a the ethyl ester of the product which had only reacted at one side. Separated after the next reaction step.

ES+ mass spectrum: calcd. from $C_{19}H_{25}NO_4Na^+$ (M + Na^+) 354.17 g mol-1, Found *m/z* 354.17. Calcd. from $C_{15}H_{19}NO_4Na^+$ 300.12 g mol^{-1}, found *m/z* 300.12.

7.3.13. 2,6-Di(5-*tert*but-1*H*-pyrazol-3-yl)pyridine (L^{12}).

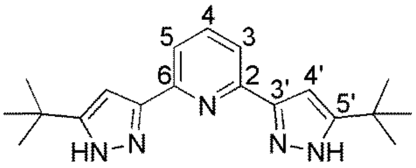

2,6-Di(4-dimethyl-3-oxo-pentanoyl)pyridine (1.32 g, 4.0 mmol) was dissolved in ethanol (40 mL) and hydrazine monohydrate (0.60 g, 11.9 mmol) was added. The mixture was then heated at reflux for 16 hours after which a white precipitate was formed by reducing the solvent by ~50 % and adding water. The white precipitate was removed via filtration and dried. Purified by silica gel column chromatography using ethyl acetate/methanol (9:1) eluent. Approximates as the methanol solvate. 0.16 g, 12.7 %.

CHN analysis: Calcd. from $C_{19}H_{25}N_5{\cdot}CH_4O$ C, 67.58; H, 8.22; N, 19.70 %. Found C, 68.30; H, 7.80; N, 19.95 %.

ES^+ mass spectrum: calcd. from $C_{19}H_{26}N_5^+$ 324.22 g mol^{-1}, found *m/z* 324.22.

^1H NMR δ_H (500 MHz, CHLOROFORM-*d*): 1.35 (s, 18 H, C(CH_3)$_3$), 6.66 (s, 2 H, Pz $H^{4'}$), 7.62 (m, 3 H, Py $H^{3/5}$ and Py H^4).

^{13}C NMR δ_C (500 MHz, CHLOROFORM-*d*): 30.4 (C(CH_3)$_3$), 30.9 (C(CH$_3$)$_3$), 99.9 (Pz $C^{4'}$), 118.6 (Py $C^{3/5}$), 137.4 (Py C^4), 146.0 (Pz $C^{3'}$), 149.5 (Pz $C^{5'}$), 159.7 (Py $C^{2/6}$).

7.3.14. 2,6-Di(3-oxo-3-pyridin-4-yl-propionyl)pyridine[13]

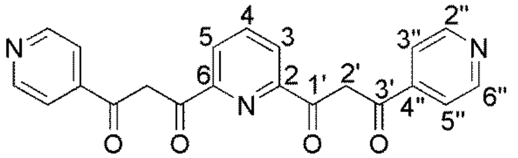

Sodium (0.77 g, 33.4 mmol) was stirred under nitrogen atmosphere in dry ethanol (15 mL) until it was consumed. The ethanol was removed under vacuum. Dry toluene (30 mL) and 4-acetylpyridine (4.66 g, 38.5 mmol) was added to the freshly prepared sodium ethoxide and stirred for a few minutes before adding dimethylpyridine-2,6-dicarboxylate (2.50 g, 12.8 mmol). The mixture was then stirred for 12 hours and the resulting yellow precipitate was removed via filtration. The yellow solid was added to a solution of acetic acid (15 mL), water (25 mL) and ice (50 g) with stirring and then filtered. The solid was then dissolved in dichloromethane (150 mL) and washed with sodium carbonate solution (2 x 30 mL). The organic layer was dried ($MgSO_4$) and solvent removed under vacuum to leave a yellow solid. 0.90 g, 18.8 %.

ES$^+$ mass spectrum: Calcd from $C_{21}H_{16}N_3O_4^+$ 374.11 g mol^{-1}. Found *m/z* 374.11.

^{1}H NMR δ_H (500 MHz, DMSO-d_6): 3.38 (s, 4 H, CH_2) 7.76 (d, *J*=4.5 Hz, 4 H, Py $H^{3''/5''}$) 7.92 (t, *J*=7.5 Hz, 1 H, Py H^4) 8.05 (d, *J*=7.5 Hz, 2 H, Py $H^{3/5}$) 8.60 (d, J=4.5 Hz, 8 H, Py $H^{2''/6''}$).

^{13}C NMR δ_C (500 MHz, DMSO-d_6): 62.8 (CH_2), 120.7 (Py $C^{3'}$), 121.1 (Py C^3), 137.1 (Py C^4), 149.7 (Py $C^{2'}$), 150.9 (Py $C^{4'}$), 156.9 (Py C^2), 180.0 – 180.9 (*C*=O).

7.3.15. 2,6-Di(5-(4-pyridyl)-1*H*-pyrazol-3-yl)pyridine[14] (L^{13}).

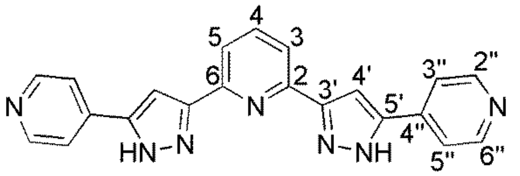

2,6-Di(3-oxo-3-pyridin-4-yl-propionyl)pyridine (1.00 g, 2.7 mmol) was suspended in an ethanol/acetic acid (7:3) mix (50 mL) and hydrazine hydrate (0.40 g, 8.0 mmol) was added. The mixture was then stirred at room temperature overnight and the resulting orange precipitate was removed via filtration and washed with ethanol. Recrystallised from hot ethanol. 1.00 g, quantitative.

CHN analysis: Calcd. from $C_{21}H_{15}N_7{\cdot}2H_2O$ C, 62.83; H, 4.77; N, 24.42%. Found C, 62.95; H, 5.15; N, 23.00%.

ES$^+$ mass spectrum: calcd. from $C_{21}H_{16}N_7^+$ 366.15 g mol^{-1}. Found *m/z* 366.15.

^{1}H NMR δ_H (500 MHz, METHANOL-d_4) 7.41 (s, 2 H, Pz $H^{4'}$) 7.74 (d, *J*=7.8 Hz, 2 H, Py $H^{3/5}$), 7.85 (d, *J*=10.0 Hz, 4 H, Py $H^{3''/5''}$) 7.90 (t, *J*=7.6 Hz, 1 H, Py H^4), 8.55 (d, *J*=10.0 Hz 4 H, Py $H^{2''/6''}$).

^{13}C NMR δ_C (75 MHz, DMSO-d_6) 102.1 (Pz $C^{4'}$), 118.6-119.5 (Py$C^{3/5}$ and Py $C^{3''/5''}$), 138.8 (Py C^4), 150.2 (Py $C^{2''/6''}$), 172.0 (Pz $C^{3'}$ and Pz$C^{5'}$), 206.4 (PyC$^{4''}$).

7.3.16. 4,4-Dimethyl-1-[6-(3-oxo-butyryl)-pyridin-2-yl]-pentane-1,3-dione

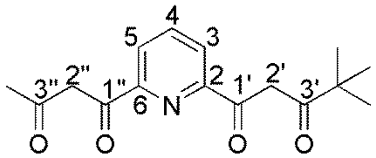

Dimethyl-2,6-pyridine dicarboxylate (3.00 g, 18.4 mmol) and sodium methoxide (1.00 g, 18.4 mmol) was suspended in dry toluene (350 mL) under nitrogen. Pinacolone (1.80 g, 18.4 mmol) was then added and the mixture was heated at 70 °C. After 48 hours the mixture was a red colour, and acetone (0.80 g, 13.7 mmol) was added, followed by more sodium methoxide (1.11 g, 20.5 mmol) and the mixture was again heated at 70 °C for 72 hours. The mixture was allowed to cool and the precipitate removed via filtration and washed with water. 1.50 g, 28.2 %.

ES$^+$ mass spectrum: Calcd. from $\mathrm{C_{16}H_{19}NO_4Na^+}$ 312.1 g mol^{-1}. Found *m/z* 312.1.

^{1}H NMR δ_H (500 MHz, DMSO-d_6) 1.18 (s, 9 H, $\mathrm{C(C}H_3)_3$), 1.98 (s, 3 H, $\mathrm{C}H_3$), 5.97 (br. s, 1 H, $\mathrm{C}H_2^{2'}$), 6.19 (br. s, 1 H, $\mathrm{C}H_2^{3''}$), 7.79 (t, J=10.0 Hz, 1 H, Py H^4) 7.88 (d, J=7.8 Hz, 2 H, Py $H^{3/5}$).

^{13}C NMR δ_C (126 MHz, DMSO-d_6) 28.6 ($\mathrm{C(}C\mathrm{H_3)_3}$), 29.6 ($C\mathrm{H_3}$), 88.7 ($C^{3''}$), 94.5 ($C^{2'}$), 120.4 (Py $C^{3/5}$), 136.8 (Py C^4), 157.6 (Py$C^{2/6}$), 158.1 (Py$C^{2/6}$), 177.1 ($C^{1'}$=O and $C^{4''}$=O), 191.2 ($C^{2''}$=O), 198.8 ($C^{3'}$=O).

7.3.17. 2-(5-tert-Butyl-1*H*-pyrazol-3-yl)-6-(5-methyl-1*H*-pyrazol-3-yl)-pyridine (L^{14})

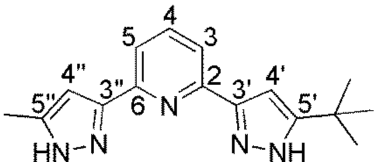

4,4-Dimethyl-1-[6-(3-oxo-butyryl)-pyridin-2-yl]-pentane-1,3-dione (1.30 g, 4.5 mmol), without further purification, was dissolved in ethanol (35 mL) and acetic acid (15 mL). Hydrazine monohydrate (0.68 g, 13.5 mmol) was then added and the mixture stirred at room temperature for 12 hours. The mixture was then neutralised using sat. sodium hydroxide solution, and water added until a precipitate formed. The mixture was cooled and the precipitate collected via filtration and washed with water. Micro approximates with 0.5 water. 0.84 g, 68.0 %.

CHN analysis: calcd. from $\mathrm{C_{16}H_{19}N_5{\cdot}0.5H_2O}$ C; 66.18; H, 6.94; N, 24.12 %. Found C, 66.20; H, 7.00; N, 23.70 %.

ES$^+$ mass spectrum: Calcs. from $\mathrm{C_{16}H_{20}N_5^+}$ 282.2 g mol^{-1}. Found *m/z* 282.2.

^{1}H NMR δ_H (300 MHz, CHLOROFORM-d) 1.39 (s, 9 H, $\mathrm{C(C}H_3)_3$), 2.37 (s, 3 H, $\mathrm{C}H_3$), 6.55 (s, 1 H, Pz $H^{4'}$), 6.63 (s, 1 H, Pz $H^{4''}$), 7.53 (d, J=7.7 Hz, 1 H, Py H^3) 7.60 (d, J=7.3 Hz, 1 H, PyH^5), 7.73 (t, J=8.21 Hz, 1 H, Py H^4).

^{13}C NMR δ_C (126 MHz, CHLOROFORM-d) 12.9 ($C\mathrm{H_3}$), 30.4 ($C\mathrm{(CH_3)_3}$), 30.9 ($\mathrm{C(}C\mathrm{H_3)_3}$), 99.8 (Pz $C^{4''}$), 102.9 (Pz $C^{4'}$), 118.5 (Py C^3), 118.7 (Py C^5), 137.5 (Py C^4).

7.3.18. 3-[6-(4,4-Dimethyl-3-oxo-pentanoyl)-pyridin-2-yl]-3-oxo-propionitrile

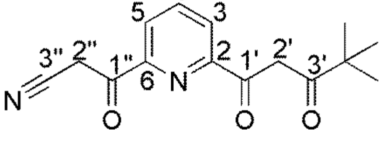

Sodium methoxide (1.00 g, 18.3 mmol) and pinacolone (1.80 g, 18.3 mmol) were added to a stirred suspension of dimethyl-2,6-pyridine dicarboxylate (3.00 g, 18.3 mmol) in toluene (150 mL) and the mixture was stirred at 70 °C overnight under nitrogen. Sodium hydride (1.10 g, 27.5 mmol) was washed with pentane and transferred to the mixture along with acetonitrile (1.13 g, 27.5 mmol). The mixture was then heated to reflux for 4 hours and then 65 °C for 12 hours. The mixture was allowed to cool and the precipitate was collected via filtration. The solid was redissolved in water and acidified to ~pH 5 which gave a yellow oil. The mixture was extracted with chloroform, dried ($MgSO_4$) and evaporated to leave a yellow oil. 2.53 g, 50.8 %

^{1}H NMR δ_H (500 MHz, CHLOROFORM-*d*) 1.30 (s, 9 H, $C(CH_3)_3$), 4.37 (s, 2 H, CH_2CN), 7.01 (s, 0.7 H, $COCH_2CO$ (tautomeric)), 8.08 (t, *J*=7.9 Hz, 1 H, Py H^4), 8.21 (dd, *J*=6.7, 1.1 Hz, 1 H, Py$H^{3/5}$), 8.34 (dd, *J*=7.8, 1.1 Hz, 1 H, Py$H^{3/5}$).

7.3.19. 5''-[6-(5-tert-Butyl-1*H*-pyrazol-3-yl)-pyridin-2-yl]-1*H*-pyrazol-5-ylamine (L^{15})

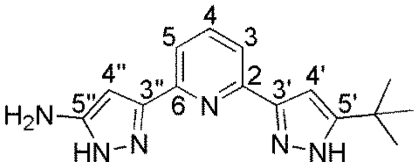

3-[6-(4,4-Dimethyl-3-oxo-pentanoyl)-pyridin-2-yl]-3-oxo-propionitrile (2.53 g, 9.3 mmol) was used without further purification and dissolved in ethanol/acetic acid (7:3, 50 mL). Hydrazine hydrate (1.86 g, 37.2 mmol) was added and the mixture stirred at room temperature for 48 hours. The solvent was then reduced by ~50 % and neutralised with sodium hydrogen carbonate. The remaining solvent was then removed to leave a sticky orange substance which was sonicated in diethyl ether to leave a white precipitate which was removed via filtration. 2.27 g, 86.5 %.

CHN analysis: calcd. from $C_{15}H_{18}N_6$ C, 63.81; H, 6.43; N, 29.77 %. Found C, 63.30; H, 6.55; N, 29.70 %.

ES$^+$ mass spectrum: Calcd. from $C_{15}H_{19}N_6^+$ 283.17 g mol^{-1}. Found *m/z* 283.17.

^{1}H NMR δ_H (500 MHz, DMSO-d_6) 1.34 (s, 9 H, $C(CH_3)_3$), 6.07 (s, 1 H, Pz $H^{4'}$) 6.85 (s, 1 H, Pz $H^{4''}$), 7.61 (dd, *J*=7.7, 0.8 Hz, 1 H, Py H^5), 7.73 (d, *J*=7.6 Hz, 1 H, Py H^3), 7.82 (t, J=7.6 Hz, 1 H, Py H^4).

^{13}C NMR δ_H (126 MHz, DMSO-d_6) 30.2 ($C(CH_3)_3$), 31.1 ($C(CH_3)_3$) 88.9 (Pz $C^{4'}$), 99.8 (Pz $C^{4''}$), 117.3 (Py C^5), 117.4 (Py C^3), 137.5 (Py C^4), 149.0 (Pz $C^{3'/3''}$), 150.0 (Pz $C^{3'/3''}$), 154.3 (Py C^6), 156.4 (Py C^2), 168.1 (Pz $C^{5'}$), 173.7 (Pz $C^{5''}$).

7.3.20. 4-Chloro-pyridine-2,6-dicarboxylic acid diethyl ester[15]

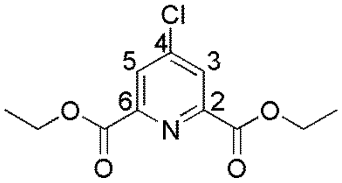

Chelidamic acid hydrate (5.00 g, 27.3 mmol) and phosphorous pentachloride (17.16 g, 82.4 mmol)were heated at reflux in chloroform (25 mL) until effervescence stopped. Ethanol (25 mL) was then added and once the mixture stopped giving off HCl the solvent was reduced. The mixture was then added to ice water (100 mL) and the resulting precipitate removed via filtration. This was redissolved in dioxane, treated with charcoal, added to ice water and filtered to leave a crystalline white solid. 2.01 g, 28.6 %.

CHN analysis: calcd from $C_{11}H_{12}ClNO_4$ C, 51.27; H, 4.69; N, 5.44; Cl, 13.76 %. Found C, 51.30; H, 4.70; N, 5.30; Cl, 13.90 %.

ES$^+$ mass spectrum: calcd from $C_{11}H_{13}ClNO_4^+$ 258.0 g mol^{-1}. Found m/z 258.1.

^{1}H NMR δ_H (500 MHz, Acetone-*d*$_6$): 1.40 (t, *J*=7.1 Hz, 6 H, CH_2CH_3), 4.44 (q, *J*=7.1 Hz, 4 H, CH_2CH_3), 8.27 (s, 2 H, Py $H^{3/5}$).

7.3.21. 4-Chloro-2,6-bis(1-pyrrolidinylcarbonyl)pyridine[16]

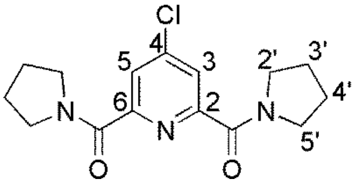

A solution of pyrrolidine (7.65 g, 0.10 mol) in dichloromethane (25 mL) was added dropwise to a solution of 4-Chloro-pyridine-2,6-dicarbonyl dichloride (5.52 g, 23.3 mmol) in dichloromethane (25 mL) at 0ºC. The mixture was allowed to warm to room temperature and stirred for 2 hours. The resulting mixture was poured into 2M HCl (50 mL) and the layers separated. The aqueous layer was extracted with dichloromethane (3 x 30 mL). The organic layers were combined, dried ($MgSO_4$) and evaporated to leave an off-white product which was washed with hexane. 6.17 g, 86.2 %

ES$^+$ mass spectrum: calcd from $C_{15}H_{19}ClN_3O_2^+$ 308.12 g mol^{-1}. Found *m/z* 308.12.

^{1}H NMR δ_H (501 MHz, CHLOROFORM-*d*): 1.83 - 1.96 (m, 9 H, $CH_2^{3'}$ and $CH_2^{4'}$), 3.58 - 3.68 (m, 9 H, $CH_2^{2'}$ and $CH_2^{5'}$), 7.85 (s, 2 H, Py $H^{3/5}$).

^{13}C NMR δ_C (126 MHz, CHLOROFORM-*d*) 23.93 - 26.56 ($CH_2^{3'}$ and $CH_2^{4'}$), 46.99 - 49.05 ($CH_2^{2'}$ and $CH_2^{5'}$), 125.3 (Py C^3), 146.0 (Py C^4) 154.2 (Py C^2) 164.7 (C=O).

7.3.22. 4-Hydroxy-pyridine-2,6-dicarboxylic acid dimethyl ester

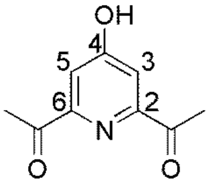

Chelidamic acid (4.00 g, 21.8 mmol) was suspended in methanol (300 mL) and dissolved on addition of sulphuric acid (3.3 mL). The solution was then heated at reflux for 10 hours and then concentrated. Saturated sodium chloride solution was then added and the solution was extracted with dichloromethane (3 x 30 mL). The combined dichloromethane layers were dried ($MgSO_4$) and the solvent was evaporated. 3.01 g, 65.4 %.

CHN analysis: calcd. from $C_9H_9NO_5$ C, 51.19; H, 4.30; N, 6.63 %. Found C, 51.00; H, 4.40; N, 6.45 %.

ES^+ mass spectrum: calcd. from $C_9H_{10}NO_5^+$ 212.06. g mol^{-1}. Found *m/z* 212.06.

^{1}H NMR δ_H (500 MHz, CHLOROFORM-*d*) 4.01 (s, 6 H, CH_3), 7.51 (s, 2H, Py $H^{3/5}$).

^{13}C NMR δ_C (126 MHz, CHLOROFORM-*d*) 53.6 (CH_3), 114.2 (Py $C^{3/5}$), 118.6 (Py $C^{2/6}$), 163.3 (Py C^4), 165.1 (*C*=O).

7.3.23. 4-Benzyloxy-pyridine-2,6-dicarboxylic acid dimethylester

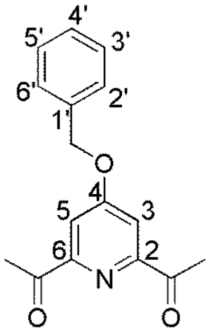

4-Hydroxy-pyridine-2,6-dicarboxylic acid dimethyl ester (2.40 g, 11.3 mmol), potassium carbonate (3.30 g, 23.9 mmol) and benzyl bromide (4.05 g, 23.7 mmol) were suspended in acetone (75 mL) and heated at reflux overnight. The resulting mixture was filtered and the solvent removed from the filtrate. The residue was redissolved in chloroform, washed with water (3 x 30 mL), dried (Na_2SO_4) and the evaporated. 1.66 g, 48.8 %.

CHN analysis: Calcd. from $C_{16}H_{15}NO_5$ C, 63.78; H, 5.02; N, 4.65%. Found C, 62.85; H, 5.00; N, 4.55%.

ES^+ mass spectrum: calcd. from $C_{16}H_{16}NO_5^+$ 302.10 g mol^{-1}. Found *m/z* 302.10.

^{1}H NMR δ_H (500 MHz, CHLOROFORM-*d*) 3.94 (s, 6 H, OCH_3), 5.16 (s, 2 H, CH_2), 7.31 – 7.38 (m, 5 H, Bz *H*), 7.83 (s, 2 H, PyH_3).

^{13}C NMR δ_C (126 MHz, CHLOROFORM-*d*) 53.3 (OCH_3), 70.8 (OCH_2Bz), 114.9 (Py $C^{3/5}$), 127.7-128.9 (Bz $C^{2'/6'}$, Bz $C^{3'/5'}$, Bz $C^{4'}$), 134.6 (Bz $C^{1'}$), 149.8 (Py $C^{2/6}$), 165.1 (Py C^{4}), 166.7 (C=O).

7.3.24. Pyrazol-1-tetrahydropyran[17]

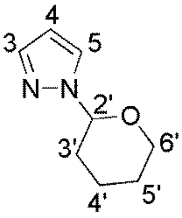

1H-pyrazole (5.00 g, 73.4 mmol) was dissolved in toluene (20 mL) and trifluoroacetic acid (0.3 mL, 3.6 mmol) and heated to 80 °C. 3,4-dihydro-*2H*-pyran (7.1 mL, 83.5 mmol) was then added dropwise over 15 minutes and the mixture was stirred at 80 °C for 1 hour. The solvent was then reduced to leave a pale yellow liquid which was used in the next step without further purification. 9.28 g, 83.1 %.

ES^+ mass spectrum: Calcd from $C_8H_{12}N_2ONa$ 175.08 g mol^{-1}. Found *m/z* 175.08.

^1H NMR δ_H (500 MHz, CHLOROFORM-*d*) 1.50 – 2.20 (m, 8H, $CH_2^{4'}$, $CH_2^{5'}$,$CH^{2'}_{axial}$, $CH^{3'}_{axial}$, $CH^{6'}_{axial}$), 3.63 (dt, *J*=2.4, 11.6 Hz, 1 H, $CH^{3'}_{equatorial}$), 3.99 (dd, *J*=2.3, 12.1 Hz, 1 H, $CH^{6'}_{equatorial}$), 5.33 (dd, *J*=9.69, 2.5 Hz, 1 H, $CH^{2'}_{equatorial}$), 6.23 (t, *J*=2.1 Hz, 1 H, CH^4), 7.49 (d, *J*=1.2 Hz, 1 H, CH^3), 7.54 (d, *J*=2.3 Hz, 1 H, CH^5).

7.3.25. 1-(Tetrahydro-pyran-2-yl)-5-(4,4,5,5-tetramethyl-[1,3,2]dioxaborolan-2-yl)-1*H*-pyrazole[17]

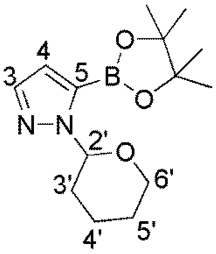

Pyrazol-1-tetrahydropyran (6.31 g, 41.5 mmol) was dissolved in dry THF (100 mL) and cooled to -78 °C. 1.6 M n-butyl lithium (27.2 mL, 43.5 mmol) was added slowly maintaining the temperature of the reaction mixture below -50 °C. After stirring for 10 minutes triisopropyl borate (10.6 mL, 45.8 mmol) was added over 15 minutes before allowing the mixture to warm to room temperature. Pinacol (5.39 g, 45.6 mmol) and acetic acid (4.98 g, 82.9 mmol) were then added which caused a gel like substance to form. The mixture was then stirred for 4 hours before being poured into a mixture of pentane (100 mL) and saturated ammonium chloride solution (70 mL). The organic phase was separated and washed with sodium hydrogen carbonate solution (40 mL) and brine (40 mL). The solution was then dried over Na_2SO_4, evaporated and left to crystallise at 5 °C.

ES$^+$ mass spectrum: Calcd. from $C_{14}H_{23}BN_2O_3Na$ 301.2 g mol^{-1}. Found *m/z* 301.2.

^{1}H NMR δ_H (500 MHz, CHLOROFORM-*d*) 1.27 (s, 12 H, CH_3), 1.45 – 1.55 (m, 1 H, C$H^{4'}{}_{axial}$), 1.57 – 1.71 (m, 2 H, Pn H_{axial}), 1.87 – 1.95 (m, 1 H, Pn H_{axial}), 1.97 – 2.05 (m, 1 H, Pn H_{axial}), 2.35 – 2.45 (m, 1 H, CH$^{6'}{}_{axial}$), 3.60 (dt, *J*=2.4, 11.4 Hz, 1 H, C$H^{3'}{}_{equatorial}$), 3.98 (dd, *J*=1.8, 9.6 Hz, 1 H, C$H^{6'}{}_{equatorial}$) 5.79 (dd, *J*=2.3, 10.1 Hz, 1 H, C$H^{2'}{}_{equatorial}$) 6.67 (d, *J*=1.7 Hz, 1 H, CH^4) 7.50 (d, *J*=1.2 Hz, 1 H, CH^3).

7.3.26. 2-Chloro-6-[2-(tetrahydro-pyran-2-yl)-2*H*-pyrazol-3-yl]-pyridin-4-ylamine

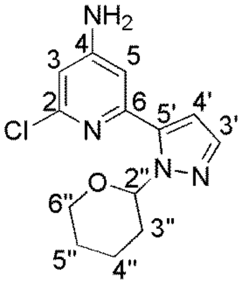

4-amino-2,6-dichloropyridine (2.25 g, 13.8 mmol), 1-(Tetrahydro-pyran-2-yl)-5-(4,4,5,5-tetramethyl-[1,3,2]dioxaborolan-2-yl)-1*H*-pyrazole (6.00 g, 30.4 mmol), potassium phosphate tribasic (14.53 g, 68.5 mmol), Bis(dibenzylideneacetone)palladium(0) (0.35 g, 0.6 mmol) and Tricyclohexylphosphine tetrafluoroborate (0.27 g, 0.7 mmol) were suspended in dry Tetrahydrofuran (75 mL) under a dry N_2 atmosphere. The mixture was heated at 70 °C for 20 hours. The resulting mixture was poured into diethyl ether (100 mL) and brine (100 mL), separated and the ether layer evaporated to leave a brown oil. The crude product was purified on silica using diethyl ether as the eluent to give the monosubstituted product. The disubstituted product was also isolated by washing the column with a water/dichloromethane/methanol (2:2:6) mixture. 0.18 g, 4.8%.

CHN analysis: calcd. from $C_{13}H_{15}ClN_4O$ C, 56.02; H, 5.42; N, 20.10; Cl, 12.72 %. Found C, 55.70; H, 5.40; N, 19.80; Cl, 11.10 %.

ES$^+$ mass spectrum: calcd. from $C_{13}H_{16}ClN_4O^+$ 279.1 g mol^{-1}. Found *m/z* 279.1.

^{1}H NMR δ_H (300 MHz, CHLOROFORM-*d*) 1.50 – 1.85 (m, 3 H, Pn $H^{4''}$and Pn $H^{5''}$), 1.98 – 2.12 (m, 2 H, Pn $H^{3''}{}_{equatorial}$ and Pn $H^{4'}$), 2.40 – 2.58 (m, 1 H, Pn $H^{3''}{}_{axial}$), 3.66 (dt, *J*=8.5, 2.6 Hz, 1 H, Pn $H^{6''}{}_{axial}$), 3.99 – 4.09 (m, 1 H, C$H^{6''}{}_{equatorial}$), 4.49 (br. s, 2 H, NH_2), 6.16 (dd, *J*=10.2, 2.1 Hz, 1 H, Pn $H^{2''}$), 6.48 (overlapping doublets, *J*=2.8 Hz, 2 H, Py H^3 and Py H^5), 6.68 (d, *J*=1.9 Hz, 1 H, Pz $H^{4'}$), 7.55 (d, *J*=1.7 Hz, 1 H, Pz $H^{3'}$).

^{13}C NMR δ_C (126 MHz, CHLOROFORM-*d*) 23.0 (Pn $C^{4''}$), 25.1 (Pn $C^{5''}$), 29.7 (Pn $C^{3''}$), 68.0 (Pn *C*$^{6''}$), 85.1 (Pn *C*$^{2''}$), 107.4 (Py *C*^{3} or Py *C*^{5}), 107.6 (Py *C*^{3} or Py *C*^{5}), 108.0 (Pz *C*$^{4'}$), 139.1 (Pz *C*$^{2'}$), 141.0 (Pz *C*$^{5'}$), 149.8 (Py *C*^{2}), 151.6 (Py *C*^{6}), 155.4 (Py *C*^{4}).

7.3.27. 2-Pyrazol-1-yl-6-(1*H*-pyrazol-3-yl)-pyridin-4-ylamine

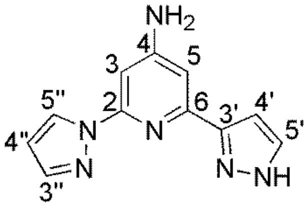

Pyrazole (0.12 g, 1.8 mmol) and sodium hydride (60 % dispersion in mineral oil, 0.09 g, 2.2 mmol) were suspended in diglyme (25 mL) and stirred under a dinitrogen atmosphere until effervescence ceased. 2-Chloro-6-[2-(tetrahydro-pyran-2-yl)-2H-pyrazol-3-yl]-pyridin-4-ylamine (0.50 g, 1.8 mmol) was then added and the mixture was heated at 110ºC for 5 days. Only starting material was obtained.

7.3.28. 2,6-Di(1*H*-pyrazol-3-yl)-pyridin-4-ylamine (L^{16})[17]

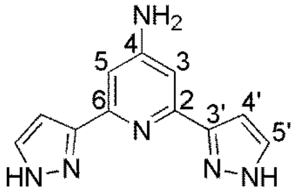

1-(Tetrahydro-pyran-2-yl)-5-(4,4,5,5-tetramethyl-[1,3,2]dioxaborolan-2-yl)-1*H*-pyrazole (10.00 g, 50.7mmol), 4-amino-2,6-dichloropyridine (3.75 g, 23.0 mmol), tribasic potassium phosphate (24.22 g, 114.1 mmol), Bis(dibenzylideneacetone)palladium(0) (0.58 g, 1.0 mmol) and Tricyclohexylphosphine tetrafluoroborate (0.45 g, 1.2 mmol) were suspended in dry THF (125 mL) under a nitrogen atmosphere. The mixture was then heated at 70ºC for 20 hours before being poured into diethyl ether (100 mL) and brine (100 mL). The organic layer was separated, dried (Na_2SO_4) and evaporated to leave an orange oil. LC-MS shows around 70% of the protected product is present. Attempts at isolating the protected product via flash column chromatography failed. The oil was dissolved in a mixture of methanol (70 mL) and hexane (70 mL) and a few drops of conc. Hydrochloric acid were added. The mixture was stirred for 20 hours at room temperature before being separated and the methanol layer evaporated to leave a sticky orange oil. This was then sonicated in diethyl ether to leave an off-white precipitate. 0.36 g, 6.9%.

CHN analysis: Calcd. from $C_{11}H_{10}N_6 \cdot H_2O$ C, 54.09; H, 4.95; N, 34.41% Found C, 53.60; H, 4.50; N, 30.85%.

HPLC-MS shows *m/z* 227.0 [**L**^{16}H]$^{+}$.

^{1}H NMR δ_H (500 MHz, METHANOL-d_4) 6.79 (br. s, 2 H, Py $H^{3/5}$), 6.95 (br. s, 2 H, Pz $H^{4'}$), 7.62 (br. s, 2 H, Pz $H^{5'}$).

7.3.29. 4-Bromo-2,6-di(1*H*-pyrazol-3-yl)-pyridine[18]

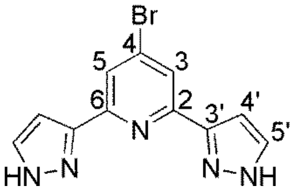

2,6-Di(1*H*-pyrazol-3-yl)-pyridin-4-ylamine (336 mg, 1.5 mmol) and sodium nitrite (2 mg, 0.03 mmol) were suspended in dry acetonitrile (25 mL) under a nitrogen atmosphere. HBr solution (48%, 8.60 mL, 51 mmol) and KBr (0.43 g, 3.6 mmol) were added and the mixture was stirred for 1 hour until nitrogen evolution had ceased. The mixture was then heated at 80°C for 1 hour before being allowed to cool and poured into sodium thiosulphate solution. An orange precipitate formed which was removed via filtration. HPLC-MS showed a peak at *m/z* 227.0 which corresponds to the starting material [**L**^{16}H]$^+$.

7.3.30. 2,6-Di(4-chloro-1*H*-pyrazol-3-yl)-pyridine (L^{17})[19]

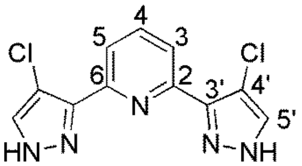

Sodium hypochlorite (10 mL, 10-15 %) in water (100 mL) was added to a solution of 2,6-di(1*H*-pyrazol-3-yl)pyridine (1.06 g, 5 mmol) in acetic acid (70 mL) and the mixture was stirred for 2 hours at room temperature. The mixture was then poured into 200 mL ice water before being extracted with 200 mL chloroform and 2 x 80 mL chloroform. The combined organic layers were washed with saturated potassium carbonate solution (20 mL) followed by water (20 mL) before being dried ($MgSO_4$) and evaporated to give a yellow solid. This was then purified by triturating in ethanol and drying in a desiccator. 0.38 g, 27.2 %.
CHN analysis: calcd. from $C_{11}H_7Cl_2N_5{\cdot}0.5H_2O$ C, 45.70; H, 2.79; N, 24.22, Cl, 24.52 %. Found C, 46.30; H, 2.30; N, 23.90; Cl, 25.00.
ES$^+$ mass spectrum: Calcd. from $C_{11}H_8Br_2N_5$ 369.9 g mol^{-1}. Found *m/z* 369.9.
^{1}H NMR δ_H (501 MHz, DMSO-d_6) 7.81 (s, 2 H, Pz $H^{5'}$), 8.02 (d, *J*=7.0 Hz, 2 H, Py $H^{3/5}$), 8.09 (t, *J*=7.9 Hz, 1 H, Py H^4).

7.3.31. 2,6-Di(4-bromo-1*H*-pyrazol-3-yl)-pyridine (L[18])

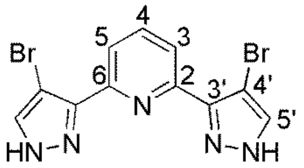

N-bromosuccinamide (1.69 g, 9.4 mmol) and 2,6-di(1*H*-pyrazol-3-yl)pyridine (1.00 g, 4.7 mmol) were dissolved in dry tetrahydrofuran (~40 mL) and the mixture was heated to 80 ˚C for 24 hours, after which a white precipitate had formed. The mixture was allowed to cool to room temperature before the solid was removed via filtration and washed benevolently with water followed by methanol, before being allowed to dry in air. 0.93 g, 53.7 %.

CHN analysis: calcd. from $C_{11}H_7Br_2N_5$ C, 35.80; H, 1.91; N, 18.98 %. Found C, 36.30; H, 1.90; N, 19.40 %.

ES^+ mass spectrum: calcd. from $C_{11}H_7Br_2N_5$ 369.01 g mol^{-1}. Found *m/z* 369.91.

^{1}H NMR δ_H (500 MHz, DMSO-d_6) 7.82 (br. s., 2 H, PzH^4), 8.14 (br. s., 2 H, PzH^5), 8.20 (br. s., 1 H, PyH^4), 13.90 (br. s., 2 H, PzN*H*).

7.3.32. 2,6-Di(4-biphenyl-4-yl-1*H*-pyrazol-3-yl)-pyridine

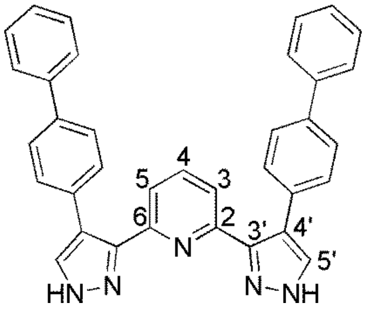

2,6-Di(4-bromo-1*H*-pyrazol-3-yl)-pyridine (0.50 g, 1.4 mmol), 4-biphenylboronic acid (0.54 g, 2.7 mmol), tribasic potassium phosphate (0.87 g, 4.0 mmol), Bis(dibenzylideneacetone)palladium(0) (14.5 mg, 0.05 mmol) and Tricyclohexylphosphine tetrafluoroborate (2.4 mg, 0.06 mmol) were suspended in dry THF (50 mL) under a nitrogen atmosphere. The mixture was then heated at 70°C for 20 hours. HPLC-MS showed the presence of starting material (*m/z* 369.8, $[\mathbf{L}^{18}H]^+$).

7.3.33. $[Fe(L^5)_2](ClO_4)_2\cdot H_2O$[20]

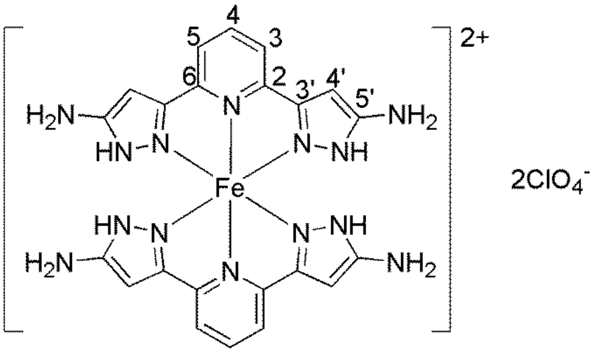

2,6-Di(5-amino-1*H*-pyrazol-3-yl)pyridine (0.20 g, 0.8 mmol) was suspended in nitromethane (15 mL) and iron perchlorate hydrate (0.10 g, 0.4 mmol) was added. The solution initially turned a green colour, but this eventually turned to a dark brown. The mixture was stirred for 30 minutes before being filtered. Crystals were formed using slow vapour diffusion of diethyl ether using the filtrate. Approximates as the monohydrate. 0.17 g, 56.6 %.

CHN analysis: Calcd. from $C_{22}H_{22}Cl_2FeN_{14}O_8\cdot H_2O$ C 34.99; H, 3.20; N, 25.96 %. Found C, 34.45; H, 2.80; N, 25.20 %.

ES$^+$ mass spectrum: Calcd. from $C_{22}H_{22}FeN_{14}$ 538.15 g mol^{-1}. Found *m/z* 269.07.

^{1}H NMR δ_H(500 MHz, DMF) 9.88 (br. s., 8 H, NH_2), 27.82 (br. s., 4 H, Pz N*H*), 31.21 (br. s., 2 H, Py H^4), 50.42 (br. s., 4 H, Py $H^{3/5}$ or Pz $H^{4'}$), 59.69 (br. s., 4 H, Py $H^{3/5}$ or Pz $H^{4'}$).

7.3.34. $[Fe(L^6)_2](BF_4)_2\cdot H_2O$[20]

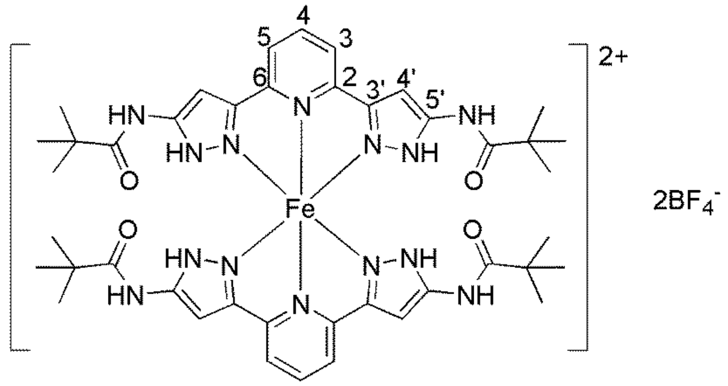

Iron(II) tetrafluoroborate hexahydrate (0.06 g, 0.2 mmol) was added to a stirred solution of 2,6-di(5-*tert*butylamido-1*H*-pyrazol-3-yl)pyridine (0.13 g, 0.3 mmol) and left to stir for 30 minutes. Diethyl ether was then added until a yellow precipitate formed, which was collected via filtration and dried. Approximates as the monohydrate. 0.11 g, 66.2 %. Crystals obtained using slow vapour diffusion using methanol/diisopropyl ether.

CHN analysis: Calcd. from $C_{42}H_{54}B_2F_8FeN_{14}O_4\cdot H_2O$ C, 47.30; H, 5.29; N, 18.40 %. Found C, 47.15; H, 5.25; N, 18.10 %.

ES$^+$ mass spectrum: Shows only free ligand at *m/z* 410.2 [$\mathbf{L^6}$H]$^+$.

^{1}H-NMR δ_H (500 MHz, ACETONE-*d*6) 3.0 (30 H, C*H*$_3$), 15.2 (4 H, CON*H*), 24.3 (2 H, Py *H*^{4}), 31.4 (4 H, Pz N*H*), 55.0 (7 H, Py *H*$^{3/5}$ or Pz *H*$^{4'}$), 60.3 (7 H, Py *H*$^{3/5}$ or Pz *H*$^{4'}$).

IR mid: ν(N–H)$_{amide}$ = 3501 cm^{-1} (w), ν(C–H)$_{aromatic}$ = 3143 cm^{-1} (m), ν(C=O)$_{amide}$ = 1678cm^{-1} (s), ν(B–F) = 1058 cm^{-1} (broad, vs).

7.3.35. [Fe(L^6)$_2$](ClO$_4$)$_2$·2H$_2$O[20]

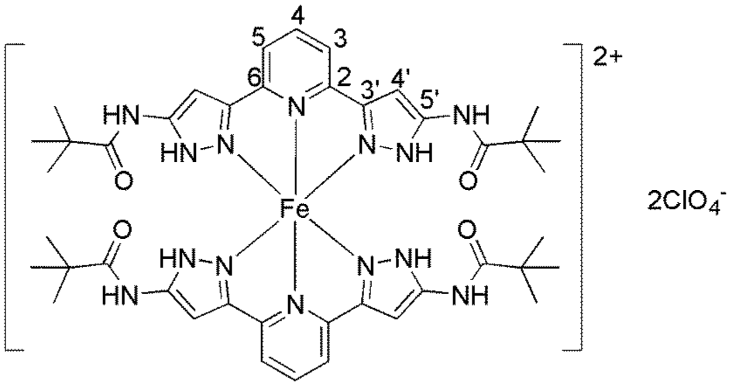

Iron(II) perchlorate hydrate (0.07 g, 0.2 mmol) was added to a stirred solution of 2,6-di(5-*tert*butylamido-1*H*-pyrazol-3-yl)pyridine (0.20 g, 0.4 mmol) in nitromethane (15 mL) and left to stir for 30 minutes. The resulting mixture was then filtered and to the filtrate diethyl ether was added until a yellow precipitate formed, which was removed by filtration and washed with diethyl ether. Approximates as the dihydrate. 0.11 g, 39.4 %.

CHN analysis: Calcd from $C_{42}H_{54}Cl_2FeN_{14}O_{12}\cdot 2H_2O$ C, 45.46; H, 5.27; N, 17.67 %. Found C, 45.70; H, 5.05; N, 17.80 %.

ES$^+$ mass spectrum: Calcd from $C_{21}H_{27}N_7O_2$ 409.2 g mol^{-1}. m/z 410.2 [$\mathbf{L^6}$H]$^+$, 432.2 [$\mathbf{L^6}$Na]$^+$.

^{1}H-NMR δ_H (500 MHz, ACETONE-*d*6) 3.0 (30 H, C*H*$_3$), 15.2 (4 H, CON*H*), 24.3 (2 H, Py *H*^{4}), 31.4 (4 H, Pz N*H*), 55.0 (7 H, Py *H*$^{3/5}$ or Pz *H*$^{4'}$), 60.3 (7 H, Py *H*$^{3/5}$ or Pz *H*$^{4'}$).

IR mid: ν(N–H)$_{amide}$ = 3544 cm^{-1} (w), ν(C–H)$_{aromatic}$ = 2968 cm^{-1} (m), ν(C=O)$_{amide}$ = 1675 cm^{-1} (s), ν(Cl–O) = 1098 cm^{-1} (vs).

7.3.36. $[Fe(L^7)_2](BF_4)_2$

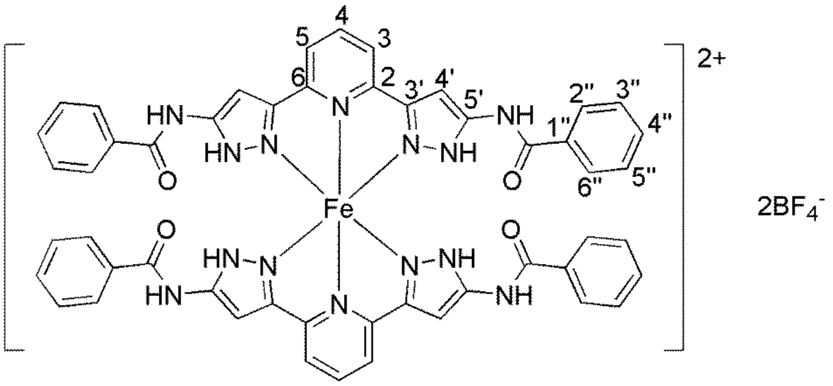

2,6-Di(5-benzylamido-1*H*-pyrazol-3-yl)pyridine (0.2 g, 0.4 mmol) was added to a solution of iron tetrafluoroborate hexahydrate (0.07 g, 0.2 mmol) in methanol (10 mL) immidiately producing a yellow precipitate. The mixture was stirred for a further 30 minutes before filtering to remove a yellow solid. 0.15 g, 59.6 %.

CHN analysis: Calcd. from $C_{50}H_{38}B_2F_8FeN_{14}O_4$ C, 53.22; H, 3.39; N, 17.38 %. Found C, 52.80; H, 3.60; N, 17.30 %.

7.3.37. $[Fe(L^7)_2](ClO_4)_2$

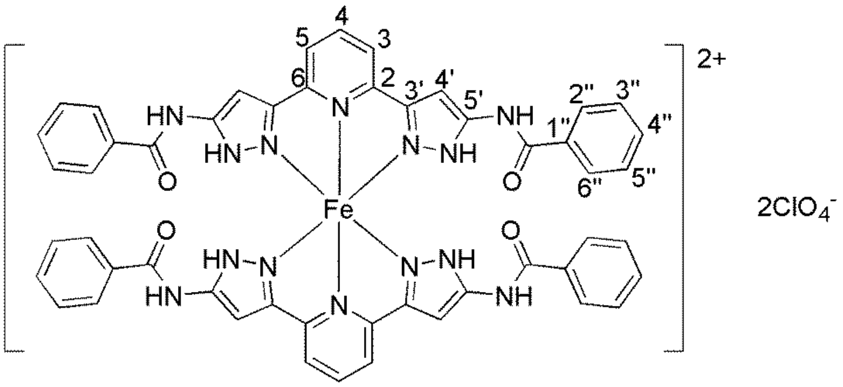

Iron(II) perchlorate hydrate (0.06 g, 0.2 mmol) was added to a stirred suspension of 2,6-Bis(5-{benzylamide}-1*H*-pyrazol-3-yl)pyridine (0.20 g, 0.4 mmol) in nitromethane (15 mL) and the mixture was stirred for 30 minutes. The mixture was filtered and to the filtrate diethyl ether was added until a yellow precipitate formed which was removed via filtration. 0.16 g, 69.3 %.

CHN analysis: Calcd. from $C_{50}H_{38}Cl_2FeN_{14}O_{12}$ C, 52.05; H, 3.32; N, 17.00 %. Found C, 52.40; H, 3.50; N, 17.45 %.

7.3.38. $[Fe(L^8)_2](BF_4)_2$

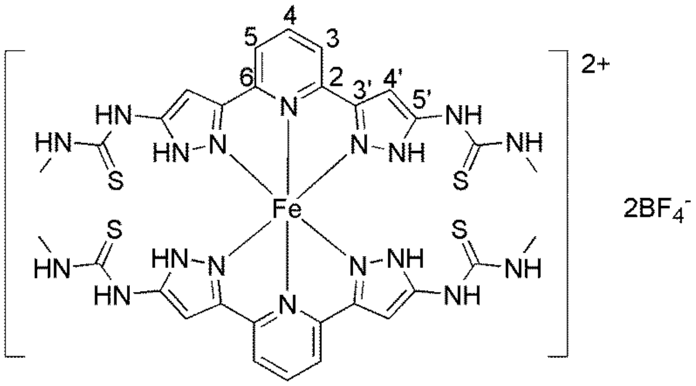

2,6-Di(5-{methylthiourea}-1*H*-pyrazol-3-yl)pyridine (0.20 g, 0.5 mmol) was dissolved in methanol and iron(II) tetrafluoroborate hexahydrate (0.09 g, 0.2 mmol) was added and the mixture stirred for 30 minutes. The mixture was then filtered and diethyl ether was added until a light brown precipitate formed, which was collected via filtration. 0.14 g, 53.7 %. CHN analysis: Calcd. from $C_{30}H_{34}B_2F_8FeN_{18}S_4$ C, 35.87; H, 3.41; N, 25.10 %. Found C, 36.65; H, 3.45; N, 25.40 %.

IR mid: ν(N-H) = 3351 cm^{-1} (m), ν(N-H) = 5515 cm^{-1} (m), ν(C-H) = 3219 cm^{-1} (w), $\nu(C{=}C)_{aromatic}$ = 1605 cm^{-1} (s), ν(C=S) = 1341 cm^{-1} (s).

7.3.39. $[Fe(L^{10})_2](BF_4)_2{\cdot}2H_2O$

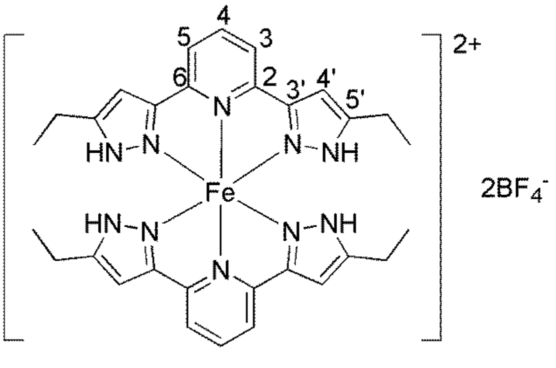

2,6-Di(5-ethyl-1*H*-pyrazol-3-yl)pyridine (0.20 g, 0.7 mmol) was dissolved in methanol (15 mL) and iron(II) tetrafluoroborate hexahydrate (0.13 g, 0.3 mmol) was added. The mixture was then stirred for 30 minutes at room temperature, before the solvent was removed. Toluene was added to the sticky residue and sonicated until the residue became a powder, which was removed via filtration. 0.20 g, 86.6 %.

CHN analysis: Calcd. from $C_{30}H_{34}B_2F_8FeN_{10}{\cdot}2H_2O$ C, 45.03; H, 4.79; N, 17.51%. Found C, 45.70; H, 4.90; N, 15.60%.

ES^+ mass spectrum shows only free ligand at *m/z* 290.1 $[\mathbf{L^{10}}Na]^+$.

^1H NMR δ_H (300 MHz, METHANOL-d_4) 0.2 (s, 12 H, CH_3), 17.3 (br. s., 8 H, CH_2), 21.7

(br. s, 2 H, Py H^4), 46.3 (br. s, 4 H, Py $H^{3/5}$ or Pz $H^{4'}$), 53.3 (br. s, 4 H, Py $H^{3/5}$ or Pz $H^{4'}$).

7.3.40. [Fe(L^{10})$_2$](ClO$_4$)$_2$·2H$_2$O

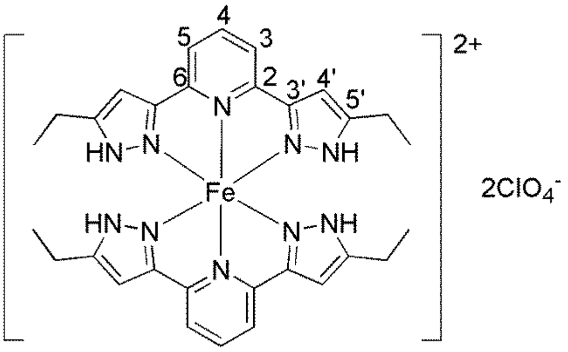

2,6-Di(5-ethyl-1*H*-pyrazol-3-yl)pyridine (0.20 g, 0.7 mmol) was dissolved in methanol (15 mL) and iron(II) perchlorate hydrate (0.09 g, 0.3 mmol) was added. The mixture was then stirred for 30 minutes at room temperature, before the solvent was removed. Toluene was added to the sticky residue and sonicated until the residue became a powder, which was removed via filtration. 0.19 g, 94.2 %.

CHN analysis: Calcd. from $C_{30}H_{34}ClFeN_{10}O_4{\cdot}2H_2O$ C, 49.63; H, 5.28; N, 19.29%. Found C, 47.20; H, 4.80; N, 17.80%.

ES$^+$ mass spectrum shows only free ligand at *m/z* 268.2 [**L^{10}**H]$^+$.

^{1}H NMR δ_H (300 MHz, METHANOL-*d*$_4$) 0.5 (s, 12 H, CH_3), 17.6 (br. s., 8 H, CH_2), 22.0 (br. s, 2 H, Py H^4), 46.6 (br. s, 4 H, Py $H^{3/5}$ or Pz $H^{4'}$), 53.6 (br. s, 4 H, Py $H^{3/5}$ or Pz $H^{4'}$).

IR mid: ν(O-H)$_{water}$ = 3100-3400cm^{-1} (m), ν(C-H) = 2973 cm^{-1} (m), ν(Cl-O) = 1058 cm^{-1} (vs).

7.3.41. [Fe(L^{11})$_2$](BF$_4$)$_2$

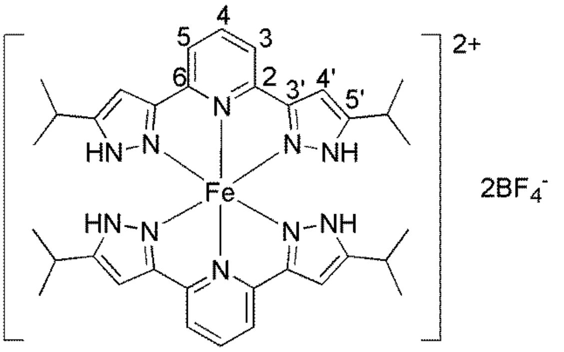

2,6-Di(5-*iso*propyl-1*H*-pyrazol-3-yl)pyridine (0.20 g, 0.7 mmol) was dissolved in methanol (15 mL) and iron(II) tetrafluoroborate hexahydrate (0.11 g, 0.3 mmol) was added and the solution stirred at room temperature for 30 minutes. The solvent was evaporated, the resulting residue was sonicated in diethyl ether and filtered to leave a brown solid. 0.26 g, 94.3 %.

CHN analysis: Calcd. from $C_{34}H_{42}B_2F_8FeN_{10}{\cdot}2H_2O$ C, 47.69; H, 5.41; N, 16.36%. Found C, 46.60; H, 5.10; N, 15.60%.

ES^+ mass spectrum: ligand peak at *m/z* 296.19 $[\mathbf{L^{11}}]^+$.

^{1}H NMR δ_H (500 MHz, ACETONITRILE-d_3) 0.6 (br. s., 24 H, C*H*$_3$), 16.6 (br. s., 4 H, C*H*(CH$_3$)$_2$), 23.0 (br. s., 2 H, Py H^4), 31.2 (br. s., 4 H, Pz N*H*), 50.2 (br. s., 4 H, Py $H^{3/5}$ or Pz H^4), 57.3 (br. s., 4 H, Py $H^{3/5}$ or Pz H^4).

IR mid: ν(O-H)$_{water}$ = 3200-3450 cm^{-1} (m), ν(C-H) = 2969 cm^{-1} (m), ν(B-F) = 1023 cm^{-1} (vs).

7.3.42. $[Fe(L^{12})_2](BF_4)_2{\cdot}CF_3CH_2OH$

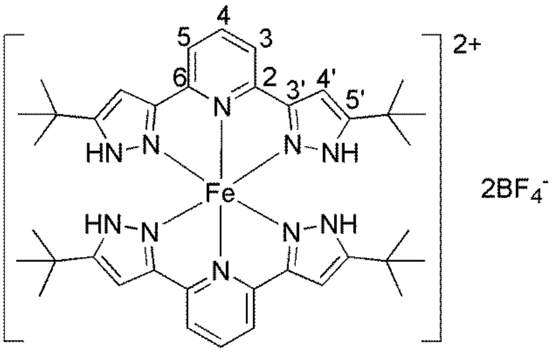

Iron(II) tetrafluoroborate hexahydrate (0.10 g, 0.3 mmol) was added to a stirred solution of 2,6-di(5-*tert*but-1*H*-pyrazol-3-yl)pyridine (0.20 g, 0.6 mmol) in methanol and stirring continued for a further 30 minutes. The solvent was evaporated and the resulting brown solid was recrystallised from trifluoroethanol/diethyl ether. Crystals suitable for x-ray diffraction were obtained via slow vapour diffusion from trifluoroethanol using diisopropyl ether as the anti-solvent. Approximates as the CF_3CH_2OH solvate, which agrees with the crystal structure. 0.16 g, 58.3 %.

CHN analysis: Calcd. from $C_{38}H_{50}B_2F_8FeN_{10}{\cdot}CF_3CH_2OH$ C 49.21; H, 5.47; N, 14.35 %. Found C, 48.80; H, 5.60; N, 14.80 %.

ES^+ mass spectrum: calcd. from $C_{38}H_{49}FeN_{10}$ 701.3 g mol^{-1}. Found *m/z* 701.3.

^{1}H NMR δ_H (300 MHz, ACETONE-*d*6): 2.1 (36 H, C(C*H*$_3$)$_3$), 23.1 (2 H, Py H^4), 35.7 (4 H, Pz N*H*), 53.1, 59.0 (4 H, Py $H^{3/5}$ and Pz $H^{4'}$).

IR mid: ν(O-H)$_{water}$ = 3200-3500 cm^{-1} (m), ν(C-H) = 2965 cm^{-1} (m), ν(B-F) = 1020 cm^{-1} (vs).

7.3.43. $[Fe(L^{14})_2](BF_4)_2{\cdot}0.5CF_3CH_2OH$ [20]

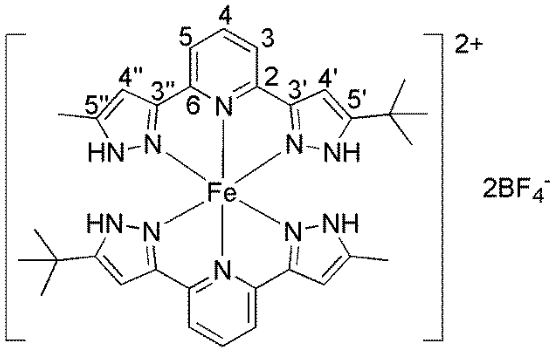

Iron tetrafluoroborate hexahydrate (0.12 g, 0.4 mmol) was added to a stirred solution of 2-(5-tert-Butyl-1*H*-pyrazol-3-yl)-6-(5-methyl-1*H*-pyrazol-3-yl)-pyridine (0.2 g, 0.7 mmol) in methanol (15 mL) and the solution was stirred for 30 minutes. The resultant brown solution was concentrated and water was added until a precipitate formed. This was removed via filtration and dried. Crystals suitable for x-ray diffraction were obtained via slow vapour diffusion from trifluoroethanol using diethyl ether as the anti-solvent. Approximates as having 0.5 trifluoroethanol molecules per formula unit. 0.20 g, 71.0%.

CHN analysis: calcd. from $C_{32}H_{38}B_2F_8FeN_{10}{\cdot}0.5CF_3CH_2OH$ C, 47.06; H, 4.73; N, 16.63%. Found C, 47.30; H, 5.15; N, 16.60%.

ES^+ mass spectrum: Shows only free ligand at *m/z* 282.2 $[\mathbf{L^{14}}]^+$.

^1H NMR δ_H (300 MHz, METHANOL-*d*6) 1.0 (s, 9 H, $C(CH_3)_3$), 20.6 (s, 3 H, CH_3), 23.0 (s, 1 H, Py H^4), 48.7 (s, 1 H, Pz $H^{4'}$), 53.0 (s, 1 H, Pz $H^{4''}$), 56.3 (s, 1 H, Py H^3), 60.1 (s, 1 H, Py H^5).

IR mid: $\nu(O\text{-}H)_{water}$ = 3200-3500 cm^{-1} (m), $\nu(C\text{-}H)$ = 2968 cm^{-1} (m), $\nu(B\text{-}F)$ = 1037 cm^{-1} (vs).

7.3.44. $[Fe(L^{15})_2](ClO_4)_2{\cdot}0.5C_7H_8\ CH_3NO_2$ [20]

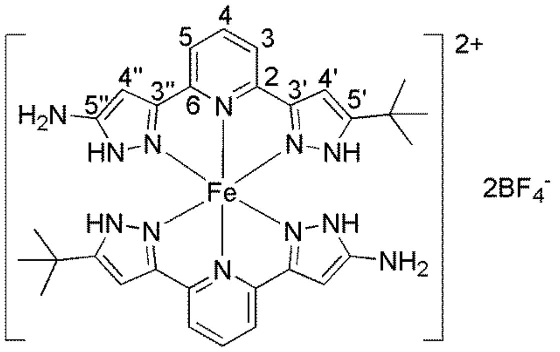

5-[6-(5-tert-Butyl-1*H*-pyrazol-3-yl)-pyridin-2-yl]-1*H*-pyrazol-5-ylamine (0.20 g, o.7 mmol) was suspended in nitromethane (15 mL) and iron perchlorate hydrate (0.10 g, 0.4 mmol) was added. The mixture slowly bagan to dissolve into a brown solution. This was then layered with toluene to give a brown precipitate which was removed via filtration. Approximates as one nitromethane and 0.5 toluene molecules per formula unit. 0.20 g, 69.0 %.

CHN analysis: Calcd. from $C_{30}H_{36}Cl_2FeN_{12}O_8{\cdot}0.5C_7H_8$ CH_3NO_2 C, 44.72; H, 4.68; N, 19.65 %. Found C, 44.50; H, 4.60; N, 19.60 %.

ES^+ mass spectrum: Shows only free ligand at *m/z* 283.17 [$\mathbf{L^{15}}$]$^+$.

^{1}H NMR δ_H (500 MHz, CHLOROFORM-*d*) 6.3 (s, 18 H, C(CH_3)$_3$), 31.8 (br. s., 2 H, Py H^4), 53.9 (br. s., 2 H, Pz $H^{4'}$), 56.7 (br. s., 2 H, Pz $H^{4''}$), 63.0 (br. s., 2 H, Py H^3), 65.8 (br. s., 2 H, Py H^5).

IR mid: ν(O-H)$_{water}$ = 3200-3500 cm^{-1} (m), ν(C-H) = 2968 cm^{-1} (m), ν(B-F) = 1063 cm^{-1} (vs).

7.3.45. [Fe($\mathbf{L^{16}}$)$_2$](ClO$_4$)$_2$

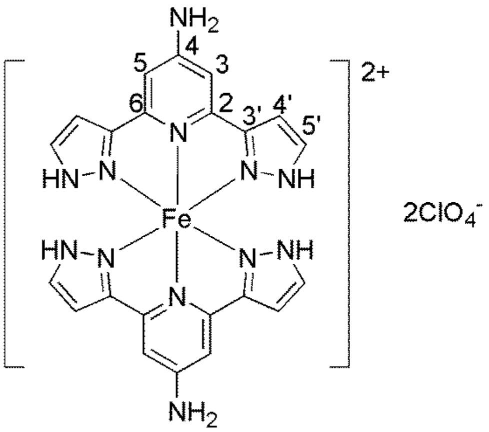

2,6-Di(1*H*-pyrazol-3-yl)-pyridin-4-ylamine (0.10 g, 0.4 mmol) was dissolved in methanol (15 mL) and iron(II) perchlorate hydrate (0.06 g, 0.2 mmol) was added. After stirring for 1 hour diethyl ether was added to the solution until a brown precipitate formed, which was removed via filtration and dried. 0.03 g, 19.1 %

CHN analysis: Calcd. from $C_{22}H_{20}Cl_2FeN_{12}O_8$ C, 37.36; H, 2.85; N, 23.77%. Found C, 38.70; H, 3.30; N, 21.00%.

ES^+ mass spectrum: shows only free ligand at *m/z* 227.1 [$\mathbf{L^{16}}$H]$^+$.

^{1}H NMR δ_H (500 MHz, ACETONITRILE-d_3) 46.1 (br. s., 4 H, Pz H^5), 47.7 (br. s., 4 H, Pz H^4 or Py $H^{3/5}$), 49.1 (br. s., 4 H, Pz H^4 or Py $H^{3/5}$), 78.0 (br. s., 4 H, Pz NH).

IR mid: ν(N-H) = 3472 cm^{-1} (m), ν(C-H) = 2960 cm^{-1} (w), ν(Cl-O) = 1083 cm^{-1} (vs).

7.3.46. [Fe(L1^{7})$_2$](ClO$_4$)$_2$

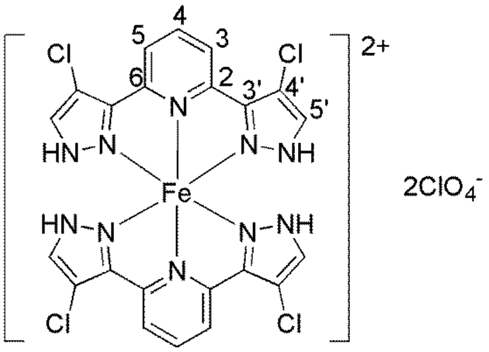

2,6-Di(4-chloro-1*H*-pyrazol-3-yl)-pyridine (0.10 g, 0.4 mmol) was suspended in methanol (15 mL) and iron(II) perchlorate hydrate (0.04 g, 0.2 mmol) was added. The mixture was stirred at room temperature for 30 minutes before being filtered. Diethyl ether was added to the filtrate and the resulting microcrystalline orange solid was removed via filtration. 0.034 g, 20.9%.

CHN analysis: Calcd. from $C_{22}H_{14}Cl_6FeN_{10}$ C, 32.42; H, 1.73; N, 17.19%. Found C, 31.50; H, 1.55; N, 16.30%.

^{1}H NMR δ_H (501 MHz, METHANOL-d_4) 13.6 (br. s., 2 H, Py H^4), 35.8 (br. s., 4 H, Pz H^5 or Py$H^{3/5}$), 38.8 (br. s., 4 H, Pz H^5 or Py$H^{3/5}$).

IR mid: ν(N-H) = 3134 cm^{-1} (m), ν(C-H) = 2926 cm^{-1} (w), $\nu(C{=}C)_{\text{aromatic}}$ = 1607 cm^{-1} (m), ν(Cl-O) = 1039 cm^{-1} (vs).

7.3.47. [Fe(L^{18})$_2$](ClO$_4$)$_2$·CH$_3$OH

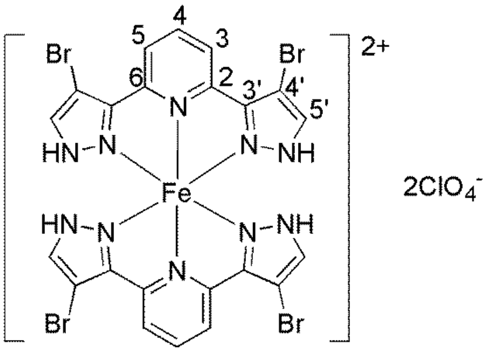

2,6-Di(4-bromo-1*H*-pyrazol-3-yl)pyridine (0.20 g, 0.7 mmol) was suspended in methanol (15 mL) and iron(II) perchlorate hydrate (0.09 g, 0.3 mmol) was added. The mixture was stirred for 1 hour until a brown solution was formed. The mixture was filtered and diethyl ether was added to the filtrate until a red precipitate formed. The precipitate was isolated via filtration and washed with ether. Microanalysis shows the complex approximates as the methanol solvate, which is also confirmed by the crystal structure. 0.15 g, 51.6 %.

CHN analysis: calcd. from $C_{22}H_{14}Br_4Cl_2FeN_{10}O_8{\cdot}CH_3OH$ C, 26.96; H, 1.77; N, 13.67 %. Found C, 27.15; H, 1.50; N, 14.20 %.

ES^+ mass spectrum: *m/z* 391.89 [$\mathbf{L^{18}}$Na]$^+$.

^1H NMR δ_H (501 MHz, METHANOL-d_4) 11.3 (br. s., 2 H, Py H^4), 23.7 (br. s., 4 H, Pz H^5 or Py$H^{3/5}$), 24.6 (br. s., 4 H, Pz H^5 or Py$H^{3/5}$).

IR mid: ν(N-H) = 3134 cm^{-1} (m), ν(C-H) = 2926 cm^{-1} (w), $\nu(C{=}C)_{aromatic}$ = 1607 cm^{-1} (m), ν(Cl-O) = 1039 cm^{-1} (vs).

7.4. Chapter 5:
Iron(II) Complexes Incorporating 2,6-Di(5-methyl-1*H*-pyrazol-3-yl)pyridine and Resulting Perchlorate and Tetrafluoroborate Solid Solutions

7.4.1. $[Fe(L^9)_2](BF_4)_2{\cdot}2H_2O$[21]

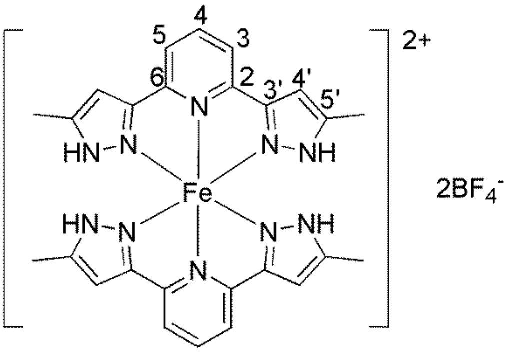

2,6-Di(5-methyl-1*H*-pyrazol-3-yl)pyridine (0.40 g, 1.7 mmol) was dissolved in methanol (15 mL) and iron(II) tetrafluoroborate hexahydrate (0.28 g, 0.8 mmol) was added. The solution was then stirred for 30 minutes at room temperature before diethyl ether was added until a precipitate formed. The dark red precipitate was then removed via filtration, washed with diethyl ether and dried. 0.50 g, 88.2%

CHN analysis: calcd. from $C_{26}H_{26}FeN_{10}B_2F_8{\cdot}2H_2O$ C, 41.97; H, 4.06; N, 18.83%. Found C, 42.30; H, 4.00; N, 18.80%.

ES^+ mass spectrum: *m/z* 240.12 [$\mathbf{L^9}$H]$^+$.

^1H NMR δ_H (300 MHz, METHANOL-d_4): 18.8 (12 H, CH_3), 21.4 (2 H, Py H^4), 44.3, 51.0 (4 H, Py $H^{3/5}$ and Pz $H^{4'}$).

7.4.2. [Fe(L^9)$_2$](ClO$_4$)$_2$[22]

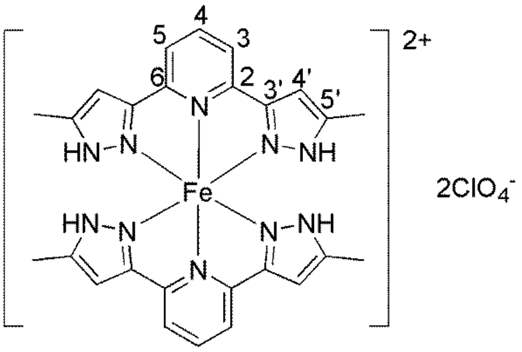

2,6-Di(5-methyl-1*H*-pyrazol-3-yl)pyridine (0.40 g, 1.7 mmol) was dissolved in methanol (15 mL) and iron(II) perchlorate hydrate (0.21 g, 0.8 mmol) was added. The solution was then stirred for 30 minutes at room temperature before diethyl ether was added until a precipitate formed. The dark red precipitate was then removed via filtration, washed with diethyl ether and dried. 0.42 g, 72.0%.

CHN analysis: calcd. from $C_{26}H_{26}FeN_{10}Cl_2O_8$ C, 42.59; H, 3.57; N, 19.10; Cl, 9.67%. Found C, 42.50; H, 4.00; N, 19.05; Cl, 9.35%.

ES$^+$ mass spectrum: *m/z* 240.12 [**L**^{9}H]$^+$.

^{1}H NMR δ_H (300 MHz, METHANOL-*d*$_4$): 18.9 (12 H, C*H*$_3$), 21.5 (2 H, Py *H*^{4}), 44.3, 51.0 (4 H, Py *H*$^{3/5}$ and Pz *H*$^{4'}$).

7.4.3. 9:1 (BF$_4$:ClO$_4$) Complex Mixture

9(BF$_4$)$_2$ (100 mg, 0.14 mmol) and **9**(ClO$_4$)$_2$ (12 mg, 0.02 mmol) were dissolved methanol (2 mL). The solution was then filtered and set up for slow vapour diffusion with diethyl ether at 4°C. Quantitative.

7.4.4. 3:1 (BF$_4$:ClO$_4$) Complex mixture

9(BF$_4$)$_2$ (29 mg, 0.04 mmol) and **9**(ClO$_4$)$_2$ (10 mg, 0.01 mmol) were dissolved methanol (2 mL). The solution was then filtered and set up for slow vapour diffusion with diethyl ether at 4°C. Quantitative.

CHN analysis: calcd. from $C_{26}H_{26}FeN_{10}Cl_{0.5}O_2B_{1.5}F_6\cdot 2H_2O$ C, 42.64; H, 3.85; N, 19.13; Cl, 2.42%. Found C, 41.80; H, 3.95; N, 18.50; Cl, 2.30%.

7.4.5. 1:1 (BF_4:ClO_4) Complex Mixture

9(BF_4)$_2$ (677 mg, 1.00 mmol) and **9**(ClO_4)$_2$ (700 mg, 1.00 mmol) were dissolved methanol (2 mL). The solution was then filtered and set up for slow vapour diffusion with diethyl ether at 4°C. Quantitative.

CHN analysis: calcd. from $C_{26}H_{26}FeN_{10}ClO_4BF_4{\cdot}2H_2O$ C, 41.27; H, 4.00; N, 18.51; Cl, 4.69%. Found C, 41.50; H, 3.90; N, 18.40; Cl, 4.40%.

7.4.6. 1:3 (BF_4:ClO_4) Complex Mixture

9(BF_4)$_2$ (32 mg, 0.04 mmol) and **9**(ClO_4)$_2$ (100 mg, 0.14 mmol) were dissolved methanol (2 mL). The solution was then filtered and set up for slow vapour diffusion with diethyl ether at 4°C. Quantitative.

CHN analysis: calcd. from $C_{26}H_{26}FeN_{10}Cl_{1.5}O_6B_{0.5}F_2{\cdot}2H_2O$ C, 40.93; H, 3.96; N, 18.36; Cl, 6.97%. Found C, 41.10; H, 3.80; N, 17.90; Cl, 6.50%.

7.5. Chapter 6:

Ruthenium Transfer Hydrogenation Catalysts Based on 2,6-Di(1*H*-pyrazol-3-yl)pyridine Derivatives

7.5.1. [Ru(L^6)(PPh_3)$_2$]$Cl_2{\cdot}H_2O$[23]

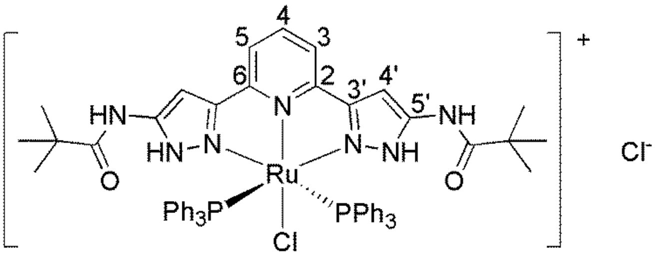

Dichloro*tris*(triphenylphosphine)ruthenium(II) (0.36 g, 0.4 mmol) and 2,6-Di(5-*tert*butylamido-1*H*-pyrazol-3-yl)pyridine (0.15 g, 0.4 mmol) were suspended in dry dichloromethane (15 mL) and stirred for 3 hours at room temperature. The solvent was reduced and diethyl added to form a precipitate which was removed via filtration. Washed with diethyl ether to remove excess triphenyl phosphine and dried in air. 0.11 g, 27.4 %.

CHN analysis: calcd. from $C_{57}H_{57}Cl_2N_7O_2P_2Ru{\cdot}H_2O$ C, 60.91; H, 5.29; N, 8.72; Cl, 6.31 %. Found C, 60.50; H, 5.30; N, 9.20; Cl, 6.10 %.

ES^+ mass spectrum shows free ligand at *m/z* 410.23 [$\mathbf{L}^6$H]$^+$.

^{1}H NMR δ_H (500 MHz, DMSO-d_6) 1.25 (s, 18 H, CH_3), 7.20 (s, 2 H, Pz H^4), 7.22 - 7.46 (m, 24 H, aromatic), 7.54 - 7.97 (m, 9 H, aromatic).

$^{31}P\{^1H\}$-NMR δ_P (121 MHz, CHLOROFORM-*d*) 34.8 (s, *P*Ph$_3$).

IR mid: *v*(O-H)$_{water}$, *v*(N-H)$_{amide}$ = 3100-3400 cm^{-1} (w), *v*(C-H) = 3055 cm^{-1} (w), *v*(C=O) = 1645 cm^{-1} (m).

7.5.2. [Ru(L^7)(PPh$_3$)$_2$]Cl$_2$[23]

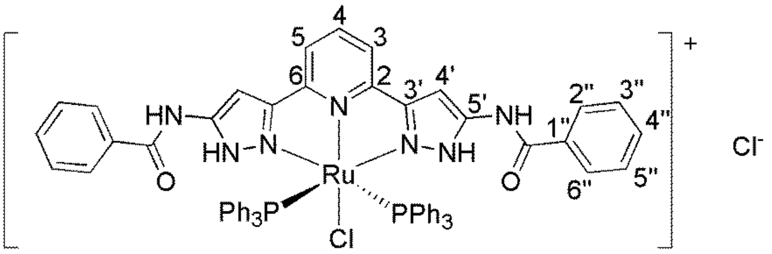

2,6-Di(5-benzylamido-1*H*-pyrazol-3-yl)pyridine (0.17 g, 0.4 mmol) and dichloro*tris*(triphenylphosphine)ruthenium(II) (0.36 g, 0.4 mmol) were suspended in dry dichloromethane (~50 mL) and the mixture was stirred at room temperature for 12 hours. Diethyl ether was added until a white precipitate formed which was removed via filtration (uncoordinated ligand). The filtrate was then evaporated to leave a yellow solid. 0.25 g, 59.5 %.

CHN analysis: calcd. from $C_{61}H_{49}Cl_2N_7O_2P_2Ru$ C, 63.93; H, 4.31; N, 8.56 %. Found C, 63.30; H, 4.30; N, 8.70 %.

^1H NMR δ_H (300 MHz, CHLOROFORM-*d*) 6.73-7.39 (m, 30 H, PPh$_3$), 7.41 (d, *J*=7.7 Hz, 4 H, Bz $H^{2''/6''}$), 7.49-7.59 (m, 4 H, Bz *H*), 7.70 (t, *J*=7.7 Hz, 1 H, Py H^4), 7.79 (d, *J*=7.2 Hz, 2 H, Py $H^{3/5}$).

$^{31}P\{^1H\}$ NMR δ_P (121 MHz, CHLOROFORM-*d*) 36.5 (s, *P*Ph$_3$).

IR mid: *v*(O-H)$_{water}$, *v*(N-H)$_{amide}$ = 3100-3400 cm^{-1} (w), *v*(C-H) = 3055 cm^{-1} (w), *v*(C=O) = 1681 cm^{-1} (m).

7.5.3. [Ru(L^9)(PPh$_3$)$_2$]Cl$_2$·H$_2$O[23]

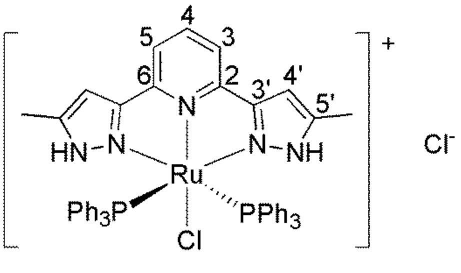

Dichloro*tris*(triphenylphosphine)ruthenium(II) (0.36 g, 0.4 mmol) and 2,6-di(5-methyl-1*H*-pyrazol-3-yl)pyridine (0.09 g, 0.4 mmol) were suspended in dry dichloromethane (15 mL) and stirred for 3 hours at room temperature. The solvent was reduced and diethyl added to form a precipitate which was removed via filtration. Washed with diethyl ether to remove excess triphenyl phosphine and dried in air. Crystals suitable for x-ray diffraction were obtained via slow vapour diffusion from methanol/diisopropyl ether. 0.23 g, 90.7 %.

CHN analysis: Calcd. from $C_{47}H_{43}Cl_2N_5P_2Ru{\cdot}H_2O$ C, 59.06; H, 4.53; N, 10.26; Cl, 7.42%. Found C, 59.10; H, 4.60; N, 7.50; Cl, 7.60%.

ES$^+$ mass spectrum: calcd. from $C_{31}H_{28}ClN_5PRu^+$ 638.08 g mol^{-1}. Found *m/z* 638.08.

^{1}H NMR δ_H (300 MHz, METHANOL-d_4) 2.21 (s, 6 H, CH_3), 6.37 (s, 2 H, Pz H^4), 7.01 (d, J=7.7 Hz, 2 H, Py $H^{3/5}$), 7.09 - 7.35 (m, 33 H, PPh$_3$ and Py H^4).

^{31}P{^{1}H} NMR δ_P (121 MHz, CHLOROFORM-*d*) 24.4 (s, *P*Ph$_3$).

IR mid: ν(O-H)$_{water}$ = 3100-3300 cm^{-1} (w), ν(C-H) = 2901 cm^{-1} (w), ν(C=C)$_{aromatic}$ = 1653 cm^{-1} (m).

7.5.4. [Ru(L^{10})(PPh$_3$)$_2$]Cl$_2$·H$_2$O[23]

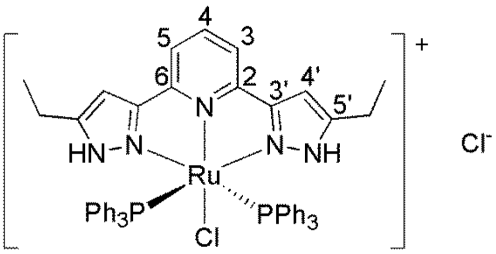

Dichloro*tris*(triphenylphosphine)ruthenium(II) (0.36 g, 0.4 mmol) and 2,6-di(5-ethyl-1*H*-pyrazol-3-yl)pyridine (0.10 g, 0.4 mmol) were suspended in dry dichloromethane (15 mL) and stirred for 3 hours at room temperature. After this time a precipitate had formed which was removed via filtration and washed with diethyl ether to remove excess triphenyl phosphine. 0.24 g, 66.5 %.

CHN analysis: calcd. from $C_{51}H_{47}Cl_2N_5P_2Ru{\cdot}H_2O$ C, 62.38; H, 5.03, N, 7.13; Cl, 7.22 %. Found C, 62.20; H, 5.10; N, 7.40; Cl, 7.20 %.

ES$^+$ mass spectrum: calcd. from $C_{51}H_{47}ClN_5P_2Ru^+$ 928.20 g mol^{-1}. Found *m/z* 928.20.

^{1}H NMR δ_H (300 MHz, METHANOL-d_4) 1.06 (t, J=7.6 Hz, 6 H, CH$_2$CH_3), 2.56 (q, J=7.6 Hz, 4 H, CH_2CH$_3$),6.40 (s, 2 H, Pz H^4), 7.00 (d, J=7.8 Hz, 2 H, Py $H^{3/5}$), 7.08 - 7.32 (m, 31 H, PPh$_3$ and Py H^4).

^{31}P{^{1}H} NMR δ_P (121 MHz, METHANOL-*d*4) 24.4 (s, *P*Ph$_3$).

IR mid: ν(O-H)$_{water}$ = 3100-3300 cm^{-1} (w), ν(C-H) = 3052 cm^{-1} (w), ν(C=C)$_{aromatic}$ = 1559 cm^{-1} (m).

7.5.5. [Ru(L^{12})(PPh_3)$_2$]Cl_2·$2H_2O$[23]

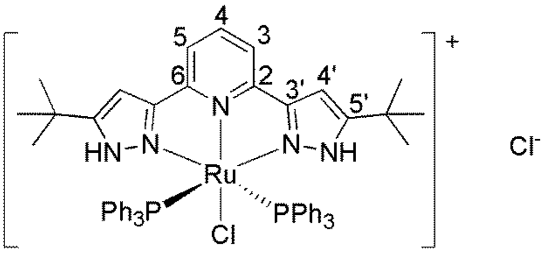

$RuCl_2(PPh_3)_3$ (0.36 g, 0.4 mmol) and 2,6-Bis(5-*tert*but-1*H*-pyrazol-3-yl)pyridine (0.09 g, 0.4 mmol) were suspended in dry dichloromethane (15 mL) and stirred for 3 hours at room temperature. The solvent was reduced and diethyl added to form a precipitate which was removed via filtration. Washed with diethyl ether to remove excess triphenyl phosphine and dried in air. Crystals suitable for x-ray diffraction were obtained from deuterated chloroform. 0.29 g, 76.9 %.

CHN analysis: calcd. from $C_{55}H_{55}Cl_2N_5P_2Ru\cdot 2H_2O$ C, 62.55; H, 5.63; N, 6.63; Cl, 6.71 %. Found C, 61.90; H, 5.40; N, 6.30; Cl, 6.80 %.

ES^+ mass spectrum: calcd. from $C_{55}H_{55}N_5P_2RuCl$ 984.27 g mol^{-1}. Found *m/z* 984.27.

^1H NMR δ_H (300 MHz, CHLOROFORM-*d*) 1.14 (s, 18 H, CH_3), 6.30 (s, 2 H, Pz H^4), 6.92 (d, *J*=7.9 Hz, 2 H, Py $H^{3/5}$), 7.01 - 7.18 (m, 31 H, aromatic), 12.05 (br. s, 2 H, Pz N*H*).

$^{31}P\{^1H\}$ NMR δ_P (121 MHz, CHLOROFORM-*d*) 23.7 (s, *P*Ph_3).

IR mid: ν(C-H) = 3052, 2962 cm^{-1} (w), $\nu(C=C)_{aromatic}$ = 1611 cm^{-1} (m).

7.5.6. [Ru(L^{12})(OH_2)(PPh_3)$_2$](PF_6)$_2$

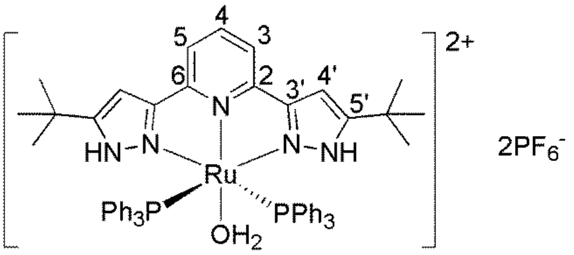

[Ru(**L**^{12})(PPh_3)$_2$]Cl_2 (0.10 g, 0.01 mmol) was dissolved in dichloromethane (15 mL) and silver hexafluorophosphate (0.05 g, 0.02 mmol) was added. The mixture was filtered and the filtrate evaporated. 0.11 g, 91.4 %.

CHN analysis: Calcd. from $C_{55}H_{55}F_{12}N_5P_4Ru\cdot H_2O$ C, 52.55; H, 4.57; N, 5.57%. Found C, 51.60; H, 4.40; N, 5.30%.

^1H-NMR δ_H (300 MHz, METHANOL-d_4) 1.22 (s, 18 H, CH_3), 6.53 (br. s, 2 H, Pz $H^{4'}$), 7.03-7.35 (m, 33 H, PPh_3, Py $H^{3/4/5}$).

$^{31}P\{^1H\}$ NMR δ_P (121 MHz, METHANOL-*d*4) 23.9 (s, *P*Ph_3), -144.6 (hept, *J*=751 Hz, PF_6).

IR mid: ν(C-H) = 2963 cm^{-1} (w), $\nu(C=C)_{aromatic}$ = 1653 cm^{-1} (m), ν(P-F) = 846 cm^{-1} (s)

7.6. References

[1] E. M. Schubert, *J. Chem. Educ.* **1992**, *69*, 62.

[2] D. F. Evans, *J. Chem. Soc.* **1959**, 2003-2005.

[3] S. A. D. W. A. Felsing, *J. Am. Chem. Soc.* **1926**, *48*, 2885-2893.

[4] G. Sheldrick, *Acta Crystallographica Section D* **2010**, *66*, 479-485.

[5] A. L. Spek, *J. Appl. Crystallogr.* **2003**, *36*, 7-13.

[6] O. V. Dolomanov, L. J. Bourhis, R. J. Gildea, J. A. K. Howard and H. Puschmann, *J. Appl. Crystallogr.* **2009**, *42*, 339-341.

[7] E. Bejan, H. A. Haddou, J. C. Daran and G. G. A. Balavoine, *Synthesis* **1996**, 1012-1018.

[8] S. A. J. L. Y. I. Lin, *J. Heterocycl. Chem.* **1977**, *14*, 345-347.

[9] C. M. Che, C. F. Chow, M. Y. Yuen, V. A. L. Roy, W. Lu, Y. Chen, S. S. Y. Chui and N. Zhu, *Chem. Sci.* **2011**, *2*, 216-220.

[10] T. D. Roberts, M. A. Little, L. J. Kershaw Cook, S. A. Barrett, F. Tuna and M. A. Halcrow, *Polyhedron* **2013**, *64*, 4-12.

[11] K. A. Ali, *Arkivoc* **2010**, *11*, 55-63.

[12] C. M. Pask, C. A. Kilner, and M. A. Halcrow, *Tetrahedron Lett.* **2006**, *47*, 2531-2534.

[13] Y. Zhou, W. Chen and D. Wang, *Dalton Trans.* **2008**, 1444-1453.

[14] G. A. Craig, L. A. Barrios, J. S. Costa, O. Roubeau, E. Ruiz, S. J. Teat, C. C. Wilson, L. Thomas and G. Aromí, *Dalton Trans.* **2010**, *39*, 4874-4881.

[15] D. G. Markees and G. W. Kidder, *J. Am. Chem. Soc.* **1956**, *78*, 4130-4135.

[16] P. V. Ivchenko, I. E. Nifant'ev and I. V. Buslov, *Tetrahedron Lett.* **2013**, *54*, 217-219.

[17] M. McLaughlin, K. Marcantonio, C. Y. Chen and I. W. Davies, *J. Org. Chem.* **2008**, *73*, 4309-4312.

[18] L. J. Kershaw Cook in *Crystal Engineering and Bifunctionality in Spin-Crossover Materials*, *PhD* University of Leeds, **2013**.

[19] R. Pritchard, H. Lazar, S. A. Barrett, C. A. Kilner, S. Asthana, C. Carbonera, J. F. Létard and M. A. Halcrow, *Dalton Trans.* **2009**, 6656-6666.

[20] T. D. Roberts, M. A. Little, L. J. Kershaw Cook and M. A. Halcrow, *Dalton Trans.* **2014**.

[21] T. D. Roberts, F. Tuna, T. L. Malkin, C. A. Kilner and M. A. Halcrow, *Chem. Sci.* **2012**, *3*, 349-354.

[22] T. D. Roberts, M. A. Little, F. Tuna, C. A. Kilner and M. A. Halcrow, *Chem. Commun.* **2013**, *49*, 6280-6282.

[23] T. Jozak, D. Zabel, A. Schubert, Y. Sun and W. R. Thiel, *Eur. J. Inorg. Chem.* **2010**, 5135-5145.

Conclusions and Future Work

In this work a number of novel ligands based on the 2,6-di(1*H*-pyrazol-3-yl)pyridine structure, bearing substituents on the pyridine *C*4 and pyrazolyl *N*1, *C*4 and *C*5 positions have been successfully synthesised. These synthetic pathways were discussed in detail in Chapter 2. Substitution with alkyl groups at the pyrazolyl *N*1 position proceeded favourably to give the desired ligands in high purity, however this pathway is not suitable for attaching sp^2 hybridised centres such as benzene. In an attempt to obtain this product phenyl hydrazine was used in the pyrazole ring formation instead of hydrazine, however this resulted in a mixture of isomers which could not be separated. Additional work could attempt to attach a pyridyl group to the pyrazolyl *N*1 position, as pyridines are more susceptible to S_NAr and whether 2-halopyridine or 4-halopyridine is used could result in differing hydrogen bonding networks and topologies. Methods were also used which allowed the substitution of substituents on the pyrazolyl *C*5 position. This was largely successful and allowed alkyl, amino, amido, thiourea and pyridyl groups to be placed on the pyrazole *C*5 position. In the instance of *tert*butyl groups the incompleteness of the reaction allowed asymmetrically substituted 3-bpp ligands to be synthesised, which are the first of their kind in the literature. Substitution at the pyridyl *C*4 position proved troublesome, but eventually 2,6-di-(1*H*-pyrazol-3-yl)-pyridin-4-ylamine ($\mathbf{L^{16}}$) was successfully synthesised, however in poor yields. As a result further modifications at this position could not be carried out, so improving the synthetic pathway towards pyridyl *C*4 substituted 3-bpp ligands requires more work.

These novel ligands, along with some which have already been synthesised in the literature were then used to make their respective iron(II) and ruthenium(II) complexes in order to elucidate the existence of any structure/function relationships which may exist. Iron(II) complexes made using 3-bpp ligands substituted at the pyrazolyl *N*1 position show that their bulk phases are all fully HS over the entire temperature range. For the bulkier substituents such as the *iso*propyl, allyl and benzyl groups this behaviour is expected as these groups could clash with the ligand backbone upon the contraction of the coordination sphere accompanying a HS→LS transition. Methyl substituents, however, are not expected to hinder a spin transition and iron(II) complexes of isomeric 1-bpp ligands do show SCO behaviour. Indeed, it was observed in the crystal structure of $[\mathrm{Fe}(\mathbf{L^1})_2](\mathrm{BF_4})_2{\cdot}\mathrm{H_2O}$ that one symmetrically inequivalent iron centre was partially HS, making it a promising candidate for SCO. The bulk phase, however, showed no such behaviour and remained fully HS over the entire temperature range. The bulk phase was shown to be different to that of the single crystal by PXRD which is likely to be due to the loss of water over time. The difference in the behaviour of the iron(II) complexes of $\mathbf{L^1}$ and those of its isomeric 1-bpp equivalent is likely to be a result of subtle steric and electronic factors.

In Chapter 4 the effect on the corresponding iron(II) complexes of a number of modifications to the 3-bpp structure were investigated. It appears that retaining the pyrazolyl NH functionality can lead to hydrogen bonding and a number of different topologies. Perhaps the most pronounced of these structures is that of the complex $[Fe(\mathbf{L}^5)_2](ClO_4)_2{\cdot}2(C_2H_5)_2O{\cdot}CH_3NO_2$ which exhibits an interpenetrating, 3-dimensional hydrogen bond network between dications and anions which shares similarities with the fluorite topology. It was expected that this complex would show a high degree of cooperativity and possibly show a hysteretic, discontinuous spin transition. This seems to be the case, however due to the instability of this complex magnetic measurements could not be performed on a phase pure sample. Complexes of ligands bearing bulky groups on the pyrazolyl *C*5 position, such as the *tert*butylamido groups of $\mathbf{L}^6$, can result in a large distortion of the iron coordination sphere favouring the HS state. In this case the energy required to rearrange the surrounding lattice required for a HS→LS transition is too great and the complex remains trapped in the HS state over the entire temperature range. The substitution of alkyl groups onto the pyrazolyl *C*5 position generally gave complexes with continuous spin transitions, indicating a lack of cooperativity. The magnetic susceptibility of these complexes in acetone solution suggests that the addition of alkyl groups to the pyrazolyl *C*5 position stabilises the HS state and increases $T_{1/2}$. The opposite behaviour is expected by inductive effects and perhaps density functional calculations may provide an explanation for this behaviour. Also in Chapter 4, an interesting reaction of the complex $[Fe(\mathbf{L}^{15})_2](ClO_4)_2$ resulted in two ligands in adjacent complex molecules becoming linked by a six-membered ring formed from two acetone molecules. It is uncertain whether this reaction is the result of the properties of the ligand itself, or if it is somehow mediated by the iron. Further mechanistic studies would be required to fully understand this observation.

Chapter 5 was concerned with the synthesis of mixed anion complexes of the type $[Fe(\mathbf{L}^9)_2](BF_4)_x(ClO_4)_{2-x}$ in order to understand the differences between the isostructural perchlorate and tetrafluoroborate salts. The effects of thermal cycling and thermal scan rate were investigated on these complexes after repeated scanning the 1:1 (BF_4:ClO_4) mixture showed seemingly bizarre magnetic behaviour. This behaviour is believed to be a result of the dependence of this sample on the thermal scan rate involving a kinetically slow transition from HS→LS. Therefore when a scan rate of 5 K min^{-1} was used, the complex appeared to be trapped in the HS state and showed a magnetic profile similar to the pure perchlorate. Reducing the scan rate, however, shows an incomplete two-step transition in the cooling mode and what initially appears to be a reverse spin transition in the warming mode. This behaviour could follow a mechanism similar to that observed in the LIESST effect, where the complex is trapped in a metastable state at low temperatures but slowly increasing the temperature eventually allows it to relax to the more thermodynamically stable LS state. Thermal cycling at a rate of 0.5 $Kmin^{-1}$ shows an asymmetric, hysteretic spin transition with a two-step HS→LS conversion and a single, abrupt LS→HS conversion. Because of this slow kinetic conversion between the two spin states it would be interesting to conduct LIESST experiments on this sample to determine the lifetime of the metastable excited state.

Some of the novel 3-bpp ligands synthesised in Chapter 1 were then employed to make ruthenium(II) pincer type complexes for applications in transfer hydrogenation. In Chapter 6 a number of these complexes were synthesised and their efficacy as catalysts determined. The formation of two isomers, where the triphenylphosphine ligands are either *cis* or *trans*, complicated the synthesis of the catalysts. While they could be separated based on their differing solubilities this separation did not always occur cleanly and greatly reduced the yield of these complexes. Because of this full optimisation of the catalytic reaction could not be done, however the relative activities of this series of complexes remains valid. In addition a chlorido complex was exchanged with PF_6 to give $[Ru(\mathbf{L}^{12})(PPh_3)_2]PF_6$ which was shown to have a water molecule coordinating to the site *trans* to the bpp ligand. The more labile water molecule was expected to make binding of the substrate easier, thus speeding up the reaction. As expected $[Ru(\mathbf{L}^{12})(PPh_3)_2]PF_6$ showed the highest catalytic activity of these complexes. It was desirable to make the PF_6 salts of other complexes, however this was not possible due to either low yields of the chloride or re-equilibration of the isomers during the salt exchange. Additional work in this area should focus on the acquisition of the ruthenium complexes in sufficient isomeric purity and yield in order to allow the formation of more PF_6 salts and a more comprehensive catalytic study, which would include the TH of a wider range of substrates.